Thermomechanical behaviour of interface between pavement layers in bituminous mixtures

Thien Nhan Tran

Thesis National Number: 2024ENTP0006

A THESIS OF ENTPE
Member of the Université de Lyon

Doctoral school N° 162
Mécanique, Energétique, Génie Civil et Acoustique (MEGA)
To obtain the graduation of
PhD in Civil Engineering

Publicly defended the 04th of April 2024 by:
Thien Nhan Tran

Thermomechanical behaviour of interface between pavement layers in bituminous mixtures

---

In front of the following examination committee:

HAMMOUM Ferhat, DR1 HDR, University Gustave Eiffel	President/Examiner
RAAB Christiane, Prof. Dr., EMPA	Reviewer
GRAZIANI Andrea, Prof., Marche Polytechnic University, Italy	Reviewer
SAUZEAT Cédric, ICTPE HDR, Prof., ENTPE	Supervisor
MANGIAFICO Salvatore, Dr, ENTPE	Co-supervisor
DI BENEDETTO Hervé, Prof. emeritus, ENTPE	Co-supervisor
ATTIA Thomas, Dr, Eiffage Route	Co-supervisor

Numéro national de thèse (NNT) : 2024ENTP0006

THÈSE DE DOCTORAT DE L'ENTPE
Membre de l'Université de Lyon

École Doctorale N° 162
Mécanique, Energétique, Génie Civil et Acoustique (MEGA)
Spécialité / discipline de doctorat :
Génie Civil

Soutenue publiquement le 04/04/2024, par :
Thien Nhan Tran

Comportement thermomécanique de l'interface entre couches de chaussée en enrobé bitumineux

---

Devant le jury composé de :

HAMMOUM Ferhat, DR1 HDR, Université Gustave Eiffel	Président/Examinateur
RAAB Christiane, Prof. Dr., EMPA	Rapporteure
GRAZIANI Andrea, Prof., Università Politecnica delle Marche	Rapporteur
SAUZEAT Cédric, ICTPE HDR assimilé Prof., ENTPE	Directeur de thèse
MANGIAFICO Salvatore, Dr, ENTPE	Co-encadrant
DI BENEDETTO Hervé, Prof. émérite, ENTPE	Co-encadrant
ATTIA Thomas, Dr, Eiffage Route	Co-encadrant

TABLE OF CONTENTS

ACKNOWLEDGEMENTS

I would like to express in few words my thankfulness to all the people who encouraged and helped me during my PhD project and this manuscript.

I sincerely thank and admire Dr. Cédric Sauzéat, my supervisor, for his direction and encouragement during the research. I truly appreciate all of the time he gave me to go through technical issues with the equipment, to listen patiently to my ideas, and to give me advice. I appreciate all the compliments he gave me after my presentations at international conferences. That is for sure an encouragement, so that I will always trust myself.

My co-advisors, Dr. Salvatore Mangiafico, Dr. Thomas Attia, and Prof. Hervé Di Benedetto, have been instrumental in the successful completion of this PhD project. I really appreciate the opportunity to work with them.

I also want to express my gratitude to the members of my PhD defense committee, Dr. Ferhat Hammoum, who served as the president of the jury, Dr. Chistiane Raab, and Dr. Andrea Graziani, who served as reviewers of my dissertation. The discussions with them during the defense were really fruitful. That was a scientific exchange and practice for me before starting my professional career in pavement engineering.

I also appreciate the valuable time I spent with my colleagues in the laboratory. I had great discussions, whether they were scientific or just small talks. The barbecues in the park Miribel Jonage during summers with Nuh, Frank, Yufeng, Xin, Youneng, Alexiane, etc. became one of my best memories in Lyon. Such an occasion helps me to understand you and your amazing journeys in France.

I would like to thank the company Eiffage for providing materials for this PhD project. I cannot forget to thank the technicians for their assistance with the apparatus and sample preparation. Thanks, Joachim Blanc Gonnet, Stéphane Cointet, and Romain Vintejoux.

During more than five years in France for my master's degree and then PhD thesis, I returned to see my family only once. That was hard for my family, and with the COVID-19 complications, I know they worried too much for me. I want to apologize and thank them for letting me do what I love and live my life as I wish.

Thank you, my dear friend Raphael Heinzmann, for being there for me. He was the one who helped me through all of the difficult moments since the day I moved to France. He and

his family offer me a place to come every Christmas, so that I feel like I belong here in Europe. With him and his family, I never feel alone.

Finally, I would like to thank François Munoz for our great time in the Alpes. I look forward to starting new adventures with him. I really appreciate his endless help.

ABSTRACT

Most pavement design methods assume that the interface between bituminous layers shows a perfect bonding capacity throughout its service life. However, the actual behaviour of the interface in all mechanical behaviour domains needs to be studied and implemented into the design methods. An apparatus (2T3C hollow cylinder apparatus) has been developed at the University of Lyon/ENTPE and integrated with 3D Digital Image Correlation (3D-DIC) in order to investigate the behaviour of bituminous interfaces. The focus of the thesis is the investigation of various thermomechanical behaviours, including Linear ViscoElasticity (LVE), Visco-Elasto-Plastic behaviour, non-linearity and fatigue behaviour of the interface and two bituminous mixture layers in shear mode. To accomplish this, the shear complex modulus tests include various combinations of two global shear strains (50 µm/m, and 200 µm/m), three axial stresses (-0.026 MPa, -0.125 MPa, and -0.250 MPa), five temperatures (between 0 °C and 40 °C) and five frequencies (from 0.01 Hz to 1 Hz). Fatigue tests were performed at a global shear strain of 50 µm/m, combined with three axial stresses (-0.026 MPa, -0.125 MPa, and -0.250 MPa), a loading frequency of 3 Hz (the measurement of complex moduli and stiffness was conducted during three loading cycles of 1 Hz). Fatigue tests were conducted at a temperature of 10 °C. To determine the effects of applied global shear strain on fatigue behaviour, two additional fatigue tests were performed at the same temperature and frequency as the initial fatigue tests, each with an axial stress of -0.026 MPa and global shear strain amplitudes of 150 µm/m and 200 µm/m. The tested samples are double-layered hollow cylinders with a bitumen emulsion interface and two layers of different materials. Three residual bitumen contents were applied (250 g/m^2, 350 g/m^2, and 450 g/m^2) and two types of bitumen (a pure 160/220 pen-graded bitumen, and a polymer modified bitumen).

From the experimental campaign, the interfaces validate the Time Temperature Superposition Principle (TTSP) and show the LVE behaviour as the samples are loaded with a global shear strain of 50 µm/m combined with the aforementioned axial stresses, temperatures, and frequencies. The experimental data were successfully simulated using the 2S2P1D LVE model. However, the model cannot simulate the complex interface stiffness applied at the higher global strain amplitude (200 µm/m) because of an underestimation of the phase angle. The DBN_{PDSC} model is then used and fits well with experimental phase angle. The variation of

interface configurations does not significantly affect the thermomechanical behaviour of the interface.

Fatigue test results at the interfaces show good repeatability. Six fatigue criteria were recommended according to the evolution the complex interface stiffness, the evolution of the shear stress inside the samples and the displacement gap at the interface, as well as the evolution of the dissipated energy of the interface during the fatigue tests. Wöhler curves were built based on these fatigue criteria. The modification of pure bitumen with a polymer (SBS) significantly improves the fatigue behaviour of the interfaces.

INTRODUCTION

Road pavements are constructed of several layers over a subgrade layer. Although each layer fulfils a distinct function, they collectively bear the load of traffic and transmit it to the subgrade and the natural ground. In accordance with their respective functions, the layers are constructed with different material compositions and thicknesses. A solid pavement structure is capable of withstanding the effects of weather and traffic loads throughout its service life. Additionally, it must provide security and comfort for both vehicles and passengers. The adjacent asphalt layers within a pavement structure are bonded with bitumen, which may be applied either as a heated product or as an emulsion. The layers are intentionally bonded perfectly. The durability of a pavement structure is significantly influenced by the adhesive coat's ability to bond firmly at the interface. The deterioration of the tack coat over time as a result of weather and traffic loading may cause premature failures to a pavement structure. It is unlikely that optimal bonding at the interface will be preserved throughout the pavement structure’s service lifespan.

In order to gain a more comprehensive understanding of the real behaviour occurring at the interface, various experimental setups have been utilised both in situ and in laboratory. These devices are capable of applying monotonic or cyclic shear loading, as well as varying temperatures and loading rates, to samples within laboratory settings. Nevertheless, a prevalent drawback of these apparatuses is the presence of non-homogeneous stress and strain (or displacement) fields at the interface, which prevents the ability to determine the intrinsic properties of the interface.

The 2T3C hollow cylinder apparatus, developed at the Laboratoire de Tribologie et Dynamique des Systèmes (LTDS, UMR 5513) of the University of Lyon/Ecole Nationale des Travaux Publics de l’Etat (ENTPE), enables the application of quasi-homogeneous stress and strain fields in two mixture layers. The apparatus is capable of applying cyclic loading in both tension/compression and torsion modes. It is equipped with four cameras and a 3D Digital Image Correlation (3D-DIC) technology system, which enables the analysis of the behaviour of the interface.

This thesis aims to investigate the Linear ViscoElastic (LVE) behaviour, Visco-Elasto-Plastic behaviour, nonlinearity behaviour and fatigue behaviour of the interface, as well as the two bituminous mixture layers. In order to achieve the stated objectives, three distinct

experimental campaigns will be implemented, each utilising a different combination of shear strain amplitudes and number of loading cycles.

The manuscript will be structured in five chapters.

Chapter 1 presents a literature review examining the material scale of a pavement, comprising aggregates, sand, filler, and binder, as well as the structural scale. In addition, emphasis will be placed on the pivotal role of interfaces between bituminous layers in a pavement structure. To assess the behaviour of an interface, a combination of in-situ and laboratory-based methodologies has been developed. Some of them will be discussed in detail in the present chapter. In addition, several models will be presented to characterise the thermomechanical behaviour domains of an interface and bituminous mixture in layers.

In Chapter 2, the 2T3C hollow cylinder apparatus (2T3C stands for "Torsion, Traction, Compression sur Cylindre Creux" in French or "Torsion, Tension, Compression on Hollow Cylinder" in English) is introduced. This apparatus was developed at the University of Lyon/ENTPE with the purpose of investigating the thermomechanical properties of the interface between bituminous layers. The computational method used to determine the displacement gap at the interface and the strain in each layer is based on displacement fields obtained from three-dimensional digital image correlation (3D-DIC) analysis of two pairs of cameras.

Chapter 3 outlines the testing protocols for double-layered hollow cylinders using the 2T3C Hollow Cylinder Apparatus. The first section presents an analysis of the material compositions found at the interface and in bituminous layers. The fabrication of the slabs and the procedures for samples preparation are described in detail. The next sections introduce the three realized experimental campaigns. In the experimental campaign #1, the complex shear modulus test was performed with a small strain amplitude and a small number of cycles. The experimental campaign #2 introduced the non-linearity tests with a combination of five shear strain amplitudes and a small number of loading cycles. The experimental campaign #3 was dedicated to shear fatigue behaviour of the interface and the two bituminous layers. This was achieved by combining small strain amplitudes with high numbers of loading cycles.

Chapter 4 provides a comprehensive investigation of the results obtained from the shear complex modulus tests and the nonlinearity tests. Initial section provides a step-by-step explanation of the calculation of the complex interface stiffness and complex modulus of bituminous layers using the 2T3C Hollow Cylinder Apparatus and the Digital Image Correlation (DIC) system.

In Chapter 5, the equipment utilised to analyse the fatigue properties of double-layered hollow cylinder specimens with emulsified bituminous tack coat interfaces is described. The fatigue behaviour of the bituminous layers and the interface from different configurations will be analysed.

In its concluding section, the manuscript emphasizess the significance of the findings presented in this thesis and delineates potential avenues for future research.

Figure I is a flowchart describing the content of the manuscript.

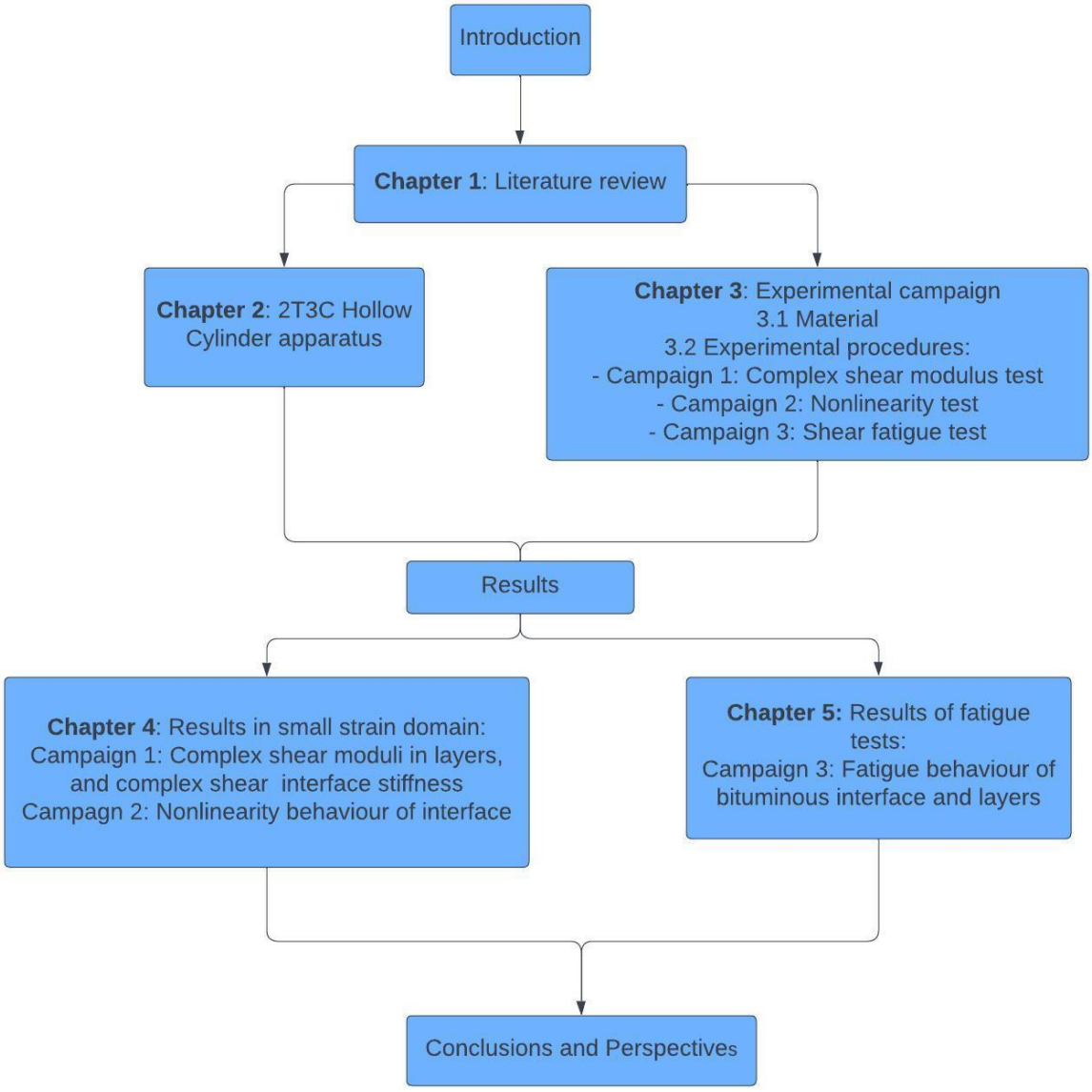

Figure I: Flow chart of the manuscript

Chapter 1:LITERATURE REVIEW

Chapter 1 presents a literature review on the material scale of a pavement including aggregates, sand, filler and binder. Some insights into the structural scale of a pavement will be introduced. Furthermore, the importance of interfaces between layers in a pavement structure will be highlighted. In order to assess the interface behaviour, several approaches have been developed, both in situ and in laboratory. This chapter will present some of these approaches. Finally, some models will be introduced to characterise interfaces and bituminous mixtures in different domains of thermomechanical behaviour.

1.1 Bituminous materials

1.1.1 Aggregate

Crushed stone is mined and then processed in a crushing system. This type of aggregate is more suitable for asphalt mixes because of their angular shapes. The shapes of particles play an important role in maintaining the stable condition of the whole structure. Therefore, if they are too flat or/and elongated, they are not selected for asphalt mixes (Speight, 2016b).

Fine aggregates used in bituminous mixes are sand. Sand can be natural or manufactured. The manufactured sand is more angular than the natural one, so it is more preferred in asphalt mixes (Speight, 2016b)

Aggregates are the main component of dense or open graded bituminous mixtures, which constitute 95% of the total mass and 80-85% of the total volume (Di Benedetto & Corté, 2004). Aggregates constitute the skeleton of the mixture. They receive traffic loadings and transmit them to lower layers. Aggregates are exploited from natural resources. Also, various technologies of operating and grinding generate different shapes of aggregates particles. These differences will have an impact on the behaviour of the general structure because the shapes of granular particles (round or distorted particle, angular, or not angular surface) influence the interface or connection between particles in the mixture.

Besides the shape and the angularity of particles, aggregates have to meet all of the below requirements. These prerequisites make sure that aggregates have sufficient mechanical and physical properties to work in a bituminous mixture (Mangiafico, 2014):

- freeze/thaw resistance;
- polishing resistance;
- binder/aggregate compatibility.

Aggregates are classified in groups of sizes, in which d is the minimum size, and D is the nominal maximum size of that group. According to the European Standard (NF EN 13043, 2003), the lower (d) and upper (D) sieve sizes used to classify aggregates. The D/d ratio must not exceed 1.4 to avoid the size dispersion within a category. The aggregates are separated using the standard sieves in the European Standard.

1.1.2 Filler

Filler particles pass through a 0.063 mm sieve. As stated by Csanyi (1962), the purpose of incorporating filler into a bituminous mixture is to fill the voids that are created by the coarse aggregate. This results in a bitumen mixture that is more compacted, stable, and rigid. In combination with bitumen, a filler-bitumen mastic is produced wherein filler particles are either encapsulated in bitumen or mixed with it in a colloidal and mechanical suspension. An excessive quantity of filler increases the material's fragility, susceptibility to cracking, and stability. Conversely, a reduced quantity of filler results in a composition containing a greater volume of air voids, making it more unstable and softer.

Two kinds of filler are listed in the European Standard (NF EN 13043, 2003):

- Natural fillers are crushed from larger aggregates to expected sizes. In a conventional bituminous mixture, the percentage of natural filler can range from 4 to 6%.
- The added filler is manufactured in commercial companies to achieve filler content in a mixture and to obtain some mechanical properties (Nouffou Tapsoba, 2012). This filler can contribute 1 to 6% by the total mass of a mix. Some of the popular added fillers are limestone and hydrated lime, which were proved to enhance the adhesive between them and bitumen.

As mentioned above, the percentage of filler in an asphalt mixture is up to 6% of a total mass. Moreover, in some special aggregate gradations, for example stone mastic asphalt (SMA), the content of filler is relative higher than 6%. In a SMA mix, a high percentage of bitumen and filler generates a strong mastic stabilizing the aggregate skeleton’s working condition.

1.1.3 Binder

Bitumen is defined as a hydrocarbon mixture derived from crude oil through the process of refining. Additionally, natural bitumen deposits mines are found in various locations around the world. Bitumen is a binder that possesses unique flexible characteristics. This makes bitumen an essential material for the construction and maintenance industry. Furthermore,

bitumen can resist the effects of acids, alkalis, and salts (G.Speight, 2016). The process of dilution or fractionation of the constituent components of crude oil is conducted within a steel tower. The tower incorporates steel containers with perforations, which facilitate the upward movement of vapour within the tower. In addition, each hole is adorned with a bubble cap that transforms the orientation of the vapor's movement into that of a condensed liquid. The temperatures of hydrocarbon gases fall below their respective boiling points when subjected to controlled temperatures in containers, resulting in the condensation of these gases into liquids. The tower's temperature proceeds upwards as it ascends (Read & Whiteoak, 2003).

Bitumen is a colloidal system comprised of a variety of functional groups and species, including sulphur, nitrogen, and oxygen atoms, in addition to hydrocarbons. The composition of the colloidal constituents is contingent upon the crude oil source from which bitumen is extracted, in addition to the manufacturing processes employed in bitumen production. However, bitumen constituents can be classified chemically into asphaltenes and maltenes (with maltenes subsequently being refined into aromatics, saturates, and resins (Figure 1.1)) (Read & Whiteoak, 2003).

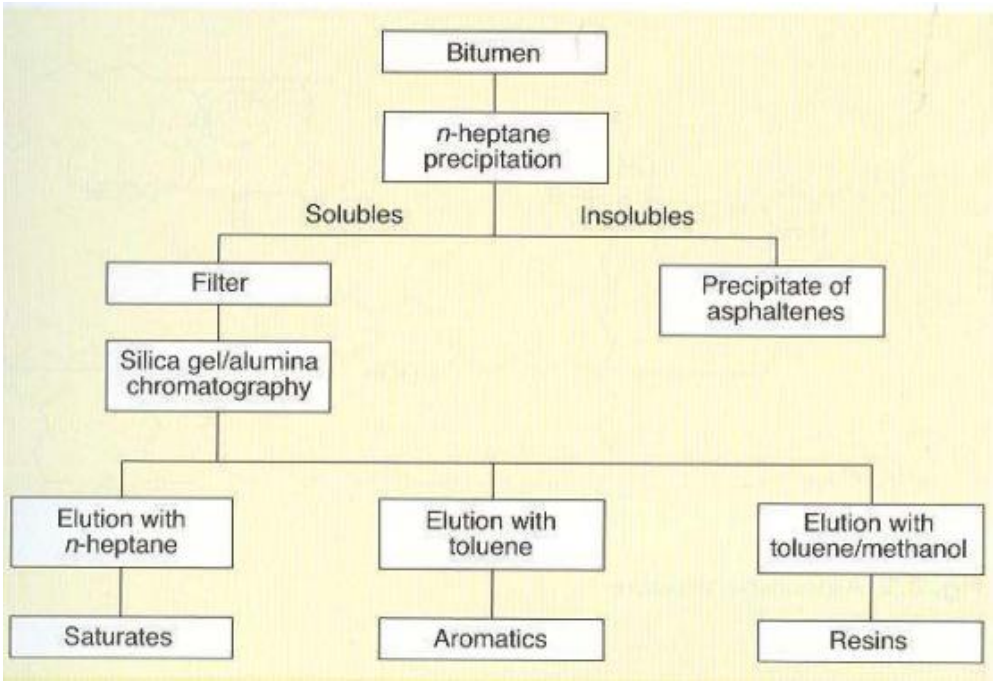

Figure 1.1: Chemical composition of bitumen (Read & Whiteoak, 2003)

Those four main components of bitumen are described by (Di Benedetto & Corté, 2004; Yarranton, 2000) as below:

- Asphaltenes comprise a quantity ranging from 5% to 25% of the overall bulk of bitumen. They are solid phases that are dark, amorphous, and insoluble in n-heptane. These substances are complex aromatic substances that are quite polar.

Their molecular weights vary between 1000 and 100,000 g/mol, and their particle sizes span from 5 to 30 nm.

- Resins exhibit solubility in n-heptane. They are solid or semi-solid, dark in colour, and extremely polar and adhesive. Resins function as asphaltene peptizers, preserving asphaltene particles in the colloidal medium. A molecule of resin has an approximate mass of 500,000 g/mol and a diameter of 1 to 5 nm.
- Aromatics are viscous dark substances with the smallest molecular weights, ranging from 300 to 2000 g/mol. Nevertheless, they account for the largest proportion (40–65%) of the overall mass of bitumen. They are non-polar carbon chains.
- Saturates are non-polar viscous oils composed of aliphatic hydrocarbons with straight and branch chains. Saturates comprise between 2 % and 20 % of the total mass of bitumen.

Bitumen is used as a glue or a binder when it is mixed with aggregates. The combination of bitumen and filler is called mastic ensuring the interlock between aggregate particles during the service life and construct the stiffness of bituminous mixtures. In a bituminous mixture, bitumen is mixed with fine and coarse aggregates, with or without additives. The mixing process occurs at high temperatures in mixing plants. Mixtures are later transported to working site, spread, and paved on top of a subgrade or an existing bituminous layer. The bituminous layers support the traffic loadings and transmit them the lower layers (Speight, 2016a). The mastic also works as the waterproofing material which does not allow water permeate into the pavement structure and deteriorate it. Furthermore, emulsified bitumen is used as an interlayer of bituminous layers which generate the bonding between bituminous layers, and allow the whole pavement working together in a structure, limiting the tensile stress or strain at the bottom of asphalt layer (Attia et al., 2020; Attia, Benedetto, et al., 2021). In emulsified bitumen, bitumen is mixed with water and an emulsifier in this composition. The emulsion agents facilitate the stable suspension of bitumen within the water medium. Bituminous emulsion has the multiple potential of serving as either at an interface between bituminous layers or a constituent in cold bituminous mixtures. Cold bituminous materials are regarded as environmentally friendly and energy-efficient materials with lower environmental impact (Lévenard et al., 2023).

Several tests may be performed to classify bitumen in different grades. Three of the most important and popular tests in the world nowadays are penetration test and softening point

test; which is also called rings and balls test, and the rolling thin-firm oven test (RTFOT).

- The penetration test (NF EN 1426, 2018) consists of measuring the penetration of a needle in the bitumen for five seconds. This test allows for the evaluation of the consistency of bitumen. The standard weight of the needle is 100g. The test can be performed at several temperatures, but 25°C is the retained temperature for classification.
- The softening point test (NF EN 1427, 2018) the result obtained is a temperature at which steel balls of 3.5g placed on the surface on a bitumen fall and touch a base plate 25 mm below the ring. The heating rate is 5°C in a minute.
- The rolling thin-firm oven test (RTFOT) (NF EN 12607-1, 2014) is used to test the hardening of bitumen undergone the oxidation and evaporation processes. An amount of 35 ±0.5 g of bitumen is poured into a glass container which is then rotated at 163 ^{0}C for 75 minutes. The air is blown into each container every 3 to 4 seconds. The purpose of this test is to evaluate the change of bitumen properties after the ageing process. Therefore, the resulting bitumen can be used to compare the penetration point at 25°C or softening point with the initial bitumen.

Table 1.1 below, extracted from (EN 13924-2, 2014) shows the classification of neat bitumen using in the road construction.

Table 1.1: Specifications for multi-grade bitumen

Property	Test method	Unit	Class			
			1	2	3	4
Penetration at 25°C	(NF EN 1426, 2018)	0.1 mm	Declared value by manufacturer	20 to 30	35 to 50	50 to 70
Softening point	(NF EN 1427, 2018)	°C	Declared value by manufacturer	54 to 64	59 to 69	64 to 74

As can be seen from Table 1.1, bitumen is graded by how deep a needle penetrate into it at 25°C. However, the disadvantage of this grading system is that bitumen is classified at one

temperature (25^{o}C), while bitumen has complex behaviours, they behave differently in different levels of temperature and frequency (Read & Whiteoak, 2003).

1.1.4 Bituminous mixtures

By mixing bitumen and aggregates at a high temperature, hot mix asphalt is produced. By weight, the mixture comprises approximately 95% aggregate (Di Benedetto & Corté, 2004). The significance of aggregate distribution or gradation is dependent on the task performed by the bituminous layer. In specific cases, the paving surface that is utilised to improve slip resistance or discharge precipitation may be thin and less resistant to traffic. In such cases, the aggregate gradation should be permeable and open, with a reduced filler content. However, a solid aggregate skeleton composed of highly angular particles typically facilitates the transfer of traffic loading across layers within a road structure. Bitumen comprises an approximate 5% weight percentage of the mixture, and combined with filler to impart rigidity to the entire mixture and bolster the aggregate skeleton's stability (Di Benedetto & Corté, 2004).

The temperature, loading frequency, loading amplitude, and number of cycles all influence the thermomechanical behaviour of a bituminous mixture. Di Benedetto & Corté (2004) provided a description of the dependency in Figure 1.2. A bituminous mixture exhibits linear viscoelastic behaviour when subjected to a small number of cycles and a small amplitude of strain. Nevertheless, fatigue damage occurs in the materials when the strain amplitude is applied for a significant number of repetitions. Non-linear behaviour is observed in bituminous mixtures when a high strain amplitude is applied within a few repetitions. Alternatively, the material may sustain rutting damage when subjected to a greater number of repetitions at a high strain amplitude.

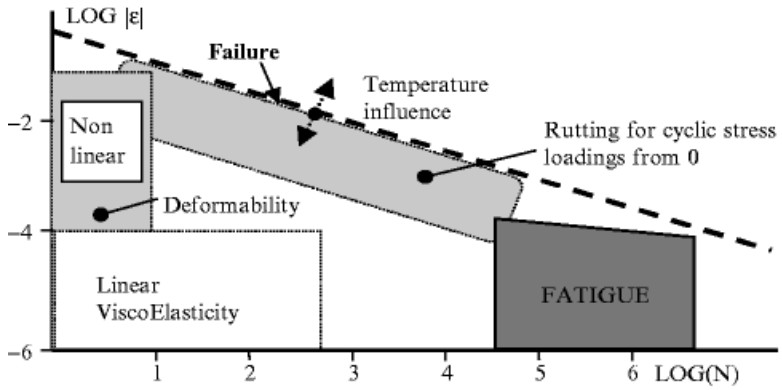

Figure 1.2: The mechanical behaviour of bituminous mixtures (Di Benedetto & Corté, 2004)

1.1.5 Bituminous emulsions

The phenomenon wherein one liquid becomes dispersed into another is referred to as an

emulsion. Additionally, bitumen emulsion refers to the process by which bitumen is dispersed in water. In contrast to solutions, however, they coexist independently rather than being combined. As described in Section 1.1.3, bitumen is a dense colloidal mixture of asphaltenes and maltenes. Overall, bitumen exhibits non-polarity, with electrons dispersed throughout its constituent molecule. As a consequence, bitumen in general does not exhibit charge concentration. Water, on the contrary, is a polar medium. Electrons accumulate in the vicinity of oxygen atoms, imparting a negative charge to the oxygen, before departing with a positive charge around hydrogen atoms. An emulsifier is a two-tailed surface activator that possesses opposing properties. One tail is hydrophobic, or abhorrent to water, while the other is oleophobic, or averse to oil, but attracted to water. Surfactants generally fall into three distinct categories: anionic, cationic, and nonionic (Needham, 1996). Once a bitumen emulsion is applied, the emulsifier becomes more attracted to the surface of aggregates after a brief period, after which it departs from the bitumen (Lévenard et al., 2023). Bitumen retains its original properties on the surface to which it is applied, while the water in the emulsion evaporates into the atmosphere. The bitumen emulsion can be used for cold bituminous pavement, since the hot paving process is not required. That economises the consumed energy during the application, and is environmental-friendly. The bitumen emulsion is also applied as a tack coat at the surface between two bituminous layers, keeps the pavement working in the whole structure.

1.2 Flexible pavement structure and design method

A road pavement is a multi-layered structure, as illustrated on Figure 1.3, which is constructed atop a subgrade layer. Each layer plays its own role, but they together receive the traffic loading and transfer to the subgrade and the natural ground. Based on their roles, layers are designed differently in term of materials used and thicknesses. In general, a good pavement structure can withstand the traffic loadings, weather conditions during its service life. It should also provide the safety and comfort to users and vehicles travelling on it. Layers in a pavement structure are generally described as follows (SETRA-LCPC, 1994):

- **The surface course** comprises the uppermost layer of a pavement structure. As a result, the surface course serves numerous functions within the structure. It initially receives the traffic loads, transfers them to subsequent layers, and ensures the passengers' comfort. It must be impermeable to water throughout the entire structure. Conversely, the surface course must enhance adhesion with vehicle tyres and prevent slipping. To reduce surface water in rainy regions, a special layer with a high air-void ratio can be constructed on top. Occasionally, the surface course is compacted into two distinct

layers: the wearing course and the binder course. They are composed of bonded materials with bitumen serves as a binder.

- Underneath, **the base course** serves as an intermediate layer. It receives the traffic and climate loading from the surface course and transfer them to the subgrade. Base course is a layer that strengthen the mechanical behaviour of the whole structure. This layer comprises bound materials which is a bituminous mixture. Base course can be found in many cases divided into two or three sublayers. Under the base course, a subbase course can be paved with unbound granules.
- Under the base course, **a subbase course** can be paved with unbound granules.
- **The subgrade layer**: this layer is the lowest layer in a pavement structure, and has a direct interaction with the natural ground. It is natural soil with passages of compacting rollers to increase the stiffness or treated soil with hydraulic binder.

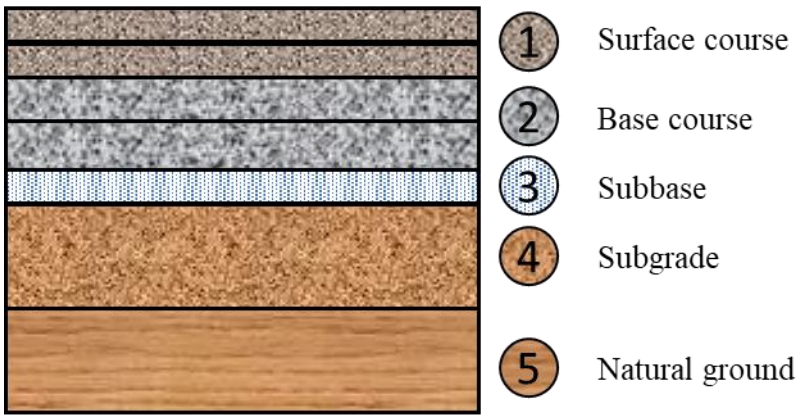

Figure 1.3: Scheme of a typical pavement structure

The French design guide (SETRA-LCPC, 1994) presents a number of typical flexible pavement structures.

A flexible pavement has its surface course and base course made of bituminous mixtures. These layers can be different regarding the bitumen, and the aggregate gradation curves. The thickness of surface course is 5 cm and that of basecourse is 15 cm. They are paved on top of a 20 cm subbase of unbound granular materials.

For a higher traffic loading, a thick bituminous pavement is preferred. The number and order of layers are kept the same with the regular flexible pavement. However, the base course of bituminous mixtures has a thickness up to 40 cm.

The mixed structure can be also served for the high traffic demand. Instead of increasing the thickness of the bituminous layer in the base course up to 40 cm, the mixed structure keeps

the same thickness as it is in the flexible pavement. However, to support the high traffic a hydraulic bound material can be built under the bituminous base course as a second base course.

The road design method in France was developed by the Laboratoire Central des Ponts et Chaussées (LCPC) and Service d'Etudes sur les Transports, les Routes et leurs Aménagements (SETRA) (SETRA-LCPC, 1994). The method is based on mechanical principles and takes into account road pavements as multilayered structures. The Burmister's model is considered for calculation of stress and strain in the pavement structure. Layers are assumed to be homogeneous, elastic and isotropic. The interface between layers can be in one of three configurations: perfectly bounded, completely unbounded, and semi-bounded. The design procedure comprises six stages:

I. The pre-designed pavement structure is proposed. The first step consists of choosing materials that satisfy some requirements for uniformity, adherence, draining, photometric, and acoustic.

II. The second step devote to calculate stresses and strains using the Burmister model. The calculation is applied to the pre-designed structure. The loading is presented by a reference semi-axle load of 65 kN applies to two discs (as dual tyres) of 0.125 m in radius and 0.375 m from one to the other. This is equivalent to the compression of 0.662 MPa applied uniformly to the whole area of two discs.

III. The third step keen on verifying fatigue behaviour and strain in sub-grade. By using results from the previous calculation in step II, the stresses and strains will be compared with admissible values. These values are obtained considering the traffic during the service life, the fatigue endurance of material, thermal behaviour, admissible risks during the service life.

IV. The fifth step is used for the thickness adjustment. The chosen thickness will count on the constrain on the possible thickness range to satisfy the capacity and the uniformity. On the other hand, the chosen thicknesses have to reduce risks to interfaces between them.

V. The fifth step consider the behaviour of the designed structure faced to thermal effect which is freeze-thaw cycling.

VI. In the final step, the cross-section of a pavement structure is designed in accordance with the aforementioned verifications.

1.3 Types of loading to a bituminous structure

Pavement, being a multi-layered structure, experiences concurrent loadings throughout its service life. However, these loads can be categorised into two primary sources (Figure 1.4): traffic and climate (Di Benedetto & Corté, 2004):

Traffic applies the mechanical loads on a pavement. The amplitudes of the mechanical stresses exerted on a pavement by traffic are determined by the weights and velocities of the vehicles traversing the structure. That are intricate and varied in nature. The French design method employs a distinctive standard axle denoted by a double wheel in order to simplify the issue. A uniform vertical compression of 0.662 MPa is applied by the two wheels to all surfaces in contact with the pavement, which are denoted by two discs. The distance between the centres of the discs is 37.5 cm. Each disc has a diameter of 12.5 centimetres. When considering the entire structure, it can be observed that vertical tension induces flexion, resulting in compression at the top and tensile at the bottom (Attia, 2020). At interfaces where the structure is discontinuous, the tensile tension will be apparent at the bottom of the upper layer. Furthermore, the load transfer is irregular and not carried out according to design, resulting in some premature damage. Conversely, deepen to the structure tensile stress progressively replaces compression stress under wheels when the layers are firmly adhered. The structure withstands shear stress at the wheels' extremities and from a close distance from the wheels. Shear stress can be detected in a structure when sudden changes in the speed and direction of motion of a vehicle occur.

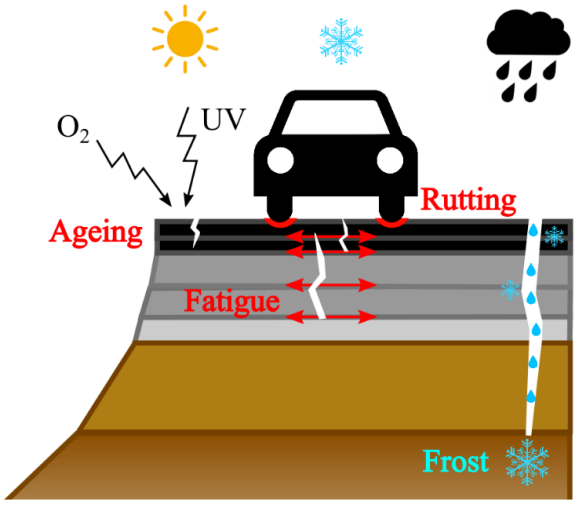

Figure 1.4: traffic and climate loading on a pavement structure and their responses (Attia, 2020)

The pavement structure can experience a variety of mechanical, physical, and chemical effects as a result of climate loadings. Oxygen in the air and sunlight can accelerate the ageing process of the bitumen in the mixture. Bitumen that has aged is generally more rigid and more vulnerable. Therefore, bitumen gradually transforms from a binder to a fracture-prone aggregate as a result of the ageing process. When combined with traffic loadings, temperature can cause a variety of pavement damage, including fatigue cracking and rutting. Rutting is the result of an excessive quantity of traffic passages. Two distinct forms of rutting have been identified: rutting with a large radius and rutting with a small radius. Rutting with a large radius is attributed to soil deformation in the subgrade layer or natural ground. Conversely, low-radius rutting is induced by heavy traffic and the viscous characteristics of bituminous materials when subjected to elevated temperatures. In addition, low temperature cracking can be generated within the bituminous materials. Temperature-induced expansion or shrinkage of a hydraulically bound material layer within a multi-layered structure can result in the formation of reflection cracks towards the upper layer of a hydrocarbon binder. In the event that fractures are initiated due to variations in temperature or heavy traffic, rainwater has the potential to infiltrate the structure and disrupt the orderly accumulation of loose materials in the subgrade layer and the natural ground. Frost-and-thaw is another type of damage caused by the combination of water and temperature. Existing water solidifies and subsequently expands in volume, generating stresses within the structure (Attia, 2020; Di Benedetto & Corté, 2004).

1.4 Interface in bituminous structures

The contact surface between layers is called interface. Since a pavement structure is a multi-layered structure, the interface can be found between bound or unbound materials, between two unbound materials, between two bound materials, or even between two bound materials from different binders. The tack coat's bitumen adheres to the lower layer's bituminous mixture. The application at high temperature of the bituminous mixture in the upper layer can result in a partial mixing of its bitumen and the bitumen from the tack coat. At the interface, the aggregates from both layers become entangled. Nevertheless, the embedment of the aggregates from the upper layer into the lower layer is constrained, resulting in a discontinuity in the contact between the layers. Figure 1.5 demonstrate an example of a real interface between two bituminous layers which does not show the continuity from one layer to the other.

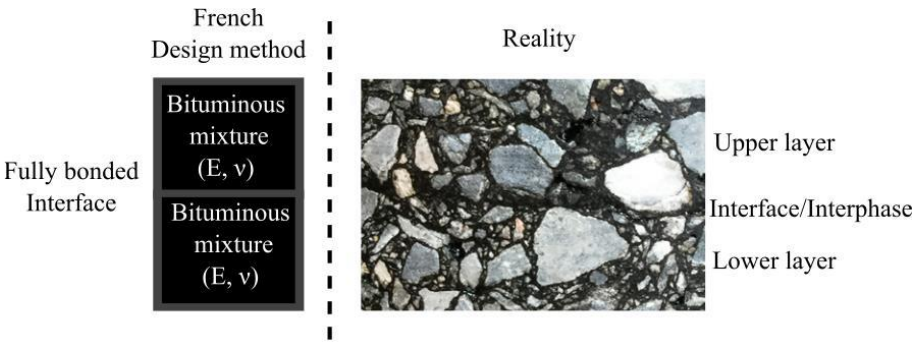

Figure 1.5: Double bituminous layer: interface modelled in the French design method on the left, interface from real pavement on the right (Attia, 2020)

Bituminous materials are complex materials, and the interface between them seems to be more complex. At the interface, tack coat is used to bind to two adjacent layers together. Hot-to hot compaction, on the other hand, is a method that does not require tack coat at the interface (Somé et al., 2020). This method basically requires the upper layer to be paved while the lower layer is still hot. Aggregates from the upper layer can embed to the lower layer with less restriction, and the bitumen from two layers adheres well at a high temperature. Somé et al. show that the samples from hot-to-hot compaction method have higher shear strength compared to samples compacted with the traditional method. However, this compaction method may pose a challenge in technology.

In the traditional compaction method; which is hot-to-cold method, the tack coat needs to be used. Before the application of the tack coat, the surface needs to be clean of durst and dry. After the application, any passage of truck is prohibited not to let the truck's tires remove the tack coat from the surface. The breaking time for tack coats is approximately four hours, although this may vary depending on the production technologies employed and the prevailing weather conditions on the day of application. The residual dosage of the tack coat varies in the range of 250 g/m^2 to 350 g/m^2 (NF P 98-150-1, 2010), depending on the surface to which it is applied. If the surface is rough (or there is a geogrid), a higher content should be chosen. The base bitumen before the emulsification can be either neat bitumen or a modified bitumen. The modification can be really important for some pavements in high traffic flow areas, and in areas with frequent changes of speed and direction, for example: intersections, roundabouts, areas in front of traffic lights, …

As a bituminous material, the tack coat also participates to the ageing process when it is exposed to environmental conditions. The aging process makes the bitumen stiffer and, more fragile. That turns bitumen from a bonding agent to a fragile solid, losing its working ability. The bituminous layers are assumed to be perfectly bonded or fully unbonded at the interface.

However, the aging is a long-term process and degrade the interface progressively during its service life. It is also important to mention that insufficient coat dosage, or a dirty applied surface, or incomplete breakage of the emulsion are factors that interfere with the assumption of a perfect bond at the interface. The imperfect bond leads to the discontinuity of stress and strain along the deep of a pavement structure. This imposes tensile stress to the bottom of the upper layer at the interface. It is possible to model the multi-layered bituminous pavement with bonded and unbonded interfaces by the software Alizé. Sauterey et al. (1972) show the important of a good bonding at the interface in reducing tensile strain at the bottom of layers (Figure 1.6). The results align well with the previous assumption about the tension strain appears at the bottom of each layer. An overestimation of bonding capacity of tack coat at the interface risks to overestimate the service life of a pavement structure. Premature deteriorations can take place at the unbonded interface and propagate into the pavement structure.

A rational pavement design method must consider the thermomechanical behaviour of interface in all domain. The introduction of interface stiffness in a normal working condition into the design method is necessary. Furthermore, its fatigue behaviour should also be studied and implemented to design methods.

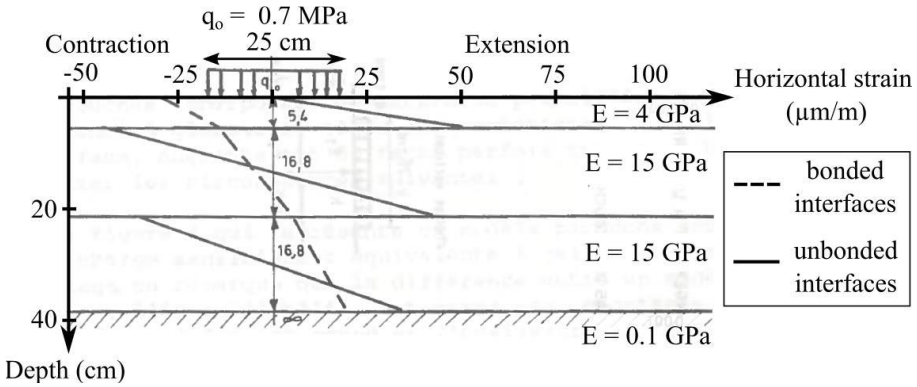

Figure 1.6: Interfaces between layers and the effect of bonding condition to strain distribution on a pavement structure (Sauterey et al., 1972)

1.5 Experiments on interfaces between bituminous layers

1.5.1 In situ tests

1.5.1.1 Coring

A pavement sample is drilled through with a core drilling equipment (Figure 1.7). A cored sample can be evaluated based on the materials in layers, and the interface between them. Cored samples can be tested in a laboratory for having more precise information. However, a quick visual check also reveals the states of materials and interface. A straightforward determination

can be obtained through a visual inspection of the interface to determine if it is bonded. As previously stated, a cored sample can be subsequently tested in the laboratory to study precisely its thermomechanical behaviour.

Figure 1.7: Pavement coring (source : (Liquidlabswa, n.d.))

1.5.1.2 Torque bond test

The torque bond test focuses on testing the interlayer strength of the first interface that is closest to a pavement surface. To accomplish this, a core drilling machine is employed to penetrate to a depth of a few centimetres into the second layer from the first. The sample is not extracted, but inner-cored surface is glued with cap of the torque bond test device. Subsequently, a torque will be applied manually in a constant speed until a failure appear at the interface (Figure 1.8). The results obtained from this test is shear bond strength.

Figure 1.8: Torque bond test device in-situ (Attia, 2020)

1.5.1.3 Ovalization test

The ovalization test was standardised in the French norm (NF P 98-203-1, 1997). It is necessary

to core the pavement, with a minimum of two penetrated layers prior to undertaking the test. The ovalization test initiates with the placement of sensors at different depth through the cored surface. The objective of the sensors is to determine the variation in diameter of the cored surface when a moving load is applied on the pavement surface. Strains in the upper and lower layers can be calculated based on the measured diameter variation. If no discontinuity at the interface appears in the measurement, layers are considered bonded. The behaviour of the interface could not be defined more precisely. An example of the ovalization test and measurements from sensors can be found on Figure 1.9.

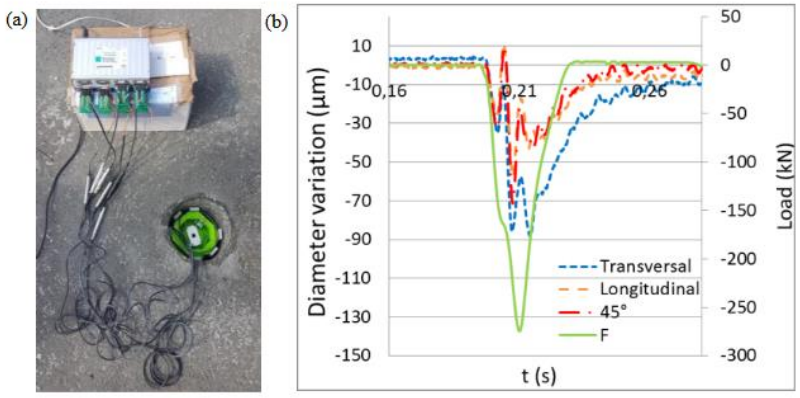

Figure 1.9: (a) Ovalization test set-up, (b) the measurements from sensors (Gharbi et al., 2020)

1.5.1.4. Ground-Penetrating Radar system (GPR)

GPR testing is a non-destructive method including two important components: the electromagnetic pulses sender and the electromagnetic signal receiver. The electromagnetic signal travels through a continuous material, but is reflected if there is a change in the materials. By analysing the reflected signals, it is possible to determine the thickness of layers and their status. The condition of interfaces in a pavement structure can be identified if there is any debonding issue. One advantage of this method is that it causes minimal disruption to traffic while the test is being conducted. Furthermore, the results obtained from this test are more representative of the entire testing site (not localised). A set-up of the GPR system is introduced on Figure 1.10.

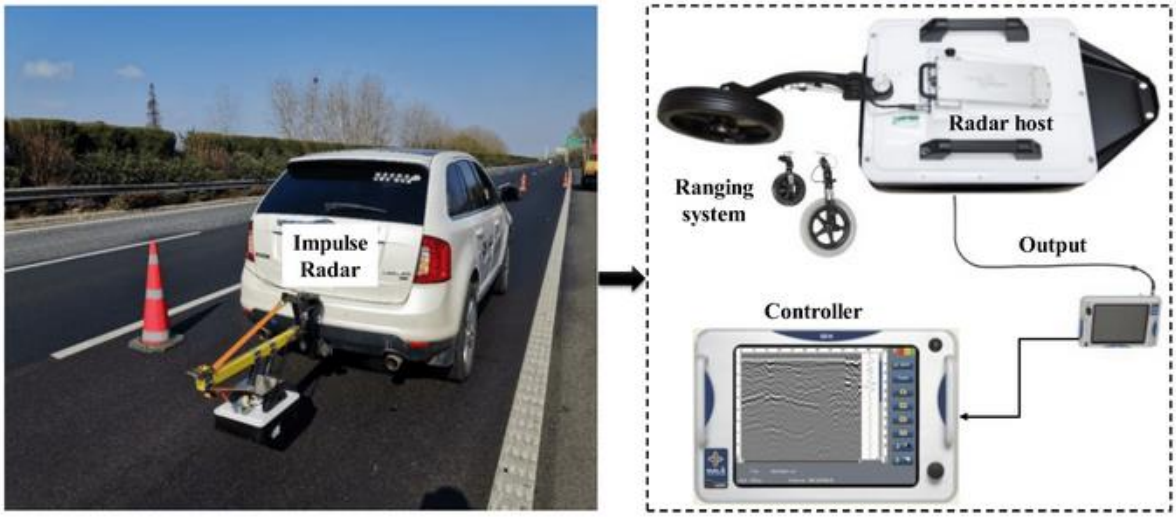

Figure 1.10: Ground-Penetrating Radar system (Liu et al., 2023)

1.5.1.5 Heavy weight Deflectometer (HWD)

The HWD testing system consists of a heavy weight of 720 kg falling from a certain height to a support (foot) of 45 cm in diameter. Geophones (or deflection sensors) are positioned from different distances to the impact (Attia, 2020; Roussel et al., 2019). A set-up of HDW can be seen in Figure 1.11. The wave from the shock propagates in the pavement and is recorded by geophones. The accelerations that comprise the unprocessed data are deduced to represent deflection. To generate the deflection basin, the maximum deflections measured from each geophone are graphed against their distances from the impact. Initially intended for the investigation of materials in layers, the system can deduce the mechanical behaviour of materials in layers by combining it with a back-calculation method. Moreover, the deflection measured at an imperfect interface is greater than that at an ideal interface. This can be utilised to identify interface defects.

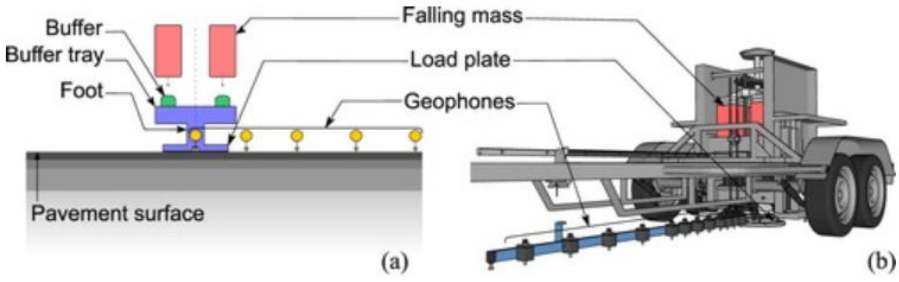

Figure 1.11: Heavy Weight Deflectometer (HWD) system: (a) loading and geophones; (b) overview of the HWD system (Roussel et al., 2019)

1.5.2 Laboratory tests

1.5.2.1 Leutner and modified Leutner tests

Leutner test was invented and named after the author (Leutner, 1979). The test consists in testing the shear strength of the interface between double-layered cylindrical samples. The lower layer is fixed to the device so that the shear plane aligns with the interface of the tested sample. The shear strength of the interface is determined by applying a shear force to the side of the upper layer. The interface thickness is imposed by the equipment was originally designed at 1 mm, which corresponds to the distance separating two clamps (Collop et al., 2009; C. Raab & Partl, 2004b). This distance can be adjusted in a new modification shown by Raab & Partl (2009).

Following that, various functions were incorporated into the Leutner test in order to more accurately simulate the operational state of an interface within a pavement structure. To begin with, the inclusion of normal force enables an examination of the impact that normal force has on the shear mode behaviour of the interface (Francesco Canestrari et al., 2013; Romanoschi & Metcalf, 2001). Recent studies have attempted to incorporate a dynamic component into the Leutner test in order to investigate the fatigue behaviour of the interface (Isailović et al., 2017). The schematic of the cyclic version of the Leutner shear test, which was devised at the Dresden University, is illustrated in Figure 1.12.

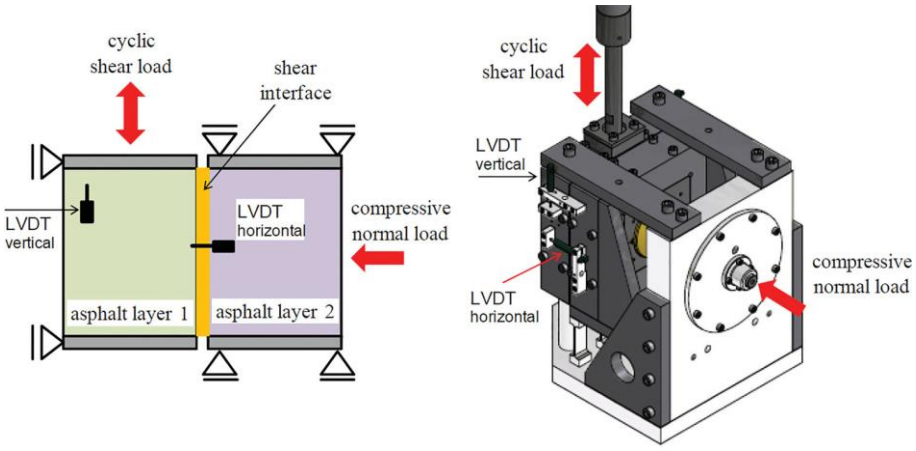

Figure 1.12: Schematic of cyclic version of Leutner shear test (Isailović et al., 2017)

1.5.2.2 Shear box test

The shear box test was initially designed to perform tests on soils under the name of Casagrande box. For the version used to test bituminous interface, the upper layer of a sample is fixed on

the top part of the box, when the other layer is fixed to the other part. Samples used in this testing device can be cuboids or cored cylinders (Francesco Canestrari et al., 2013). The actuator moves the lower part to apply shear stress to the interface, while the top part stays fixed. A constant axial loading can apply to the top part to study the influence of axial stress on the shearing performance of the tested interface. The thickness of interface is defined as the gap between two clamps. The schematic of a version of shear box test called Ancona shear testing research and analysis (ASTRA) device is introduced on Figure 1.13.

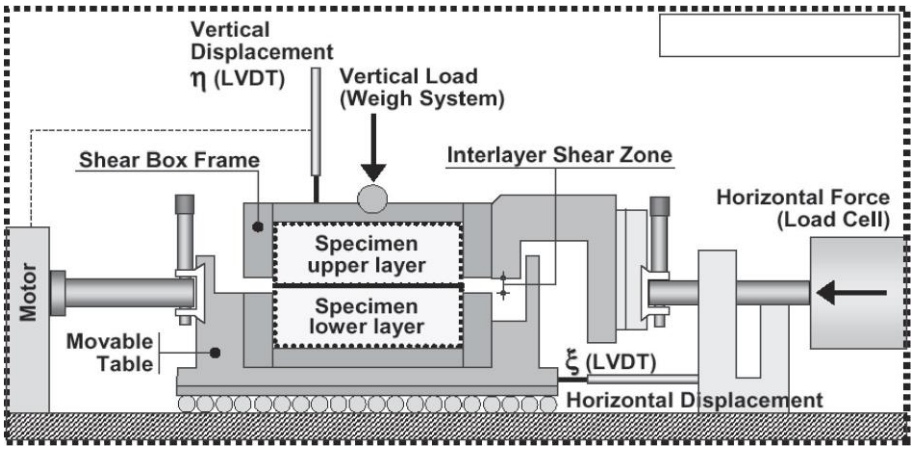

Figure 1.13: Schematic of Ancona shear testing research and analysis (ASTRA) device (Francesco Canestrari et al., 2013)

1.5.2.3 Inclined shear test

An inclined shear test involves the application of a normal force to a tested sample while a shearing-mode test is performed. One advantage of the device is that there is only one actuator. By adjusting the relative angle α between the central axis of the sample the loading direction, the ratio between the load in normal direction of the tested sample and the one in shearing direction is $\tan\alpha$. The relative movement between the top and the bottom of the tested sample is not restricted. Similar to the previous apparatus, the gap between two clamps is considered the interface thickness. Figure 1.14 shows a version of the inclined shear tests called the shear fatigue test (Romanoschi & Metcalf, 2001). Another version of the inclined shear tests, the Sapienza inclined shear test machine (SISTM) (D'Andrea & Tozzo, 2016) can be seen on Figure 1.15.

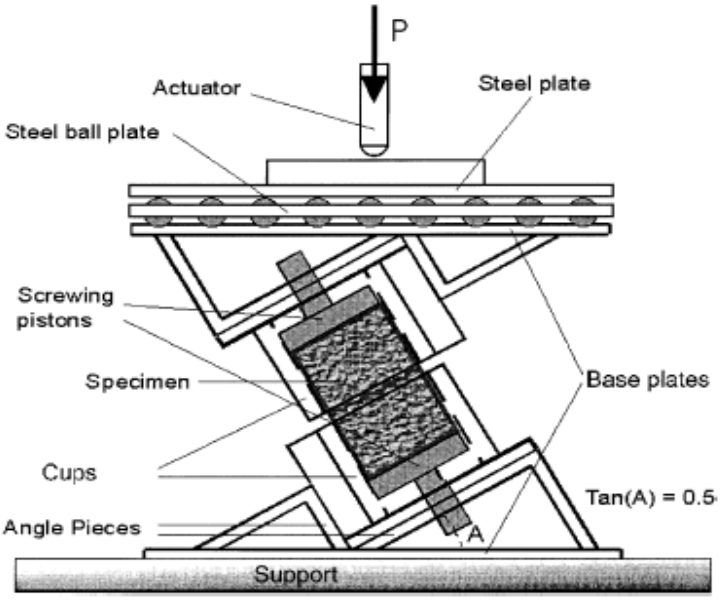

Figure 1.14: Schematic of the inclined shear test (the shear fatigue test) (Romanoschi & Metcalf, 2001)

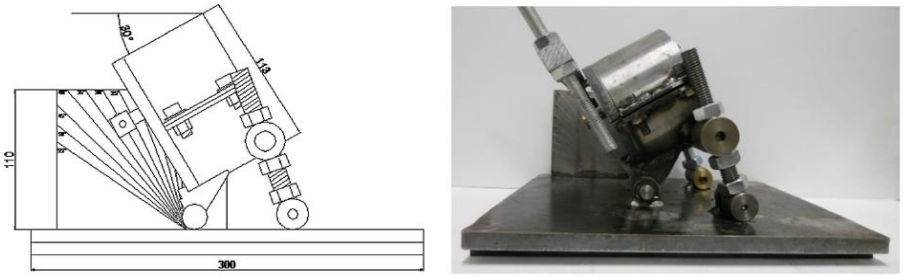

Figure 1.15: Schematic and a picture of Sapienza inclined shear test machine (SISTM) (D'Andrea & Tozzo, 2016)

1.5.2.4 Double Shear test

The Double Shear test was developed at the University of Limoges (France) (Diakhaté et al., 2011). The tested specimen includes two cut double-layered sample glued at their top surface. Materials in layers and the interface are the same. The specimen is fixed to the apparatus so as for two interfaces aligning with the two shear planes of the apparatus. The shearing load is applied to the middle part of the specimen (the top glued layers). The schematic of this apparatus is shown in Figure 1.16.

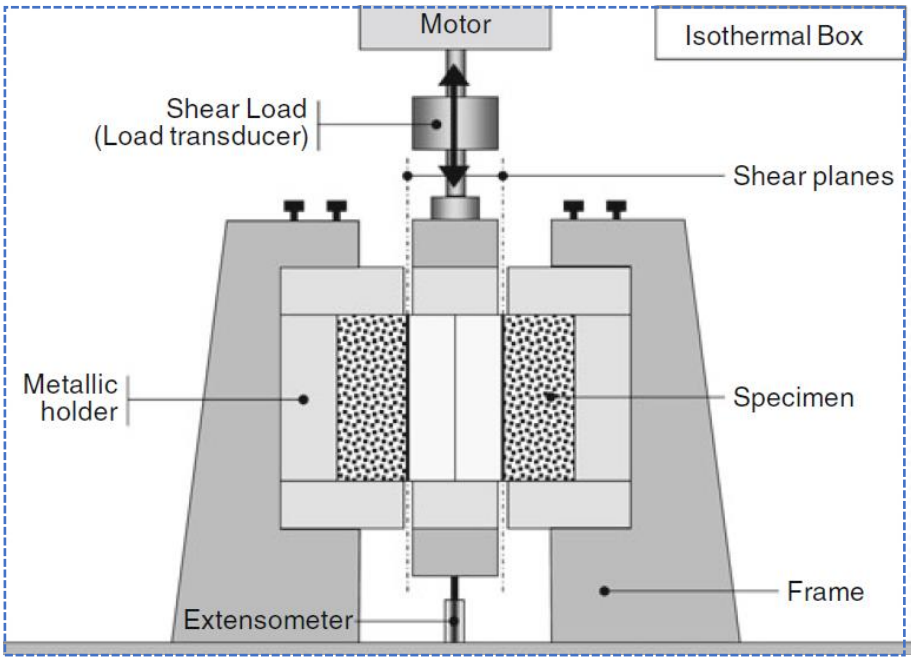

Figure 1.16: Schematic of double shear test (Diakhaté et al., 2011)

1.5.2.5 Torsion tests

The principle of testing interfaces with torsion tests in laboratories is similar with that in in situ. The top surface is glued to top plate of the apparatus, while the other surface is fixed to the bottom plate. The actuator applies torque to the top plate either in monotonic or cyclic to the top cap. Shear stress is not homogeneous inside the tested sample, with the maximum value at the outer surface and nil at the centre of the sample. Figure 1.17 shows the schematic and a picture of torsion test at the University of Nottingham (Collop et al., 2011). Figure 1.18 shows another version of torsion test developed at the University of Limoges (Ragni et al., 2021). At this new version, Ragni and his co-authors combined this apparatus with Digital Image Correlation technology or Acoustic Emission technology to study the fatigue behaviour of the interface (Ragni et al., 2021; Ragni, Ferrotti, et al., 2020; Ragni, Takarli, et al., 2020).

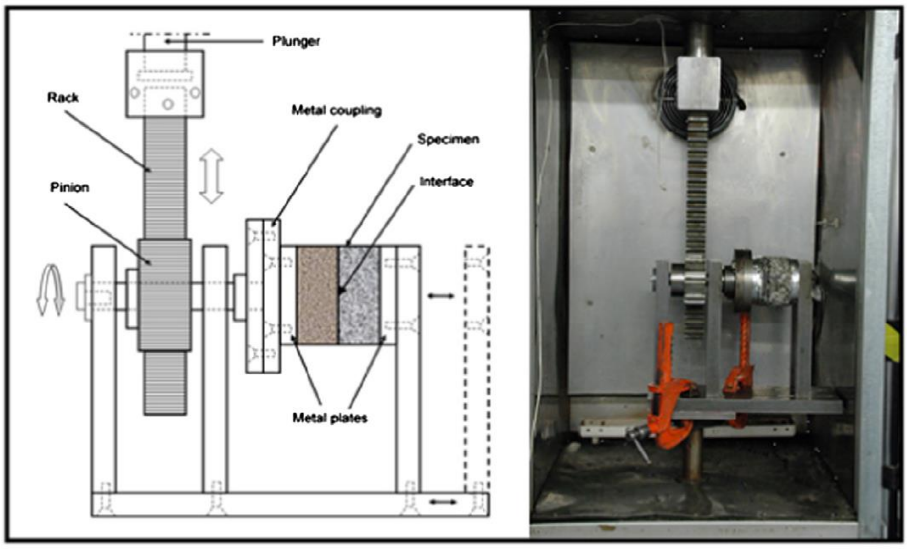

Figure 1.17: Schematic and a picture of automatic torque equipment (Collop et al., 2011)

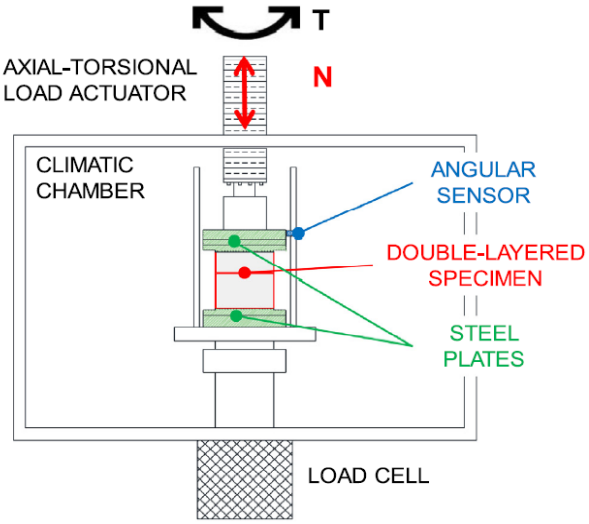

Figure 1.18: Schematic of the shear torque fatigue device (Ragni, Ferrotti, et al., 2020)

1.5.2.6 Flexural tests

Initially, the flexural test was devised to evaluate the resistance of bituminous mixtures to fracture. The test simulates the flexion of bituminous layers in a pavement under traffic loading, with a vertical load applied on a rectangular beam. The first version of flexural tests is known as the three-point bending test; it consists of two supports at the bottom of the sample being tested and a single point at the sample's midpoint on the upper surface that is connected to the actuator. This device was used to study the behaviour of interfaces reinforced with geogrid (Canestrari et al., 2015; Pasquini et al., 2013). The second version of flexural test is the four-point bending test. In this device, two point are at the bottom as they are in the three-point

bending test device. Two other points are linked with the actuator, placed on the top surface of the tested samples. Freire and his co-authors combined the four-point bending test (Figure 1.19) with DIC technology to study the behaviour of interfaces reinforced with geogrid (Freire et al., 2021). The five-point bending test can be found in the literature, with three supports and the last two points are linked to the actuator (Attia, 2020).

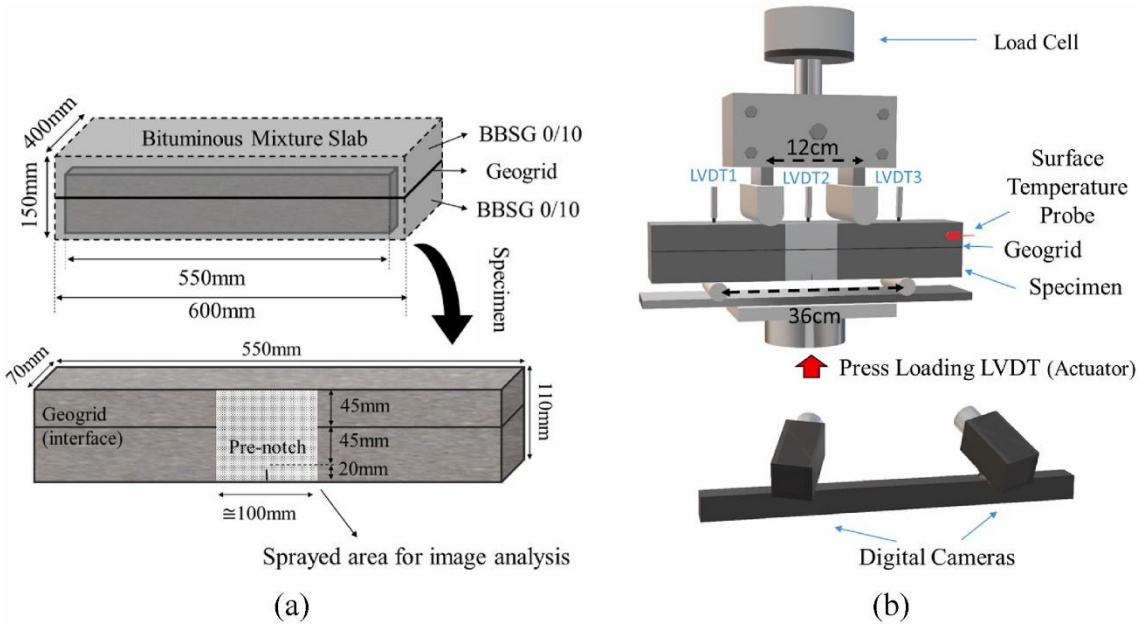

Figure 1.19: Schematic of Four Points Bending Notched Fracture (FPBNF) test: (a) double-layered beam, and (b): testing device and camera system (Freire et al., 2021)

1.5.2.7 Tension-compression tests

The tension-compression tests are usually used to study the thermomechanical of bituminous mixture. The advantage of this apparatus is the normal stress and strain fields are homogenous. Freire and his co-authors adapted this apparatus to study the interface between two bituminous layers (Freire et al., 2022). In order to do that; extensometers of two different lengths are placed cross the interface around a tested cylindrical sample. The displacement at the interface can be deduced from measurements two extensometer types. Both cyclic and monotonic test can be performed. A schematic of a tension-compression test on double-layered cylinder is shown on Figure 1.18.

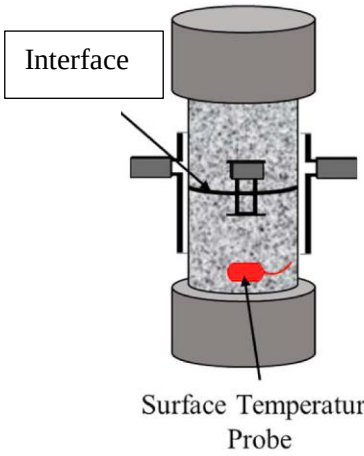

Figure 1.20: Schematic of tension-compression test on a double-layered cylinder (Freire et al., 2022)

1.6 Factors influencing interface behaviour

1.6.1 Temperature and loading speed

Bituminous mixtures are thermo-viscoelastic materials, which means that their behaviour depends on temperature and loading speed or frequency. The interface between two bituminous layers is constituted of bitumen, which serves the function of bounding the layers. It follows that the behaviour exhibited by the interface is directly inherited of the used bitumen.

The results of monotonic tests show that as the applied temperature decreases, the interface shear resistance (defined as the highest shear stress at the failure of the interface) increases (Mohammad et al., 2002), and the interface shear stiffness (defined as the ratio between the shear stress and displacement at the interface) also increases (Canestrari & Santagata, 2005). Cyclic tests have demonstrated that an increase in temperature results in an increase of interface stiffness (Hristov, 2018). Furthermore, the fatigue life of the interface can be improved with an increase in applied temperature (Collop et al., 2011; Isailović et al., 2017).

In contrast to the impact of temperature, an increase in interface shear resistance has been observed with an increase in applied loading speed (Canestrari et al., 2005, 2013). Similarly, in cyclic tests, an increase in test frequency has been observed to result in an increase in shear interface stiffness (Attia, 2020; Hristov, 2018).

The TTSP has been validated for the interface shear strength, as determined through monotonic tests (Francesco Canestrari et al., 2016; Graziani et al., 2017). A master curve built from experimental interface shear strength from different temperatures and loading speeds is

shown in Figure 1.21. The TTSP has also been validated for complex shear interface stiffness in cyclic tests (Attia, 2020; Hristov, 2018).

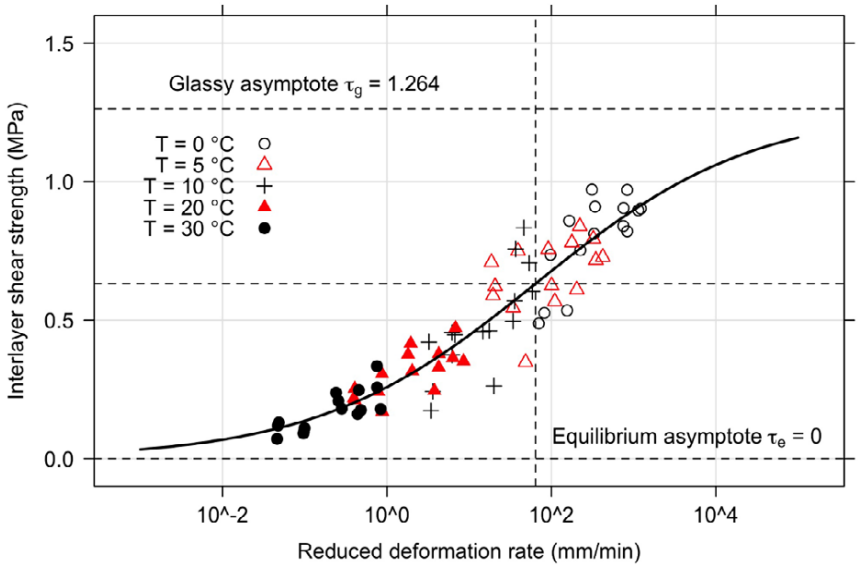

Figure 1.21: Interface shear strength master curve (Canestrari et al., 2016)

1.6.2 Tack coat type and content

The application of tack coat was observed to play a crucial role in the interlayer bonding process. The application of tack coat has been demonstrated to result in significant improvements in shear strength and shear resistance at the interface, when compared with the results obtained without the use of tack coat (Canestrari & Santagata, 2005; Collop et al., 2011; D'Andrea et al., 2012; Diakhaté et al., 2011).

The application of an appropriate residual bitumen content facilitates effective interlayer bonding without compromising the interlock between aggregates from the two layers. The optimal residual bitumen content of a tack coat has been determined to be between 250 g/m2 and 400 g/m2 (Raposeiras et al., 2012). The presence of insufficient bitumen at the interface does not ensure the effective bonding of the two adjacent bituminous layers. According to Attia (2020), interfaces with 350 g/m2 and 450 g/m2 residual bitumen content demonstrate superior resistance to shear stresses in comparison to those with a residual bitumen content of 250 g/m2. However, excessive bitumen at the interface can result in the slippage of the two bituminous layers, which in turn limits the interlocking of the aggregates.

The modification of bitumen used for the tack coat at the interface is expected to improve the bonding ability at the interface. However, laboratory tests show unexpected results. The application of polymer modified bitumen at the interface has been observed to result in a decrease in the shear strength of the interface (Attia, 2020; Canestrari et al., 2015). However,

the addition of sand to the tack coat (Mohammad et al., 2002), and chips (D'Andrea et al., 2013) has been observed to increase the shear strength of the interface. The mixture of bitumen and sand (resulting in a mastic) is expected to increase the stiffness of interface, while the addition of chips increases the roughness surface at the interface. Geogrids can be used at the interface to mitigate the occurrence of reflective cracking (Ferrotti et al., 2012; Freire, 2020).

1.6.3 Bituminous mixture types in layers

In addition to the bonding capacity of the tack coat at the interface, the aggregates from two adjacent layers play an important role in interlocking each other and resisting the relative shear displacement of the two layers. Considering the roughness of mixtures used in the layers allows for the simplification of interface configurations to four: smooth-on-smooth, smooth-on-rough, rough-on-smooth, and rough-on-rough (Attia, 2020). The four configurations are illustrated in Figure 1.22. The configuration of smooth-on-rough is expected to have higher shear resistance compared to the other configurations. This can be explained by the increase in the number of valleys present in the rough mixture in lower layers, which provide spaces for the small aggregate particles present in the upper layer. These configurations were studied using model materials comprising steel balls of two diametrical sizes, 5.5 mm and 9.5 mm (Raab et al., 2012). In each layer a single size of ball is used: a mixture of steel balls of 5.5 mm diameter represents the smooth mixture, while the rough mixture uses balls of 9.5 mm diameter. The authors confirmed that the configuration smooth-on-rough shows higher shear strength at the interface compared to the other configurations. Three configurations, smooth-on-smooth, smooth-on-rough and rough-on-rough were modelled by using the Discrete Element Method (DEM) (Jelagin et al., 2023). The modelling results are in accordance with the experimental results indicating that the configuration of smooth-on-rough exhibits better resistance to shear loading. Figure 1.23 shows the distribution of contact forces at the interface of the three configurations modelled. The smooth-on-smooth configuration results in lower contact forces than the smooth-on-rough and rough-on-rough configurations. However, debonding occurs at the interface in the rough-on-rough configuration. Jelagin et al assumed that the higher shear strength observed in the smooth-on-rough configuration is due to the well distributed macro-scale loads. However, if the lower surface exhibit excessive roughness, the tack coat does not provide a sufficient coverage of the surface. Some studies showed that too rough lower surface result in a low shear strength (Raab & Partl, 2004b; Raposeiras et al., 2012).

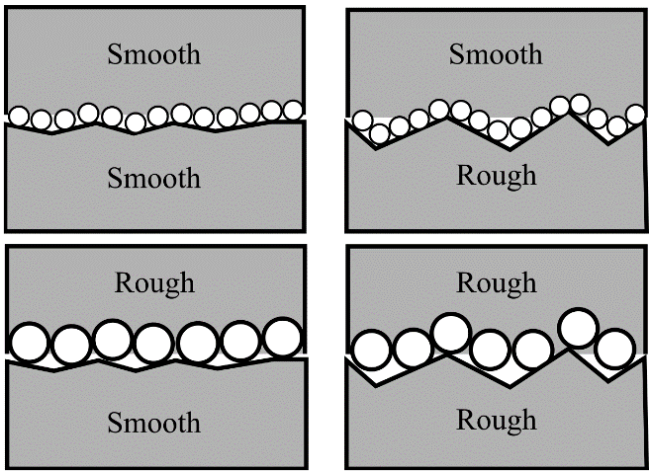

Figure 1.22: Schemes of interface configurations with different roughness of the two bituminous mixture layers

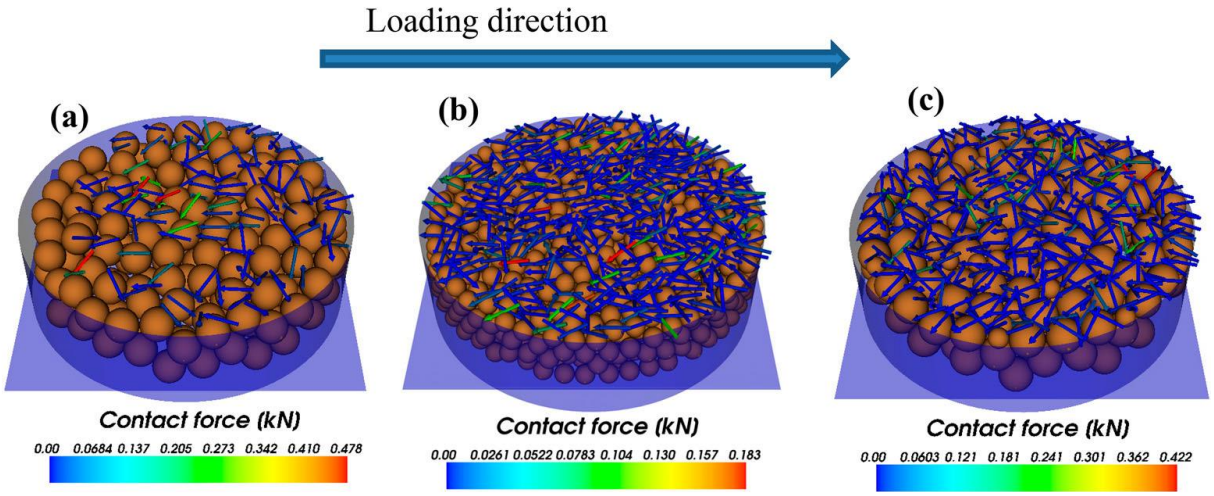

Figure 1.23: Contact shear force distribution at the shear plane observed at the peak shear and σ_{zz} = 400 kPa, for three combinations of ball diameters in layers: (a) 9.5 mm/ 9.5 mm; (b) 5.5 mm/5.5mm; (c) 5.5 mm/9.5 mm (Jelagin et al., 2023)

1.7 Bituminous layer and interface modelling

The results derived from the experiment of a bituminous material can be characterised by employing mechanical models. The subsequent subsections present models that are employed to describe the thermomechanical behaviour of the interface and bituminous layer under small or large number of cycle and small strain amplitudes.

1.7.1 Linear viscoelasticity (LVE) of bituminous interfaces and mixtures

1.7.1.1 Definition

ViscoElasticity is a time-dependent behaviour of a material consisting of both its elastic and

viscous responses due to an applied displacement. A non-aging material (whose mechanical properties remain unchanging if it does not undergo any disturbance) is considered to have ViscoElastic behaviour when the removal of stress is complete after the unloading in a cancellation test (Mandel, 1969). It can be seen from Figure 1.24 at the time t_o an instantaneous strain is applied, the material instantaneously responds with stress. That is a typical property of elastic material. In case that applied strain is kept constant from time t_o to t_1, the stress response of material progressively reduces, and its viscous property causes this reduction. At the time t_1, if the applied strain is removed immediately, the material develops an elastic response. The stress magnitude is higher than residual stress and has the opposite sign compared to that before discharging. Because the strain remains zero, the stress response gradually reduces to zero at time t_∞.

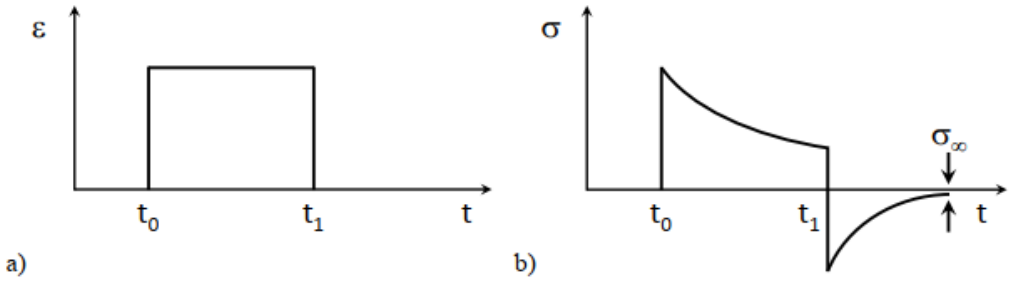

Figure 1.24: "Cancellation test" (a) applied strain; (b) responding stress

A material has Linear ViscoElastic (LVE) properties if its response to a superposition of different loads is the summation of the responses due to the single loads (Salençon, 1983). This criterion is called the Boltzmann principle, illustrated in Table 1.2 below:

Table 1.2: The superposition of Boltzmann principle

Action	Response
$\varepsilon_1(t)$	$\sigma_1(t)$
$\varepsilon_2(t)$	$\sigma_2(t)$
$\gamma\varepsilon_1(t) + \mu\varepsilon_2(t)$	$\gamma\sigma_1(t) + \mu\sigma_2(t)\ \forall\ (\gamma, \mu) \in R^2$

1.7.1.2 Creep function

Creep refers to the progressive deformation of a material over time when it is subjected to a constant stress. σ_o applied at the time t_o, at constant temperature, as it can be seen in Figure 1.25.

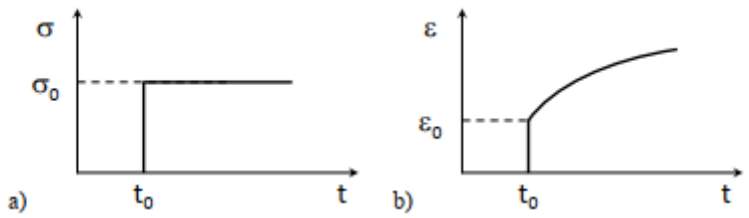

Figure 1.25: Creep test of a linear viscoelastic material: (a) applied stress; (b) responding strain

The stress at the time t is shown in Equation (1.1):

$$\sigma(t) = \sigma_o H(t - t_o) \tag{1.1}$$

With $H(t - t_0) = 0\ if\ (t - t_0) \leq 0, and\ H(t - t_0) = 1\ if\ (t - t_0) > 0$

Equation (1.2) presents responding strain:

$$\varepsilon(t) = \sigma_o F(t_o, t) \tag{1.2}$$

Where $F(t_o, t)$ is the creep function of material at any instant t (with the applied stress at t_o).

In case stress varies in time (Figure 1.26), the incremental notation is used. The responding strain at the instant t and caused by the stress increment $d\sigma(\tau)$ is illustrated in Equation (1.3):

$$d\varepsilon(t) = d\sigma(\tau)F(t_o, t) \tag{1.3}$$

By applying the Boltzmann principle for linear viscoelastic material, the strain ε(t) summarized from all elemental strains caused by elemental stresses as Equation (1.4):

$$\varepsilon(t) = \int_{t_0}^{t} d\sigma(\tau)F(t_0, t) = \sigma(t_0)F(t_0, t) + \int_{t_0}^{t} \dot{\sigma}(\tau)F(\tau, t)d\tau \tag{1.4}$$

For non-aging material, the strain becomes as shown in Equation (1.5):

$$\varepsilon(t) = \sigma(t)F(0) + \int_{t_0}^{t} \sigma(t - \tau)\frac{\partial F}{\partial \tau}(\tau)d\tau \tag{1.5}$$

The instantaneous response is denoted by the first term in Equation (1.5), while the previous stress history is represented by the second term (Mangiafico, 2014).

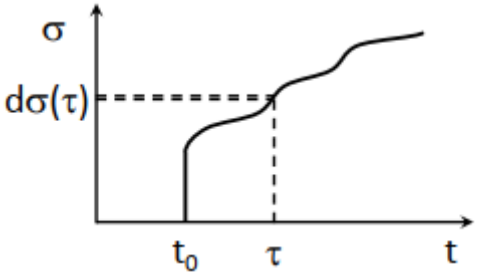

Figure 1.26: Applied stress varies in time

1.7.1.3 Relaxation

When a material is subjected to a constant strain, relaxation is the decrease in stress with respect to time (Figure 1.27). A constant strain is applied at a given time t_o at a constant temperature; the deduced function is given in Equation (1.6) below.

$$\varepsilon(t) = \varepsilon_o H(t - t_o) \tag{1.6}$$

With $H(t - t_o) = 0,\ if(t - t_o) \leq 0$, and $H(t - t_o) = 1,\quad if(t - t_o) > 0$

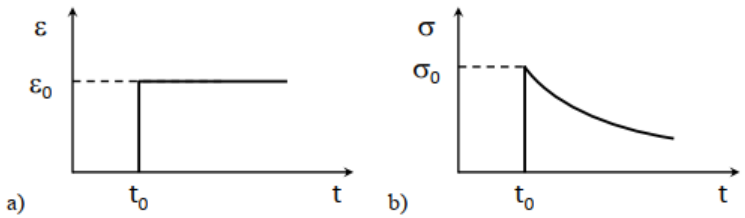

Figure 1.27: Relaxation test for a linear viscoelastic material: (a) applied strain; corresponding stress

Equation (1.7) presents the responding stress:

$$\sigma(t) = \varepsilon_o R(t_o, t) \tag{1.7}$$

with $R(t_o, t)$ being the relaxation function.

Appling an inconstant deformation during a period at a constant temperature, the resulting stress in a non-aging material is shown in Equation (1.8):

$$\sigma(t) = \varepsilon(t)R(0) + \int_{t_o}^{t} \varepsilon(t - \tau)\frac{\partial R}{\partial \tau}(\tau)d\tau \tag{1.8}$$

The first term represents the instantaneous response, while the second term shows the applied strain history at the time τ.

1.7.2 Time-temperature superposition principle

In the linear domain of a ViscoElastic material, complex modulus E* depends on two variables: frequency f (or pulsation ω=2πf) and temperature. However, complex modulus norm can be plotted with a unique curve on Cole-Cole graph or Black diagram being independent on the test temperature and frequency ($E^*(\omega_1, T_1) = E^*(\omega_2, T_2)$ with $(\omega_1, T_1) \neq (\omega_2, T_2)$). This property is called the time-temperature superposition principle (TTSP) (Nguyen, 2011) as shown in Equation (1.9), and g is a real function.

$$E^*(\omega_1, T_1) = E^*(\omega_2, T_2) \quad with\ \omega_1 g(T_1) = \omega_2 g(T_2) \tag{1.9}$$

By using TTSP property, it is possible to plot a single curve (master curve) for $|E^*|$at an arbitrarily chosen reference temperature T_{ref}. This curve is obtained by shifting isothermal

curves parallel with the frequency axis. Figure 1.28 below presents an example for the master curve of a bituminous mixture:

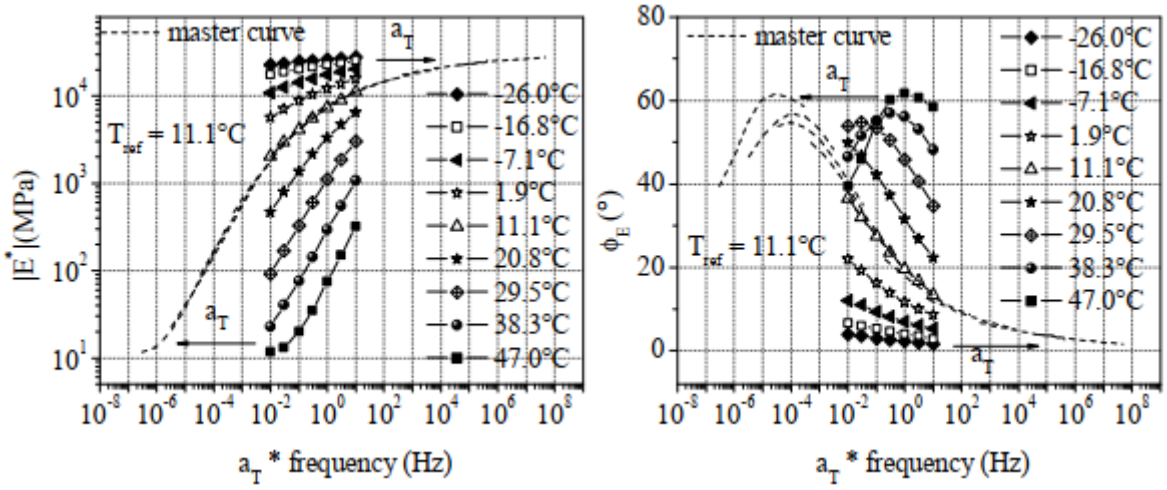

Figure 1.28: A master curve of complex modulus, (left): complex modulus; (right): phase angle (Nguyen, 2011).

As can be seen from the above figures, a master curve is constructed from the shifting of isothermal curves along the horizontal axis. A reduced frequency is calculated by shift factor having the property as the Equation (1.10):

$$a_T(T) = \frac{f(T)}{f(T_{ref})} \Rightarrow a_T(T_{ref}) = 1 \tag{1.10}$$

The values of the shift factor are dependent on temperature (Figure 1.29). Williams, Landel, and Ferry (called WLF law) proposes formula (Equation (1.11)) to fit shift factors as a function of temperature (Williams et al., 1955):

$$log(a_T) = \frac{-C_1(T - T_{ref})}{C_2 + T - T_{ref}} \tag{1.11}$$

where C_1 and C_2 are constants depending on the material and the chosen reference time T_{ref}

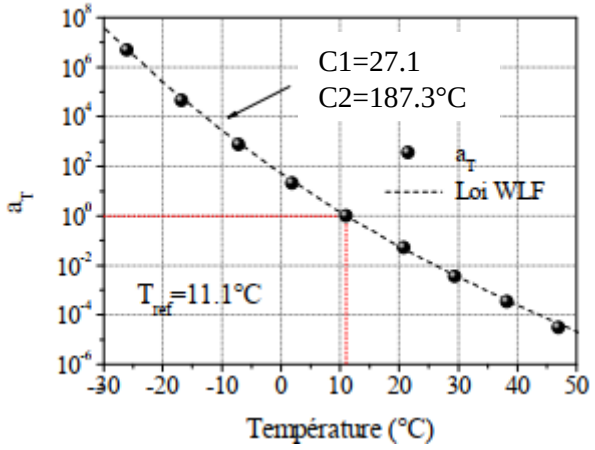

Figure 1.29: An example of shift factors and their fitting curve by WLF law for complex modulus (Nguyen, 2011)

1.7.3 Discrete spectrum models

In this section, the presented notions are focused on the characterisation of the thermomechanical behaviour of the bituminous interface between two bituminous layers using the 2T3C hollow cylinder apparatus. The equivalent notions to characterize bituminous mixture can be found on Table 1.3.

Table 1.3: Equivalent modelling notions between bituminous mixtures layers and interface using the 2T3C hollow cylinder apparatus

Interface			Layers			
	Quantity	Unit	Upper	Lower	Quantity	Unit
$K_{\theta z}$	Shear stiffness	MPa/mm	$G_{\theta z1}$	$G_{\theta z2}$	Shear modulus	MPa
$\tau_{\theta z}$	Shear stress	MPa	$\tau_{\theta z}$	$\tau_{\theta z}$	Shear stress	MPa
Δu_{θ}	Displacement gap	mm	$\varepsilon_{\theta z1}$	$\varepsilon_{\theta z2}$	Shear strain	(-)
$K^*_{\theta z\_GM}$	Stiffness of Generalised Maxwell model	MPa/mm	$G^*_{\theta z1\_GM}$	$G^*_{\theta z2\_GM}$	Modulus of Generalised Maxwell model	MPa
$K^*_{\theta z\_GKV}$	Stiffness of Generalised Kevin Voigt model	MPa/mm	$G^*_{\theta z1\_GKV}$	$G^*_{\theta z2\_GKV}$	Modulus of Generalised Kevin Voigt model	MPa

$K^*_{\theta z\_H}$	Stiffness of Generalised Huet model	MPa/mm	$G^*_{\theta z1\_H}$	$G^*_{\theta z2\_H}$	Modulus of Generalised Huet model	MPa
$K^*_{\theta z\_HS}$	Stiffness of Generalised Huet-Sayegh model	MPa/mm	$G^*_{\theta z1\_HS}$	$G^*_{\theta z2\_HS}$	Modulus of Generalised Huet-Sayegh model	MPa
$K^*_{\theta z\_2S2P1D}$	Stiffness of 2S2P1D model	MPa/mm	$G^*_{\theta z1\_2S2P1D}$	$G^*_{\theta z2\_2S2P1D}$	Modulus of model 2S2P1D	MPa
$K_{\theta z\_0}$	Glassy stiffness	MPa/mm	$G_{\theta z1\_0}$	$G_{\theta z2\_0}$	Glassy modulus	MPa
$K_{\theta z\_00}$	Static stiffness	MPa/mm	$G_{\theta z1\_00}$	$G_{\theta z2\_00}$	Static modulus	MPa

Some analytical models were built to simulate the thermomechanical behaviour of bituminous materials. They are the combinations of two elements, spring and dashpot.

1.7.3.1 Spring

A schematic of a spring is presented on Figure 1.30, where $K_{\theta z}$ is the spring stiffness. The relationship between the shear stress $\tau_{\theta z}$ and the displacement $\Delta_{u\theta}$ of a spring is shown in Equation (1.12).

Figure 1.30: A schematic of a spring

$$\tau_{\theta z}(t) = K_{\theta z}\Delta u_{\theta}(t) \quad (1.12)$$

The relaxation function of a spring with a stiffness of $K_{\theta z}$ is shown in Equation (1.13) after Laplace-Carson transformation.

$$\tilde{r}\,(\rho) = K_{\theta z} \quad (1.13)$$

1.7.3.2 Dashpot

The schematic of a dashpot is introduced on Figure 1.31, where η is the dashpot viscosity. The relationship between the shear stress τθz and the displacement Δuθ of a dashpot is shown in Equation (1.14).

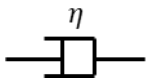

Figure 1.31: A schematic of a dashpot

$$\tau_{\theta z}(t) = \eta \frac{d\Delta u_{\theta}(t)}{dt} \tag{1.14}$$

The relaxation function of a dashpot with a viscosity of η is shown in Equation (1.15) after Laplace-Carson transformation.

$$\tilde{r}\,(\rho) = \eta\rho \tag{1.15}$$

1.7.3.3 Generalised Maxwell (GM) model

Generalized Maxwell or Kelvin-Voigt model consists of a finite number *n* of Maxwell models or Kelvin-Voigt models respectively in parallel or in series. A generalized Maxwell or Kelvin-Voigt can well describe the characteristic of bituminous mixtures if a sufficient number *n* of elementary models is used (Nguyen, 2011).

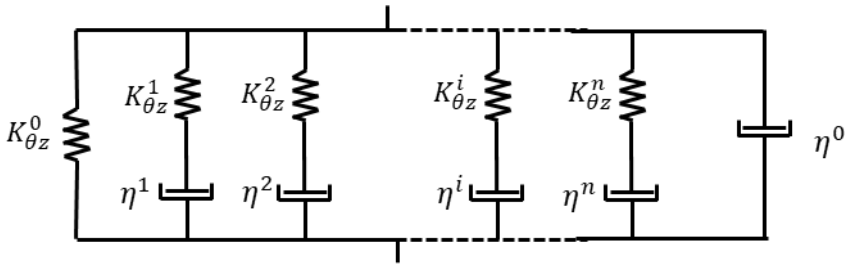

Figure 1.32: Generalized Maxwell model

A Generalized Maxwell model is presented in Figure 1.32. A system of n Maxwell models connected in parallel, a spring is placed on one side of this system, while a dashpot is assembled on the other side.

The relaxation function is written as Equation (1.16):

$$R(t) = K_{\theta z}^{0} + \eta_o \delta + \sum_{i=1}^{n} K_{\theta z}^{i}\, e^{-\frac{t}{\tau_i}} \tag{1.16}$$

$$\text{With } \tau_i = \frac{\eta^i}{K_{\theta z}^{i}}$$

Complex interface stiffness is presented in Equation (1.17):

$$K_{\theta z}{}^{*}(\omega) = K_{\theta z}^{0} + j\omega\eta_o + \sum_{i=1}^{n} K_{\theta z}^{i} \frac{j\omega\tau_i}{1 + j\omega\tau_i} \tag{1.17}$$

1.7.3.4 Generalised Kevin-Voigt (GKV) model

A generalized Kevin-Voigt model is a system of n finite Kelvin-Voigt elements connected in series as Figure 1.33:

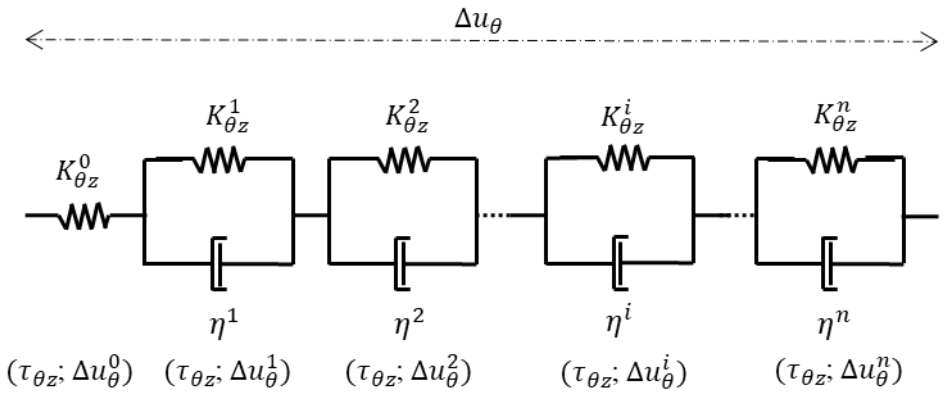

Figure 1.33: Generalized Kevin-Voigt model

The creep function is expressed as Equation (1.18):

$$J(t) = \frac{1}{K_{\theta z}^0} + \sum_{i=1}^{n} \left(1 - e^{-\frac{t}{\tau_i}}\right) \tag{1.18}$$

The complex modulus is shown as Equation (1.19):

$$K_{\theta z}^*(j\omega) = \left(\frac{1}{K_{\theta z}^0} + \sum_{i=1}^{n} \frac{1}{K_i + j\eta_i\omega}\right)^{-1} \tag{1.19}$$

1.7.4 Continuum spectrum models

1.7.4.1 The parabolic element

With the addition of a parabolic element, the LVE behaviour can be described precisely with a smaller number of parameters compared to a generalised Kelvin-Vogt or a generalised Maxwell model. The schematic of the parabolic element is presented on Figure 1.34.

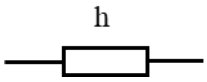

Figure 1.34: Schematics of a parabolic element

Its creep function is shown in Equation (1.20), where a, h and τ are parameters of the element.

$$f(t) = a\left(\frac{t}{\tau}\right)^h \tag{1.20}$$

With the Laplace-Carson transformation, the relaxation function of that parabolic element is presented in Equation (1.21), Γ is the gamma function.

$$\tilde{r}(\rho) = \frac{(\rho\tau)^h}{a\Gamma(h+1)} \tag{1.21}$$

1.7.4.2 Huet-Sayegh model

The Huet model (Figure 1.35) is an analogical model, including three elements connected in series: a spring with a stiffness $K_{\theta z\_0}$ and two parabolic elements with creep functions given in Equation (1.22):

$$J_1 = a(t)^h \quad ; \quad J_2 = b(t)^k \tag{1.22}$$

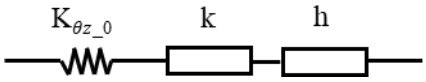

Figure 1.35: Huet model

The creep function is expressed as Equation (1.23):

$$J(t) = \frac{1}{K_{\theta z\_0}}\left(1 + \delta\frac{\left(\frac{t}{\tau}\right)^k}{\Gamma(1+k)} + \frac{\left(\frac{t}{\tau}\right)^h}{\Gamma(1+h)}\right) \tag{1.23}$$

The complex modulus is described as the form below:

$$K^*_{\theta z\_H}(\omega) = \frac{K_{\theta z\_0}}{1 + \delta(j\omega\tau)^{-k} + (j\omega\tau)^{-h}} \tag{1.24}$$

The use of this model to describe a bituminous materials has a drawbacks. As temperature decreases and frequency increases, the complex stiffness tends asymptotically towards $K_{\theta z\_0}$. Conversely, the complex stiffness tends towards zero as temperature increases and frequency decreases. For the latter case, the model does not allow describing the behaviour

of bituminous mixtures correctly as the stiffness of the skeleton remains at those temperatures and frequencies (Mangiafico, 2014).

Sayegh subsequently addressed this drawback by incorporating a linear spring with a stiffness $K_{\theta z\_00}$ in parallel with the existing Huet model. The magnitude of $K_{\theta z\_00}$ is quite small compared to that of $K_{\theta z\_0}$. This modified model was named Huet-Sayegh as Figure 1.36:

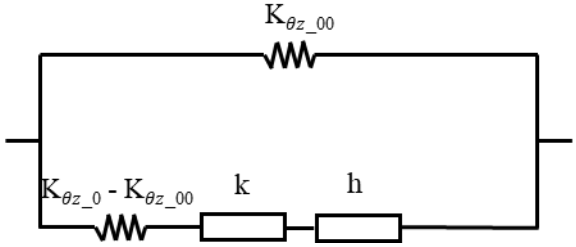

Figure 1.36: Huet-Sayegh model

The complex modulus is determined as Equation (1.25):

$$K^*_{\theta z\_HS} = K_{\theta z\_00} + \frac{K_{\theta z\_0} - K_{\theta z\_00}}{1 + \delta(i\omega\tau)^{-k} + (i\omega\tau)^{-h}} \quad (1.25)$$

As can be seen from Equation (1.25), when the temperatures increase and frequencies decrease, the complex modulus towards asymptotically to $K_{\theta z\_00}$ (static stiffness).

In fact, at high temperatures and low frequencies, a bitumen behaves like a pure liquid. Therefore, to describe that behaviour by using a linear dashpot is better than parabolic elements.

1.7.4.3 2S2P1D model

The 2S2P1D model was developed by Olard and Di Benedetto (2003) at ENTPE for modelling linear viscoelastic behaviour of bituminous materials (bitumen, mastic and mixture). The schematic of the 2S2P1D model is shown in Figure 1.37.

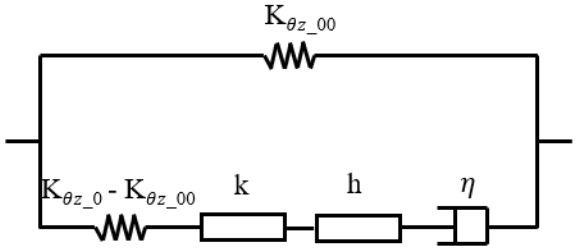

Figure 1.37: Schematic of model 2S2P1D (2 Springs, 2 Parabolic elements, 1 Dashpot) adapted for interface

In this study, the focus is on the modelling of the shear complex interface stiffness ($K^*_{\theta z}$). The stiffness is expressed with the 2S2P1D model $K^*_{\theta z\_2S2P1D}$ via Equation (1.26). Where:

$K_{\theta z\_00}$ is the static asymptotic stiffness obtained at low frequencies, $K_{\theta z\_0}$ is the glassy asymptotic stiffness at high frequencies. The constants k, h and δ are calibration parameters of the model. τ is a temperature-related parameter, and the constant β is related to the viscosity of the dashpot. To sum up, 7 constants are used to model shear complex interface stiffness. In Equation (1.26), ω is the angular frequency and *i*, the imaginary unit with $i^2 = 1$.

$$K^*_{\theta z\_2S2P1D} = K_{\theta z\_00} + \frac{K_{\theta z\_0} - K_{\theta z\_00}}{1 + \delta(i\omega\tau)^{-k} + (i\omega\tau)^{-h} + (i\omega\beta\tau)^{-1}} \quad (1.26)$$

When Time-Temperature Superposition Principle (TTSP) is validated for a bituminous material, it is possible to build master a curve for the complex modulus (or shear complex stiffness in this study). The process consists in superimposing isothermal curves together using shift factors a_T. For a fixed reference temperature T_{ref}, one shift factors a_T is determined for each testing temperature to build the unique master curves of norm or phase angle of shear complex stiffness. Williams Landel Ferry (1955) proposed an equation (Equation (1.27)) to model shift factor aT at a temperature T according to the reference temperature Tref. In Equation (*1.29*), C_1 and C_2 are constants.

$$\log(a_T) = \frac{-C_1(T - T_{ref})}{C_2 + T - T_{ref}} \quad (1.27)$$

1.7.5 Visco-elasto-plasticity (VEP) of bituminous interfaces and mixtures - DBN_{PDSC} model

DBN_{PDSC} model was introduced by Attia (2020). This model was developed in the framework of DBN model (Di Benedetto et al., 2007; Gayte, 2016; Raschia et al., 2021) to describe Plastic Dissipation for Small Cycles applied to bituminous mixtures. DBN_{PDSC} model uses the concept of generalized Kelvin-Voigt model with the addition of plastic dissipation into the existing springs. The schematic of model DBN_{PDSC} is presented in Figure 1.38 with *n* visco-elasto-plastic elements. These Kelvin-Voigt type elements become elastoplastic with small non linearities. One of them is introduced in Figure 1.39 while its behaviour for "small" cycle amplitude is schematized in Figure 1.40 (left).

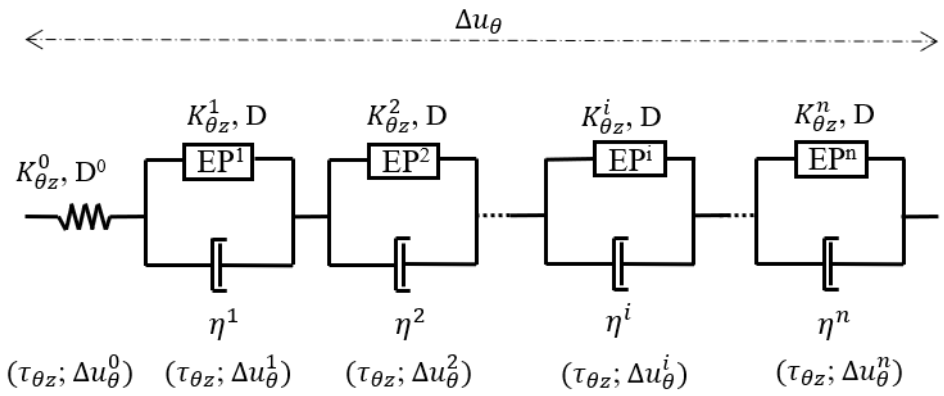

Figure 1.38: Schematic of model DBN$_{PDSC}$ adapted for interfaces

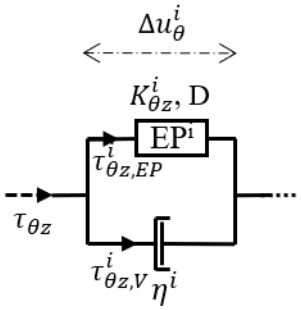

Figure 1.39: Schematic of an element of DBN$_{PDSC}$ model considered for "small" cycle amplitude

When considering one element, the total stress $\tau_{\theta z}$ can be decomposed in the sum of $\tau^i_{\theta z,EP}$ the elastoplastic stress derived from EPi element and $\tau^i_{\theta z,V}$ the viscous stress obtained from the linear dashpot as indicated in Equation (1.28).

$$\tau_{\theta z} = \tau^i_{\theta z,EP} + \tau^i_{\theta z,V} \tag{1.28}$$

Considering an element EPi, the relation between stress $\tau^i_{\theta z,EP}$ and displacement gap Δu^i_θ is expressed through Equation (1.29) with $K^i_{\theta z}$ the stiffness of element EPi.

In the linear dashpot i, the stress $\tau^i_{\theta z,V}$ relates to displacement gap rate $\Delta \dot{u}^i_\theta$ in Equation (1.30) where η^i is its viscosity.

$$\tau^i_{\theta z,EP} = K^i_{\theta z} \Delta u^i_\theta \tag{1.29}$$

$$\tau^i_{\theta z,V} = \eta^i \Delta \dot{u}^i_\theta \tag{1.30}$$

As mentioned earlier, the DBN$_{PDSC}$ model has plastic dissipation added to the springs which is a non-viscous part. Therefore, the plastic energy dissipated by EP^i elements is different from the energy dissipated by the viscous part (linear dashpot).

In order to describe the dissipated energy in an elasto-plastic element, a damping coefficient D is generally introduced. When an EP^i element is subjected to one sinusoidal cycle,

the dissipated plastic energy per unit volume during one sinusoidal cycle (W_P^i) is calculated in Equation (1.31), where $\Delta u_{\theta\_0}^i$ and $\tau_{\theta z,EP\_0}^i$ are respectively the displacement gap amplitude and stress amplitude in the element EP^i. D^i is the damping coefficient for element EP^i. The illustration for dissipated plastic energy is shown on the Figure 1.40 left.

$$W_P^i = 2\pi D^i \Delta u_{\theta\_0}^i \tau_{\theta z,EP\_0}^i \tag{1.31}$$

A linear viscoelastic material subjected to cyclic loading will dissipate viscous energy. The viscous energy dissipated per unit volume during one sinusoidal cycle (W_{VE}) is calculated in Equation (1.32). $\tau_{\theta z\_0}$ and Δu_{θ_0} are stress and displacement gap amplitude, respectively while φ is the phase angle of the viscoelastic complex stiffness. The illustration about dissipated viscous energy is shown on the right of Figure 1.40.

$$W_{VE} = \pi \Delta u_{\theta\_0} \tau_{\theta z\_0} \sin\varphi \tag{1.32}$$

Equation (1.32) applied to the purely viscous linear dashpot becomes Equation (1.33), and gives the viscous energy dissipated per unit volume during one sinusoidal cycle (W_V) with $\tau_{\theta z,V\_0}^i$ the stress amplitude in this linear dashpot.

$$W_V^i = \pi \Delta u_{\theta\_0}^i \tau_{\theta z,V\_0}^i \tag{1.33}$$

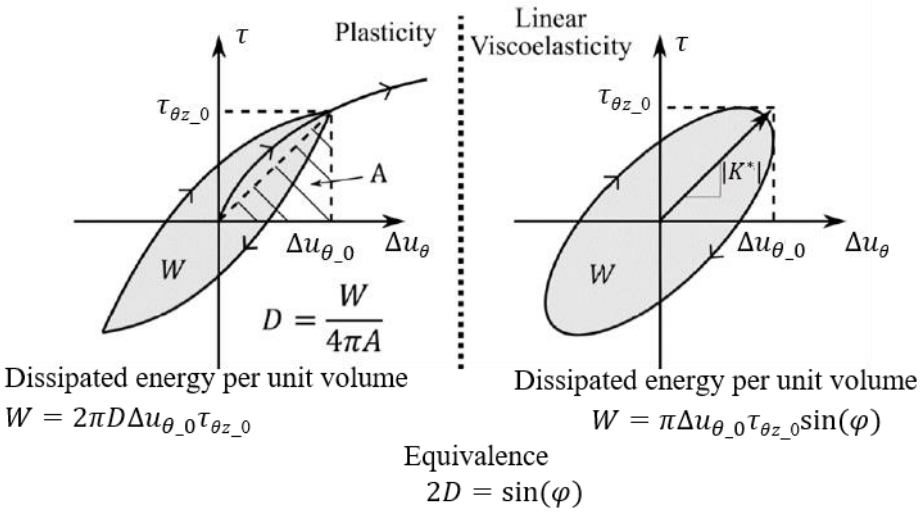

Figure 1.40: Comparison between non-viscous plastic dissipated energy and viscous dissipated energy

The coefficient of damping D^0 is added on the spring $K_{\theta z}^0$. It depends on the displacement gap amplitude of the spring ($\Delta u_{\theta\_0}^0$) following a linear relation expressed in Equation (1.34). φ_{NL_0} is a fixed parameter and Δu_{θ_0} is the total displacement gap amplitude of the model.

$$D^0\left(\Delta u_{\theta\_0}^0\right) = \frac{sin\varphi_{NL\_0}}{2} \frac{\Delta u_{\theta\_0}^0}{\Delta u_{\theta\_0}} \tag{1.34}$$

The coefficients D^i related to each element EP^i are all taken equal to D. D depends on the total displacement gap amplitude of all elements EP^i ($\sum_{i=1}^{n} \Delta u_\theta^i$) by a linear law as can be seen in Equation (1.35). φ_{NL_00} is a fixed parameter. At any time, the total displacement gap of the model (Δu_θ) is the sum of the displacement gap of the spring $K_{\theta z}^0$ (Δu_θ^0) and the total displacement gap of all elements EP^i ($\sum_{i=1}^{n} \Delta u_\theta^i$).

$$D(\sum_{i=1}^{n} \Delta u_{\theta\_0}^i) = \frac{sin\varphi_{NL\_00}}{2} \frac{\sum_{i=1}^{n} \Delta u_{\theta\_0}^i}{\Delta u_{\theta\_0}} \tag{1.35}$$

Both parameters φ_{NL_0} and φ_{NL_00} are chosen equal in this study and are called φ_{NL}.

It is assumed that the added plastic dissipations do not influence the norm of complex stiffness of the model. The norm $\left|K_{\theta z\_DBN}^*\right|$ at an angular frequency ω can be determined as for a general Kelvin-Voigt model. It is expressed in Equation (1.36) where j is the imaginary unit ($j^2 = -1$).

$$\left|K_{\theta z\_DBN}^*\right|(\omega) = \left| \frac{1}{K_{\theta z}^0} + \sum_{i=1}^{n} \frac{1}{K_{\theta z}^i + j\omega\eta^i} \right|^{-1} \tag{1.36}$$

The total dissipated energy per unit volume during one cycle (W) is the sum of the plastic energy (W_P^0) in the spring $K_{\theta z}^0$, the plastic energy (W_P^i) in all EPi elements and the viscous energy (W_V^i) in all linear dashpots, as expressed in Equation (1.37).

$$W = W_P^0 + \sum_{i=1}^{n} (W_P^i + W_V^i) \tag{1.37}$$

Using the equivalence illustrated in Figure 1.40 between dissipated energy for a linear viscoelastic material and an elasto-plastic material, it is possible to analyse the dissipated energy of the model DBN$_{PDSC}$ as resulting from a viscoelastic material having a phase angle φ_{DBN}. This phase angle is expressed in Equation (1.38), where $\tau_{\theta z\_0}$ and Δu_{θ_0} are respectively the total stress amplitude and the total displacement gap amplitude.

$$\sin \varphi_{DBN} = \frac{W}{\pi \Delta u_{\theta\_0} \tau_{\theta z\_0}} \tag{1.38}$$

Then the phase angle φ_{DBN} of the model DBN$_{PDSC}$ is obtained from Equation (1.39). Detailed calculations are presented by Attia (2020) and Raschia et al. (2021)

$$\sin \varphi_{DBN} = \left|K_{\theta z\_DBN}^*\right|(\omega) \left(\frac{2D^0 \left(\Delta u_{\theta\_0}^0\right)}{K_{\theta z}^0} + \sum_{i=1}^{n} \frac{2D(\sum_{i=1}^{n} \Delta u_{\theta\_0}^i) K_{\theta z}^i + \eta^i \omega}{\left(K_{\theta z}^i\right)^2 + (\eta^i \omega)^2} \right) \tag{1.39}$$

1.7.6 LVE behaviour of interfaces

The need to better understand the behaviour of interfaces has been raised in recent years. In laboratory, tests are either monotonic or cyclic. The monotonic tests allow for the evaluation of the strength of interfaces (Isailović & Wistuba, 2018; C. Raab & Partl, 2004a; West et al., 2005). This can be a factor in determining the quality of an interface made of tack coat for mix design before construction and quality control right after construction. However, results obtained from monotonic tests cannot be used to characterise the thermomechanical properties of the interface when a great number of small strain amplitude cycles are applied. Therefore, cyclic tests are more pertinent and interesting for the characterization of interfaces because they involve testing conditions that are closer to reality (Francesco Canestrari et al., 2022).

In order to design a sustainable pavement structure, it is necessary to understand the thermomechanical behaviour of not only the component layers but also the interface between them. A durable interface enables the reduction of strain at the bottom of bounded layers and limiting the occurrence of premature failures at the interface. However, very few studies focus on the thermomechanical behaviour of the interface between layers. Some studies show that the response of interfaces to a shear sinusoidal loading is sinusoidal (Isailović et al., 2017; Tozzo et al., 2014). Attia et al. (2021) at the University of Lyon/ENTPE developed the 2T3C Hollow Cylinder Apparatus (2T3C HCA) to investigate the mechanical properties of pavement interlayers. Tensile/compressive and torsional loadings are applied on a double-layered hollow cylinder specimen within a thermal chamber, wherein the temperature is regulated from 10 °C to 40 °C. The 2T3C hollow cylinder apparatus was developed to address the common drawbacks of previous apparatuses, as stress and strain fields are homogeneous in the sample. Furthermore, the apparatus is equipped with four cameras and Digital Image Correlation (DIC) analyses are performed, which enables direct observation of the mechanical properties of the interface and the mixture layers (Attia, 2020; Attia et al., 2020, 2021). The interface stiffnesses obtained at different temperatures and frequencies were used to build master curves of norm and phase angle. An example of master curve of norm of complex shear interface stiffness is shown in Figure 1.41. Freire et al. (2022) successfully used the linear viscoelastic model 2S2P1D to characterise the interface behaviour. The authors conducted the complex modulus on double-layered cylinder in normal direction. A geogrid was present at the interface in addition to bituminous tack coat. However, Isailović, Falchetto, and Wistuba (2017) observed that the interface did not exhibit linear viscoelastic behaviour, as evidenced by a stiffness decline during the amplitude sweep test. The test was conducted with a modified Leutner test

at 10 Hz and two temperatures, 10 °C and 20 °C. The shear displacement at the interface increased from 0.005 mm to 0.2 mm, with the gap of 1 mm. The evolution of the norm of complex shear interface stiffness during the amplitude sweep test performed at 20 °C is shown in Figure 1.42.

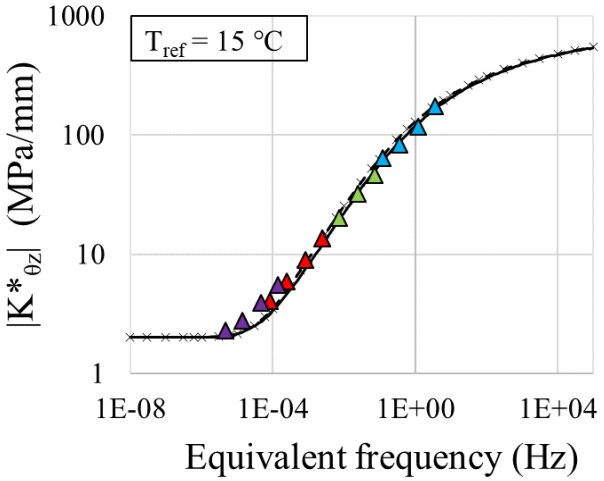

Figure 1.41: Master curve of complex shear interface stiffness (Attia, 2020)

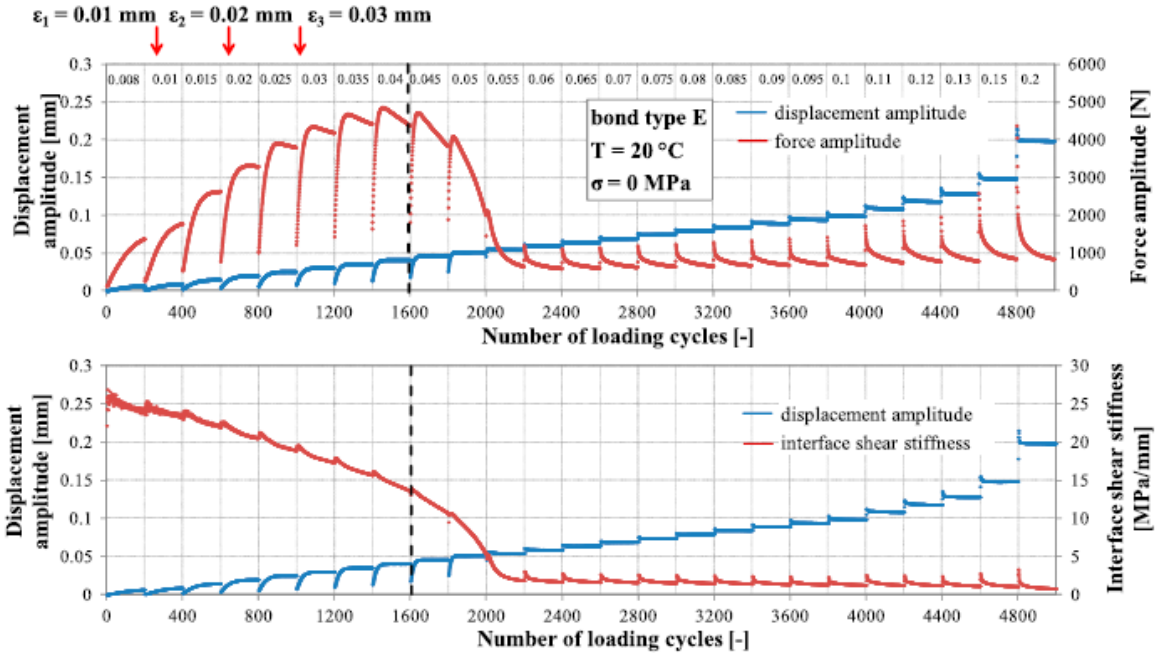

Figure 1.42: Evolution of interface shear stiffness during the displacement sweep amplitude test at 10 Hz, at 20 °C. The shear displacement at the interface ranges from 0.005 mm to 0.2 mm (Isailović et al., 2017).

For bituminous mixtures, whether they show linear or nonlinear viscoelastic depends on the strain amplitude applied. The limit for linear domain is 100 µm/m (Mangiafico et al.,

2018; Nguyen et al., 2015). As a bituminous material, the interface made of bitumen emulsion can also have linear or nonlinear viscoelastic behaviour based on the strain amplitude applied.

1.7.7 Fatigue behaviour of interfaces

Researchers have recently paid more attention to fatigue testing on the interface between bituminous mixtures layers, focusing on the shearing mode. Most of the fatigue tests on interfaces are continuous, and the N_{f50} fatigue criterion is commonly used to evaluate the fatigue life of an interface. N_{f50} is the number of cycles leading to a 50% reduction of interface stiffness/modulus (Diakhaté et al., 2011; Isailović et al., 2017; Song et al., 2016). Ragni et al. pointed out that previous tests could not localise where fatigue failures initiate and propagate, either in layer or at interfaces. The authors then employed acoustic emission to overcome the drawback and the appearance of fatigue failure was observed at the interfaces (Ragni, Takarli, et al., 2020). The cumulative number of Acoustic Event (AE) can be divided into two distinct phases, as illustrated in Figure 1.43. In the initial phase, the cumulative number of AE increases linearly. In the second stage, it increases dramatically until the end of the fatigue test. The authors assumed that microcracks form during the second stage, which begins when the interface loses 70 – 75 % of its stiffness.

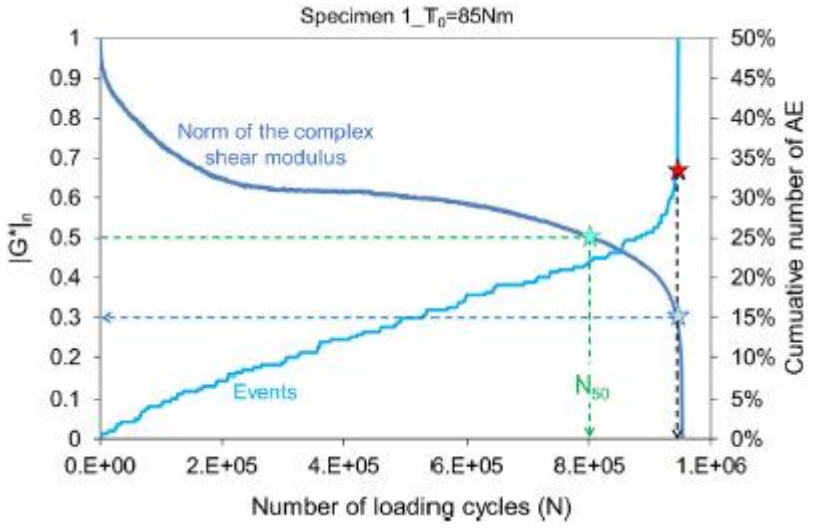

Figure 1.43: Evolution of cumulative AE events and normalised |G*| during a shear-torque fatigue test (Ragni, Takarli, et al., 2020)

The change in speed or direction of a wheel can produce shear stresses at the pavement's interface (Isailović et al., 2017). It can also be found at the edge of a wheel, so with the repetition of traffic flow, cyclic shear loading can be found at the interfaces between bituminous layers. Consequently, it is crucial to study the fatigue properties of bituminous interfaces in shearing mode. Recent apparatuses applied direct shear stress (Isailović et al., 2017; Isailović & Wistuba,

2018; Ragni et al., 2021), or torsion on a double-layered sample (Ragni, Ferrotti, et al., 2020). Isailović et al. (2017) studied the influence of axial stresses on the fatigue life of interfaces applied to the cyclic shear fatigue tests. It was observed that increasing the axial stresses applied to the double-layered samples resulted in an improvement in the fatigue life of the interface. The evolution of norm and phase angle of interface shear stiffness are shown in Figure 1.44 and Figure 1.45. However, the stress and strain fields applied on the samples are heterogeneous.

In order to evaluate the fatigue lives of interfaces, the fatigue criterion of 50 % reduction of interface stiffness is commonly used. Figure 1.46 shows an example for the evolution of interface stiffness during a shear fatigue test, and the number of cycles that leads to the diminution of 50 % of interface stiffness (N_{f50}) can be observed. However, as a bituminous material, other fatigue criteria can be taken into consideration. For example, phase angle related criteria, and the energetic approach is used as a fatigue criterion quite often for bituminous mixture. The viscous energy (W*i*) dissipated at the cycle *i* can be calculated by Equation (1.40), where $\tau_i, \Delta u_i$ are respectively the shear stress amplitude and the interface displacement the cycle *i*.

$$W_i = \pi \tau_i \Delta u_i sin\varphi_i \tag{1.40}$$

Base on the fatigue criteria, the fatigue laws can be determined through power functions as written in Equation (1.41). This function shows the relation between the loading amplitude τ (or Δu) with the number of loading cycles leads to failure. While a and b are law parameters. Fatigue laws allow to evaluate the effects of different factors to the fatigue behaviour of interfaces. Diakhaté et al. (2011) show the influence of tack coat and testing temperatures to the fatigue resistance of the interface through their fatigue laws (Figure 1.47).

$$\tau = aN^b \tag{1.41}$$

Furthermore, it is possible to obtain the Wöhler's fatigue laws from chosen fatigue criteria. Equations (1.42) shows a general Wöhler's law; when Nf is the number of cycles leading to fatigue failure, a_2 is the slope in the Log ε_0 – Log N_f diagram, and ε_6 is the strain amplitude at which a material has a fatigue life of 10^6 cycles.

$$N_f = 10^6 \left(\frac{\varepsilon_0}{\varepsilon_6}\right)^{-a_2} \tag{1.42}$$

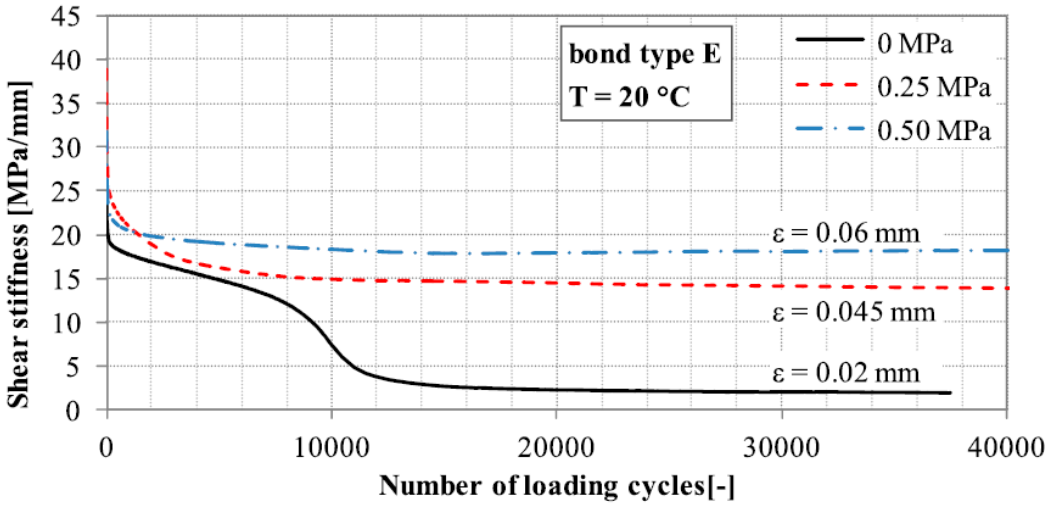

Figure 1.44: The influence of axial stresses to the evolution of norm of shear stiffness of interface during fatigue test (Isailović et al., 2017)

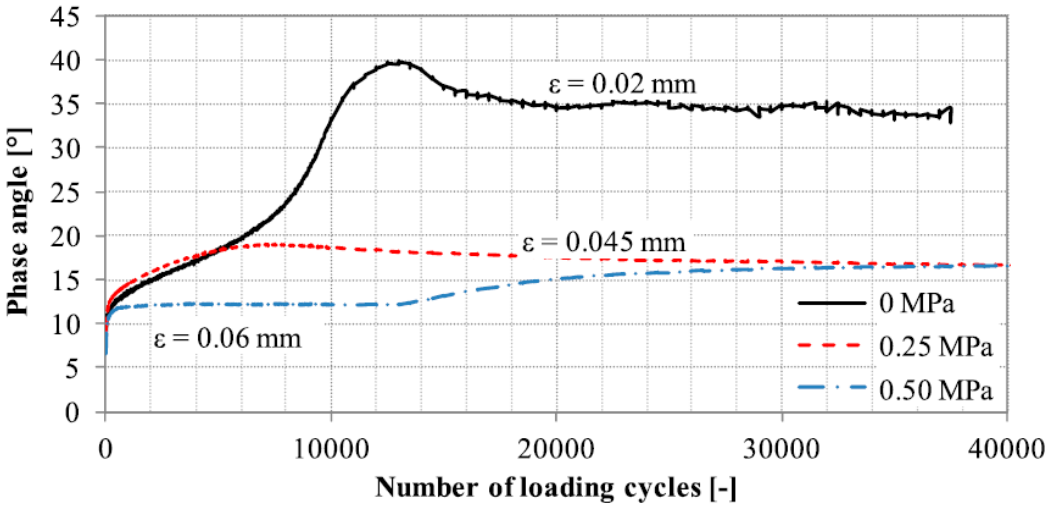

Figure 1.45: The influence of axial stresses to the evolution of phase angle of shear stiffness of interface during fatigue test (Isailović et al., 2017)

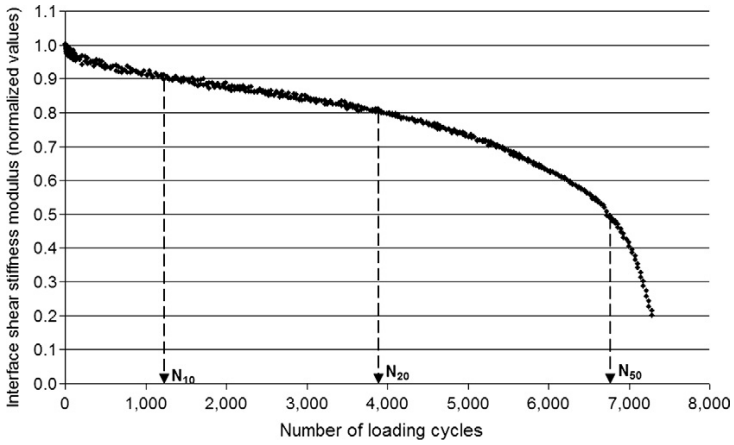

Figure 1.46: Evolution of interface stiffness during a fatigue test (Diakhaté et al., 2011)

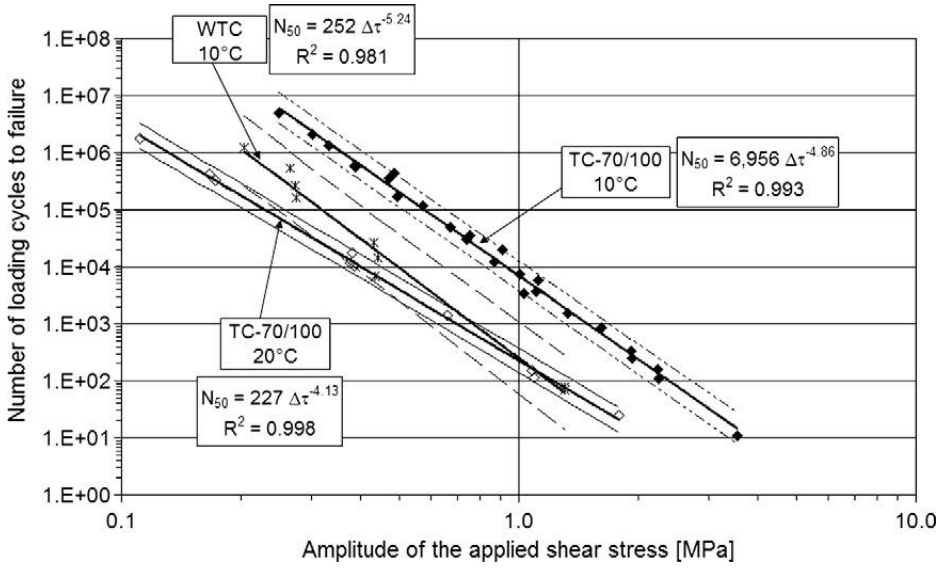

Figure 1.47: Fatigue law for interfaces without tack coat (WTC), with tack coat (TC), fatigue tests were controlled in stress (Diakhaté et al., 2011)

1.8 Conclusions

In a flexible pavement structure, emulsified bitumen is used to bind adjacent asphalt layers together. The layers are designed to be perfectly bonded. Therefore, a solid bonding capacity of the tack coat at the interface plays a key role in ensuring the lifespan of a pavement structure. Due to the traffic and climate loading, the quality of the tack coat reduces gradually, which can lead to premature failures or degradation of the whole structure. The perfect bonding at the interface is probably not maintained during the service life, as considered in most of the design methods.

The need to better understand the actual behaviour at the interface has been studied with different apparatuses both in situ and in laboratories. In laboratories, these devices are able to

apply monotonic or cyclic shear loading combined with different temperatures and loading rates on samples.

However, the common disadvantage of these apparatuses are the non-homogenous stress and strain (or displacement) fields existing at the interface, which do not allow for the characterization of the intrinsic properties of interface. The interface composed of bitumen emulsion, being a bituminous material, may exhibit linear or nonlinear viscoelastic behaviour and fatigue, contingent upon the applied strain amplitude, temperature, and number of cycles. Consequently, there are models for bituminous materials in the existing literature that can be adapted for the purpose of simulating the behaviour at the interface. The literature review presented insights on the pavement materials and structures, and testing methods for the interface. The 2T3C hollow cylinder apparatus developed in ENTPE/University of Lyon enables to apply quasi-homogenous (i) stress and strain field in the two mixture layers and, (ii) the strain fields in layers and displacement gap at the interface will be presented in the next chapter.

Chapter 2: 2T3C HOLLOW CYLINDER APPARATUS

In this chapter, a novel apparatus known as 2T3C ("Torsion, Traction, Compression sur Cylindre Creux" in French or "Torsion, Tension, Compression on Hollow Cylinder" in English) is introduced. Designed to examine the thermomechanical characteristics of the interface between bituminous layers, it was developed at the ENTPE/University of Lyon. The principle of testing a hollow cylinder will be introduced in the first section. The subsequent section defines every component that comprises the 2T3C Hollow Cylinder Apparatus. In the third section, the measurement and acquisition systems will be described. Finally, a section will outline the computational approach that is integrated with 3D-DIC technology in order to determine the strain in each layer and the displacement gap at the interface.

2.1 A principle of testing on a hollow cylinder

Hollow cylinder apparatuses have been widely employed for studying soils and sands (Duttine et al., 2007; Hight et al., 1983; Sauzéat, 2003). The materials are filled in an impermeable membrane during a test. Compressed water or air is used to generate a confinement pressure on the sample's wall. This pressurised environment allows the sample to maintain their shape during the test. Such a device was adapted for asphalt mixture sample without a confinement pressure, and named 2T3C hollow cylinder apparatus. The idea of using a hollow cylinder apparatus is to have quasi-homogenous stress and strain fields in testing samples, when applying shear by torsion.

In order to describe stresses and strains in a hollow cylinder, the cylindrical coordinates (r, θ, z) with a vector basis (er, eθ, ez), and the origin O are chosen at the centre of the bottom surface of the cylinder (Figure 2.1). The displacement field u is described through the coordinates via Equation (2.1).

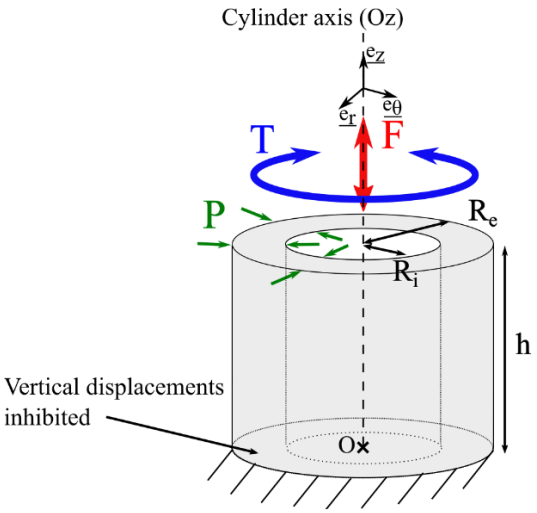

Figure 2.1: Schematic of a hollow cylinder and possible tests (Attia, 2020)

$$\underline{u}(r, \theta, z) = (u_r(r), u_\theta(r,z), u_z(z)) \tag{2.1}$$

For small displacements, the infinitesimal strain tensor $\underline{\underline{\varepsilon}}$ is defined coordinates in Equation (*2.2*), in the chosen cylindrical basis.

$$\underline{\underline{\varepsilon}} = \frac{1}{2}\left(\underline{\underline{grad}}(\underline{u}) + {}^{t}\underline{\underline{grad}}(\underline{u})\right) = \begin{pmatrix} \varepsilon_{rr} & \varepsilon_{r\theta} & \varepsilon_{rz} \\ \varepsilon_{r\theta} & \varepsilon_{\theta\theta} & \varepsilon_{\theta z} \\ \varepsilon_{rz} & \varepsilon_{\theta z} & \varepsilon_{zz} \end{pmatrix} \tag{2.2}$$

Applying Equation (2.2) for a hollow cylinder, the infinitesimal strain tensor $\underline{\underline{\varepsilon}}$ can be calculated as in Equation (2.3).

$$\begin{aligned} \underline{\underline{\varepsilon}} &= \frac{1}{2}\left(\underline{\underline{grad}}(\underline{u}) + {}^{t}\underline{\underline{grad}}(\underline{u})\right) \\ &= \begin{pmatrix} \dfrac{\partial u_r}{\partial r} & \dfrac{1}{2}\left(\dfrac{\partial u_r}{\partial r} - \dfrac{u_r}{r}\right) & 0 \\ \dfrac{1}{2}\left(\dfrac{\partial u_r}{\partial r} - \dfrac{u_r}{r}\right) & \dfrac{u_r}{r} & \dfrac{1}{2}\dfrac{\partial u_\theta}{\partial z} \\ 0 & \dfrac{1}{2}\dfrac{\partial u_\theta}{\partial z} & \dfrac{\partial u_z}{\partial z} \end{pmatrix} \end{aligned} \tag{2.3}$$

Stress tensor $\underline{\underline{\sigma}}$ is written as in Equation (*2.4*) in the chosen cylindrical basis.

$$\underline{\underline{\sigma}} = \begin{pmatrix} \sigma_{rr} & \tau_{r\theta} & \tau_{rz} \\ \tau_{r\theta} & \sigma_{\theta\theta} & \tau_{\theta z} \\ \tau_{rz} & \tau_{\theta z} & \sigma_{zz} \end{pmatrix} \tag{2.4}$$

The hollow cylinder has a height h, an external radius R_e and an internal radius R_i. In the document, the chosen convention is to define compressive stresses with a negative sign. An axial force F is applied vertically along the Oz axis, and a torque T rotating along the Oz axis. Both loadings are applied to the upper surface of the sample, while the lower surface stays fixed. Projecting the equilibrium of the upper surface on the vector e_z, one can associate stress tensor σ_{zz} to the applying force F which is shown via Equation (2.5)

$$F = \int \sigma_{zz} dS = \int_{r=R_i}^{R_e} \int_{\theta=0}^{2\pi} \sigma_{zz}(r, \theta, z = h)\, r d\theta dr \tag{2.5}$$

In order to link the stress tensor $\tau_{\theta z}$ to the applying torque T, the momentum equilibrium of the upper surface is projected on the vector ez. The relation between them can be seen in Equation (2.6).

$$T = \int_{r=R_i}^{R_e} \int_{\theta=0}^{2\pi} \tau_{\theta z}(r, \theta, z = h)\, r^2 d\theta dr \tag{2.6}$$

Stress fields are assumed to be uniformed inside the sample, then the stress tensor components σ_{zz} and $\tau_{\theta z}$ are provided in Equations (2.7) and (2.8), respectively.

$$\sigma_{zz} = \frac{F}{\pi(R_e^2 - R_i^2)} \tag{2.7}$$

$$\tau_{\theta z} = \frac{3T}{2\pi(R_e^3 - R_i^3)} \tag{2.8}$$

Considering the linear momentum balance, the remaining stress tensor components can be deduced as Equation (2.9), and (2.10).

$$\sigma_{r\theta} = \sigma_{rz} = 0 \tag{2.9}$$

$$\sigma_{rr} = \sigma_{\theta\theta} = 0 \tag{2.10}$$

Therefore, for a hollow cylinder tested with 2T3C hollow cylinder apparatus, two non-zero tensor components can be identified. With this the stress tensor becomes as can be seen in Equation (2.11).

$$\underline{\underline{\sigma}} = \begin{pmatrix} 0 & 0 & 0 \\ 0 & 0 & \tau_{\theta z} \\ 0 & \tau_{\theta z} & \sigma_{zz} \end{pmatrix} \tag{2.11}$$

2.2 Samples for testing with 2T3C Hollow Cylinder Apparatus

The idea of using a hollow cylinder apparatus is to have quasi-homogenous stress and strain fields in testing samples when applying torsion. A double-layered hollow cylinder sample tested with 2T3C apparatus has the ratio between inner and outer radius of 0.7 (61 mm/86 mm) which is within the range of the valid homogeneity assumption (0.65 - 0.82) proposed by Sayao and Vaid (Sayao & Vaid, 1991). The sample dimensions were chosen as a compensation between having good homogeneity stress fields inside the sample, well repeatable test results, and the capacity of the press in testing shear strength (Attia, 2020). The wall thickness of a sample tested with the apparatus is 25 mm. The thickness is 2.5 times higher than the nominal maximum aggregate size (NMAS) in this study. This ratio is quite small, but it still agrees with the range of 2-5 times proposed by Sayao and Vaid in order to have good repeatability. Moreover, during a shear test, the loading direction is tangential with the walls of the sample. Both inner and outer perimeters (383.27 and 540.35 mm) are quite superior to the NMAS. That is promising to have repeatable results. The homogenous stress and strain fields inside the sample allow to study directly the behaviour of the material without any back-calculation and hypothesis. The total height of a hollow cylinder sample for the 2T3C hollow cylinder apparatus is 125 mm. The layers are paved with two different mixtures and they are bonded together at the interface using bitumen, applied in the form of emulsion. Samples tested with the 2T3C hollow cylinder apparatus are normally fabricated in the laboratory; however, those which are

extracted from on-site can definitely be used. Figure 2.2 shows a photo of one of the double-layered hollow cylinder samples used in this thesis. The outer surfaces of the 2T3C double-layered hollow cylinder samples are subsequently covered with a speckle pattern. The objective is to generate the colours of an ununiform surface for the application of DIC technology. This consists of applying a thin layer of white paint on the outer surface of sample, and subsequently spraying lightly the black paint over. The procedure of speckle pattern application can be found on Figure 2.3.

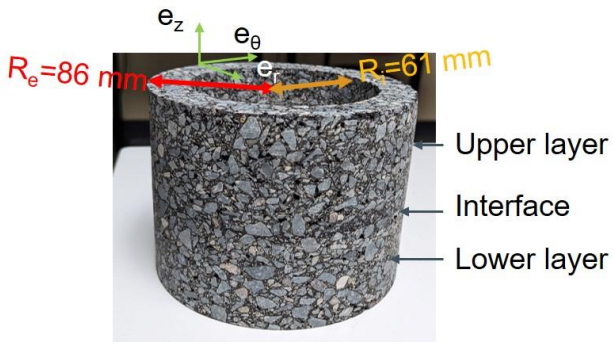

Figure 2.2: A double-layered hollow cylinder sample

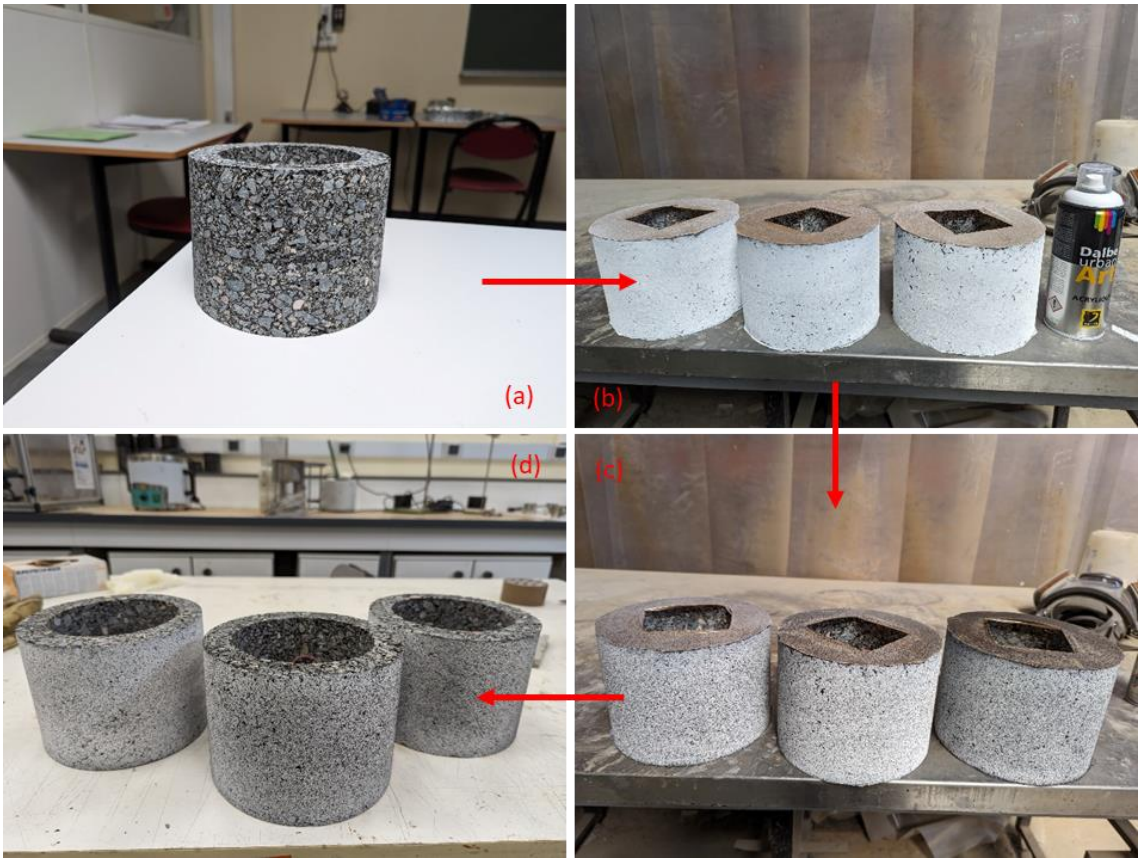

Figure 2.3: Procedure of applying speckle pattern on the outer surface of the 2T3C double-layered hollow cylinder samples: (a) sample before the application; (b) sample with the

application of white paint; (b) sample with the application of black paint; sample ready for testing

2.3 2T3C Hollow Cylinder Apparatus

The hydraulic press is used to apply mechanical loading on a sample that can be monotonic or cyclic combined with torsion or tension/compression. In each direction of cyclic loading, the apparatus can work at the highest frequency of 10 Hz. The hydraulic press used for the 2T3C hollow cylinder apparatus can apply a normal force up to 100 kN and a torque up to 2 kN.m. The loads are measured by two load cells located on the press. During a test, a sample is placed inside a thermal chamber which regulates temperature, and the temperature range of that chamber is -20 °C to 60 °C. The chamber was especially designed with two transparent windows on the two sides which allow two camera groups to take photos from the outside. Figure 2.4 presents the 2T3C hollow cylinder apparatus with its important components. Figure 2.5 demonstrates the set-up schematic for testing on a 2T3C double-layered hollow cylinder sample.

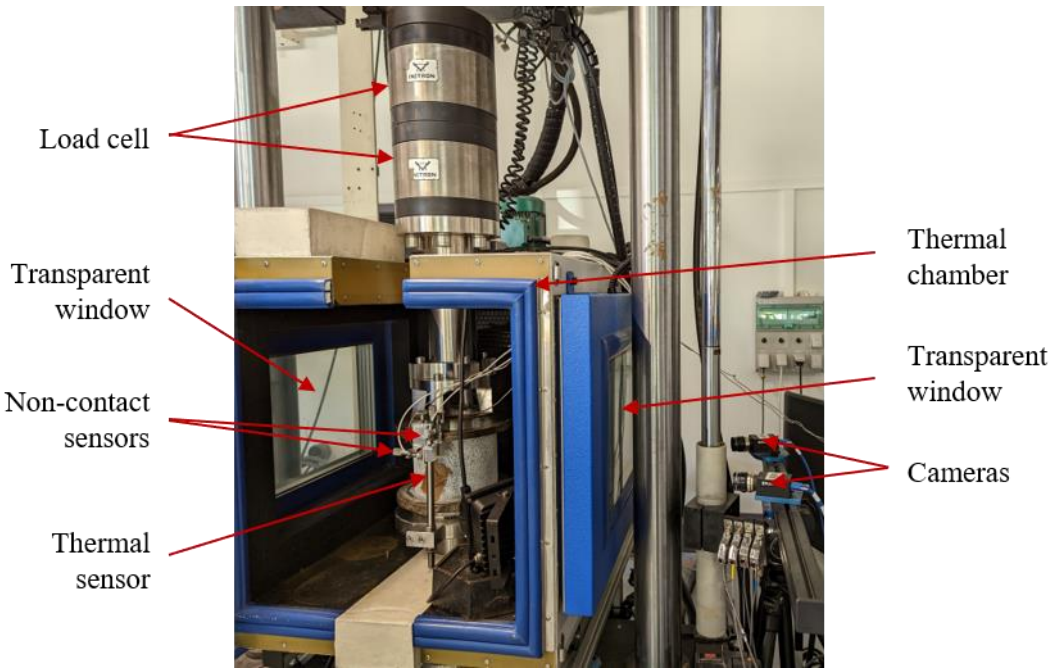

Figure 2.4: 2T3C hollow cylinder apparatus to study interface behaviour

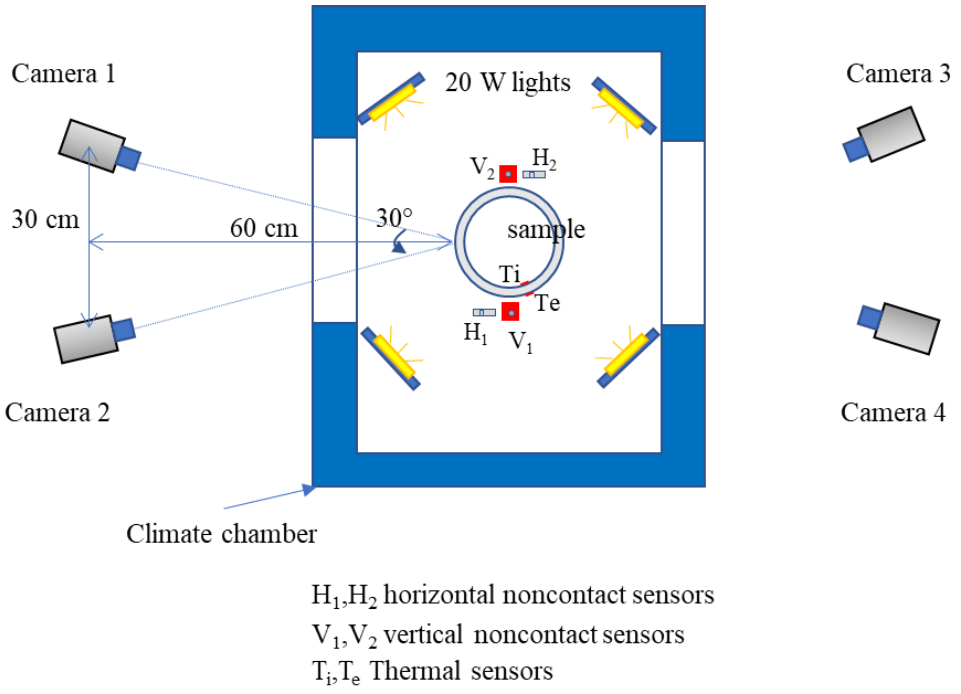

Figure 2.5: The set-up for a test on a 2T3C double-layered hollow cylinder sample

A double-layered hollow cylinder tested with 2T3C hollow cylinder apparatus is glued to two aluminium caps using epoxy resin. The caps were designed with a hollow structure, with an interior radius of 52.5 mm and an outward radius of 117.5 mm. The apertures present in the caps facilitate the ingress of air into the hollow cylinder, so promoting uniform temperature over the entire sample. A ruler helps to centre the testing sample. When the position is found, the sample with a cap is placed in a centring device. The device includes a support and four screws attached to its side wall. The specimen is fixed to the upper cap with the epoxy glue and subsequently secured to the wall using a rope, as depicted in Figure 2.6. After waiting for 4 hours, the top cap is fixed to the press. The bottom cap is also fixed to the press, and is then

glued to the specimen (Figure 2.7). This procedure ensures a good alignment and allow avoiding eventual default of parallelism between the top and the bottom surface of the sample.

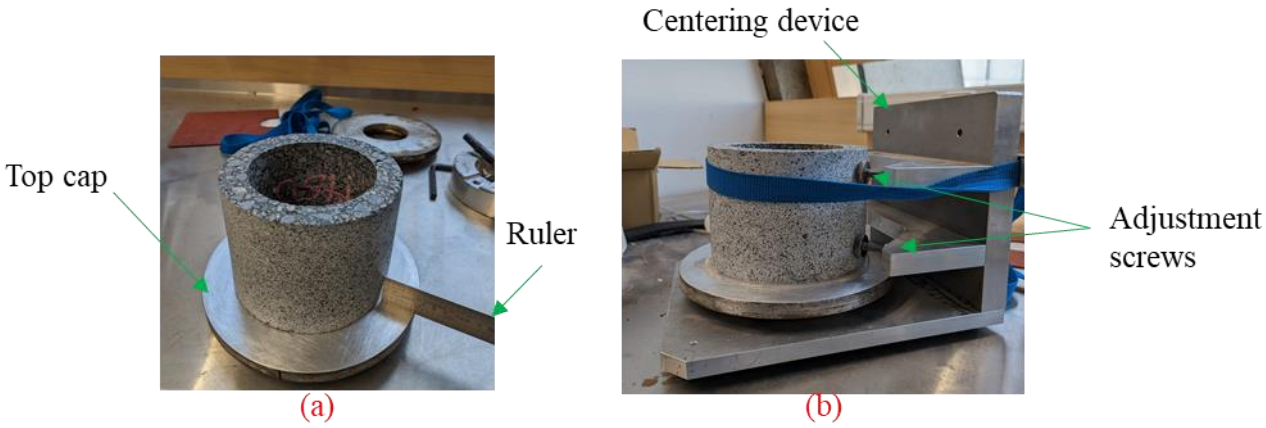

Figure 2.6: Glue sample to the top cap with the support of centering device: (a) position the sample on the top cap; (b) glue the sample with the centering device

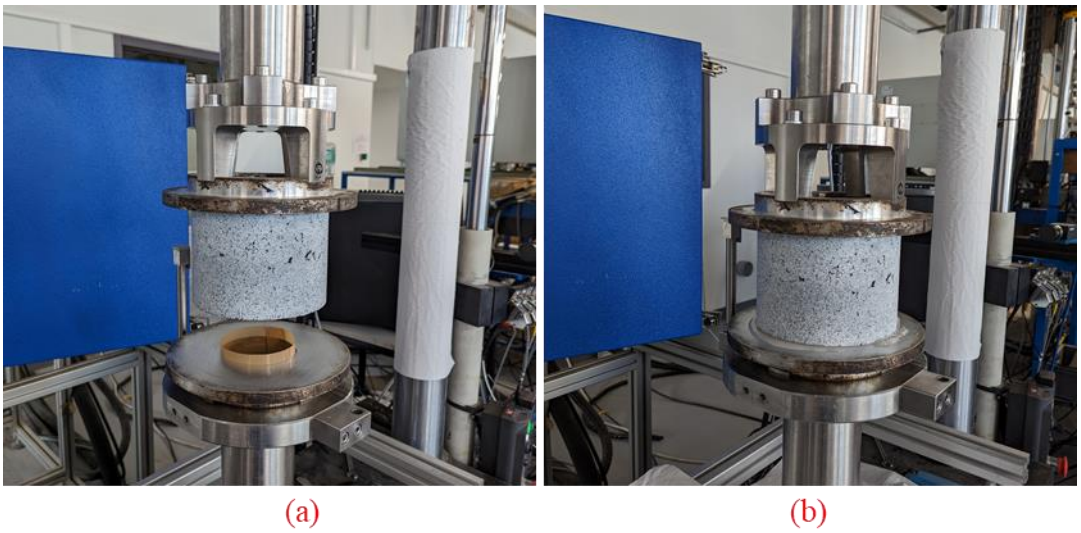

Figure 2.7: Glue the sample to the bottom cap: (a) fix the sample with the top cap to the press, (b) lower down the sample using the press to glue to the bottom cap

2.4 Measurement and acquisition systems

2.4.1 Loading cells, positional and rotational sensors

The hydraulic press is equipped with a pair of embedded load cells. The load cells provide the measurement of both the normal force and torque exerted on the testing sample. The axial load cell has the capacity to measure the maximum axial load of ± 100kN that can be exerted by the hydraulic press. In a similar vein, the rotational load cell has the capability to measure torque

up to a maximum value of ± 2000 Nm. In addition, the actuator is equipped with two sensors that are capable of measuring its vertical position and rotation angle. The measurement range for the axial direction is ± 75 mm, while for the rotational direction it is ± 45 °. Nonetheless, these two sensors are not accurate enough to control very small loading strain. Additional sensors need to be used.

2.4.2 Noncontact sensors

Four noncontact sensors are used to control the applied displacement. They are fixed to the top cap of a specimen and aim at a metallic target attached to lower cap. Two of them are used to measure the torsional displacement, and the other two are used for axial displacement. Two pairs of sensors are placed in two opposite sides, and their averaged measurement are used to control the applied displacement. The accuracy of those sensors is 0.1µm in a range of 1000 µm. Figure 2.8 shows the placement of the noncontact sensors on the top cap.

Figure 2.8: Two noncontact sensors placed in the front side used to measure axial displacement and rotation applied to the sample

2.4.3 Thermal sensors

To ascertain the precise temperature of a hollow-cylinder sample, two thermal sensors, namely PT100, are affixed to the inner and outer walls. The measurement range of the two temperature sensors spans from -50 °C to 100 °C. The temperatures obtained by the two sensors will

afterwards be compared in order to validate the uniformity of temperature within the sample. Figure 2.9 shows to the placement of the thermal sensor placed on the outer surface of the 2T3C double-layered hollow cylinder. The other sensor is placed on the inner surface, on the other side of the wall.

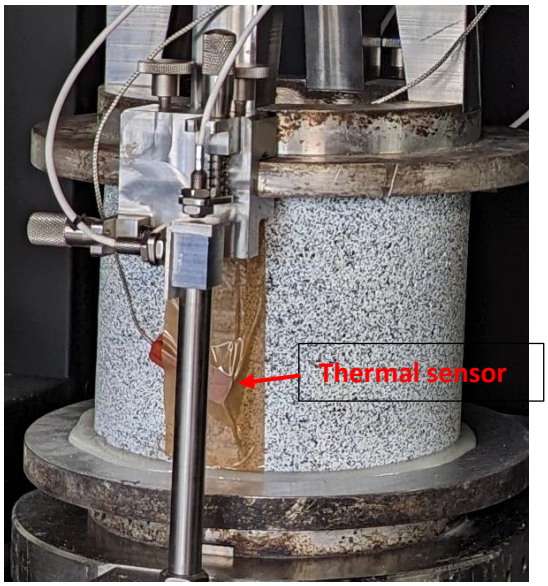

Figure 2.9: A thermal sensors placed on the outer surface of the 2T3C double-layered hollow cylinder

2.4.4 Cameras and 3D Digital Image Corellation (3D-DIC)

The displacement or strain obtained from non-contact sensors is a global value of the whole sample which contains two layers and an interface. In order to distinguish between the strain within each layer and displacement discontinuity at the interface, cameras and 3D-DIC technology are used. The displacement discontinuity of the interface is referred to as the "gap". There are four cameras divided into two groups and placed in front of two transparent windows, and two cameras from each group take photos from the external surface of a sample. Two cameras from the same group are 30 cm from one to the other and they are 60 cm away from sample's surface. The highest acquisition frequency of the cameras is 35 frames per second (fps). The idea of 3D-DIC is to correlate the 3D photos in different deformed states with a 3D photo in reference state (taken before loading) to deduce the displacement. More details about the 3D-DIC will be mentioned in the next parts.

Two cameras from the same group take two photos of the same studied surface at the same deformed states. Before the beginning of a test, a calibration of all 3D-DIC device should be done, using reference calibrated grid. The purpose of this calibration is to generate equations

which link all pixels on the photos taken from two cameras to the spatial positions of the points on the studied surface, and describe those positions in a coordinate system related to studied surface or to the cameras. Figure 2.10 shows two pictures of the same sample's surface with calibration grid taken from two cameras. 3D DIC technology can describe the studied surface in three dimensions using two photos taken from the same camera group at the same deformed state. A subset is chosen around a point needed to calculate displacement. The principle of the 3D description is to project a subset in the first photo to a virtual tangential plane, then use the results from stereo-correlation to back project and link that subset to a subset in the photo taken by the second camera. A tangential plane is defined by its position and orientation. Assembling all tangential planes projected from the area of interest creates a 3D surface. The size of each subset is 25x25 pixels, and the distance between two points for calculation is 6 pixels. A pixel has a colour within the range of 256 greyscale level. Therefore, a subset in a photo taken by the first camera having a random combination $25x25$ pixels^2 makes it distinct, and the similar subset is found in the second photo. The projection and back projection are conducted on all deformed states by the 3D-DIC software VIC®3D. The principle of the 3D-DIC correlation is schematised on Figure 2.11. The calibration algorithm searches in each deformed state two subsets that are most similar to those in the reference state. The displacement of a point in a deformed state is subsequently deduced from the relative differences in position and orientation of the tangential plane in that deformed state compared to those in the referent state. Figure 2.12 shows an example for DIC correlation of two similar subsets from two different deformed states represented by two points M_0 and M.

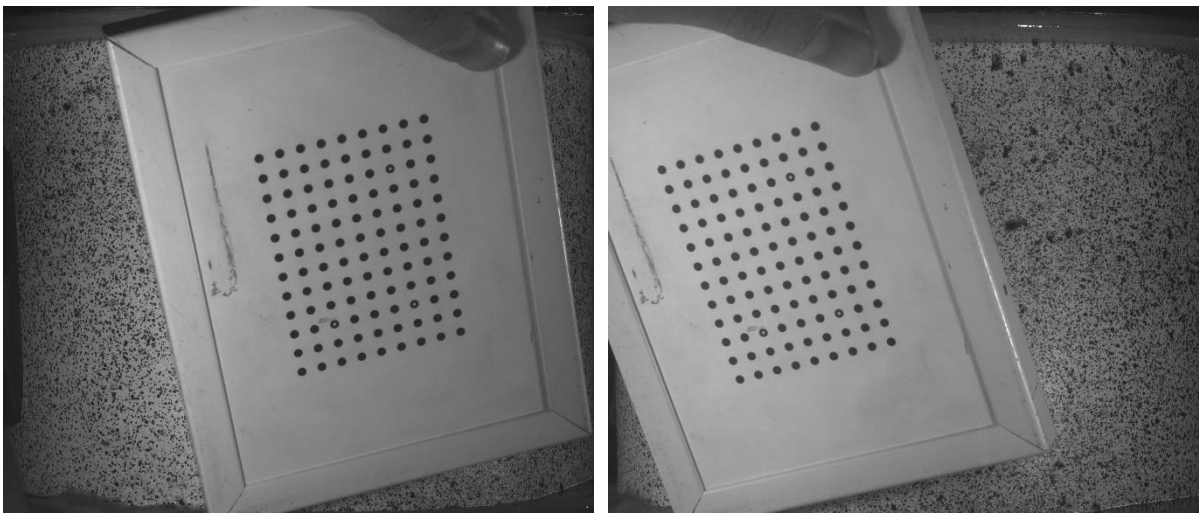

Figure 2.10: Stereo-correlation calibration for the camera system before the test; two pictures of the same area, where calibrated reference grids are placed, taken from two cameras

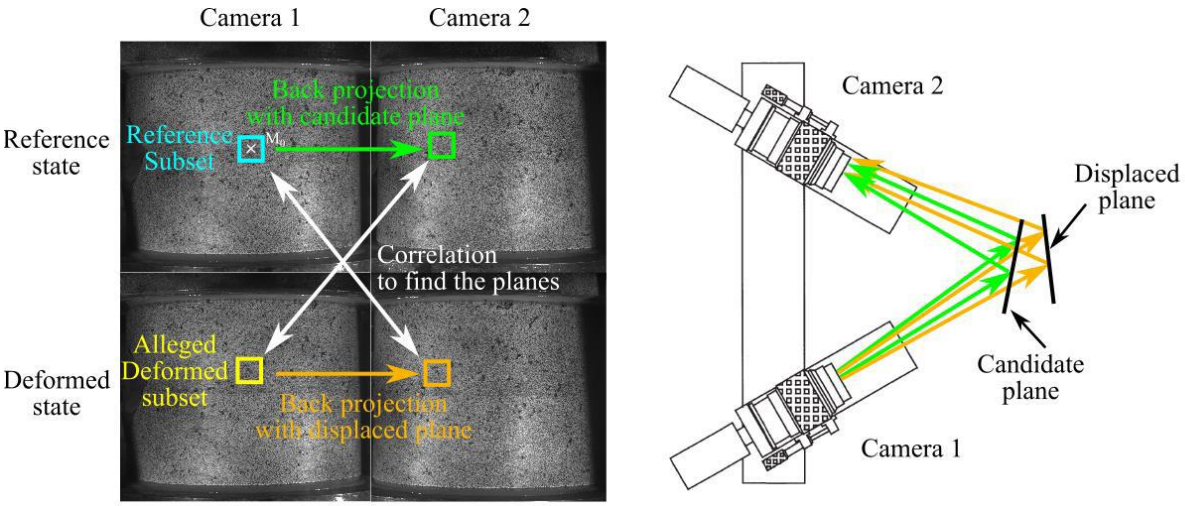

Figure 2.11: Principle of the 3D- DIC correlation (Attia, 2020)

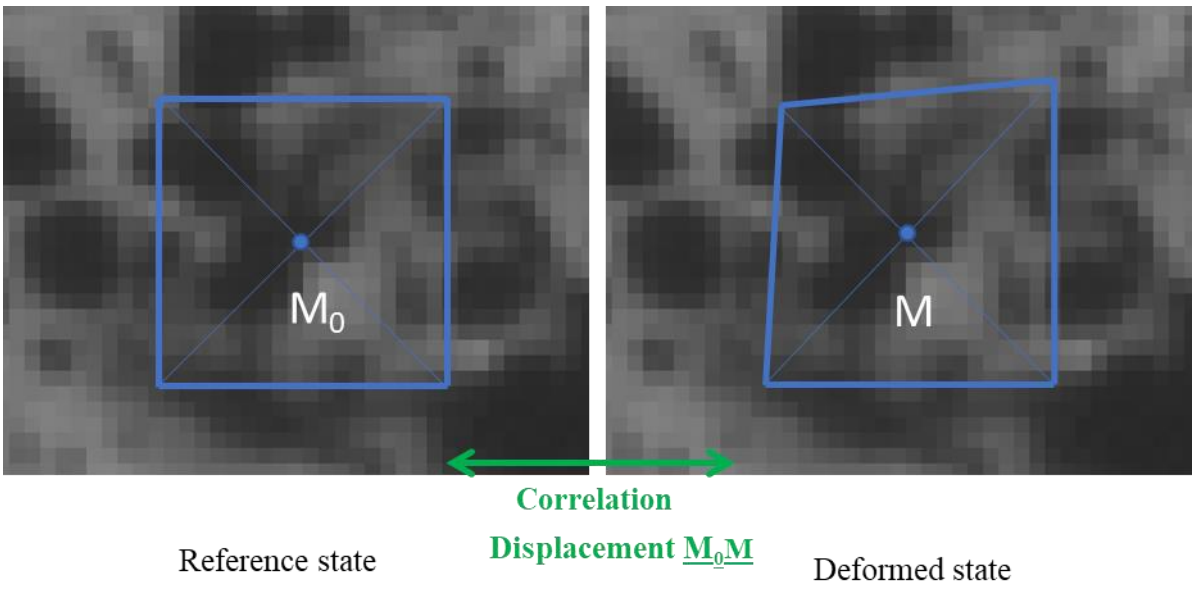

Figure 2.12: Description of the DIC principle

2.4.5 Acquisition set up

In summary, the measurement systems encompass an internal system, an external system, and a camera system as can be seen in Figure 2.13. The internal system is responsible for quantifying the forces measured by the load cell (+2 sensors) in both axial and torsional directions, as well as determining the positions of the actuators along these two directions (+2 sensors). The external system is comprised of two noncontact sensors (+2 sensors) to measure the axial displacements, and two others for torsional ones (+2 sensors). The eight sensors are connected to two acquisition cards, one of them is in charge of acquiring data in the axial direction and the other in the torsional direction. Therefore, each card includes four channels.

There is another external acquisition card consisting of 16 channels. This card allows to record data from the mentioned eight sensors and from two thermal sensors.

The camera system also has its own acquisition card which includes eight analogical channels. That is similar to the above external card, but it allows to record data at each moment a photo is taken. Therefore, all the loading information and time are linked with taken photos. Furthermore, this card includes a digital card that is connected to the internal digital card of the press. That allows the press to send the transistor-transistor logic (TTL) signal to trigger the camera system. TTL serial communication pertains to the utilisation of raw transistor voltage levels for single-ended serial transmission. There are two levels of voltage, that are 0 (low) and 1 (high). It is possible to request the camera system to take photos automatically by sending the TTL signal from the press to the camera system. That is really important for a fatigue test, since the significance of dense data capturing at the beginning, when parameters change more rapidly, with data acquisition becoming less frequent as the test progresses. Table 2.1 dedicates to the measurements and their description.

Table 2.1: Measurements with their units from the 2T3C hollow cylinder apparatus

Signal sources	Measurement system	Types of measurement	Symbol	Range of measurement
Load cells	Axial load cell	Axial load	F	± 100 kN
	Torque cell	Torque	T	± 2000 N.m
Actuators	Position sensor	Vertical position	Z	± 75 mm
	Rotation angle sensor	Rotation angle	θ	± 45 °
External source	Two vertical noncontact sensors	Global vertical displacement	u_{zg}	1000 µm
	Two rotation noncontact sensors	Global rotation displacement	$u_{\theta g}$	1000 µm
	PT100 sensor	Temperature on the inner wall	Ti	from -50 °C to 100 °C

	PT100 sensor	Temperature on the outer wall	Te	from -50 °C to 100 °C

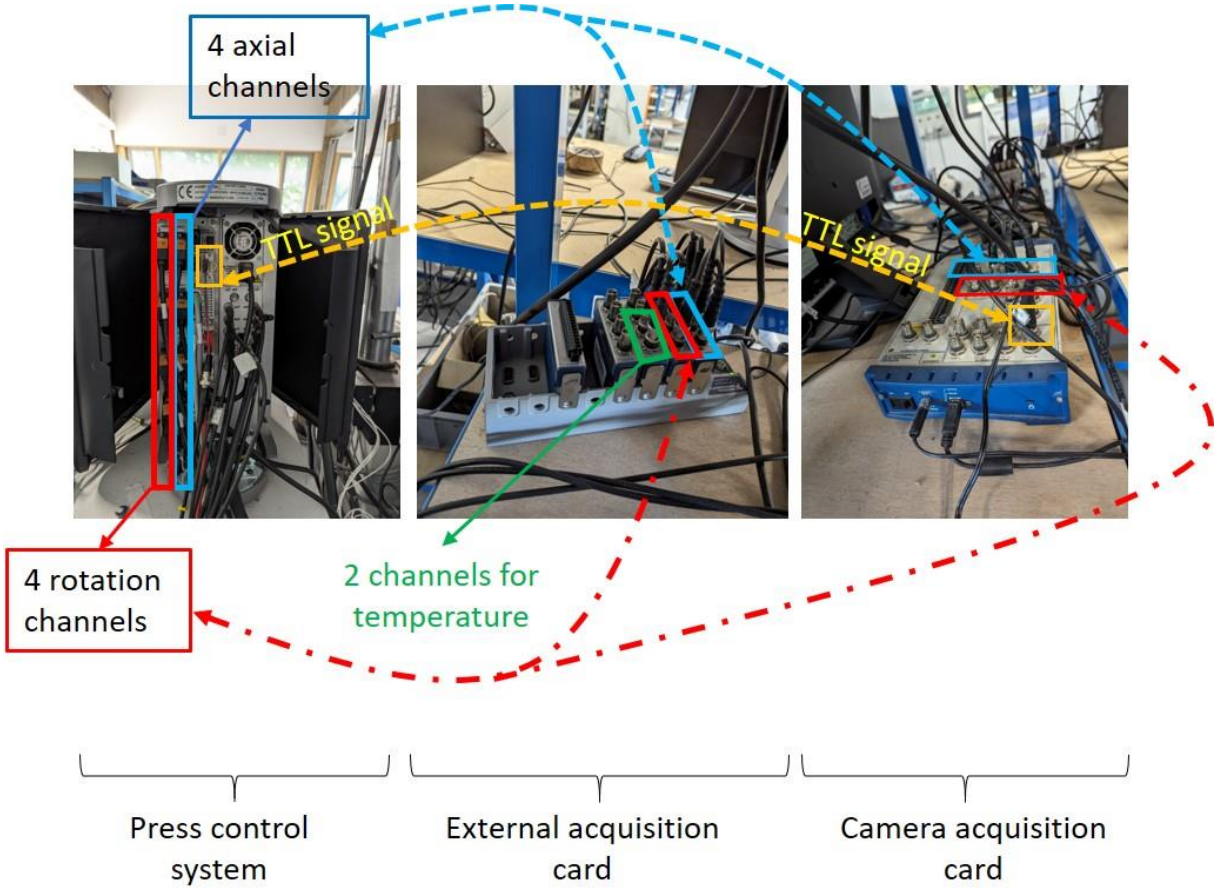

Figure 2.13: Three data acquisition systems for the 2T3C hollow cylinder apparatus

2.4.6 3D-DIC analysis and calculation method for strains in two layers and displacement gap at the interface

After the displacements are calculated for all points in the studied surface, the strains in two layers and the displacement gap can be computed by a method developed at the University of Lyon/ENTPE. The method consist in drawing 12 rectangles on each layer and the interface is considered at the middle where there is a sudden change of colour according to a colour map of displacement. The size of each rectangle is fixed at 3x100 mm as can be seen in Figure 2.14. Averaged tangential displacements (u_θ) are calculated in all the rectangles and plotted in a diagram of u_θ-z in Figure 2.14 on the right, the y axis shows heights (z) at the centres of 24 rectangles. If the materials in each layer is homogenous, there are 2 distinct linear regression lines in the diagram. The slope of each linear regression line generated by 12 values in the diagram (u_θ-z) from a layer is the strain of that layer. Since two different mixtures are used for

double-layered samples in this study, two different slopes ($\varepsilon_{\theta z.up}$ and $\varepsilon_{\theta z.low}$) can be found in a deformed state. The distance between the two regression lines at the interface is considered as the displacement gap (Δu_θ).

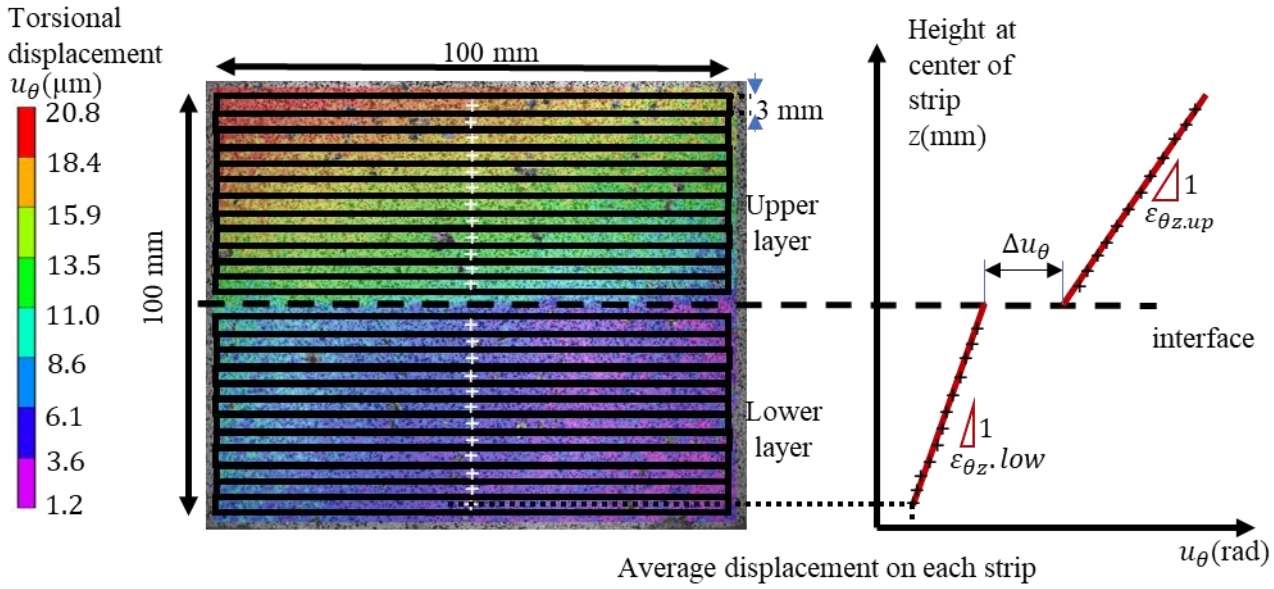

Figure 2.14: 3D-DIC technology application at one of the deformed states for the test applied with 50 μm/m global shear strain.

2.5 Conclusions

One of the advantages of the 2T3C hollow cylinder apparatus is that the stress and strain fields applied in both layers and the stress and displacement fields at the interface are quasi-homogenous. In order for this assumption to be valid, the hollow cylindrical samples wall thickness must be small enough compared with the diameter. The outer and inner radii are 86mm and 61mm, respectively. The ratio of the inner radius over the outer one is 0.71, which is within the range of an acceptable homogeneous assumption. Tested samples are double-layered hollow cylinders, and the two layers have the same approximate heights. The total height of a double-layered hollow cylinder is 125 mm.

The samples are located inside a thermal chamber, which regulates the temperature in a wide range from -20°C to 60°C, which is sufficient for testing a sample made of bituminous mixtures. Two thermal sensors (PT100) are placed on the inner and outer surfaces of the tested sample to monitor temperatures and verify a uniform temperature inside the sample. Two sides of the thermal chamber are built with transparent windows, allowing four cameras to take images from the outside.

The 2T3C apparatus is equipped with a hydraulic press that can impose axial or/and torsion loading either cyclically or monotonically. The greatest axial loading is ±100 kN, and

that of torsion is ±2 kN.m. For cyclic loading, the maximal frequency is 10 Hz in tension/compression and torsion. There are two load cells measuring normal force and torsion applied from the press. There are four noncontact sensors. Two of them measure the relative axial displacements of top and bottom caps on two opposite diametral sides of the sample. They allow obtaining the global axial strain (ε_{zzg}) as an average value. The two others give the global displacements in the tangential direction ($u_{\theta zg}$) and allow, in the same way to obtain the global shear strain ($\varepsilon_{\theta zg}$). The global shear strain is used by the press monitoring system to control shear loading during the test (sinusoidal loading). The accuracy of the sensors is 0.1 µm.

In the next chapter, experimental campaigns launched with the 2T3C hollow cylinder apparatus will be introduced.

Chapter 3: EXPERIMENTAL CAMPAIGN

Chapter 3 describes test procedures for three experimental campaigns to study the thermomechanical behaviour of interfaces using the 2T3C hollow cylinder apparatus. Compositions of materials at the interface and in layers will be discussed in the first section. Detailed descriptions are provided on the slab fabrication and sample preparation processes. The complex shear modulus test, the non-linearity test, and the fatigue test are the three experimental campaigns conducted with the following objectives in mind:

- Campaign 1: The Linear Viscoelastic and Elasto-Visco-Plastic behaviour of interfaces will be studied through the complex shear modulus. The Linear Viscoelastic of the bituminous mixture in layers will be investigated.
- Campaign 2: Through cyclic tests, the effect of nonlinearity bias on the norm and phase angle of complex interface stiffness shall be analysed.
- Campaign 3: Fatigue behaviour of interfaces and in bituminous mixtures in layers shall be investigated.

To determine the effects of varying tack coat residual content and types on the thermomechanical behaviour, fatigue performance, and nonlinearity effect of four interface configurations, experiments will be conducted on each of these three experimental campaigns.

3.1 Materials

All materials were provided by the Eiffage company.

3.1.1 Bituminous mixtures in layers

Samples tested in this thesis are double-layered hollow cylinders with two layers made of two different mixtures. The upper layer is a French BBSG3 (Béton Bitumineux-Grenu 3) mixture which has a nominal maximum aggregate size of 10 mm (EN NF 13108-1, 2017). There are 20% of Reclaimed Asphalt Pavement (RAP) content added to the mix. The total bitumen content of the mix is 5.4% bitumen graded 50/70 including RAP binder. The mixture is commonly used for a surface course of a pavement structure in France. The lower layer is a French high modulus EME2 mixture with the nominal maximum aggregate size of 14 mm, and there are 30% of RAP (EN NF 13108-1, 2017). The binder used in this mixture is bitumen graded 15/25, and a content of 5.6% of the mix weight including RAP binder. The gradation curves of two mixes are introduced in Figure 3.1. The two mixtures used 0/4 sand from the quarry Igé, and aggregates 4.0/6.3, and 6.3/10.0 fractions from the quarry Creuzeval. The fraction of 10.0/14.0 of the lower layer EME2 mixture was collected from the quarry Creuzeval.

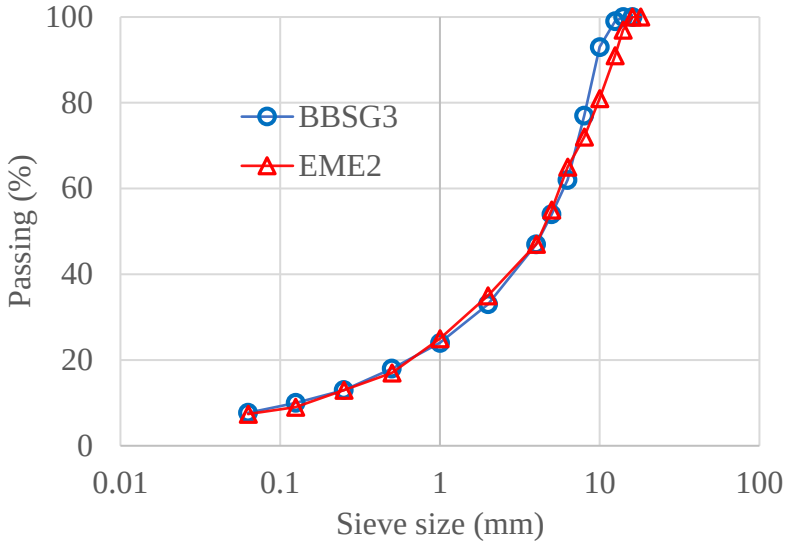

Figure 3.1: Gradation curve for upper layer (BBSG3), and lower layer (EME2)

3.1.2 Tack coat at the interface

At the interface of the two bituminous layers, two distinct tack coatings were applied. The first tack coat consists of an emulsified bitumen with a neat bitumen grade of 160/220. The bitumen concentration in the emulsion is 65%. The second tack coat is composed of bitumen modified with Styrene-Butadiene-Styrene (SBS). Likewise, the modified bitumen concentration in the emulsion is 65%. The penetration grade of the bitumen used for polymer modification is 160/220 penetration grade.

In order to study different factors from tack coat influencing mechanical behaviour of the interface, four interface configurations were chosen as can be seen in Table 3.1.

A reference 2T3C hollow cylinder sample includes the upper layer made of the BBSG3 mixture and the lower layer comprised of EME2 mixture. The interface between two layer used tack coat emulsified with pure bitumen, and the residual content of bitumen is 350 (g/m^2). There would have been 12 samples produced; however, a sample was broken during the coring. 11 samples cored from four different slabs named REFA, REFB, REFC, REFD were obtained.

To study the influence of residual bitumen dosage, two more configurations were added along with the reference one. A configuration has a lower bitumen dosage of 250 g/m^2, and another one with a higher bitumen dosage of 450 g/m^2. One slab was fabricated for each configuration, and three samples were cored from it. LDO and HDO designate the slabs with low and high bitumen dosage, respectively.

To study the influence of bitumen type, one more configuration was implemented. Instead of using pure bitumen, for this configuration, the emulsion is made of polymer modified bitumen. The type of polymer is SBS added with a dosage of 2.6% be weight of the bitumen. The dosage of residual bitumen at the interface is the same as the reference samples (350 g/m^2). The slab was named SBS after the type of modification for bitumen at the interface.

Table 3.1: Four configurations of the interface

Name	Bituminous mixtures		Tack coat at the interface		Number of slabs	Number of samples
	Upper layer	Lower layer	Type	Residual bitumen (g/m2)		
REF	BBSG3	EME2	Pure bitumen	350	4	11
LDO	BBSG3	EME2	Pure bitumen	250	1	3
HDO	BBSG3	EME2	Pure bitumen	450	1	3
SBS	BBSG3	EME2	SBS modified bitumen	350	1	3

3.1.3 Slab fabrication and sample preparation

Materials were prepared in laboratory. There are 3 main stages of fabrication: slab compaction, sample coring and surface painting.

Since samples tested with 2T3C hollow cylinder apparatus are double-layered samples, a mixture compaction needs to be done one layer after the other. Materials are compacted in a mould using the French wheel compactor standard. The final dimension of a slab is 600x400x150 mm^3. The first layer is firstly compacted to a height of 75 mm. The it is left in laboratory until it cooled down. The waiting time is 24 hours. The next step is the tack coat application using a brush to spread tack coat over the surface of the first layer. Tack coat needs at least 4 hours to break totally. Then, the mixture compaction process is repeated for the second layer of a slab to reach the final height of a slab is 150 mm. Figure 3.2 shows these steps of the

fabrication of a double-layered slab. All the slab preparation was performed at the Eiffage's laboratory in Corba, France.

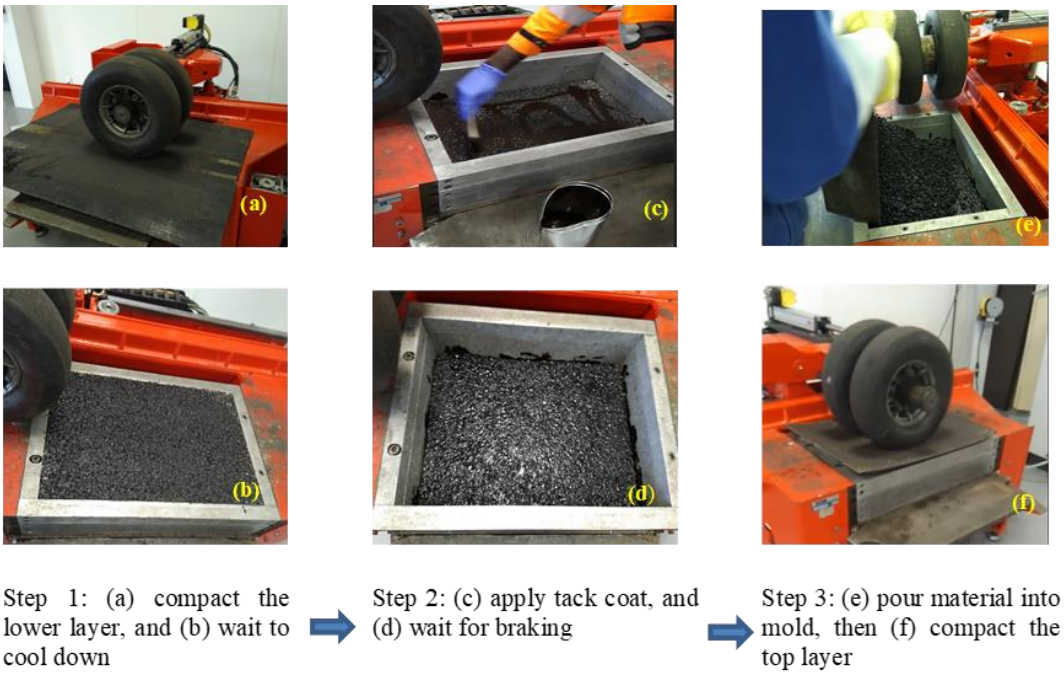

Figure 3.2: Double-layer slab fabrication in laboratory using a French wheel compactor

Operations to obtain samples from the slabs starts few days after the second layer of a slab is compacted. They were performed at ENTPE. 3 samples were cored from each slab. The coring process begins with the small drill to have the internal surface of 122 mm in diameter. Then, the sample is extracted from a slab by using the bigger drill to create a sample with an external diameter of 172 mm. A double-layered sample of 150 mm height after being extracted is then trimmed approximately 10 mm at each end, and a final sample has 125 mm height.

Figure 3.3 demonstrates the sample preparation from a slab. Figure 3.4 shows a sample cored, trimmed and painted.

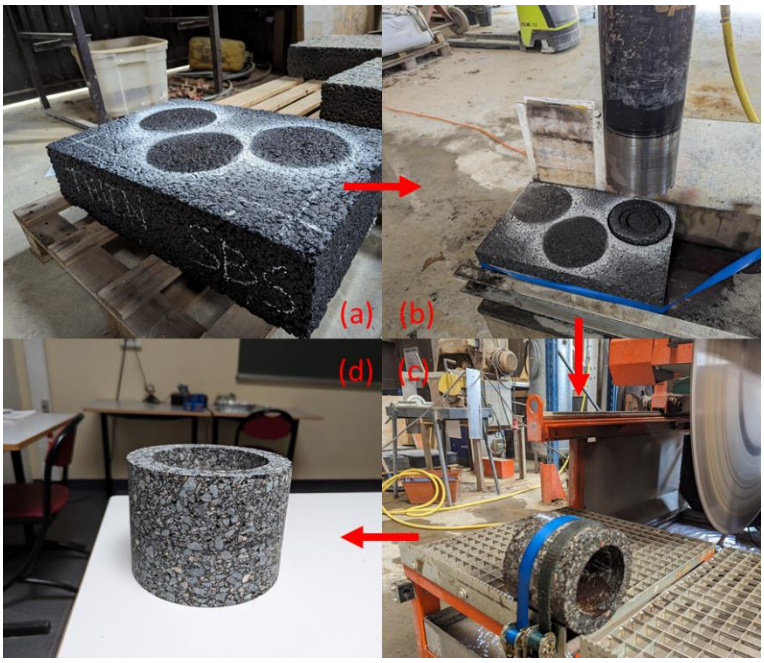

Figure 3.3: Sample preparation: (a) position samples in a slab, and cutting four edges of a slab; (b) core three sample out of a slab; (c) trim the top and bottom surfaces of samples; (d) dry sample before being painted.

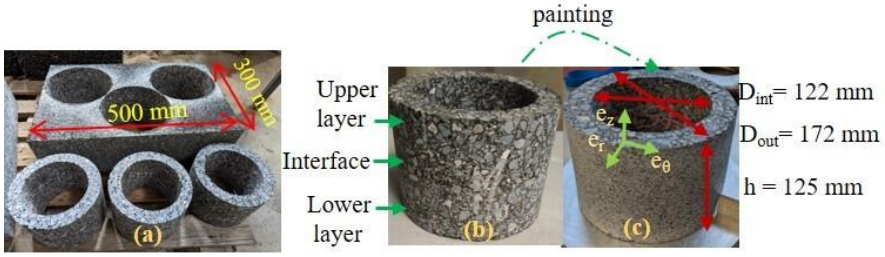

Figure 3.4: Picture of the three samples cored from a slab (a), pictures of a sample after being cored and sawed, before painting (b), and after painting (c)

3.1.4 Double-layered hollow cylinder properties

The sample is left in the laboratory at least 2 weeks for drying before testing. Later, the air-void of the double-layered hollow cylinder is calculated. The distance from the bottom of sample to the interface (h_{low}), and the total height of sample (h) are measured using a ruler with the accuracy of 1 mm. The air-void (v) of the sample is calculated using Equation (3.1), where ρ_m is the density of the sample calculated from sample's volume and weight. The real density of the bituminous mixture in lower layer (ρ_{r_l}) is 2.450 (g/cm^3) and that in upper layer (ρ_{r_u}) is 2.488 (g/cm^3). The air-voids of tested samples are shown on Figure 3.5. The height of a sample is averaged from 3 measurements around the sample with a distance of 120°. Since the air-void

of a sample is a global value calculated for the whole sample, and considering that the visibility of interface is not always perfect and the accuracy of the ruler is not high, the calculated air-voids are approximate.

$$v = 1 - \frac{\rho_m}{\frac{h_{low}}{h}\rho_{r\_l} + \frac{h - h_{low}}{h}\rho_{r\_u}} \tag{3.1}$$

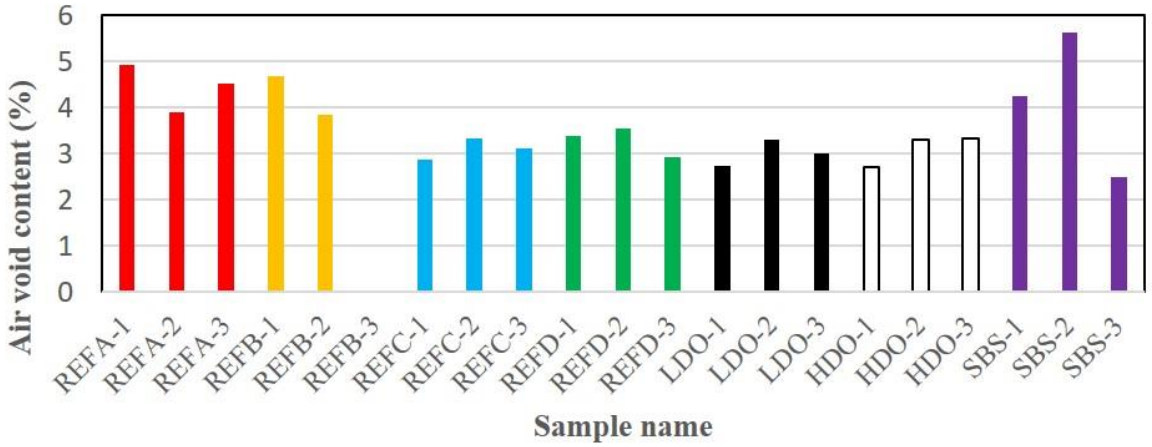

Figure 3.5: Air-void content of samples tested in thesis

3.2 Experimental procedures

As previously mentioned in Chapter 1 for the literature review, important shear stresses can be found in areas of acceleration and sudden brake of vehicles. In addition, the shear stress can also be found close to the contact area between pavement and the tires of a vehicle, even if it moves at constant speed. This can be verified by modelling a multi-layered pavement using the Burmister model from the software Alizé. The model assumes that the pavement layers exhibit elasticity and are perfectly bonded. Two 25-centimeter-diameter discs are subjected to a static vertical tension of 0.662 MPa. Effect of horizontal force developed at tire-pavement interface is not considered in calculation. Their centres are spaced 37.5 centimetres apart. Their geometries and those of the pavement can be seen on Figure 3.6. The results of shear stress calculated close to an extremity of a tire and at the closet interface to the surface (the distance of 0.3 m away from the longitudinal x axis, at the depth of 0.06 m) is shown on Figure 3.7. The findings indicate that the shear stress reaches its peak value at approximately 0.26 MPa. Consequently, an investigation into the thermomechanical characteristics of the interface under shear conditions, as well as its behaviour when subjected to normal stresses, is imperative. In following experimental campaigns for the complex shear modulus test, nonlinearity test, and shear fatigue test, the shear displacement applied on 2T3C double-layered hollow cylinders will

be subjected to different global displacement amplitudes ($u_{\theta g\_0}$) (or global shear strain amplitudes ($\varepsilon_{\theta g\_0}$). Furthermore, the integration of three distinct normal compressive stresses (σ_{zz} = -0.026, -0.125, - 0.250 MPa) will enable the assessment of their impacts on the behaviour of interfaces in the small strain domain and the fatigue domain when subjected to shearing.

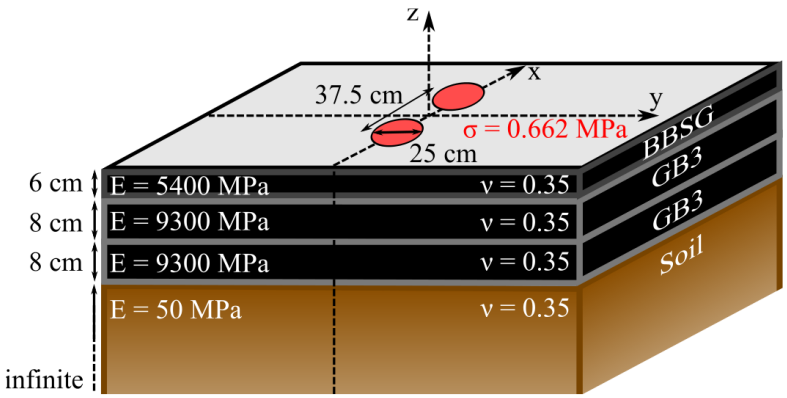

Figure 3.6: A typical multi-layered pavement structure modelled with the Burminster model (Attia, 2020)

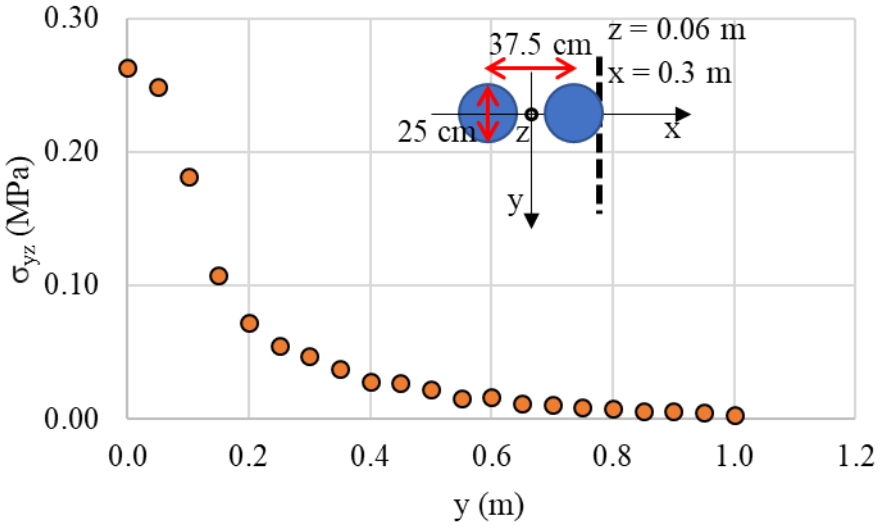

Figure 3.7: Shear stress along x = 0.3 m at the interface between the surface course and the base course (z = 0.06 m) simulated with the Burminster model.

3.2.1 Procedures for tests in the small strain domain

3.2.1.1 Complex shear modulus test

Before contemplating any possible damage that might happen to a bituminous mixture or an interface, it is essential to understand and design for its normal functioning state. A bituminous mixture sample exhibits Linear ViscoElastic behaviour when subjected to a small number of cycles of small strain amplitudes. The same conditions should be applied to investigate the potential LVE behaviour of the interface. Furthermore, the complex shear modulus is evidently dependent on the frequencies and temperatures of the testing. In order to

characterise bituminous materials and interfaces that exhibit LVE behaviour, a complex shear modulus test can be employed.

With the 2T3C hollow cylinder apparatus, the complex shear modulus test consists in applying sinusoidal torsion on bituminous material for different combination of temperatures and frequencies within the small strain domain. Five temperatures (from 0°C to 40°C) combined with five frequencies (from 0.01 Hz to 1 Hz) were applied. Two global shear strain levels were chosen to study the linear and non-linear thermomechanical behaviour at interface, 50 and 200 µm/m. Since the tests are controlled globally for a whole sample, the strains in layers and the displacement gap at the interface may vary depending on the testing temperatures and frequencies. At each testing temperature, the sample needs to be conditioned at that temperature for 4 hours before testing. Those 4 hours ensure that the temperature inside a sample is homogenous. Testing time is around 15 minutes per temperature. During tests, the axial loading is maintained at a small compression. The normal stress varies within three values: -0.026, -0.125, and -0.250 MPa to study its impact on the shear LVE behaviour of the interface as well as of the bituminous layers. The minimum normal stress value is -0.026 MPa, which effectively inhibits the interface creep in tension.

To assess the impact of various interface configurations on the thermomechanical behaviour of interfaces, shear complex modulus tests are conducted on REF, HDO, LDO, SBS samples. The identical temperatures (ranging from 0°C to 40°C), frequencies (from 0.01 Hz to 1 Hz), amplitude of global shear strain (50 µm/m), and a single normal stress of -0.026 MPa were applied to samples from each of these configurations. Figure 3.8 illustrates the protocol for the advance shear complex modulus test.

For a loading cycle, 50 images are taken by a camera for 3D DIC application, except at the loading frequency of 1Hz, where the number of images is limited to 35. Before a shear

complex modulus test, the stereo calibration with calibration grid should be done as described in Chapter 2.

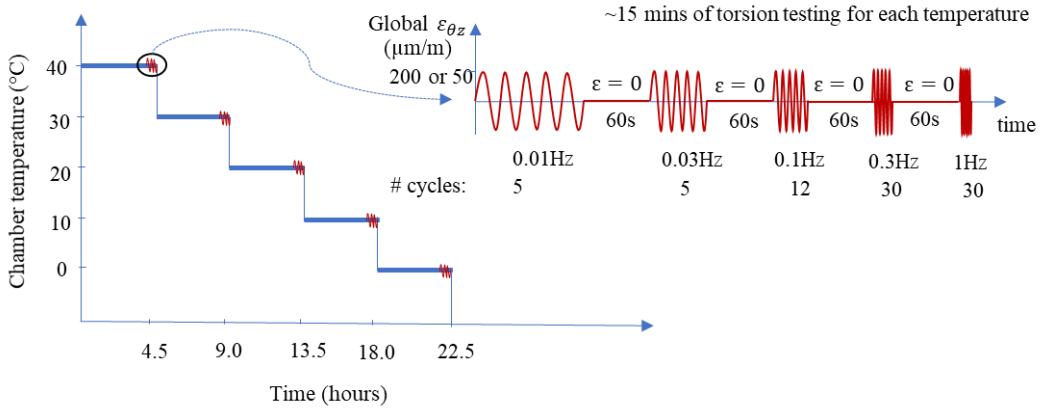

Figure 3.8: Complex shear modulus test procedure: 5 temperatures from 40 °C to 0 °C, 5 frequencies from 0.01 Hz to 1 Hz

3.2.1.2 Nonlinearity test

The nonlinearity of the interface behaviour was previously observed. It generates a reduction of the norm and an increase of the phase angle of complex modulus when increasing the applied strain (Di Benedetto et al., 2011; Mangiafico et al., 2018). The authors showed that this biasing effect appears at the beginning of a cyclic test. In order to quantify the nonlinearity that is responsible for the reduction of interface stiffness during a cyclic test, nonlinearity tests will be conducted using different global tangential strain amplitudes from 30 µm/m to 110 µm/m with steps of 20 µm/m increment, as shown in Figure 3.9. Three cycles are applied at a global strain amplitude, followed by rest periods for ten minutes between two testing strain amplitudes. Temperature and axial loading applied for this test are similar to those for the fatigue test; which are 10 °C and -0.026 MPa, respectively.

In order to evaluate the influence of different interface configurations on the nonlinearity characteristics of interfaces, nonlinearity tests are performed on different interface configurations, alongside the reference configuration (REF). HDO (high residual binder

dosage), LDO (low residual binder dosage), and SBS (tack coat utilising modified bitumen) are three additional configurations.

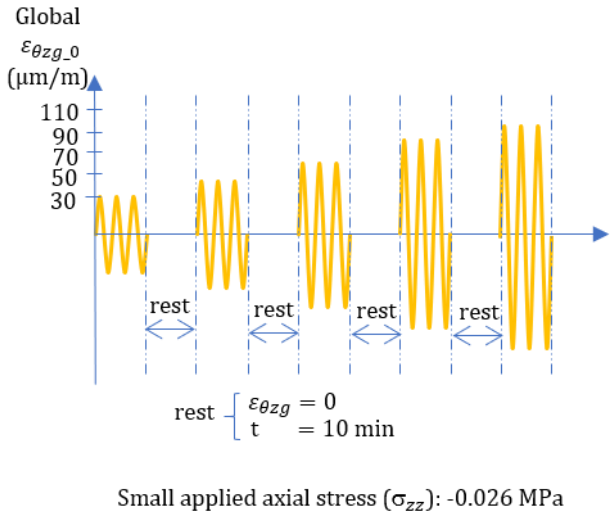

Figure 3.9: The nonlinearity test conducted in 3 cycles at 5 different global tangential strain amplitude 30, 50, 70, 90, 110 µm/m, a small applied compression σ_{zz}= -0.026 MPa.

3.2.2 Procedure for fatigue test

When a bituminous mixture subjected a loading that is below its strength during an important number of cycles, it degrades until failure. Cracks appear at the micro scale and join each other forming major cracks. It is not feasible to observe the propagation of cracks during the earlier phase of fatigue test of a bituminous mixture sample. However, by investigating the complex modulus both in norm and phase angle, one can analyse the degradation of a bituminous mixture. As a bituminous material, the interface between might also exhibit failure by fatigue if it is subjected to a high number of loading cycles. The fatigue deterioration of interfaces between bituminous layers is observed via its complex interface stiffness (its norm and phase angle). The 2T3C hollow cylinder apparatus combined with the 3D DIC technology allows to load not only the interface but also the layers. When fatigue failure occurs, it is possible to determine where the failure appears in the 2T3C hollow cylinder sample.

Shear fatigue tests were conducted at a frequency of 3 Hz and a temperature of 10 °C. Five tests were controlled with three different shearing displacement amplitudes (u_{θ_g0}), which correspond to three global shear strains of 50, 150, 200 µm/m. The global shear strain is deduced from the displacement amplitude considering a sample made of unique homogeneous material. Three samples were tested with a global shear strain of 50 µm/m in order to check the

repeatability of the proposed testing method. In the axial direction, a small constant compression of -0.026 MPa is applied during the tests.

Three additional interface configurations are incorporated in order to assess their impact on the fatigue endurance. The aforementioned configurations were previously discussed in the section devoted to the procedure for the shear complex modulus. Two configurations are presented, each containing a distinct residual binder content: HDO and LDO. Additionally, one configuration utilises modified bitumen (SBS). The fatigue test parameters for those samples are: a fatigue loading sequence at a frequency of 3 Hz, followed by three-cycle measurements at a frequency of 1 Hz (image captured at this rate during three cycles), a temperature of 10°C, a small constant compression of -0.026 MPa, and a global shear strain of 50 µm/m. The characteristics of the fatigue tests performed are shown in Table 3.4.

Since a fatigue test loaded with a global shear strain of 50 µm/m at a frequency of 3 Hz can last up to 250000 cycles, it is not only impractical but also unnecessary to measure complex shear moduli in layers and complex interface stiffness for every cycle. As shown in Figure 3.10, at the beginning of the tests, the measurements are more frequent. It allows for the observation of rapid changes in these values. As changes are slower as the fatigue test goes on, the measurements using cameras are performed less frequently. It was explained previously that the complex shear moduli and the interface stiffness are computed from displacement as the output of 3D-DIC analysis. A minimum of 30 images per loading cycle are required for accurate computations of moduli and stiffness. As the maximum acquisition frequency of the cameras is limited (35 frame per second), the loading frequency is reduced to 1 Hz during only three cycles for the measurement, while other loading parameters are kept unchanged (such as global shear strain and axial stress). There are 35 images taken per loading cycle, which are sufficient for the subsequent calculation. In order to minimise the transitory effect, only the final two cycles of each three-cycle measurement are used in the subsequent calculation.

Figure 3.11 shows the signals recorded in the test on sample REFA-2 during two cycles at a frequency of 1 Hz. Figure 3.11(a) shows the axial loading (F), global shear displacement (u_{θ_g}) and the torque (T) measured during the test. Figure 3.11(b) shows the obtained values and their sinusoidal fitting in continuous lines: strain in the upper layer ($\varepsilon_{\theta z.up}$), strain in the

lower layer ($\varepsilon_{\theta z.low}$) and displacement gap at the interface (Δu_θ). The torque (T) is also shown in this figure with its sinusoidal fitting.

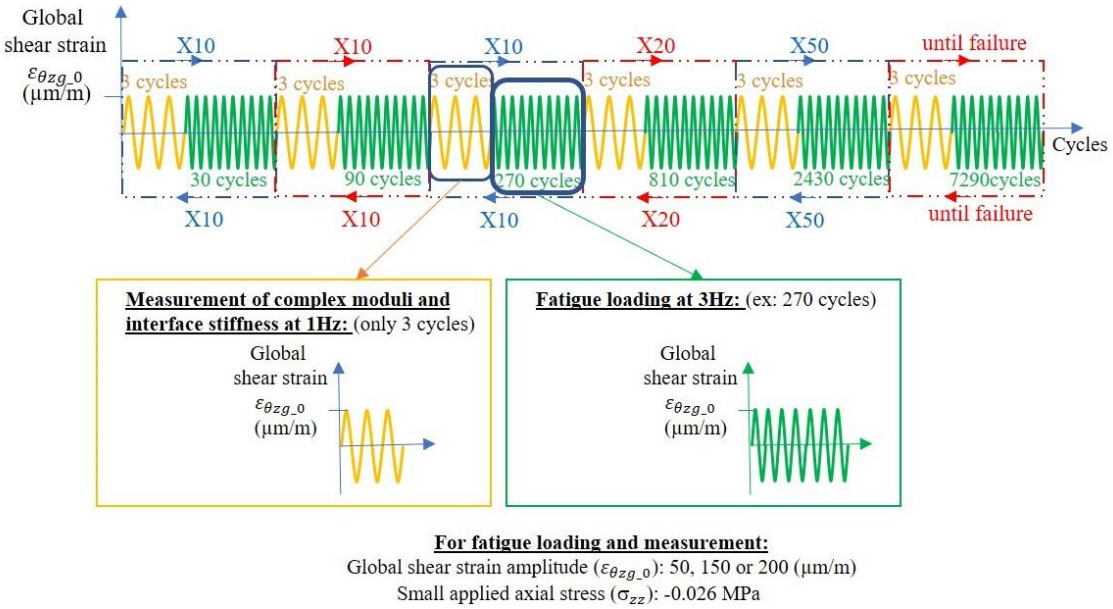

Figure 3.10: Cyclic loading history for a shear fatigue test, three global shear strains ($\varepsilon_{\theta zg\_0}$) of 50, 150, 200 µm/m

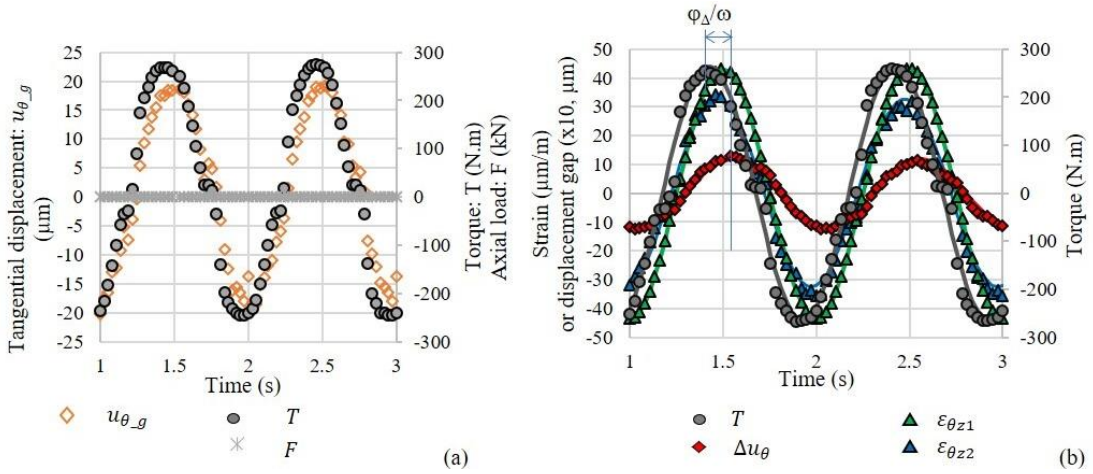

Figure 3.11: Example of signals recorded during a stiffness and moduli measurement step for sample REFA-2: (a) loading signals, i.e. global shear displacement (uθ_g), axial load (F), Torque (T); (b) response signals: strain in upper layer ($\varepsilon_{\theta z.up}$), strain in lower layer ($\varepsilon_{\theta z.low}$) and displacement gap at the interface (Δu_θ) with their sinusoidal fitting in continuous lines using the least square method

3.2.3 Shear complex modulus test on bitumen using Dynamic Shear Rheometer (DSR)

Rotational or axial loading can be applied to bitumen samples using the Dynamic Shear Rheometer (DSR) located at The University of Lyon/ENTPE (Figure 3.12). A cylindrical sample set between two plates is tested using a DSR apparatus. Shear modulus measurements

were the only ones conducted in this study. While the lower plate remains stationary, the top plate rotates. In accordance with the testing materials and temperatures, the plate diameters differ. For testing at temperatures below 0 °C, a diameter of 4 mm is chosen. A diameter of 8 mm is employed for temperatures ranging from 0 to 20 °C. Plate diameter is 25 mm when testing at temperatures exceeding 20 °C. Samples have heights of 1 mm for the 25 mm in diameter sample, and 2 mm for the 8 mm in diameter sample, and 1.75 mm for the 4 mm in diameter sample. There is only one bitumen the penetration grade of 160/200 tested with the DSR apparatus.

A shear complex modulus test using DSR apparatus involves the application sinusoidal cycles on bitumen cylindrical sample. The sample is tested at 11 different temperatures (-30 °C, -20 °C, -10 °C, 0 °C, 10 °C, 20 °C, 30 °C, 40 °C, 50 °C, 60 °C, 70 °C) combined with seven frequencies (0.01, 0.03, 0.1, 0.3, 1, 3, 10). The strain amplitude of a cycle is 0.1%.

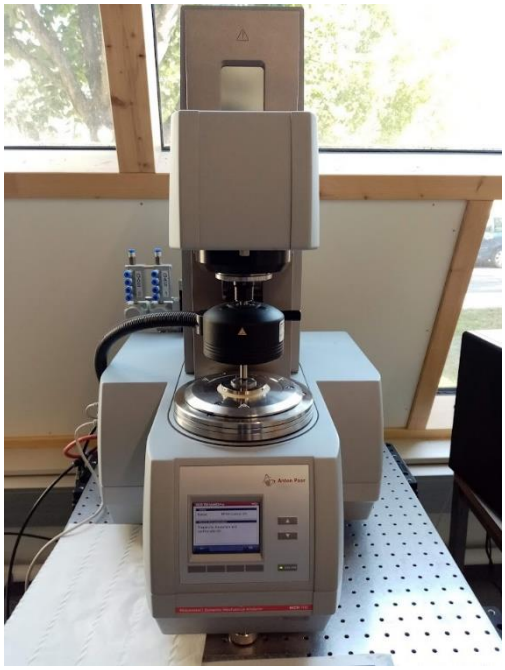

Figure 3.12: Schematic of DSR test at the Univ Lyon/ENTPE

3.2.4 Samples and tests performed

This section summarises the tested samples and the test performed. Three types of tests were performed using the 2T3C hollow cylinder apparatus: the shear complex modulus test, the nonlinearity test and the fatigue test. In total, 20 samples cored from seven slabs tested in this project. Types of tests conducted on 20 samples are listed on Table 3.2.

Table 3.3 gives parameters of the shear complex modulus on the 20 samples. In order to investigate different factors influencing the Linear Viscoelastic behaviour of the interface, three different axial stresses, and two global shear amplitudes were applied on samples. Five temperatures and frequencies were chosen for the tests as described in the section 3.2.1.1. With axial stresses higher than -0.026 MPa, samples were not tested at 40 °C because the possible influence of creep in compression.

Table 3.4 provides information about the fatigue tests on 20 samples. The fatigue results for the sample LDO1 is not presented, since there was a data acquisition problem. Two levels of global shear strains, and three levels of axial stresses were applied. All the samples were tested at 10 °C.

Table 3.2: Tests conducted with the 2T3C hollow cylinder apparatus

Sample name	Shear complex modulus test	Nonlinearity test	Fatigue test
REFA-1	X		X
REFA-2	X		X
REFA-3	X		X
REFB-1	X		X
REFB-2	X		X
REFC-1	X	X	X
REFC-2	X		X
REFC-3	X		X
REFD-1	X		X
REFD-2	X	X	X
REFD-3	X		X
LDO-1	X		X
LDO-2	X	X	X
LDO-3	X	X	X
HDO-1	X	X	X
HDO-2	X	X	X
HDO-3	X	X	X
SBS-1	X	X	X

SBS-2	X	X	X
SBS-3	X	X	X

Table 3.3: Parameters for shear complex modulus tests

	Shear complex modulus test		
Sample name	Global strain amplitude (µm/m)	Axial stress (MPa)	Temperature (°C)
REFA-1	200	-0.026	0-40
REFA-2	50	-0.026	0-40
REFA-3	50	-0.026	0-40
REFB-1	50	-0.026	0-40
REFB-2	50	-0.026	0-40
REFC-1	50	-0.026	0-40
REFC-2	50, 200	-0.026, -0.125, -0.250	0-40 (for σ_{zz} = -0.026MPa) 0-30 (for σ_{zz} = -0.125MPa, and -0.25 MPa)
REFC-3	50	-0.026, -0.125, -0.250	0-40 (for σ_{zz} = -0.026MPa) 0-30 (for σ_{zz} = -0.125MPa, and -0.25 MPa)
REFD-1	50	-0.026	0-40
REFD-2	50	-0.026	0-40
REFD-3	50	-0.026, -0.125, -0.250	0-40 (for σ_{zz} = -0.026MPa) 0-30 (for σ_{zz} = -0.125MPa, and -0.25 MPa)
LDO-1	50	-0.026	0-40

LDO-2	50	-0.026	0-40
LDO-3	50	-0.026	0-40
HDO-1	50	-0.026	0-40
HDO-2	50	-0.026	0-40
HDO-3	50	-0.026	0-40
SBS-1	50	-0.026	0-40
SBS-2	50	-0.026	0-40
SBS-3	50	-0.026	0-40

Table 3.4: Parameters for shear fatigue tests

	Shear fatigue test		
Sample name	Global strain amplitude (μm/m)	Axial stress (MPa)	Temperature (°C)
REFA-1	200	-0.026	10
REFA-2	50	-0.026	10
REFA-3	150	-0.026	10
REFB-1	50	-0.026	10
REFB-2	50	-0.250	10
REFC-1	50	-0.125	10
REFC-2	50	-0.125	10
REFC-3	50	-0.125	10
REFD-1	50	-0.250	10
REFD-2	50	-0.026	10
REFD-3	50	-0.026	10
LDO-1	50	-0.026	10
LDO-2	50	-0.026	10
LDO-3	50	-0.026	10
HDO-1	50	-0.026	10
HDO-2	50	-0.026	10
HDO-3	50	-0.026	10
SBS-1	50	-0.026	10
SBS-2	50	-0.026	10

SBS-3	50	-0.026	10

3.3 Conclusions

20 samples were tested in this study. All double-layered hollow cylinder comprise upper layers made of a BBSG3 mixture, and lower layers made of an EME2 mixture. The reference samples have tack coat at interface made of pure 160/220 bitumen with the residual content of 350 g/m^2. All the reference samples were tested with the shear complex modulus test. Two levels of global shear strain amplitudes were applied (50 and 200 µm/m), and three levels of constant axial stresses (-0.026, -0.125, -0.250 MPa) were applied during the shear complex modulus test. Shear complex modulus tests were launched at five temperatures (from 0°C to 40°C) and five frequencies (0.01 Hz to 1Hz). For samples tested with axial tests higher than -0.026 MPa, tests at 40 °C were not conducted, so as to reduce the possible creep effect at high temperature. There were two samples tested with non-linearity tests (REFC-1, REFD-2). Fatigue tests were launched at the temperature of 10 °C, and the frequency of 3 Hz (the measurement at 1Hz). Three other interface configurations, that include another tack coat type (SBS-modified bitumen for tack coat) and residual bitumen contents of tack coat (250 and 450 g/m^2), were tested to evaluate their influences to the behaviour of the interface. For these configurations, the samples were tested with the global shear strain of 50 µm/m, and the axial stress of -0.026 MPa.

Chapter 4: RESULTS IN SMALL STRAIN DOMAIN

The findings derived from the shear complex modulus tests and the investigation of nonlinearity are detailed in this chapter. These behaviours are determined within the domain of small strain. The first part outlines the procedure for deriving the complex interface stiffness and the complex modulus of bituminous layers from the outcomes of a shear complex modulus test conducted with the 2T3C Hollow Cylinder Apparatus.

The Time-Temperature Superposition Principle (TTSP) is introduced, and the Linear ViscoElastic (LVE) 2S2P1D model is utilised to simulate the bituminous layers' thermomechanical behaviour.

The 2T3C hollow cylinder samples are subjected to two levels of global shear strain amplitudes. Interfaces show different behaviour. At a global shear strain amplitude of 50 µm/m, the LVE 2S2P1D model effectively characterises the behaviour of the interface. Nevertheless, when the global shear strain is 200 µm/m, the Visco-Elasto-Plastic model DBN_{PDSC} will be implemented to analyse the thermomechanical properties of the interfaces and characterise the plastic dissipation.

Finally, this chapter will present the outcomes of nonlinearity experiments preliminary showing the impact of the bias effect on bituminous material subjected to a cyclic test.

4.1 Computational method for complex modulus in layers and complex interface stiffness

4.1.1 Fitting experimental sinusoidal signals

During a loading cycle, 50 data points corresponding to 50 photos are taken for the shear complex modulus, and 35 data points taken for the shear fatigue test. When behaviour is Linear ViscoElastic, if the applying strain is sinusoidal, so the responding stress is. The cycles are fitted couple by couple ensuring the accuracy. Therefore, each approximation includes 100 data points for the shear complex modulus test, and 70 data points for shear fatigue test. The following method is used to find the approximate function that fits to data points. The method starts with centring analysing signals around zero by Equation (4.1).

$$X_c(t_i) = X(t_i) - \frac{1}{N}\sum_{i=1}^{N} X(t_i) \tag{4.1}$$

Where $X_c(t_i)$ and $X(t_i)$ are respectively the centred and experimental data at the time t_i, N is the number of data point for each approximation (N= 100 or N = 70). The fitted function to approach X_c has the form as introduced in Equation (4.2), with ω is the angular frequency of the signal.

$$x(t_i) = A\sin(\omega t_i) + B\cos(\omega t_i) \tag{4.2}$$

Then A, and B can be calculated from Equation (4.3), and (4.4):

$$A = \frac{(\sum_{i=1}^{N} X_C(t_i)\, cos(\omega t_i)) \times (\sum_{i=1}^{N} cos(\omega t_i)\, sin(\omega t_i)) - (\sum_{i=1}^{N} X_C(t_i)\, sin(\omega t_i)) \times (\sum_{i=1}^{N} cos^2(\omega t_i))}{(\sum_{i=1}^{N} cos(\omega t_i)\, sin(\omega t_i))^2 - (\sum_{i=1}^{N} cos^2(\omega t_i)) \times (\sum_{i=1}^{N} sin^2(\omega t_i))} \tag{4.3}$$

$$B = \frac{(\sum_{i=1}^{N} X_C(t_i)\, sin(\omega t_i)) \times (\sum_{i=1}^{N} cos(\omega t_i)\, sin(\omega t_i)) - (\sum_{i=1}^{N} X_C(t_i)\, cos(\omega t_i)) \times (\sum_{i=1}^{N} sin^2(\omega t_i))}{(\sum_{i=1}^{N} cos(\omega t_i)\, sin(\omega t_i))^2 - (\sum_{i=1}^{N} cos^2(\omega t_i)) \times (\sum_{i=1}^{N} sin^2(\omega t_i))} \tag{4.4}$$

The approximated signal x is calculated by Equation (4.5), where x0 is given in Equation (4.6), and phase angle can be deduced in Equation (4.7).

$$x(t_i) = x_0 \sin(\omega t_i + \varphi_x) \tag{4.5}$$

$$x_0 = \sqrt{A^2 + B^2} \tag{4.6}$$

$$\varphi_x = \cos^{-1}\left(\frac{A}{x_0}\right) \tag{4.7}$$

Figure 4.1 demonstrates the experimental data of Torque (T), shear strain in upper layer ($\varepsilon_{\theta z1}$), shear strain in lower layer ($\varepsilon_{\theta z2}$), and displacement gap at the interface (Δu_θ) and their fitting curves using the least square method.

The quality of experimental signal Q can be computed via Equation (4.8):

$$Q = \frac{1}{N} \sum_{i=1}^{N} \frac{|X_c(t_i) - x(t_i)|}{x_0} \tag{4.8}$$

Fitting quality Q is acceptable when it is inferior to 15 % (Attia, 2020). Only signals that are inferior to 15 % will be used to calculate the complex modulus in bituminous layers and complex interface stiffness.

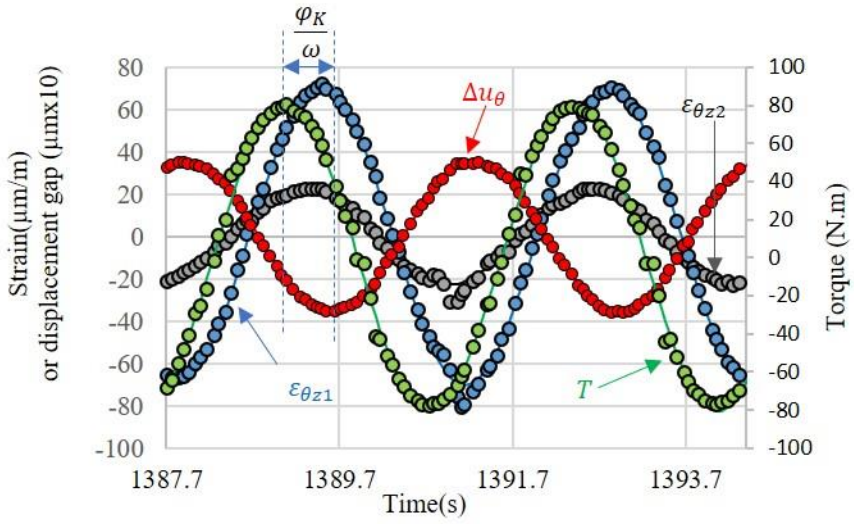

Figure 4.1: Example of 2-cycle signals recorded from shear complex modulus test of sample REFA-3 at 20°C, 0.3 Hz, global shear strain of 50µm/m: Torque (T), shear strain in upper layer ($\varepsilon_{\theta z.up}$), shear strain in lower layer ($\varepsilon_{\theta z.low}$), and displacement gap at the interface (Δu_θ)

4.1.2 Calculation of complex interface stiffness and complex moduli in layers

The shear stress in a sample is calculated as shown in Equation (4.9), where T is the measured torque from the load cells, and R_{ext} = 86 mm and R_{int} = 61 mm are respectively the external and internal radius of the hollow cylinder.

$$\tau_{\theta z} = \frac{3T}{2\pi(R_{ext}^3 - R_{int}^3)} \tag{4.9}$$

When a sinusoidal strain is applied on a linear viscoelastic material, then the shear stress signal is also sinusoidal, as shown in Equation (4.9). $\tau_{\theta z\_0}$ is the shear stress amplitude, φ_τ is the phase lag between shear stress and global shear strain, and ω is the pulsation (=2πf, with f = frequency). The phase lag depends on the tested temperature and frequency. Shear stress is homogeneous inside the double-layered hollow cylinder, which means that shear stress in the upper layer $\tau_{\theta z.up}$, shear stress in the lower layer $\tau_{\theta z.\mathrm{low}}$, and shear stress at the interface $\tau_{\theta z.inter}$ are the same. Therefore, there is a unique shear stress $\tau_{\theta z}$ as written in Equation (4.10) used for subsequent calculations.

$$\tau_{\theta z} = \tau_{\theta z\_0}\sin(\omega t + \varphi_\tau) \tag{4.10}$$

As mentioned in the previous sub-section, the shear strain in layers ($\varepsilon_{\theta z.\mathrm{up}}$ in the upper layer and $\varepsilon_{\theta z.low}$ in the lower layer) and displacement gap at the interfaces (Δu_θ) are calculated using the 3D-DIC technology. Their amplitudes are $\varepsilon_{\theta z.\mathrm{up\_0}}$, $\varepsilon_{\theta z.\mathrm{low\_0}}$, Δu_{θ_0}, respectively. The angles α_1, α_2, α_Δ in Equations (4.11), (4.12), and (4.13) are the measured phase angles of the strain in the upper layer, the strain in the lower layer and the displacement gap at the interface, respectively.

$$\varepsilon_{\theta z.up} = \varepsilon_{\theta z.up\_0} sin(\omega t + \alpha_1) \tag{4.11}$$

$$\varepsilon_{\theta z.low} = \varepsilon_{\theta z.low\_0} sin(\omega t + \alpha_2) \tag{4.12}$$

$$\Delta u_\theta = \Delta u_{\theta\_0} sin(\omega t + \alpha_\Delta) \tag{4.13}$$

The shear complex moduli $G^*_{\theta z.up}$ of the mixture of the upper layer, $G^*_{\theta z.low}$ of the mixture of the lower layer, and the shear complex interface stiffness $K^*_{\theta z}$ are given in Equations (4.14), (4.15), and (4.16) with their respective amplitude $\left|G^*_{\theta z.up}\right|$, $|G^*_{\theta z.low}|$, $|K^*_{\theta z}|$, and phase lag $\varphi_{G.up}$, $\varphi_{G.low}$, $\varphi_{K\theta z}$.

$$G^*_{\theta z.up} = \frac{\tau_{\theta z\_0}}{2\varepsilon_{\theta z.up\_0}} e^{i(\varphi_\tau - \alpha_1)} = \left|G^*_{\theta z.up}\right| e^{i\varphi_{G.up}} \tag{4.14}$$

$$G^*_{\theta z.low} = \frac{\tau_{\theta z\_0}}{2\varepsilon_{\theta z.low\_0}} e^{i(\varphi_\tau - \alpha_2)} = |G^*_{\theta z.low}| e^{i\varphi_{G.low}} \tag{4.15}$$

$$K^*_{\theta z} = \frac{\tau_{\theta z\_0}}{\Delta u_{\theta\_0}} e^{i(\varphi_\tau - \alpha_\Delta)} = |K^*_{\theta z}| e^{i\varphi_{K\theta z}} \tag{4.16}$$

4.2 Time -Temperature Superposition Principle (TTSP)

Figure 4.2 shows the Black's space plot for the complex interface stiffness of the sample REFA-3. There is a unique curve formed considering all the testing temperatures and frequencies. This validates the TTSP at the interface of the sample. Since the TTSP is verified for the bituminous interface, master curves of norm and phase angle of interface stiffness can be constructed. The procedure of building master curves consists in multiplying testing frequencies of each isothermal curve with their shifting factor a_T. A master curve is always defined at a reference temperature. The selection of the reference temperature might be initially determined by one of the available testing temperatures. At the designated reference temperature, the shift factor denoted as a_T exhibits a value of 1. In contrast, at a distinct temperature that deviates from the reference temperature, the testing frequencies of the isothermal curve must be multiplied by a corresponding $a_T(T, T_{ref})$ value. This multiplication is necessary in order to construct a unified curve that aligns with the reference curve. Figure 4.3 shows the construction of experimental master curves of norm of interface stiffness for sample REFA-3 at T_{ref} = 20°C.

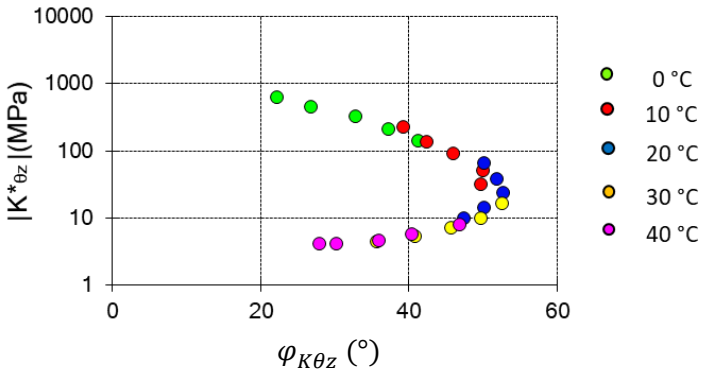

Figure 4.2: Black's space plot for the interface stiffness for the sample REFA-3

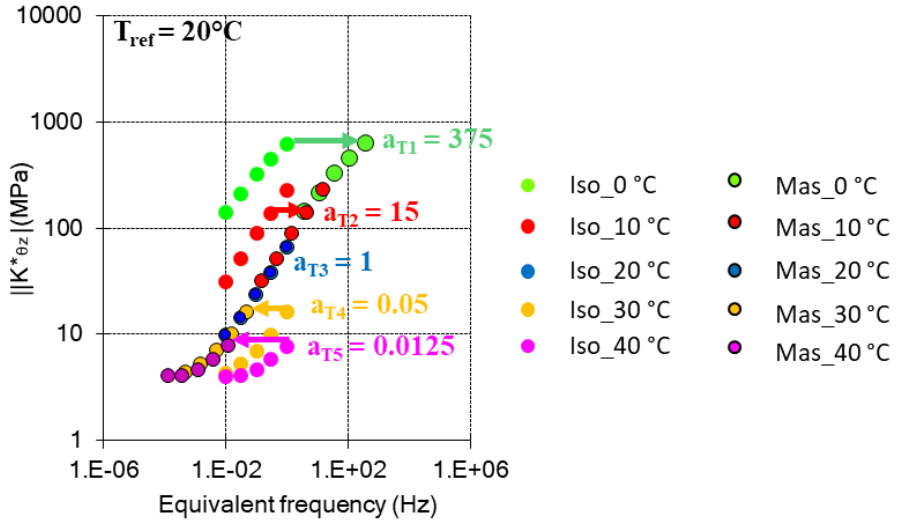

Figure 4.3: Build experimental master curves of norm of the interface stiffness for the sample REFA-3 at the T_{ref} = 20 °C

The previous mentioned shift factors (aT) are experimental ones. The WLF equation (Equation (4.17)) can be used to model shift factors at that reference temperature, where C1 and C2 are constants.

$$\log a_T = -\frac{C_1(T - T_{ref})}{C_2 + T - T_{ref}} \tag{4.17}$$

If master curves are built with different reference temperatures for different samples. A common reference temperature and be chosen and master curves can be shifted to the new reference temperature (T'_{ref}) via Equation (4.18), and (4.19), with C'_1, C'_2 are two new constants. Figure 4.4 depicts new master curves of interface stiffness of the sample REFA-3 built at a new T_{ref} = 15°C by using shift factors on Figure 4.5.

$$C'_2 = C_2 + T'_{ref} - T_{ref} \tag{4.18}$$

$$C'_1 = \frac{C_1 C_2}{C'_2} \tag{4.19}$$

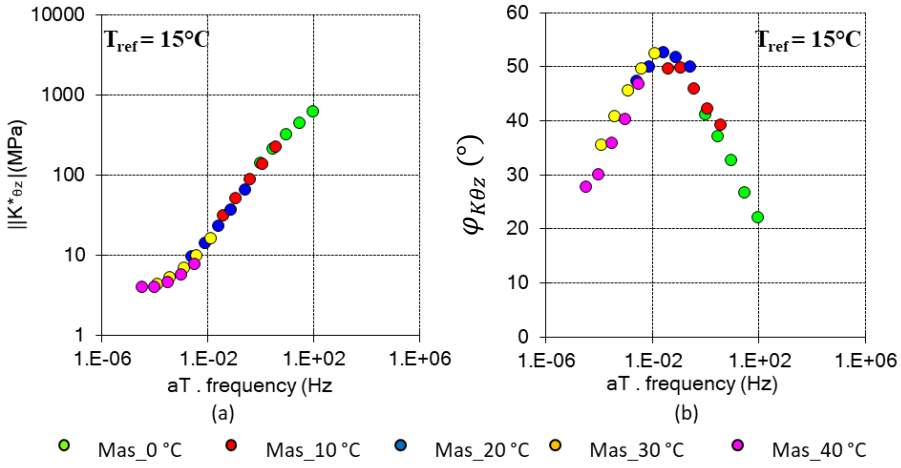

Figure 4.4: Build experimental master curves of the interface stiffness for the sample REFA-3 at the new T_{ref} = 15 °C: (a) the master curve for norm, (b) the master curve for phase angle

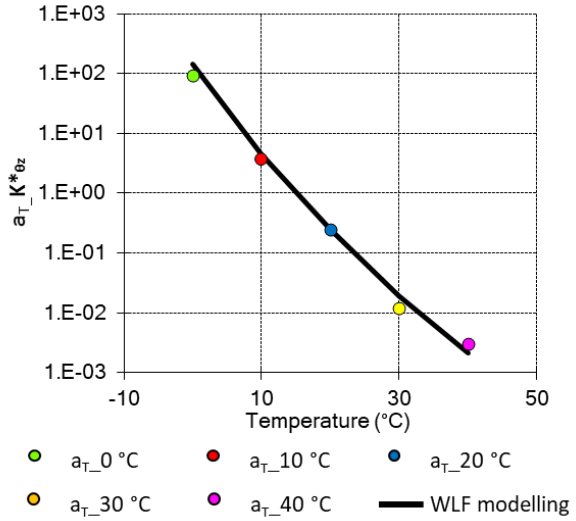

Figure 4.5: Experimental shifting factors and simulation using WLF equation for the sample REFA-3.

The master curves of the norms and phase angles of the complex shear moduli for the two layers of the REFA-3 sample are depicted in Figure 4.6. The master curves for the norm can be observed in Figure 4.6(a), while the master curves for the phase angle can be observed in Figure 4.6(b). The shift factors are depicted in Figure 4.6(c). The master curves shown in the

following figures provide confirmation of the validity of the Time-Temperature Superposition principle for bituminous layers.

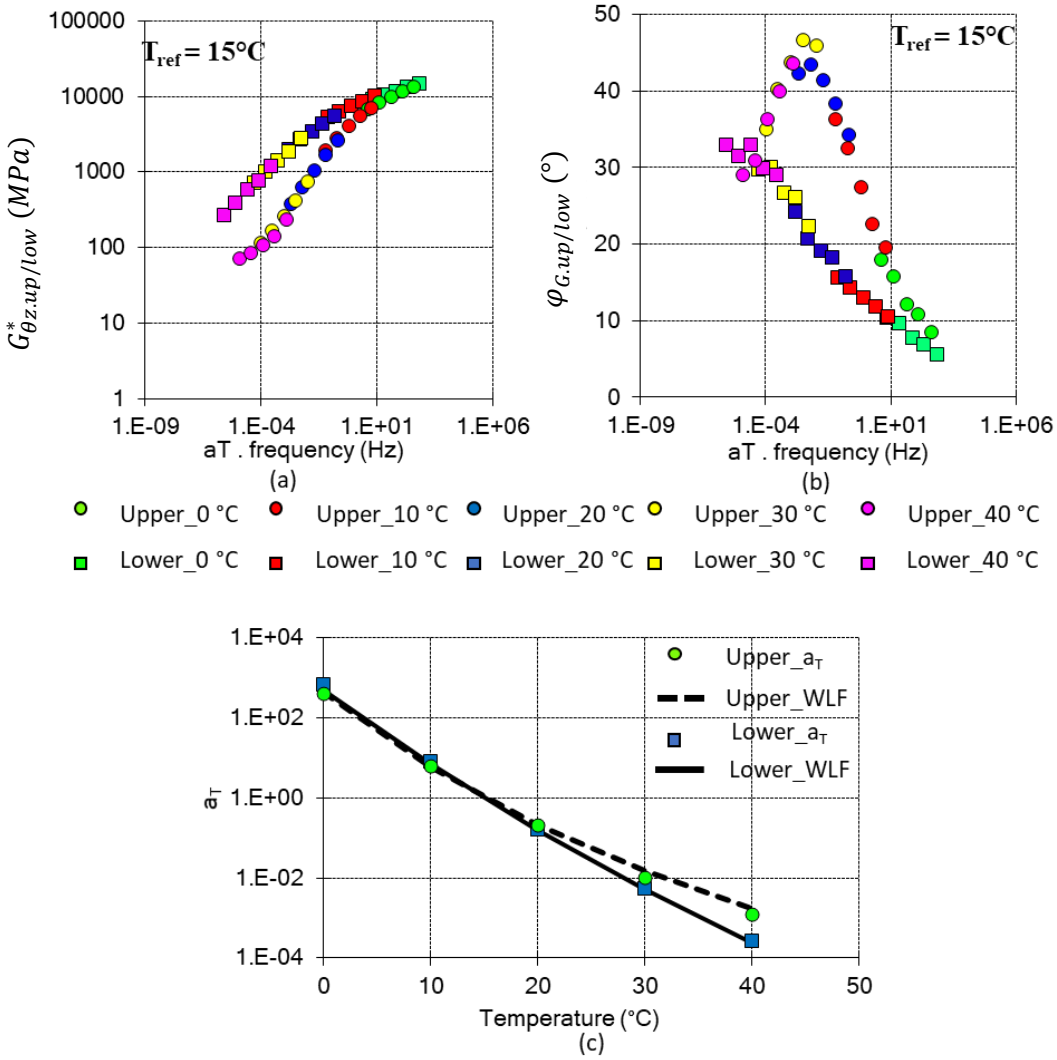

Figure 4.6: Build experimental master curves of the shear modulus of the upper and the lower layer for the sample REFA-3 at the reference temperature T_{ref} = 15 °C: (a) the master curve for norm, (b) the master curve for phase angle, (c) experimental and WLF modelling shift factors

4.3 Upper layer

4.3.1 Upper layer on samples loaded with 50 µm/m global strain

The upper layer of all 2T3C hollow cylinders were made of BBSG3 mixture. The mixture has nominal maximum aggregate size of 10 mm. The bitumen used in this mixture has a penetration grade of 50/70. In order to study the LVE behaviour of the bituminous mixture in the upper layers, the samples were tested with shear complex modulus. The method used to calculate the moduli in layers, as well as the interface stiffness is presented in the section 4.1.2. Figure 4.7 shows the calculated strain of the mixture layers in the upper layer of three samples REFA-3,

REFA-2, REFB-1. The strain varies in the range of 43 µm/m – 93 µm/m depending on temperature and frequency. The calculated strains in upper layer are mostly higher compared to the global strain applied to the samples (50 µm/m). Experimental norm and phase angle of shear complex modulus in upper layer is modelled using the 2S2P1D LVE model. Figure 4.8 demonstrates an example of the experimental data and the 2S2P1D modelling on the bituminous mixture in upper layer of the sample REFA-2. The data is plotted in the Black's space (Figure 4.8(a)), and the master curve of norm (Figure 4.8(b)). Unique curves can be found in both figures showing that the mixture in upper layer follows the TTSP. The 2S2P1D model is used to simulate experimental data. The 2S2P1D calibration parameters are presented on Table 4.1. Similar finding can be found for all the upper layers of all samples loaded with 50 µm/m global shear strain. The results of samples are well repeated. Their experimental data and the 2S2P1D modelling can be found in Figure 4.9, Figure 4.10, and Figure 4.11. They are, respectively, Black diagrams, master curves of norm, and master curves of phase angle of shear complex moduli of bituminous mixtures in upper layer.

As can be seen from Table 4.1, the 2S2P1D parameters k, h, δ and β and the constants C_1, C_2 are identical for all samples. This confirms the assumption made by several authors that those parameters are inherited from the bitumen, and used to describe the LVE behaviour of the bitumen of the mixture.

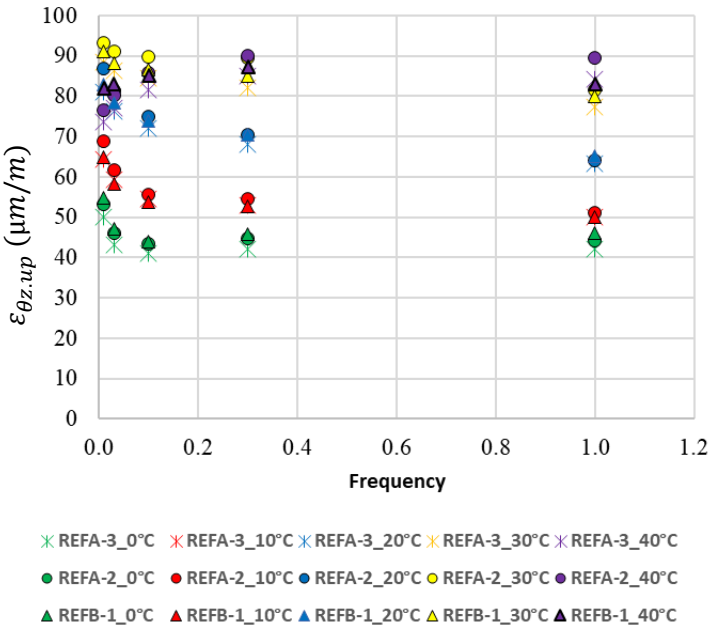

Figure 4.7: Examples of shear strain calculated for upper layer of three samples REFA-3, REFA-2, and REFB-1 applied to 50 µm/m global shear strain

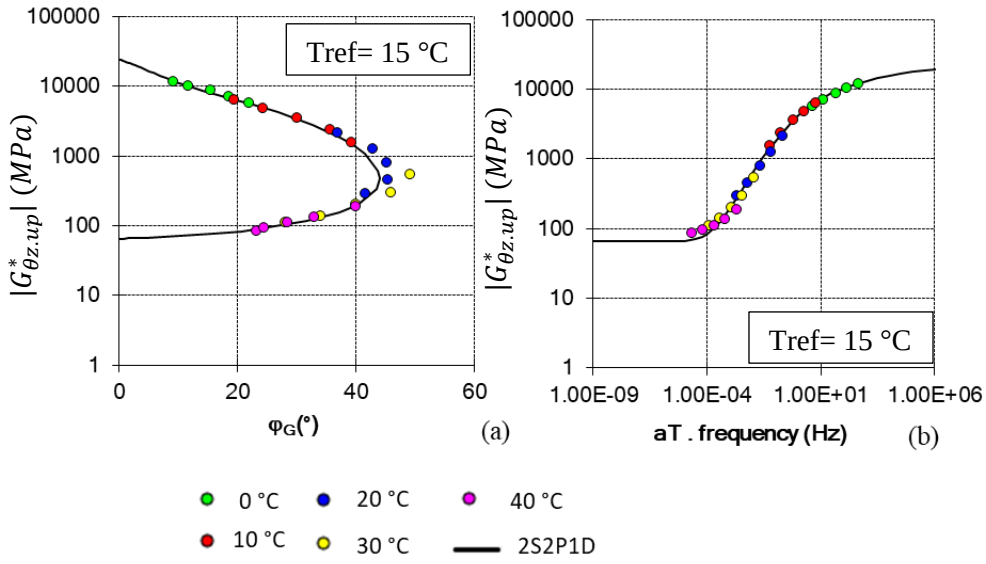

Figure 4.8: Experimental data and the 2S2P1D modelling of bituminous mixture in the upper layer of sample REFA-2: (a) Black space; and (b) master curve of norm

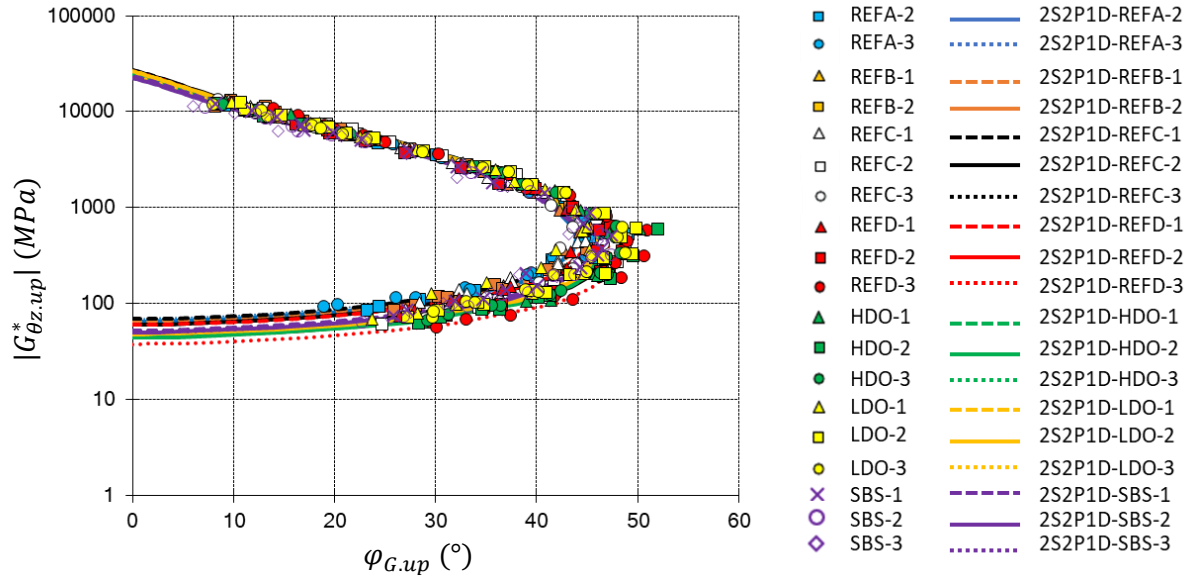

Figure 4.9: Black diagram of shear complex modulus and their 2S2P1D modelling for bituminous mixtures in the upper layer of all samples applied to 50 µm/m global strain

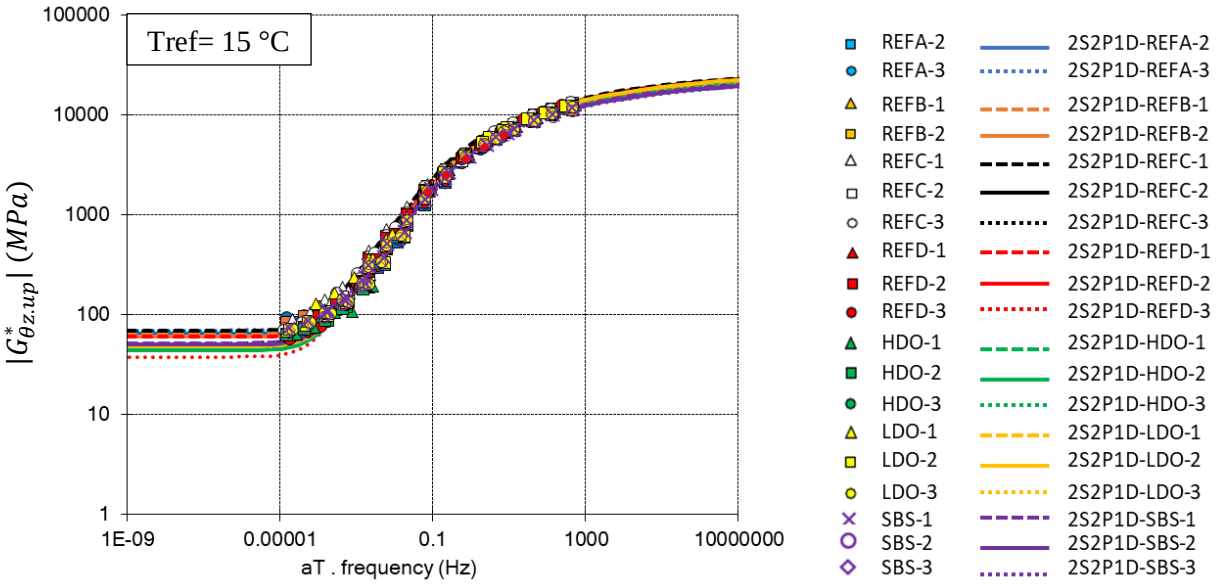

Figure 4.10: Master curve of norm of shear complex modulus and their 2S2P1D modelling for bituminous mixtures in the upper layer of all samples applied to 50 µm/m global strain

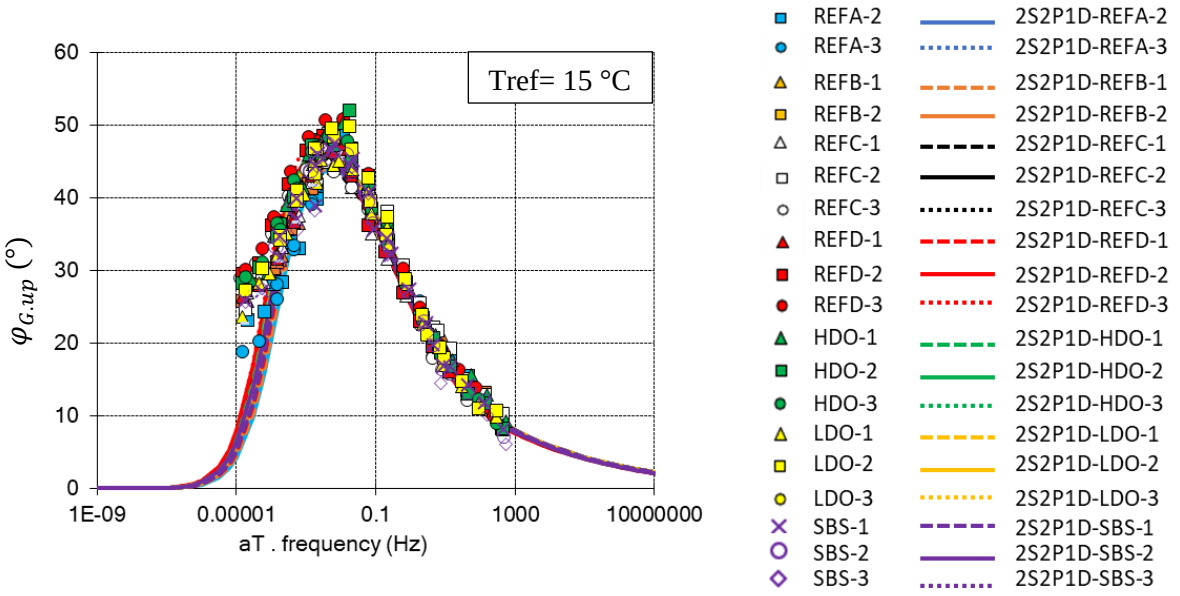

Figure 4.11: Master curve of phase angle of shear complex modulus and their 2S2P1D modelling for bituminous mixtures in the upper layer of all samples applied to 50 µm/m global strain

The experimental data and 2S2P1D modelling could also be presented in the normalised forms. The normalised modulus is calculated by Equation (4.20). The idea of using normalised values is to eliminate the influence of $G^*_{\theta z\_0}$ and $G^*_{\theta z\_00}$ which are dependent on the aggregate skeleton of the mixture. A direct insight on the effect of other parameters contributed from the bitumen is possible. They are k, h, δ, τ and β and constants C_1, C_2 for WLF equation. If the mixtures use the same bitumen, the experimental data and the 2S2P1D modelling will be

superimposed. This statement is confirmed in Figure 4.12, Figure 4.13, and Figure 4.14. Figure 4.12 shows the normalised norm of shear modulus plotted in Black's space. Figure 4.13 depicts the master curves of normalised norm of shear modulus. In addition, the master curves of phase angle of normalised shear modulus norm are presented in Figure 4.14.

$$G^*_{\theta z\_norm} = \frac{G^*_{\theta z} - G_{00}}{G_0 - G_{00}} \tag{4.20}$$

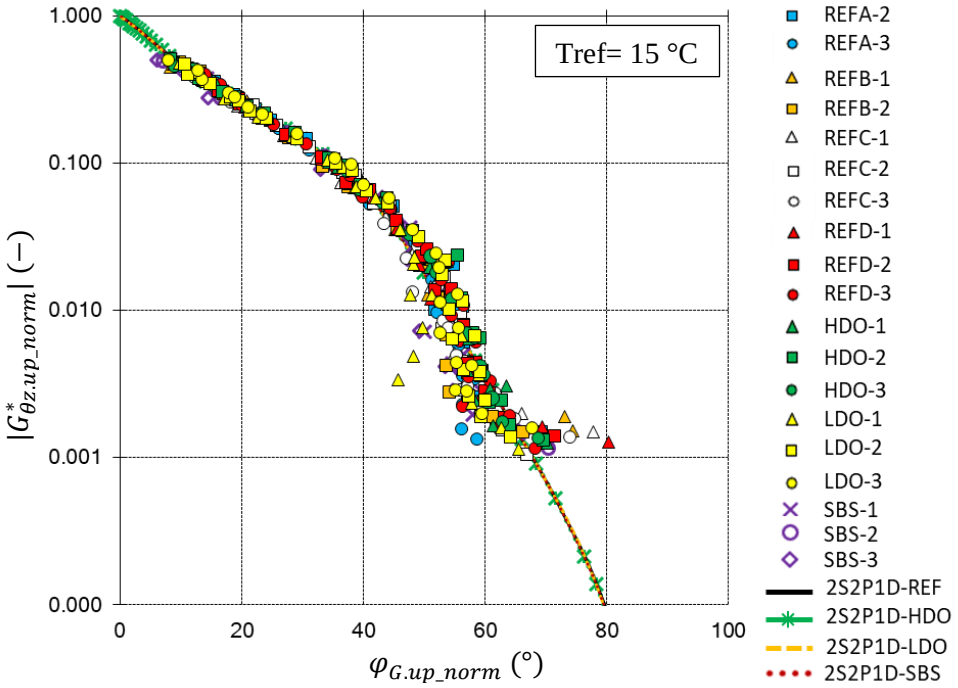

Figure 4.12: Black's space of the norm of $G^*_{\theta z.up\_norm}$ (normalised modulus) of the upper layers; experimental results and their 2S2P1D modellings

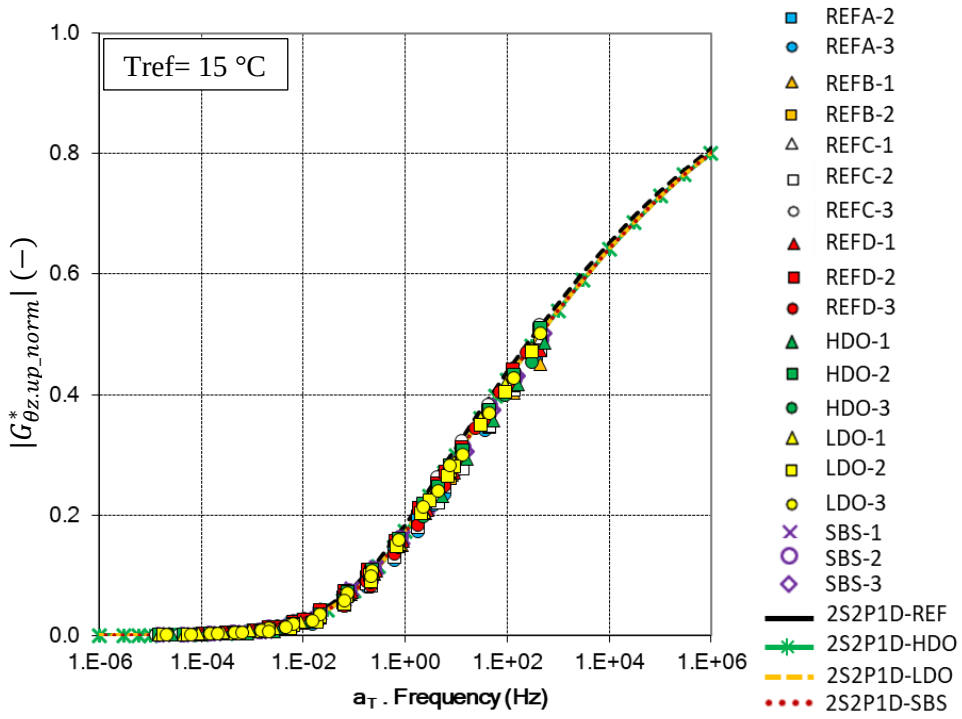

Figure 4.13: Master curves of the norm of $G^*_{\theta z.up\_norm}$ (normalised modulus) of the upper layers; experimental results and their 2S2P1D modellings

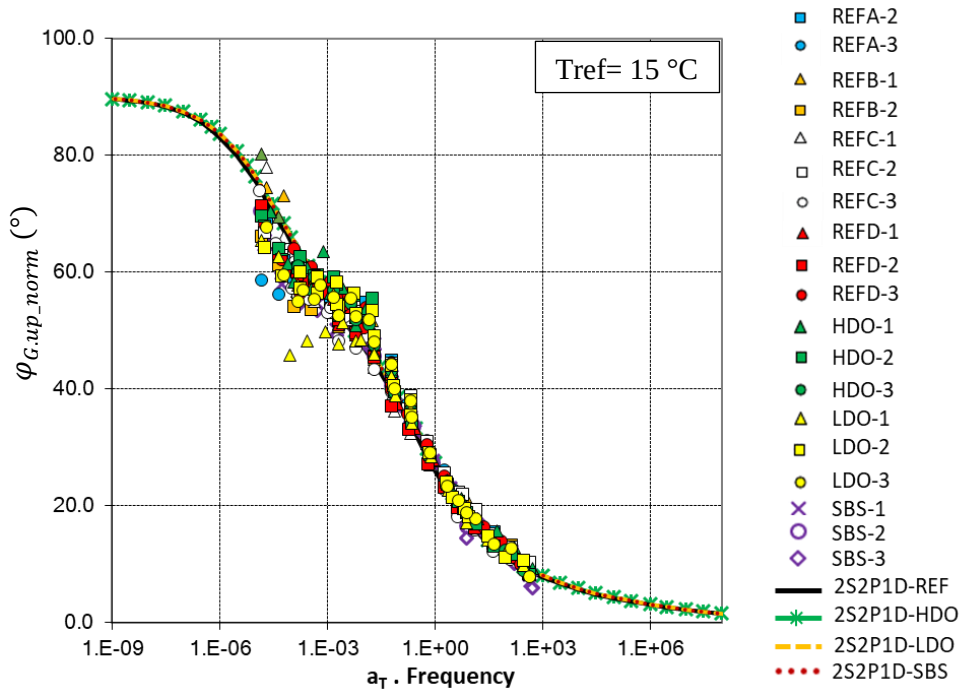

Figure 4.14: Master curves of phase angle of $G^*_{\theta z.up\_norm}$ (normalised modulus) of the upper layers; experimental results and their 2S2P1D modellings

Table 4.1: 2S2P1D constants for modelling complex modulus in the upper layer of all samples applied with the same global strain of 50 μm/m and axial stress of 0.026 MPa. Two constants C1, C2 from WLF modelling (T_{ref}=15°C)

Sample	$G_{\theta z\_00}$ (MPa)	$G_{\theta z\_0}$ (MPa)	k	h	δ	τ_G (s)	β	C1	C2 (°C)
REFA-2	65	24000							
REFA-3	70	26500							
REFB-1	65	25000							
REFB-2	60	27000							
REFC-1	69	27000							
REFC-2	45	26500							
REFC-3	52	26000							
REFD-1	60	26000							
REFD-2	45	23500							
REFD-3	38	26500	0.17	0.57	2.10	0.033	150	11.70	81.15
HDO-1	45	26000							
HDO-2	44	24000							
HDO-3	46	26000							
LDO-1	50	26200							
LDO-2	48	26300							
LDO-3	48	24000							
SBS-1	52	23600							
SBS-2	50	22500							
SBS-3	50	22400							

4.3.2 Upper layer of samples loaded with 200 µm/m global strain

Shear strain of upper layer of two samples: REFA-1, and REFC-2 loaded with 200 µm/m global strain calculated and shown in Figure 4.15. They are in the range of 110 µm/m - 440 µm/m depending on temperature and frequency, and are higher than the global shear train.

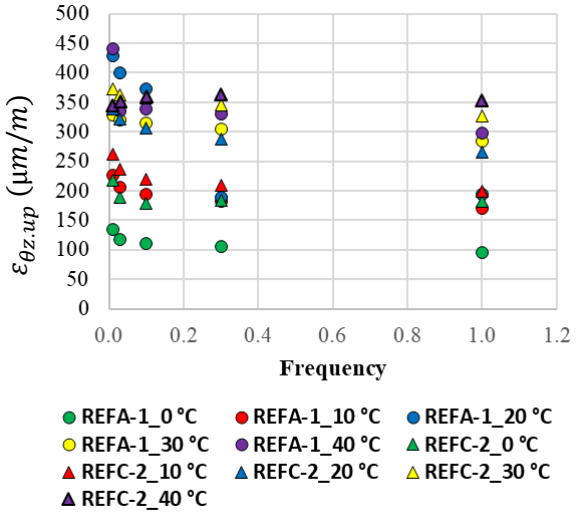

Figure 4.15: Shear strain calculated for upper layer of two samples REFA-1, and REFC-2, loaded with 200 µm/m global shear strain.

Figure 4.16(a) and (b) depict the master curves for norms and phase angle of complex shear modulus, respectively. The master curves were generated by multiplying the testing frequencies of each isothermal curve by their respective shift factors, henceforth denoted as "experimental aT" (Figure 4.17). The reference temperature that has been chosen as 15°C.

Distinct master curves are determined for the phase angle and norm of complex modulus for each individual sample (Figure 4.16). Furthermore, distinct curves denoting complex shear modulus are illustrated in Black space (Figure 4.18). This signifies that TTSP for the bituminous mixture in the upper layer has been validated at a global strain of 200 µm/m.

The 2S2P1D model has the capability to represent both the phase angle and norm of the complex shear modulus of the mixture in the upper layer. With a global shear strain of 200 µm/m, the upper layer demonstrates a Linear ViscoElastic behaviour. The WLF modelling fits well with the experimental a_Ts, as depicted in Figure 4.17. The 2S2P1D model parameters $G_{\theta z\_00}$, $G_{\theta z\_0}$, k, h, δ, τ, and β), as well as the constants C1, C2 for the WLF equation, are presented in Table 4.3. The 2S2P1D model consistently maintains constants C1, C2, and parameters k, h, β, and β, which define the Linear ViscoElastic behaviour of the bitumen

composed in the bituminous mixtures, across all samples herein and those subjected to a global shear strain of 50 µm/m.

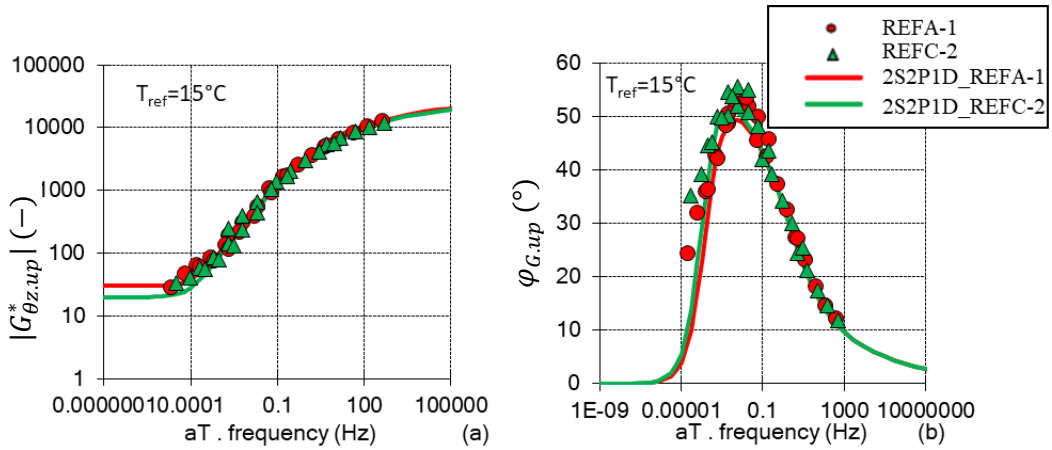

Figure 4.16: Master curves of norms of shear complex modulus of the bituminous mixture in the upper layer (a) norms; (b) phase angle (experimental data for 2 samples applied to 200 µm/m global strain: REFA-1, REFC-2, their 2S2P1D modelling)

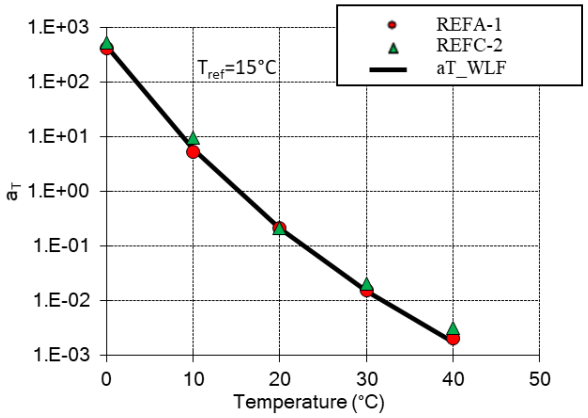

Figure 4.17: Shift factors for building master curves (experimental a_T for bituminous mixture in upper layer of two samples applied with 200 (µm/m): REFA-1, REFC-2 and WLF modelling)

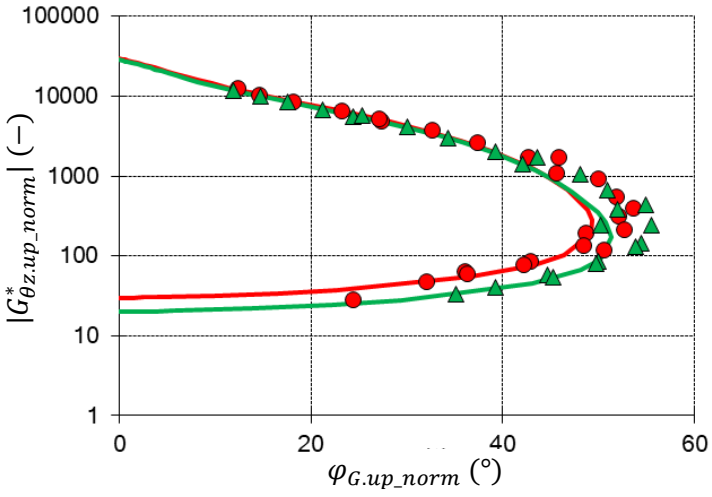

Figure 4.18: Black diagram of shear modulus of the bituminous mixture in the upper layer (experimental data for 2 samples applied to 200 µm/m global strain: REFA-1, REFC-2, their 2S2P1D modelling)

Table 4.2: 2S2P1D constants for modelling complex modulus in the upper layer of all samples applied with the same global strain of 200 µm/m and axial stress of 0.026 MPa. Two constants C1, C2 from WLF modelling (T_{ref}=15°C)

Sample	$G_{\theta z\_00}$ (MPa)	$G_{\theta z\_0}$ (MPa)	k	h	δ	τ_G (s)	β	C1	C2 (°C)
REFA-1	30	30000	0.17	0.57	2.10	$9.5x10^{-3}$	150	11.70	81.15
REFC-2	20	28500							

4.4 Lower layer

4.4.1 Lower layer on samples loaded with 50 µm/m global strain

The lower layer was compacted with the EME2 mixture. Its aggregate distribution is continuous with maximum nominal size of 14 mm. The 15/25 bitumen is used in the mix. In addition, the active bitumen in 30% of RAP also plays a role. The total bitumen content is 5.6 % by weight of the mix.

The shear modulus tests were conducted to study shear modulus in both layers and, at the interface. The norm and phase angle of complex shear modulus in the lower is calculated as presented in the section 4.1.2. The strain of the mixture layers in the lower layer of three samples (REFA-3, REFA-2, and REFB-1) is illustrated in Figure 4.19. The strain exhibits variation between 12 and 42 µm/m depending on temperatures and frequencies, which is significantly less than the global strain of 50 µm/m that was applied to the samples. Similar to the examination in the upper layer, the complex shear modulus in the lower layer is then modelled by using the 2S2P1D model and presented on Table 4.3. Figure 4.20 gives an example of the experimental data and the 2S2P1D modelling on the bituminous mixture in the lower layer of the sample REFA-2. The data is plotted in the Black's space (Figure 4.20(a)), and the master curve of norm (Figure 4.20(b)). Unique curves can be found in both figures showing that the mixture in lower layer satisfies the TTSP. The LVE 2S2P1D model characterises well with the experimental data.

The results are consistent across all lower layers of samples subjected to a 50 µm/m global shear strain. Each sample's results are precisely replicated. The experimental data and the 2S2P1D modelling illustrated in Figure 4.34, Figure 4.35, and Figure 4.37, are respectively

Black diagrams, master curves of norm, and master curves of phase angle of shear complex moduli of bituminous mixtures in the lower layer.

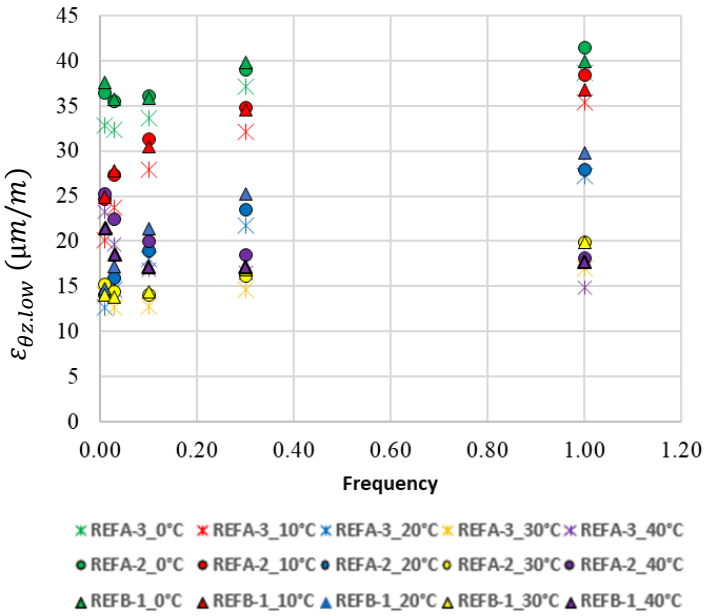

Figure 4.19: Examples of shear strain calculated for lower layer of three samples REFA-3, REFA-2, and REFB-1

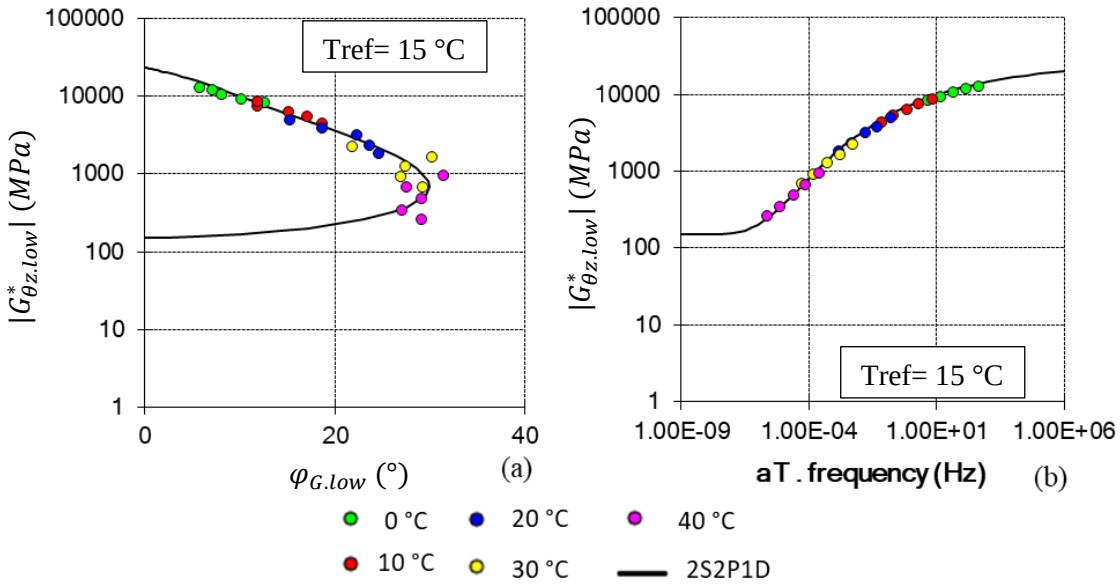

Figure 4.20: Experimental data and the 2S2P1D modelling of bituminous mixture in the lower layer of sample REFA-2: (a) Black space; and (b) master curve of norm

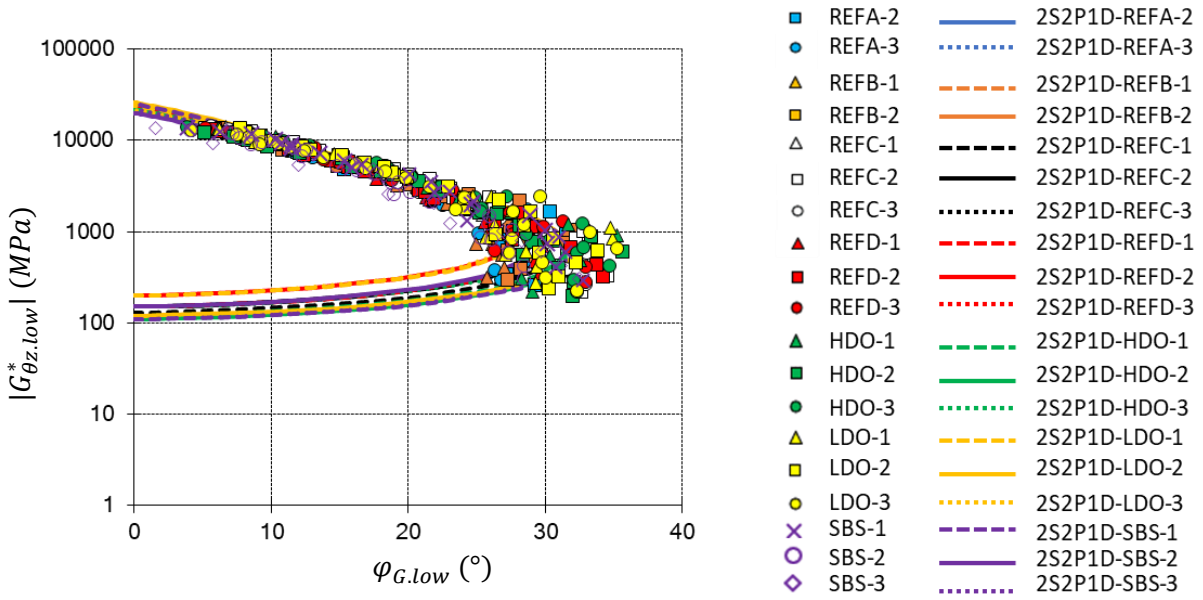

Figure 4.21: Black diagram of shear complex modulus and their 2S2P1D modelling for bituminous mixtures in the lower layer of all samples applied to 50 µm/m global strain

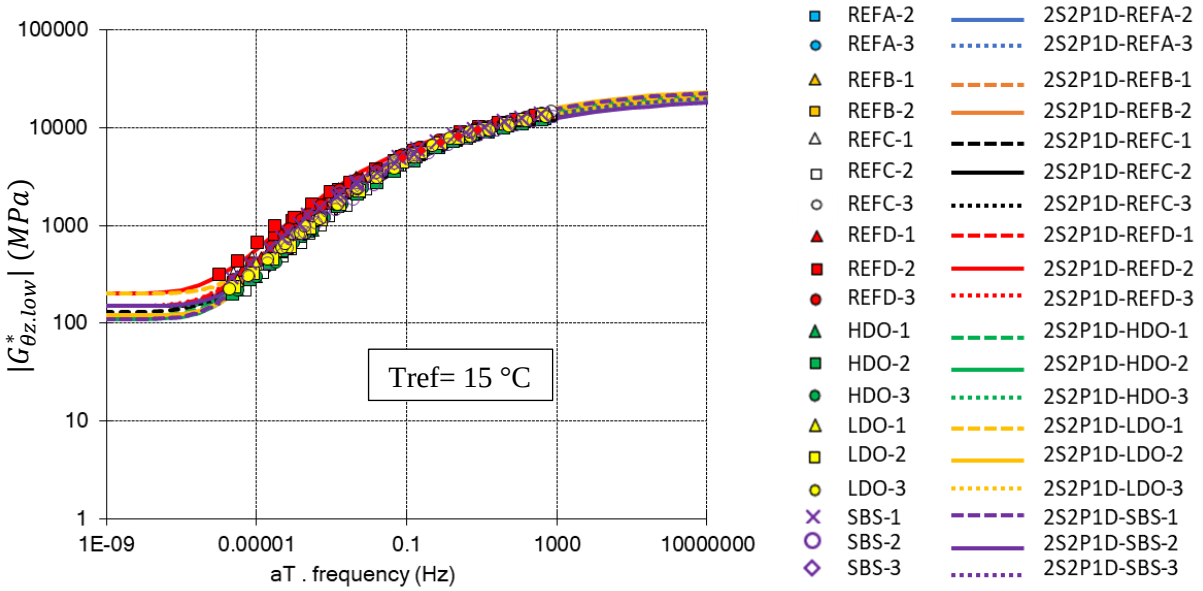

Figure 4.22: Master curve of norm of shear complex modulus and their 2S2P1D modelling for bituminous mixtures in the lower layer of all samples applied to 50 µm/m global strain

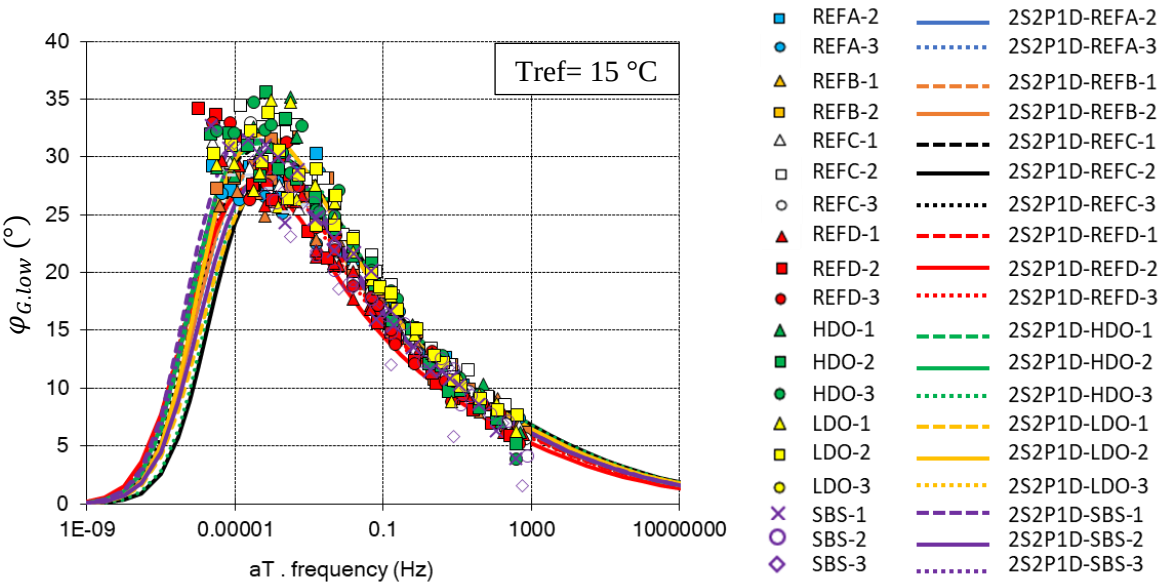

Figure 4.23: Master curve of phase angle of shear complex modulus and their 2S2P1D modelling for bituminous mixtures in the lower layer of all samples applied to 50 µm/m global strain

As can be seen on Table 4.3, the parameters k, h, δ, τ and β from the 2S2P1D and constants C_1, C_2 for WLF equation are identical for all tested samples. The normalised norm is calculated by Equation (4.20). The normalised norms are plotted, respectively, in Figure 4.24, Figure 4.25, Figure 4.26 in the Black's space, in its master curves graph, and through their phase angle master curves. It is clear that the experimental data is well overlapped, and the 2S2P1D modelling are superimposed. This suggests that both the bitumen incorporated in the mixtures and the RAP obtained from different application exhibited stability. The 2S2P1D

model characterise well the Linear ViscoElastic behaviour of the bituminous mixtures of the lower layer.

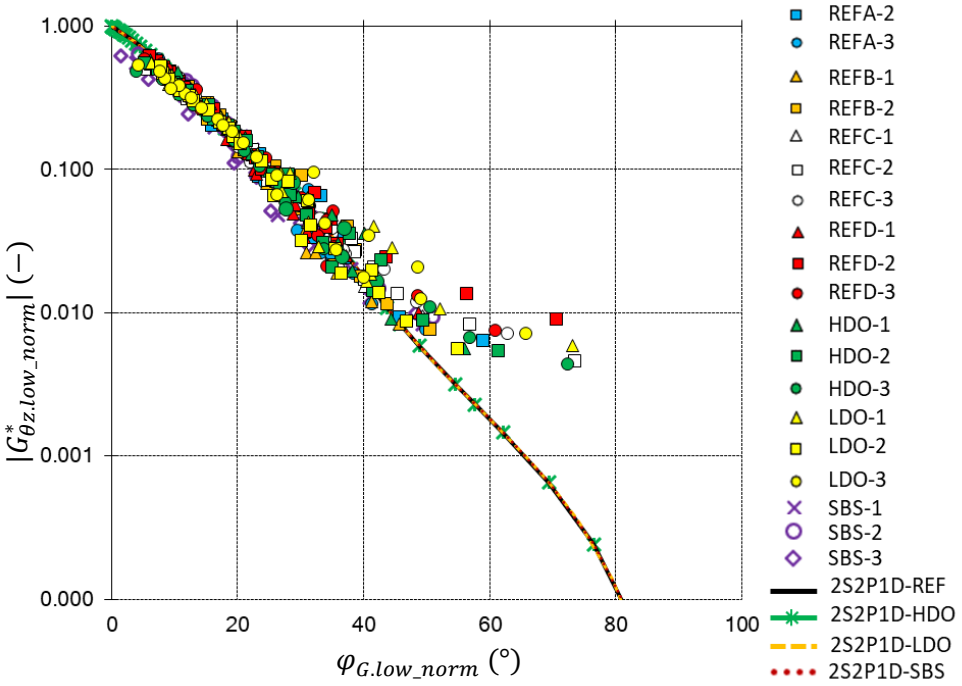

Figure 4.24: Black's space of the norm of $G^*_{\theta z.low\_norm}$ (normalised modulus) of the lower layers; experimental results and their 2S2P1D modellings

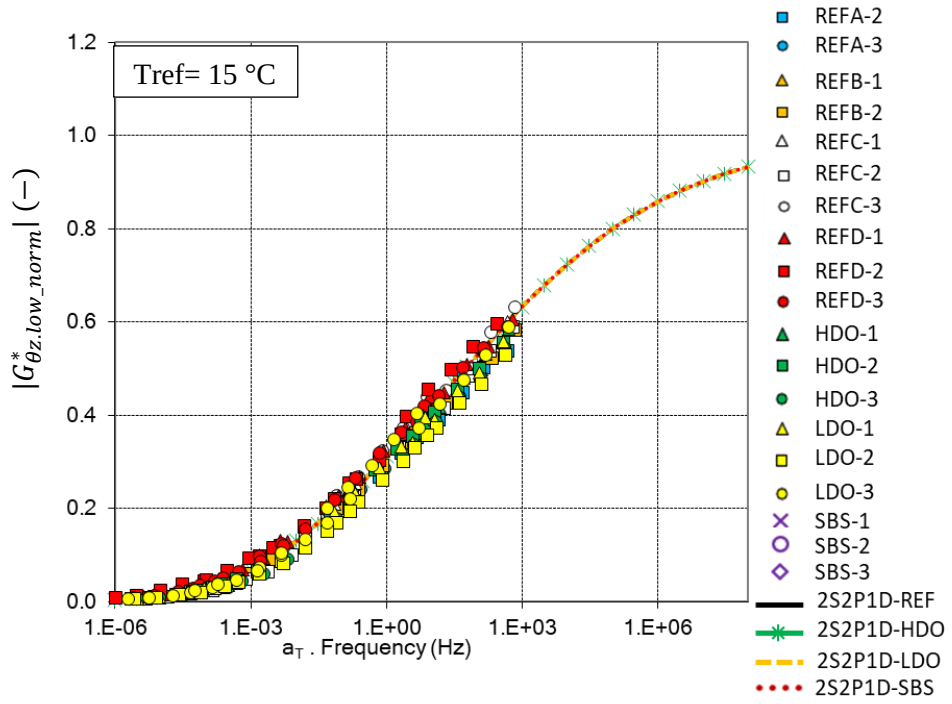

Figure 4.25: Master curves of the norm of $G^*_{\theta z.low\_norm}$ (normalised modulus) of the lower layers; experimental results and their 2S2P1D modellings

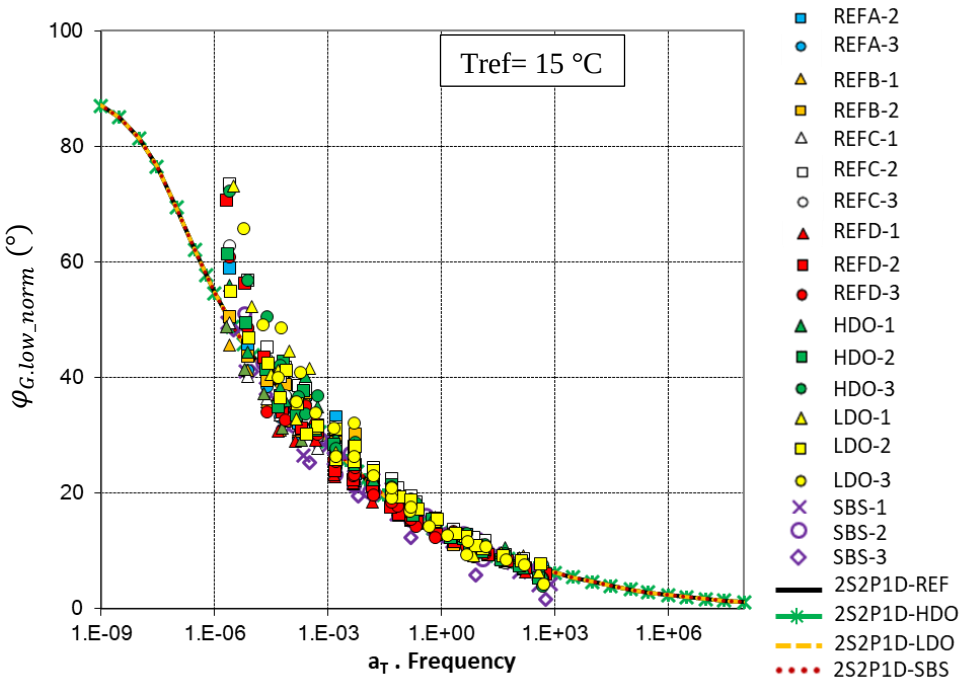

Figure 4.26: Master curves of phase angle of $G^*_{\theta z.low\_norm}$ (normalised modulus) of the layers; experimental results and their 2S2P1D modellings

Table 4.3: 2S2P1D constants for modelling complex modulus in the lower layer of all samples applied with the same global strain of 50 μm/m and axial stress of 0.026 MPa. Two constants C1, C2 from WLF modelling (T_{ref}=15°C)

Sample	$G_{\theta z\_00}$ (MPa)	$G_{\theta z\_0}$ (MPa)	k	h	δ	τ_G (s)	β	C1	C2 (°C)
REFA-2	150	23200							
REFA-3	150	22500							
REFB-1	150	23200							
REFB-2	150	23000							
REFC-1	130	23000							
REFC-2	150	26000							
REFC-3	150	23000							
REFD-1	150	23000							
REFD-2	200	21300							
REFD-3	150	23000	0.18	0.50	3.50	3.14	550	29.87	182.23
HDO-1	120	23000							
HDO-2	110	22000							
HDO-3	150	28500							
LDO-1	200	24000							
LDO-2	120	26000							
LDO-3	200	24000							
SBS-1	110	25000							
SBS-2	150	20000							
SBS-3	110	22000							

4.4.2 Lower layer on samples loaded with 200 µm/m global strain

As illustrated in Figure 4.27, the shear strain of the lower layer of two samples, REFA-1 and REFC-2. They were subjected to a 200 µm/m global strain. These calculated shear strains in lower layer vary between 41 and 160 µm/m, relying on temperature and frequency, and are lower in comparison to the global shear train.

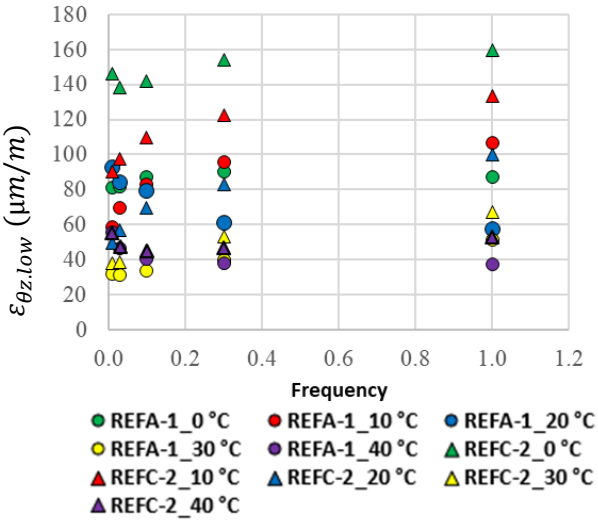

Figure 4.27: Shear strain calculated for lower layer of two samples REFA-1, and REFC-2, loaded with 200 µm/m global shear strain.

The master curves for norms and phase angle of complex shear modulus are illustrated in Figure 4.28(a) and (b). Multiplying the testing frequencies of each isothermal curve by their corresponding shift factors, henceforth denoted as "experimental a_T" (Figure 4.29), produced the master curves. The temperature selected as the reference is 15°C.

For each sample, distinct master curves are identified for the norm and phase angle of complex modulus (Figure 4.28). Additionally, unique curves for complex shear modulus are represented in Black space (Figure 4.30). This indicates that TTSP has been verified for the bituminous mixture in the lower layer under a global strain of 200 µm/m.

It is possible to model the norm and phase angle of complex shear modulus of the mixture in lower layer using the 2S2P1D model. Therefore, under such torsional loading conditions, the lower layer exhibits a Linear ViscoElastic response. As illustrated in Figure 4.30, a distinct WLF curve was constructed by fitting each experimental aT of each sample with a unique set of constants. Table 4.4 contains the 2S2P1D model parameters $G_{\theta z\_00}$, $G_{\theta z\_0}$, k, h, δ, τ, and β) and the constants C1, C2 for the WLF equation. Constants C1, C2, as well as parameters k, h, β, and β, which characterise the Linear ViscoElastic behaviour of the mixture,

are maintained consistently across all samples tested with 50 µm/m global shear strain in the 2S2P1D model. The experimental aTs fit quite well with the WLF simulation.

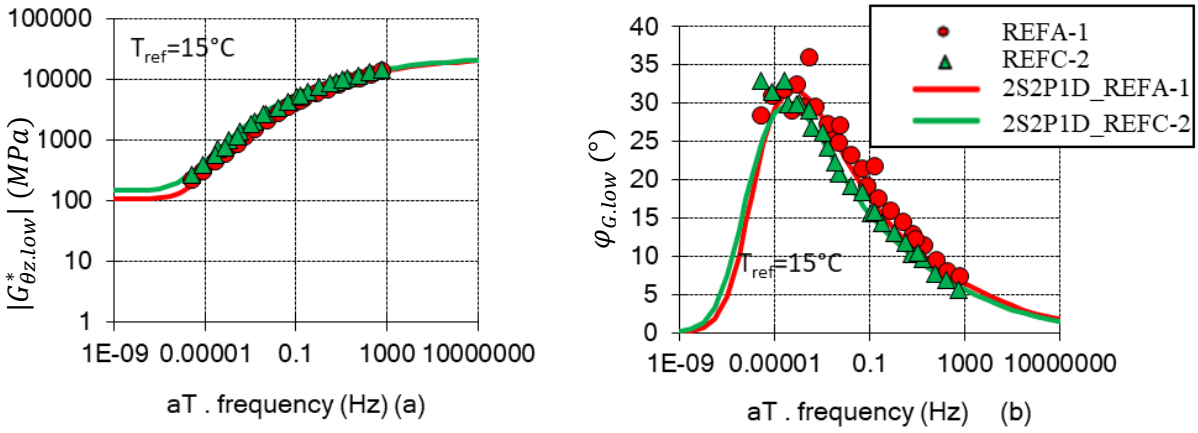

Figure 4.28: Master curves of norms of shear complex modulus of the bituminous mixture in the lower layer (a) norms; (b) phase angle (experimental for 2 samples applied with 200 (µm/m): REFA-1, REFC-2 their 2S2P1D modelling)

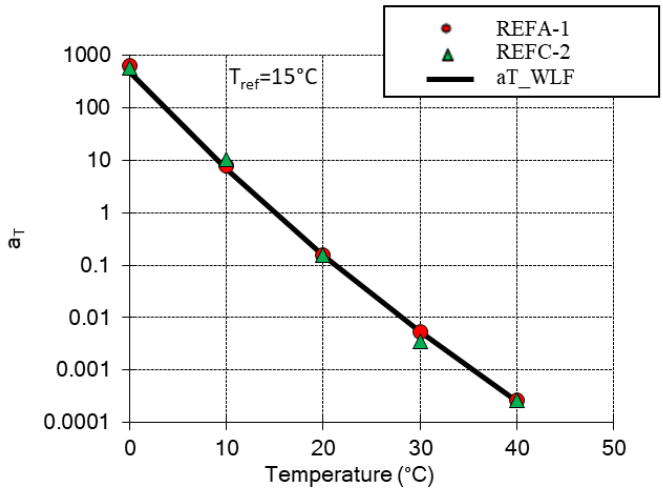

Figure 4.29: Shift factors for building master curves (experimental a_T for bituminous mixture in lower layer of two samples applied with 200 (µm/m): REFA-1, REFC-2 and WLF modelling)

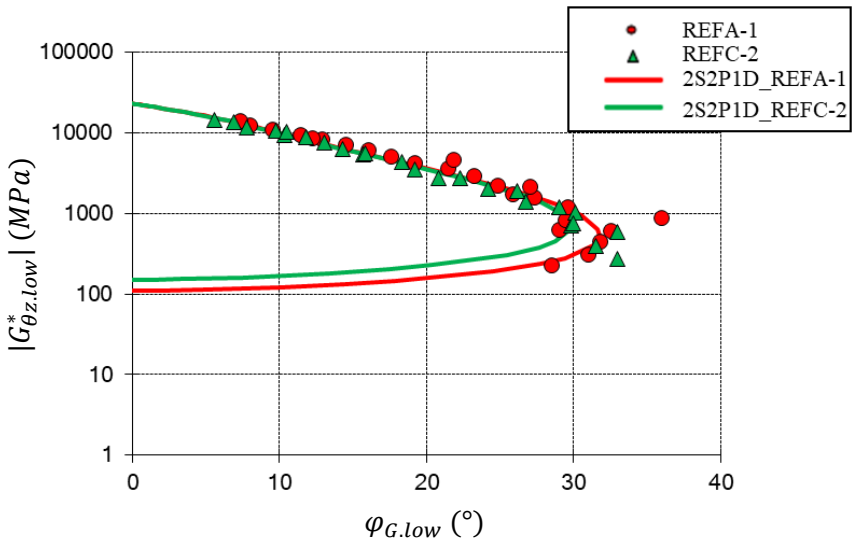

Figure 4.30: Black diagram of the complex shear modulus of the bituminous mixture in the lower layer (experimental data for 2 samples applied to 200 µm/m global strain: REFA-1, REFC-2, their 2S2P1D modelling)

Table 4.4: 2S2P1D constants for modelling complex modulus in the lower layer of all samples applied with the same global strain of 200 µm/m and axial stress of 0.026 MPa. Two constants C1, C2 from WLF modelling (T_{ref}=15°C)

Sample	$G_{\theta z\_00}$ (MPa)	$G_{\theta z\_0}$ (MPa)	k	h	δ	τ_G (s)	β	C1	C2 (°C)
REFA-1	110	23000	0.18	0.50	3.50	1.88	550	29.87	182.23
REFC-2	150	23000	0.18	0.50	3.50	5.65	550	29.87	182.23

4.5 Comparation for behaviour of two layers loaded with a 50 µm/m global shear strain

The experimental results of the shear complex moduli of two layers are well repeated, as well as their Linear ViscoElastic simulation using the 2S2P1D model. The 2S2P1D modelling for both layers of samples loaded with a 50 µm/m global shear strain are combined and presented in this subsection.

The simulation results of the complex shear moduli for two layers are represented in Black space, along with the master curves of the norm and phase angle. (Figure 4.30, Figure 4.31, and Figure 4.32, respectively). The master curve of complex shear moduli norms and the Black diagram indicate that the static moduli ($G_{\theta z\_00}$), which characterise the interlocking and

friction among bituminous mixture aggregates in the lower layer, are greater than those in the upper layer. This shows that EME2 mixtures containing aggregates with a greater maximum nominal size interlock more effectively than BBSG3 mixtures. (14.0 mm in contrast to 10.mm). It is evident from the master curves and the Black diagram that the phase angle of the upper layer is considerably greater than that of the lower layer at a medium temperature range of 20-40 °C. The upper bitumen layer is composed of 50/70 type bitumen, which is softer than the bitumen used in the lower layer (15/25 type). Therefore, it is not surprising that a mixture containing softer bitumen would exhibit a greater viscous behaviour. Additionally, the strain calculated in the upper layer is greater than that in the lower layer. This also accounts for the observation of a greater phase angle of complex shear modulus in the upper layer at medium temperatures. The glassy moduli ($G_{\theta z\_0}$) of the bituminous mixture do not really make any

difference. This implies that under extremely low temperature conditions or at high frequencies, two mixtures will exhibit comparable behaviour.

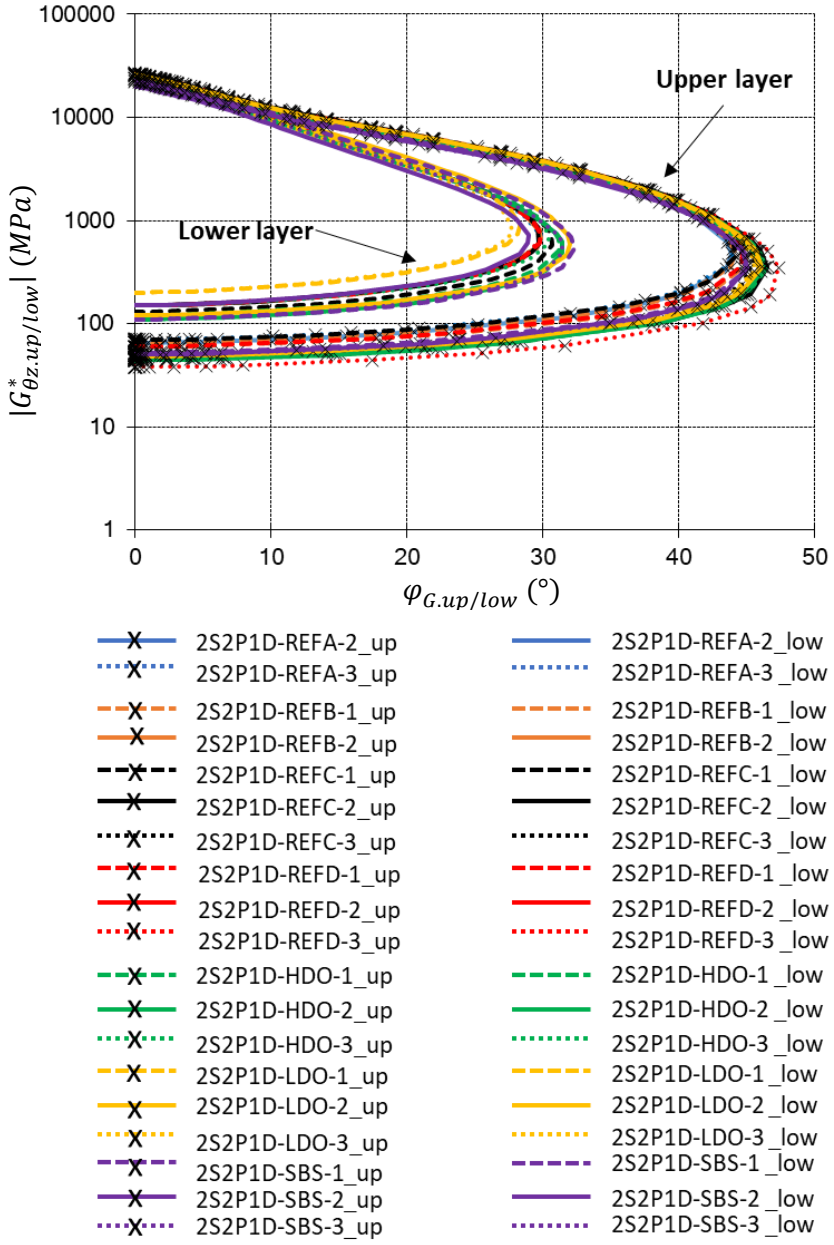

Figure 4.31: Black diagram of the complex shear moduli of the bituminous mixture in the two layers (2S2P1D modelling for all loaded with 50 µm/m global strain)

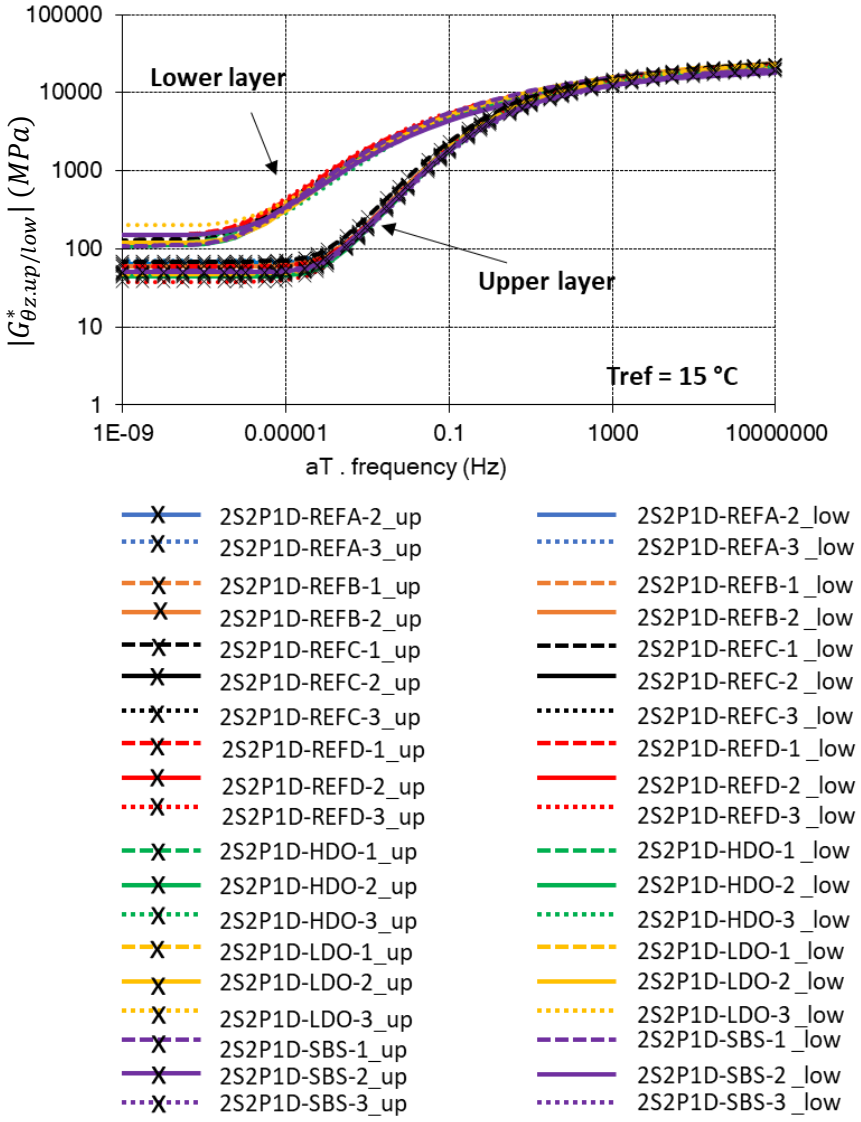

Figure 4.32: Master curve of norm of the complex shear moduli of the bituminous mixture in the two layers (2S2P1D modelling for all loaded with 50 µm/m global strain)

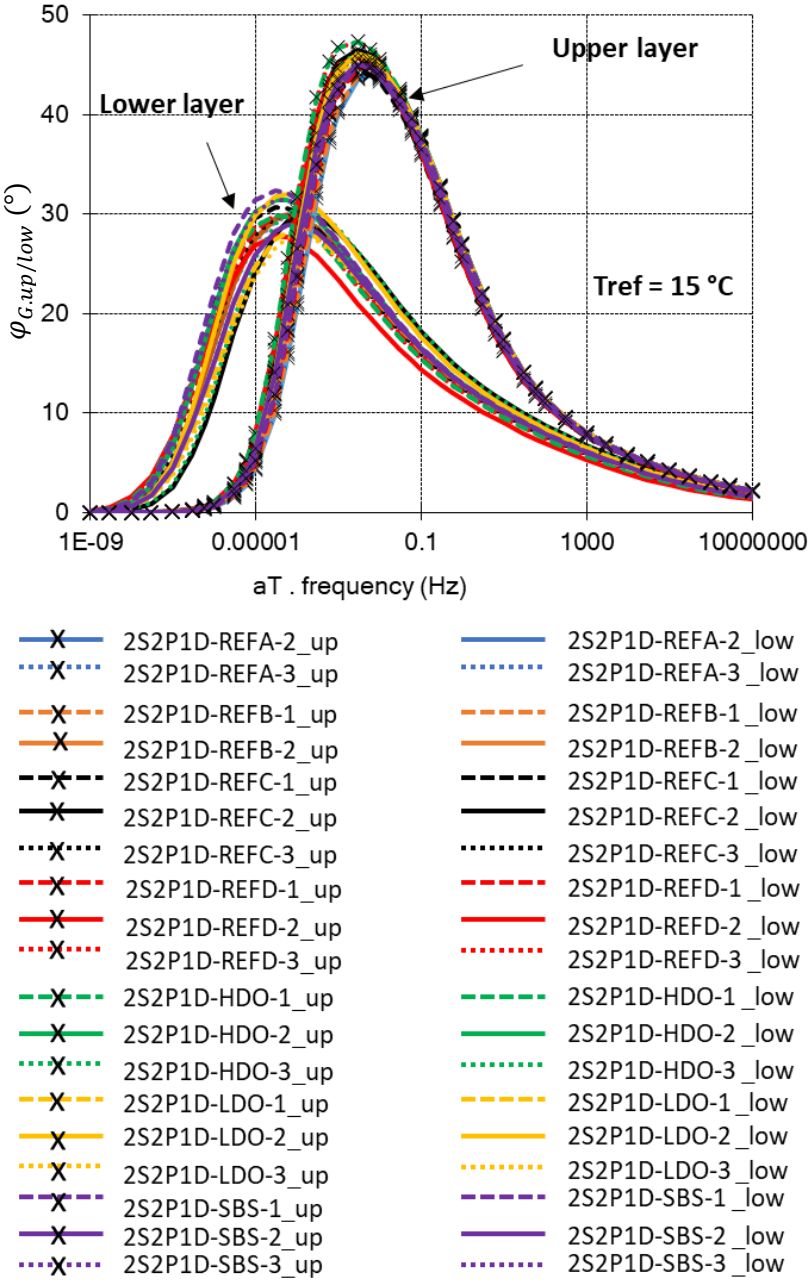

Figure 4.33: Master curve of phase angle of the complex shear moduli of the bituminous mixture in the two layers (2S2P1D modelling for all loaded with 50 µm/m global strain)

4.6 Interface

4.6.1 Behaviour of pure bitumen used for the tack coat

The 160/220 pure bitumen used for the tack coat in the reference configuration was tested using DSR apparatus in shearing mode. The experimental procedure was introduced in the Chapter 3. Figure 4.34 presents the experimental data of complex shear modulus of the pure 160/220

bitumen plotted in the Black's space. A unique curve can be found proving, as expected, that the bitumen verifies the Time-Temperature Superposition Principle (TTSP).

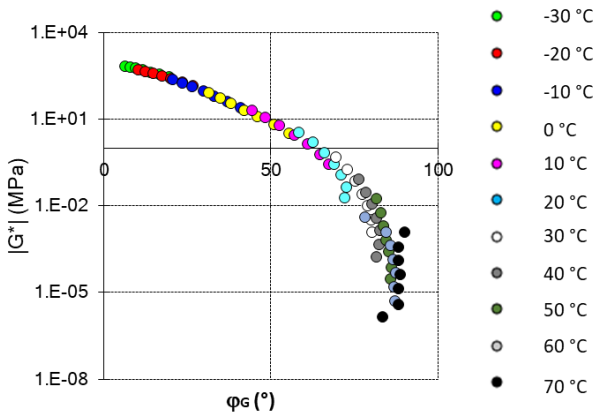

Figure 4.34: Black's space of shear complex modulus of the 160/220 bitumen used for tack coat tested by the DSR apparatus at ENTPE

Figure 4.35 (a), (b) shows the experimental master curves and 2S2P1D modelling master curves built at the reference temperature of 15°C. The shift factors are illustrated in Figure 4.35 (c). As can be observed in the figures, unique master curves for norm and phase angle of complex shear modulus could be plotted as the Time-Temperature Superposition Principle is valid. The 2S2P1D model fits well with the experimental data, which indicate the Linear ViscoElastic behaviour of the bitumen at the testing condition. The parameters of the 2S2P1D and WLF modelling are introduced on Table 4.5.

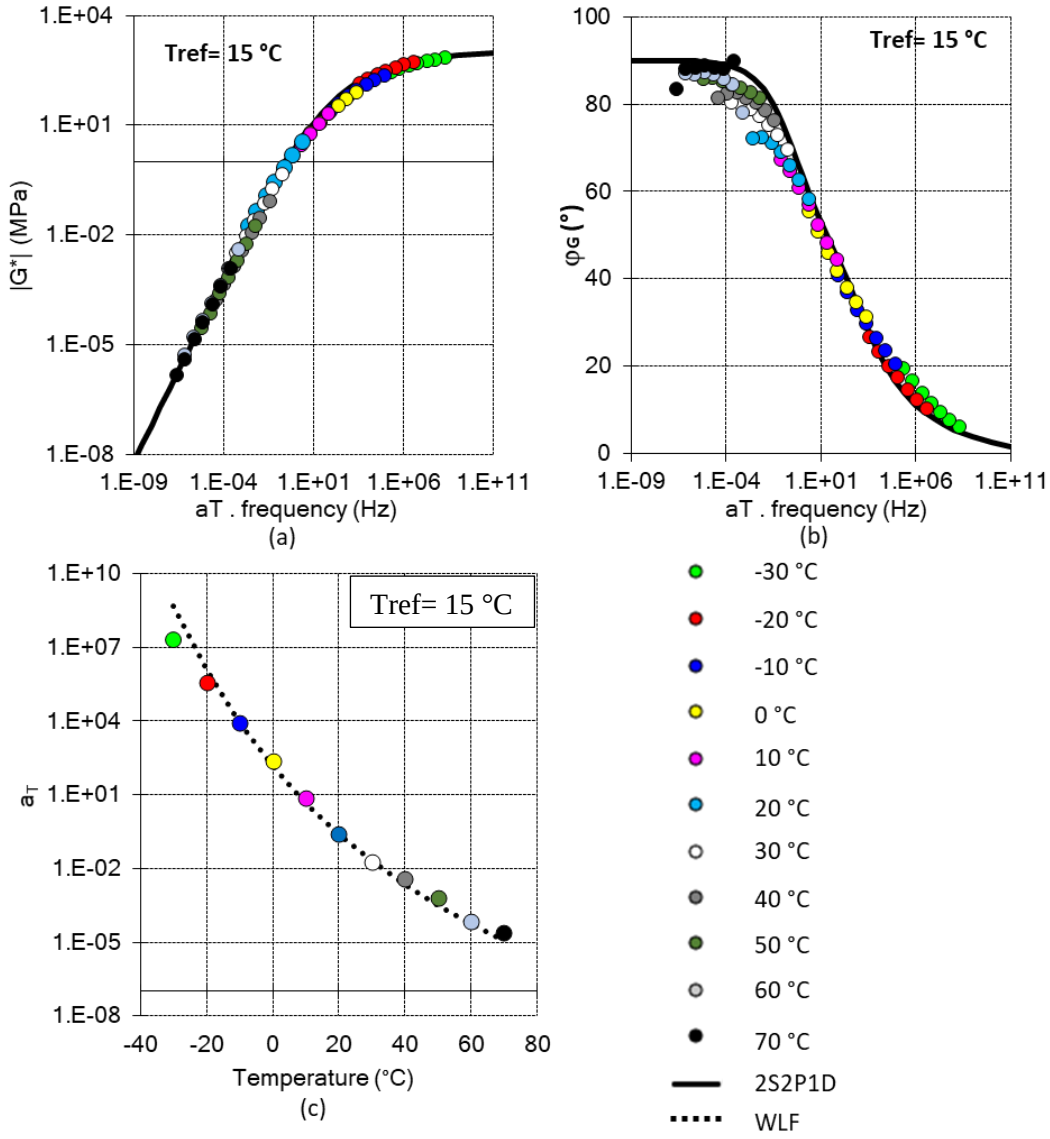

Figure 4.35: Master curves of (a) norm |G*| of complex shear modulus, (b) phase angle of complex modulus, (c) shift factors used to build master curves (for 160/220 pure bitumen)

Table 4.5: 2S2P1D and WLF constants used to model shear complex modulus of the 160/220 pure bitumen used in the reference configuration (Tref= 15 °C)

Sample	G_{00} (MPa)	G_0 (MPa)	k	h	δ	τ_G (s)	β	C1	C2 (°C)
160/220 bitumen	0	1030	0.20	0.56	2.30	8.2×10^{-6}	120	16.61	131.00

4.6.2 Influence of global shear strain amplitudes

4.6.2.1 Experimental results and LVE modelling for interface loaded with 50 µm/m global shear strain

Figure 4.36(a) and (b) show the master curves for norms and phase angle of complex shear stiffness. The master curves were built by multiplying testing frequencies of each isothermal curve with their corresponding shift factors hereafter referred to as "experimental a_T" Figure 4.37. The reference temperature chosen is 15°C.

Unique master curves for the norm and the phase angle of complex stiffness are found for all samples (Figure 4.36), and unique curves for complex stiffness plotted in Black space (Figure 4.38). This means TTSP is validated for the interface applied to 50 µm/m global strain.

The 2S2P1D model is able to characterise the norm and the phase angle of interface stiffness. So, with this level of torsional loading, the interface shows a linear viscoelastic behaviour. The amplitude of displacement gap at interface varies in the range of 0.57 µm to 3.9 µm (Figure 4.39). A unique set of constants was used to fit all experimental a_T of all samples with a unique WLF curve as shown in Figure 4.37. Parameters of the 2S2P1D model ($K_{\theta z\_0}$, $K_{\theta z\_0}$, k, h, δ, τ and β) and constants C_1, C_2 for WLF equation can be found on Table 4.6. Parameters of the 2S2P1D model to characterise Linear Viscoelastic properties of interface (k, h, δ and β) and constants C_1, C_2 are the same between samples and are identical with those used to model the pure bitumen. WLF equation fits quite well with experimental a_T.

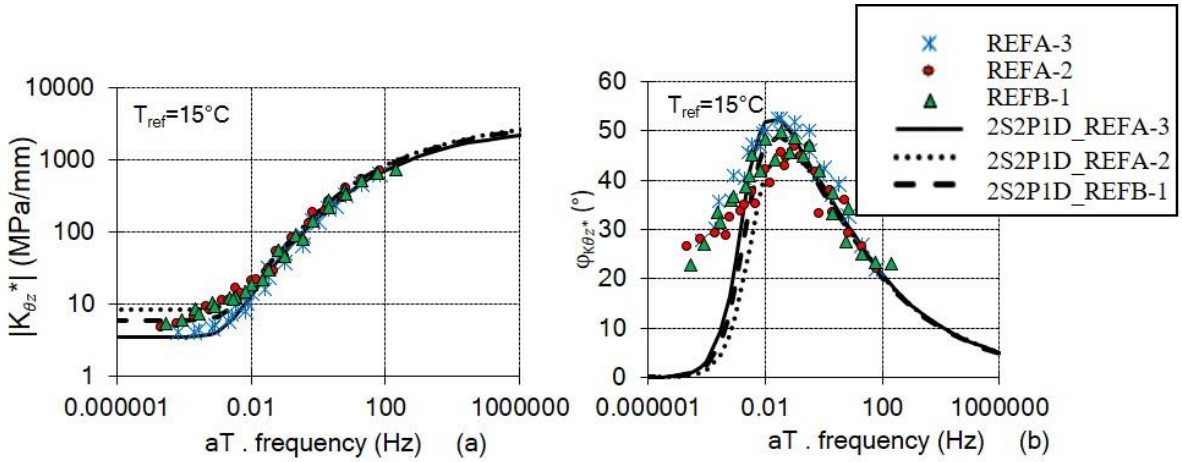

Figure 4.36: Master curves of norms of shear complex stiffness at interface (a) norms; (b) phase angle (experimental data for 3 samples applied to 50 µm/m global strain: REFA-3, REFA-2, REFB-1 and their 2S2P1D modelling)

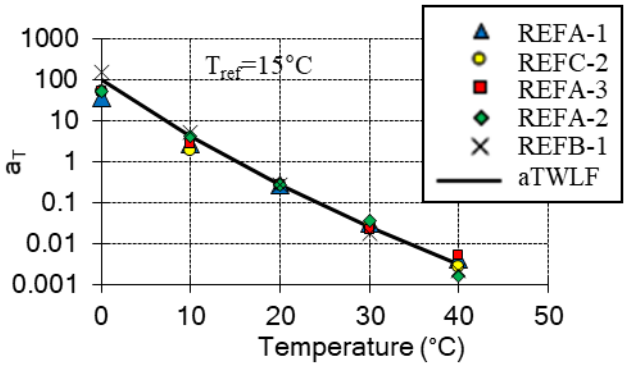

Figure 4.37: Shift factors for building master curves (experimental a_T for 3 samples applied with 50 (µm/m) strain: REFA-3, REFA-2, REFB-1; 2 samples applied with 200 (µm/m): REFA-1, REFC-2 and WLF modelling)

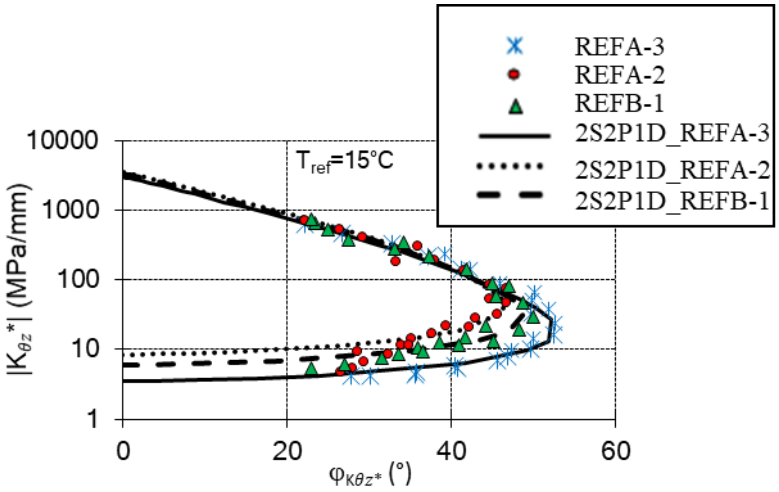

Figure 4.38: Black diagram of shear complex stiffness at interface (experimental data for 3 samples applied to 50 µm/m global strain: REFA-3, REFA-2, REFB-1 and their 2S2P1D modelling)

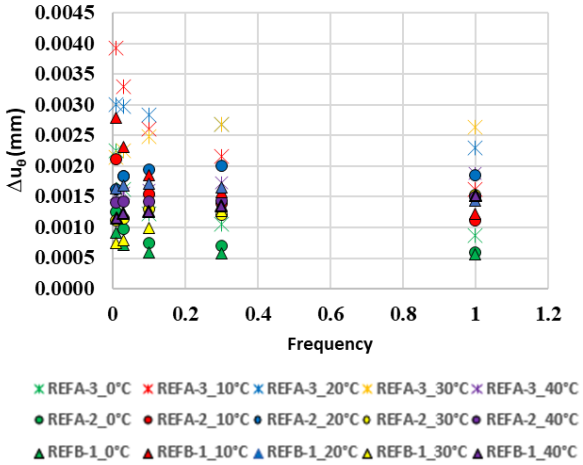

Figure 4.39: Displacement gap at the interface calculated for three samples: REFA-3, REFA-2, REFB-1 loaded with 50 µm/m global strain

Table 4.6: 2S2P1D constants used to model shear complex stiffness at interface of 3 samples applied to 50 µm/m global strain: REFA-3, REFA-2, REFB-1 Equivalent modelling notions between bituminous mixtures layers and interface using the 2T3C hollow cylinder apparatus

	$K_{\theta z\_00}$ **(MPa/mm)**	$K_{\theta z\_0}$ **(MPa/mm)**	k	h	δ	τ_K (s)	β	C1	C2 (°C)
REFA-3	3.0	3200	0.20	0.56	2.30	0.0024	120	16.61	131.00
REFA-2	7.0	3500							
REFB-1	4.5	3400							

4.6.2.2 Experimental results and LVE modelling for interface loaded with 200 µm/m global shear strain

When samples are loaded with sinusoidal cycles at 200 µm/m of global strain, the displacement gap at the interface is calculated and then presented in Figure 4.40. It varies within the range of 1 µm – 30 µm relying on the temperature and frequency. The master curves for the norm and phase angle of complex stiffness (Figure 4.41) are built using the same shift factors as those found with amplitude of 50 µm/m. Continuous master curves can be observed for both norm (Figure 4.41 (a)) and phase angle (Figure 4.41 (b)).

As it can be seen from Figure 4.41 (a), the model 2S2P1D characterise well for norm of complex interface stiffness, but not for phase angle (Figure 4.41 (b), (Figure 4.42)). There are underestimations of the model 2D2P1D for the phase angle of the complex interface stiffness which can be observed in the master curves (Figure 4.41 (b)), and Black diagram (Figure 4.42). The underestimated phase angles are about 17° and 12° for samples REFA-1 and REFC-2, respectively. The constants for 2S2P1D and WLF modelling can be found on Table 4.7. 2S2P1D parameters k, h, δ and β and constants C_1, C_2 are the same between two samples and

with those loaded with the amplitude 50 µm/m. The amplitude of displacement gap at interface varies in the range of 4.5 µm to 13 µm.

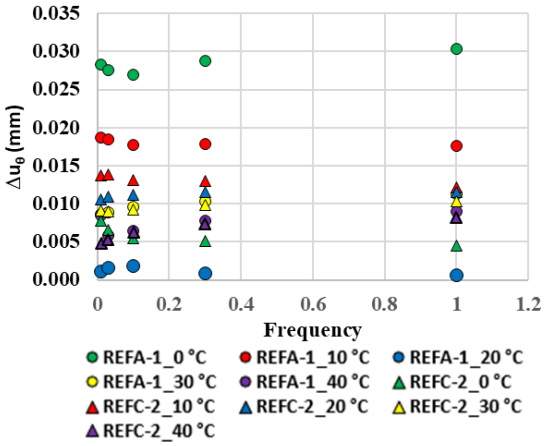

Figure 4.40: Displacement gap at the interface calculated for three samples: REFA-3, REFA-2, REFB-1 loaded with 200 µm/m global shear strain

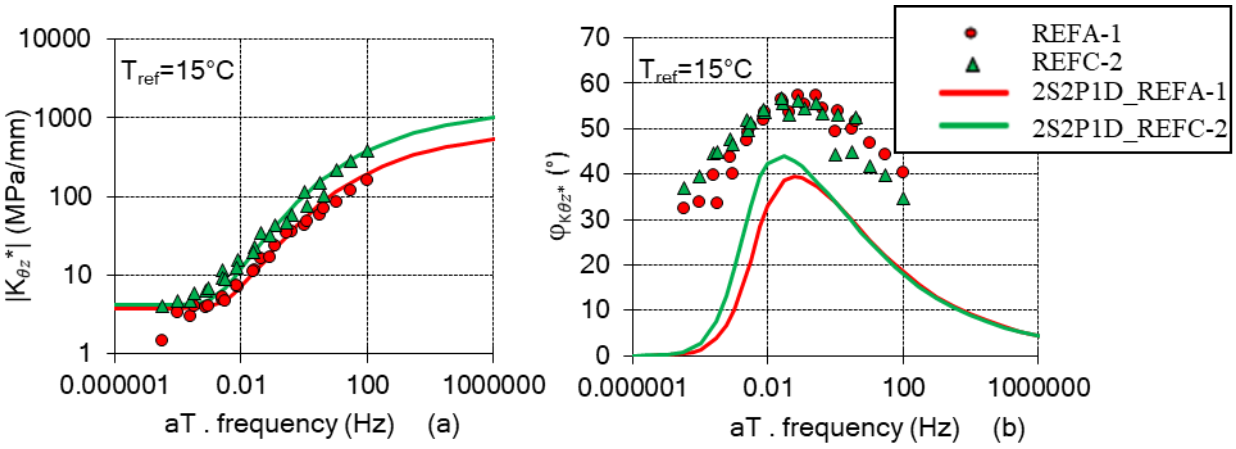

Figure 4.41: Master curves of norms of shear complex stiffness at interface (a) norms; (b) phase angle (experimental data for 2 samples applied to 200 µm/m: REFA-1, REFC-2 and their 2S2P1D modelling)

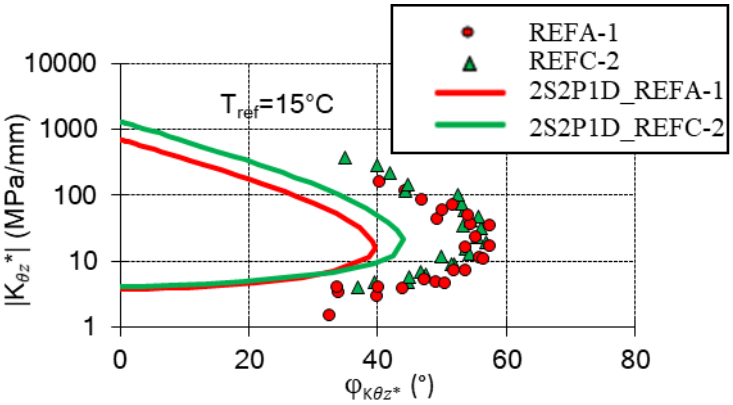

Figure 4.42: Black diagram of shear complex stiffness at interface (experimental data for 2 samples applied to 200 µm/m global strain: REFA-1, REFC-2 and their 2S2P1D modelling)

Table 4.7: 2S2P1D constants used to model shear complex stiffness at interface of 2 samples applied to 200 µm/m global strain: REFA-1, REFC-2 (T_{ref} = 15 °C)

	$K_{\theta z\_00}$ (MPa/mm)	$K_{\theta z\_0}$ (MPa/mm)	k	h	δ	τ_K (s)	β	C1	C2 (°C)
REFA-1	3.2	600	0.20	0.56	2.30	0.0049	120	16.61	131.00
REFC-2	4.0	1200				0.0041			

4.6.2.3 Experimental results and VEP modelling for interface loaded with 200 µm/m global shear strain

The model 2S2P1D fits quite well with the master curve of the norm of the complex interface stiffness, and there are underestimations in phase angle as mentioned. This indicates that the interface behaviour is not LVE for this loading amplitude. The model DBN_{PDS} was developed by Attia (2020) in order to take into account a plastic behaviour (plastic dissipation) into modelling, which is added to the viscous dissipation. The was introduced in chapter 1. To calibrate the DBN_{PDSC} model, a Generalised Kevin-Voigt (GKV) model is calibrated based on the 2S2P1D model, and the number of GKV elements is chosen to be 25 to ensure the good correlation and precision between the two models. The norm of the complex stiffness of the DBN_{PDSC} model and the GKV model are the same. Therefore, constants ($K_{\theta z\_0}$, $K_{\theta z\_i}$,η_i) for the DBN_{PDSC} model are identical to the GKV ones. The DBN_{PDSC} model's constants for both sample (REFA-1 and REFC-2) can be found on Table 4.8. The phase angle of shear complex interface stiffness for model DBN_{PDSC} (φ_{DBN}) is computed as presented in previous section. The angle φ_{NL} are chosen to be 17° and 12° for sample REFA-1 and REFC-2, respectively.

As it can be seen from Figure 4.43 (a) the master curve of norm of complex interface stiffness calculated from the DBN_{PDSC} model correlates perfectly with that of the 2D2P1D model, and fit well experimental results. Furthermore, the master curves of phase angle computed from the DBN_{PDSC} model fit successfully with those of experimental results in Figure 4.43 (b). Figure 4.44 shows the Black diagram of complex interface stiffness for the 2 samples REFA-1 and REFC-2. The DBN_{PDSC} model fits with experimental data and compensates the underestimation of the 2S2P1D model in term of phase angle. When samples are loaded with

sinusoidal cycles at 200 µm/m of global strain, the interface shows a visco-elasto-plastic behaviour which could be described by the DBN_{PDSC} model.

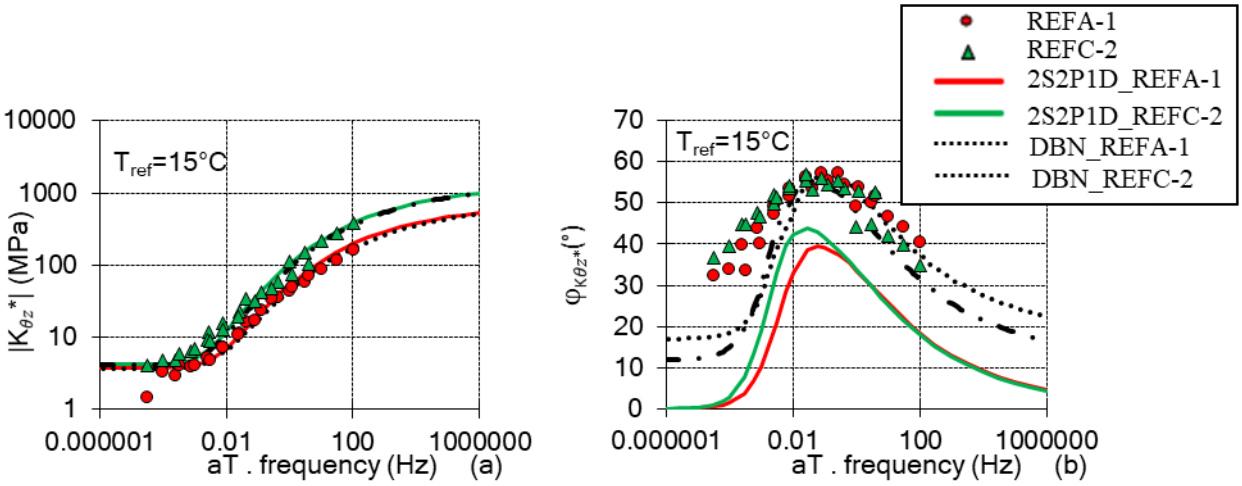

Figure 4.43: Master curves of norms of shear complex stiffness at interface (a) norms; (b) phase angle (experimental data for 2 samples applied to 200 µm/m global strain: REFA-1, REFC-2, their 2S2P1D, DBN_{PDSC} modelling)

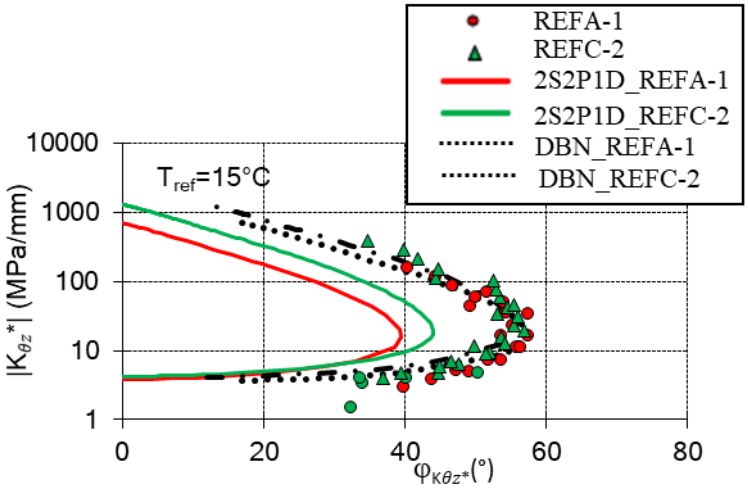

Figure 4.44: Black diagram of shear complex stiffness at interface (experimental data for 2 samples applied to 200 µm/m global strain: REFA-1, REFC-2, their 2S2P1D and DBN_{PDSC} modelling)

Table 4.8: DBN_{PDSC} constants at T_{ref} = 15°C used to model shear complex stiffness at interface of samples REFA-1, REFC-2

	REFA-1			REFC-2		
Element number	$K_{\theta zi}$ (MPa/mm)	η_i (MPa.s/mm)	φ_{NL}	$K_{\theta zi}$ (MPa/mm)	η_i (MPa.s/mm)	φ_{NL}
0	6.00E+02	0	17	1.20E+03	0	12
1	7.02E+04	6.32E-10		9.98E+04	7.63E-09	

2	7.97E+04	4.07E-09		1.21E+05	5.13E-08	
3	7.19E+04	2.08E-08		1.09E+05	2.38E-07	
4	6.67E+04	1.09E-07		1.09E+05	1.23E-06	
5	4.02E+04	3.72E-07		5.90E+04	3.71E-06	
6	3.15E+04	1.65E-06		4.88E+04	1.59E-05	
7	2.08E+04	6.16E-06		3.17E+04	5.33E-05	
8	1.53E+04	2.58E-05		2.43E+04	2.12E-04	
9	1.05E+04	9.97E-05		1.79E+04	7.44E-04	
10	7.52E+03	4.05E-04		1.32E+04	2.83E-03	
11	5.19E+03	1.58E-03		9.08E+03	1.01E-02	
12	3.63E+03	6.26E-03		6.41E+03	3.66E-02	
13	2.45E+03	2.40E-02		4.28E+03	1.26E-01	
14	1.63E+03	9.02E-02		2.79E+03	4.26E-01	
15	1.03E+03	3.21E-01		1.69E+03	1.33E+00	
16	6.05E+02	1.07E+00		9.57E+02	3.89E+00	
17	3.26E+02	3.27E+00		4.94E+02	1.04E+01	
18	1.60E+02	9.08E+00		2.36E+02	2.56E+01	
19	7.14E+01	2.30E+01		1.05E+02	5.87E+01	
20	2.96E+01	5.39E+01		4.41E+01	1.27E+02	
21	1.22E+01	1.26E+02		1.85E+01	2.76E+02	
22	7.87E+00	4.60E+02		1.05E+01	8.08E+02	
23	2.52E+01	8.34E+03		1.83E+01	7.28E+03	
24	3.00E+02	5.62E+05		9.44E+02	1.94E+06	
25	2.09E+03	2.22E+07		3.62E+02	3.84E+06	

4.6.3 The influence vertical stress on LVE behaviour of the interface

Figure 4.45 illustrates the displacement gap at the interface that was computed for two samples subjected to three distinct axial stresses (σ_{zz}= -0.026 MPa, -0.125 MPa, and -0.250 MPa) while controlling the same global shear strain amplitude ($\varepsilon_{\theta zg\_0}$) of 50 μm/m. The displacement gap at the interface exhibits variation within the following ranges: 0.8μm/m–4.5μm/m, 0.8μm/m–3.3μm/m, and 0.8μm–4.5μm/m, respectively, under the following shear stresses: - 0.026 MPa, - 0.125 MPa, and - 0.250 MPa. It can be stated that the displacement gap at the interface exhibits a narrower range as the axial stress increases. The interlock of aggregates between two layers appears to be strengthened as a result when the axial tension is increased. This observation can

be supported by the subsequent results modelling.

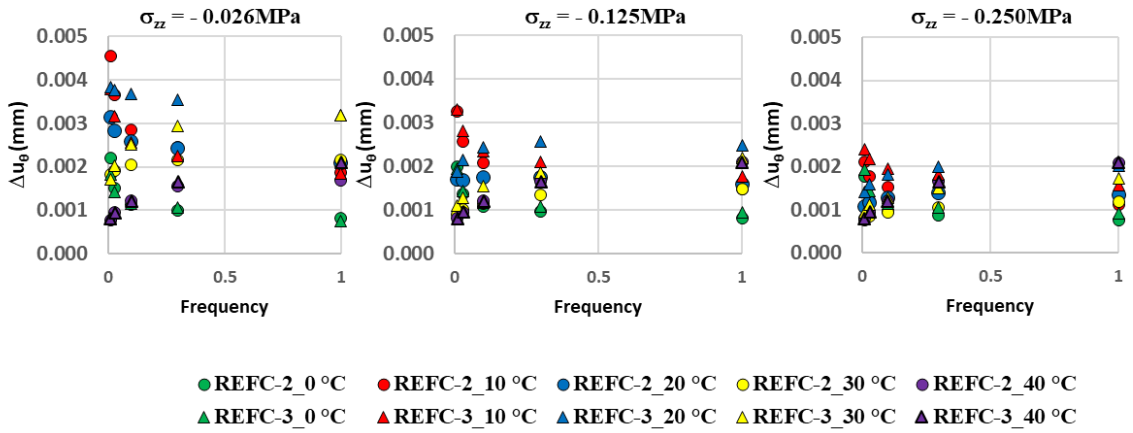

Figure 4.45: Displacement gap at the interface calculated for two samples: REFA-3, REFA-2, REFB-1 loaded with 50 µm/m global shear strain combined three constant axial stresses: -0.025 MPa, -0.125 MPa, and -0.250 MPa

Figure 4.46 (a, b) shows the Black diagram and the master curves for sample REFC-2 tested with three different axial stresses (σ_{zz}= -0.026 MPa, -0.125 MPa, and -0.250 MPa). The experimental results indicate the TTSP holds for interface stiffness in the three tests, that can be seen from the unique curves in Black diagram and master curves of norm.

Figure 4.47 (a,b) shows the Black diagram and the master curves of norm for sample REFC-3 tested with three different axial stresses (σ_{zz}= -0.026 MPa, -0.125 MPa, and -0.250 MPa). Observation from results also confirms the validation of the TTSP, the good fit of the 2S2P1D model. The master curves were built by multiplying the testing frequencies with shifting factors in Figure 4.48. The 2S2P1D model fits well with the experimental results, and the parameters used to calibrate the model is presented on Table 4.9. From Table 4.9, two samples share the same calibration parameters (k, h, δ and β and constants C_1, C_2) used to describe the LVE behaviour of a bituminous interface. However, the static interface stiffness ($K_{\theta z\_00}$) increase with the increase of axial stress. $K_{\theta z\_00}$ is a parameter inheriting from the interaction or the interlocking between aggregate particles. Therefore, it can be said that the increase of axial stress can improve the interlocking of aggregate particles from two layers.

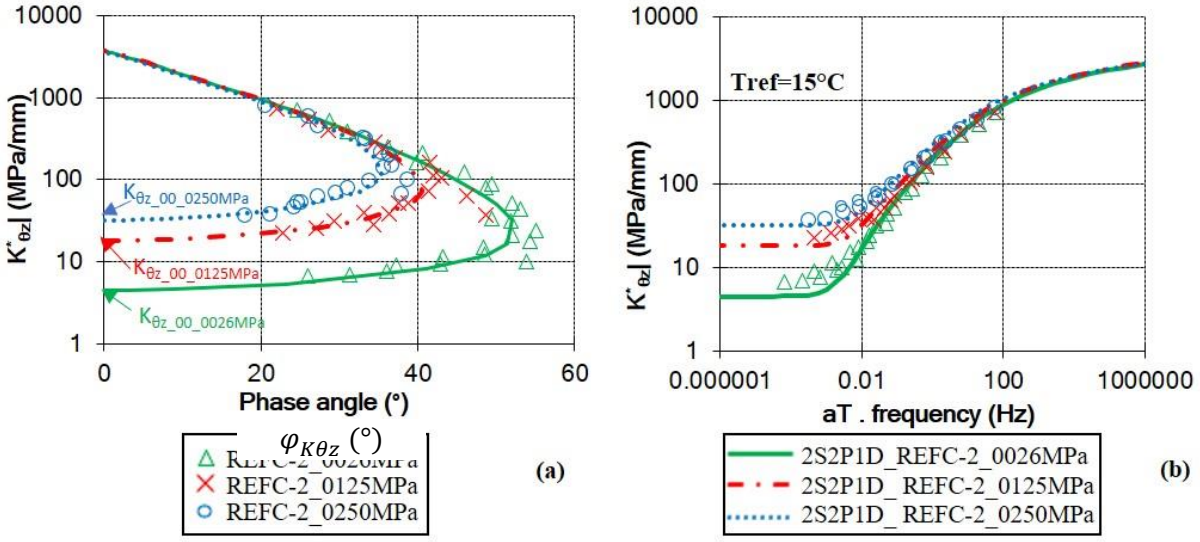

Figure 4.46: (a) Black diagram of shear complex interface stiffness for the sample REFC-2, (b) master curves of norms of shear complex interface stiffness (experimental data for 3 levels of axial stress: 0.026, 0.125, 0.250 MPa and their 2S2P1D modelling.

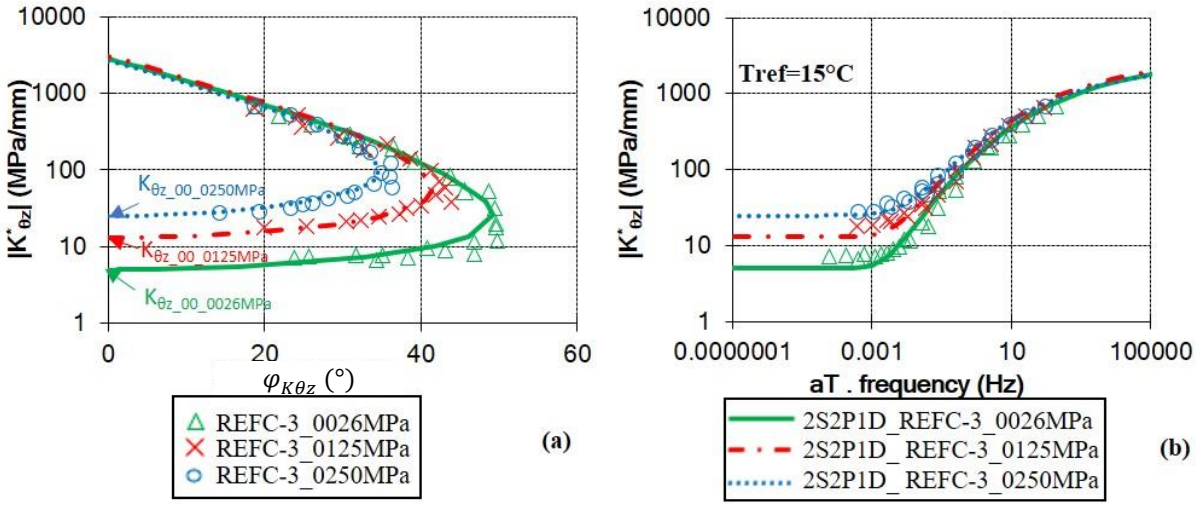

Figure 4.47: (a) Black diagram of shear complex interface stiffness for the sample *REFC-3*, (b) master curves of norms of shear complex interface stiffness (experimental data for 3 levels of axial stress: 0.026, 0.125, 0.250 MPa and their 2S2P1D modelling.

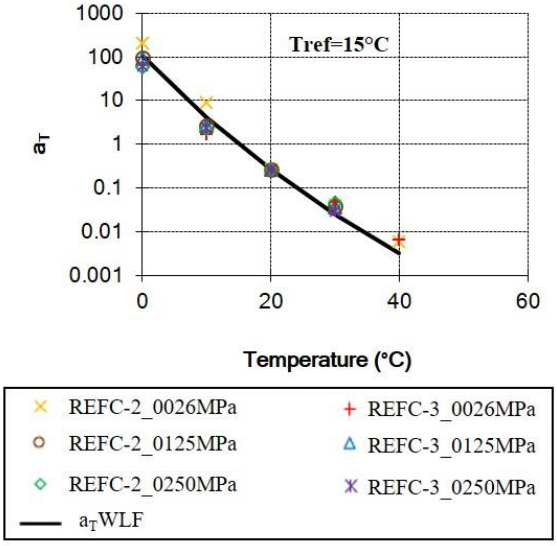

Figure 4.48: Shift fators (a_T) used to construct master curves (experimental a_T for 2 samples applied with 3 different levels of axial loading and a_T from WLF modelling)

Table 4.9: 2S2P1D constants for modelling shear complex interface stiffness of 2 samples load with 3 different axial stress 0.026, 0.125, 0.250 MPa. Two constants C1, C2 from WLF modelling (T_{ref} = 15°C)

Sample	Axial Stress (MPa)	$K_{\theta z\_00}$ (MPa/mm)	$K_{\theta z\_0}$ (MPa/mm)	k	h	δ	τ_K (s)	β	C1	C2 (°C)
REFC-2	0.026	3.5	4300	0.2	0.56	2.3	0.0024	120	16.61	131.00
	0.125	15.0	3600				0.0028			
	0.250	32.0	3700				0.0036			
REFC-3	0.026	3.5	2400				0.0024			
	0.125	15.0	2800				0.0024			
	0.250	23.0	2700				0.0032			

4.6.4 The influence of residual emulsified-bitumen doses to LVE behaviour of the interface

The application of the emulsified bitumen at the interfaces is in three different dosages 250, 350, 450 g/m^2 residual doses. The shear complex modulus tests were performed in 2T3C HCA samples to study LVE behaviour of interfaces with different tack coat dosages. The 2S2P1D model is then used to characterise the LVE behaviour of the interfaces. The parameters of the

2S2P1D calibrations are shown on Table 4.10. Samples with different emulsion dosages share the identical calibration parameter (k, h, δ and β and constants C_1, C_2) that is used to describe the LVE behaviour of the interface behaviour, and of the pure bitumen used at the interfaces. The differences can be found on K_0 and K_{00} parameters that are respectively static and glassy interface stiffnesses. The experimental data and the 2S2P1D modelling are normalised by Equation (4.21). The idea of normalisation is to eliminate the influence of K0 and K00, so as to study the influence of the parameter describing LVE behaviour.

$$K^*_{\theta z\_norm} = \frac{K^*_{\theta z} - K_{00}}{K_0 - K_{00}} \tag{4.21}$$

The normalised results are plotted in the Black's space, master curve of normalised norm and master curve of phase angle at the reference temperature (T_{ref}) of 15 °C in Figure 4.49, Figure 4.50, and Figure 4.51. As can be seen from the figures, the normalised experimental data is well superimposed whatever the tack coat dosages. The same 2S2P1D parameters to model the LVE behaviour of interface may be used. This shows that the application of different tack coat dosages does not change the LVE behaviour of interface.

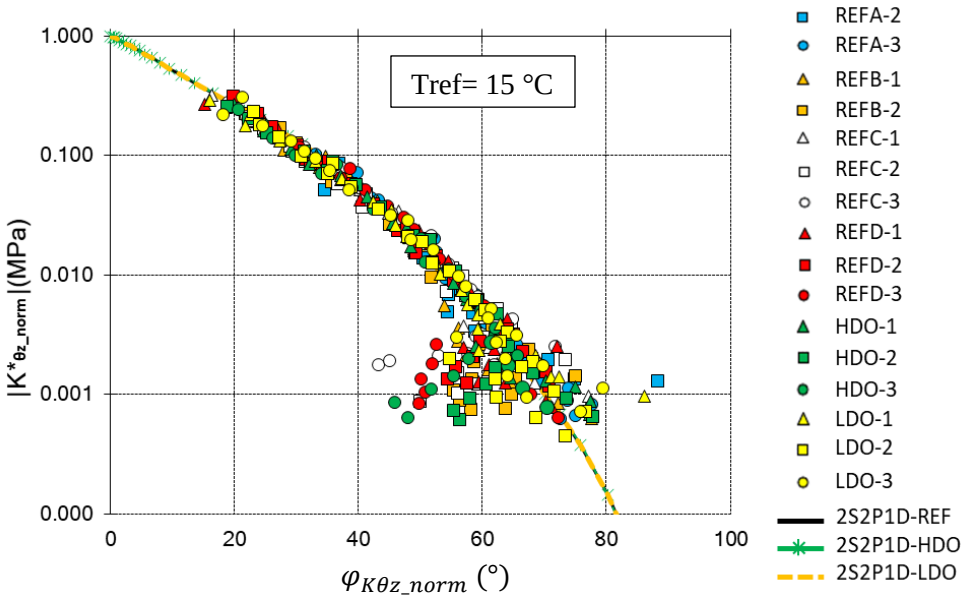

Figure 4.49: Black's space of the norm of $K^*_{\theta z\_norm}$ (normalised interfaces stiffness) for 3 interface configurations: REF: reference; HDO: high tack coat dosage; and LDO: low tack coat dosage (Experimental data and 2S2P1D modelling)

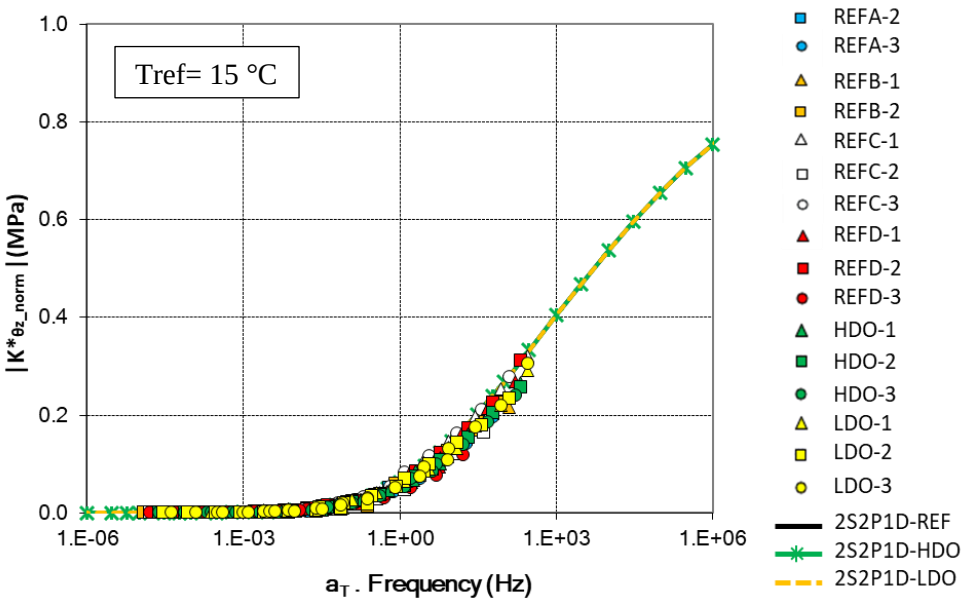

Figure 4.50: Master curves of norm of $K^*_{\theta z\_norm}$ (normalised interfaces stiffness) for 3 interface configurations: REF: reference; HDO: high tack coat dosage; and LDO: low tack coat dosage (Experimental data and 2S2P1D modelling)

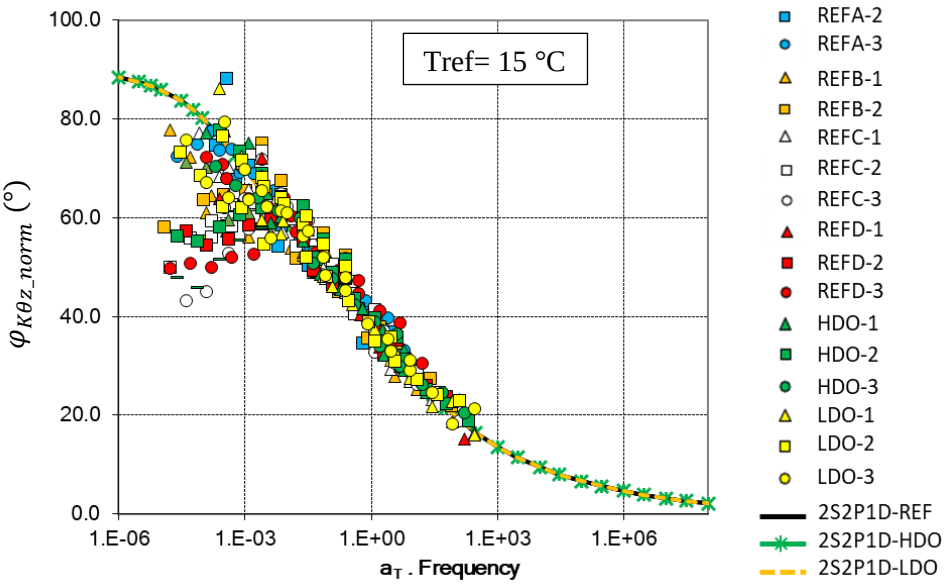

Figure 4.51: Master curves of phase angle of $K^*_{\theta z\_norm}$ (normalised interfaces stiffness) for 3 interface configurations: REF: reference; HDO: high tack coat dosage; and LDO: low tack coat dosage (Experimental data and 2S2P1D modelling)

4.6.5 The influence of emulsified bitumen types to LVE behaviour of the interface

Two types of tack coat are used to study their influence on interface LVE behaviour. One tack coat emulsified with the 160/220 pen grade bitumen and one with SBS-modification of the

160/220 pen grade bitumen. The samples are tested in shear complex modulus tests and data is modelled using the LVE 2S2P1D model.

2S2P1D parameters calibrated experimental data are shown on Table 4.10. In order to study the influence of both tack coat types, the experimental data and the 2S2P1D modelling are plotted in normalised values. Figure 4.52, Figure 4.53, and Figure 4.54 respectively show $K^*_{\theta z\_norm}$ in Black's space, master curves at T_{ref}=15 °C of $K^*_{\theta z\_norm}$, and master curves at T_{ref}=15 °C of phase angle of $K^*_{\theta z\_norm}$. It can be seen from the figures that the modification does not change significantly the behaviour of the interfaces.

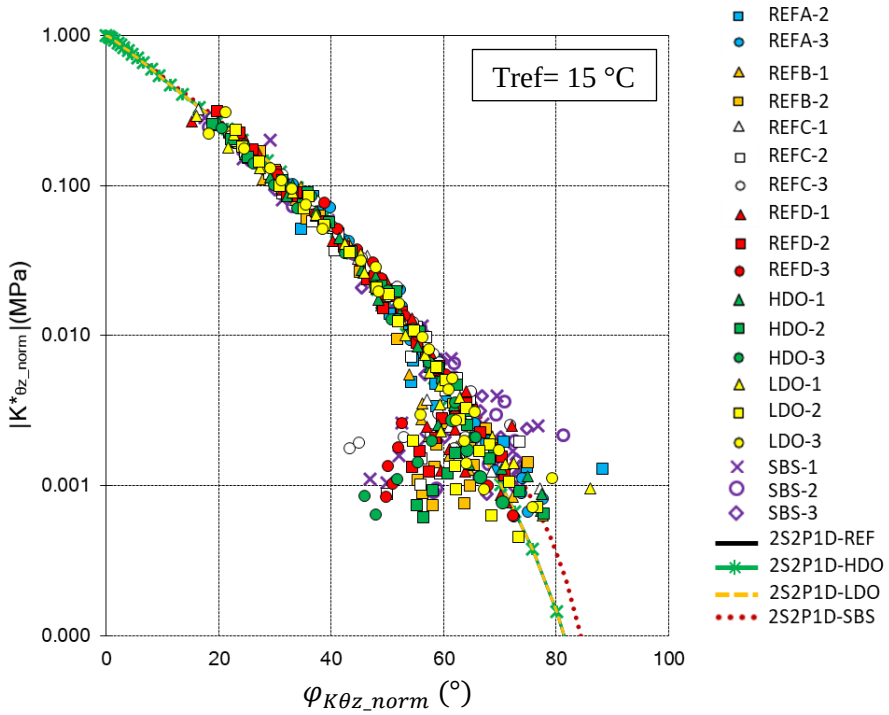

Figure 4.52: Black's space of $K^*_{\theta z\_norm}$ (normalised interfaces stiffness) for four interface configurations: REF: reference; HDO: high tack coat dosage; LDO: low tack coat dosage; and SBS: polymer modified tack coat (Experimental data and 2S2P1D modelling)

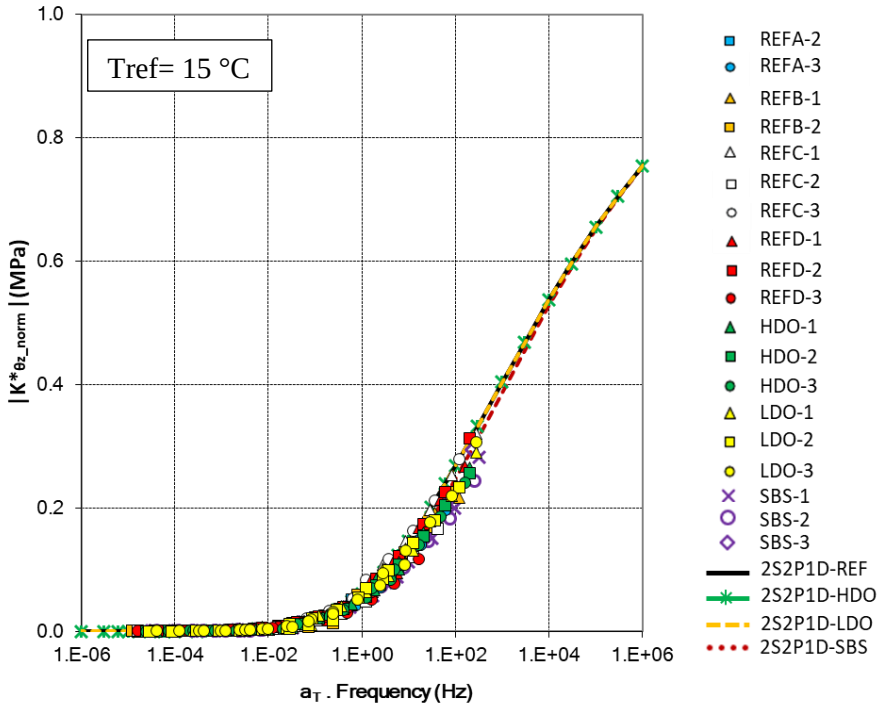

Figure 4.53: Master curves of $K^*_{\theta z\_norm}$ (normalised interfaces stiffness) for four interface configurations: REF: reference; HDO: high tack coat dosage; LDO: low tack coat dosage; and SBS: polymer modified tack coat (Experimental data and 2S2P1D modelling)

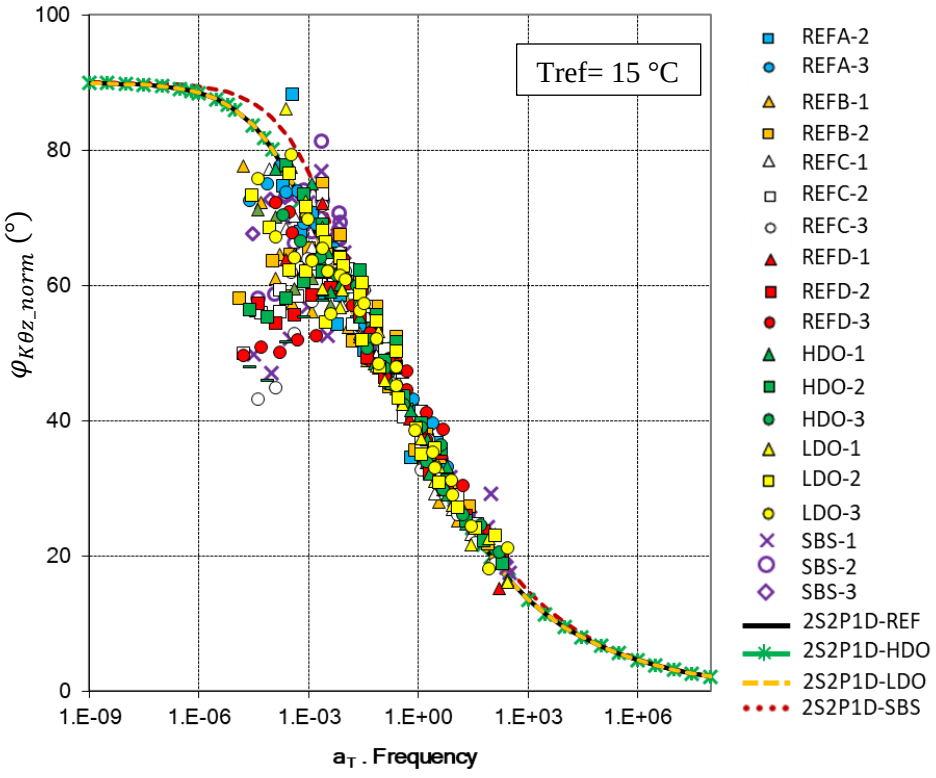

Figure 4.54: Master curves of phase angle of $K^*_{\theta z\_norm}$ (normalised interfaces stiffness) for four interface configurations: REF: reference; HDO: high tack coat dosage; LDO: low tack

coat dosage; and SBS: polymer modified tack coat (Experimental data and 2S2P1D modelling)

Table 4.10: 2S2P1D constants for modelling shear complex interface stiffness of all samples applied with the same global strain of 50 µm/m and axial stress of 0.026 MPa. Two constants C1, C2 from WLF modelling (T_{ref}=15°C)

Sample	$K_{\theta z\_00}$ (MPa/mm)	$K_{\theta z\_0}$ (MPa/mm)	k	h	δ	τ_K (s)	β	C1	C2 (°C)
REFA-2	7.0	3500	0.20	0.56	2.30	0.0024	120	16.61	131.00
REFA-3	3.0	3200							
REFB-1	4.5	3400							
REFB-2	3.0	4000							
REFC-1	3.6	2300							
REFC-2	3.5	4300							
REFC-3	3.5	2400							
REFD-1	4.0	3000							
REFD-2	4.5	3800							
REFD-3	1.5	2800							
HDO-1	3.5	3500							
HDO-2	1.8	3200							
HDO-3	2.5	3500							
LDO-1	4.5	3400							
LDO-2	2.6	4400							
LDO-3	3.5	3200							
SBS-1	6.5	3700							
SBS-2	5.0	3400							

SBS-3	5.0	3000							

4.6.6 Nonlinearity test results

The nonlinearity tests were performed with five different global shear strain amplitudes ($\varepsilon_{\theta zg\_0}$) ranging from 30 to 110 µm/m. 9 samples with four different interface configurations were tested. The tests were conducted at the temperature of 10°C and the frequency of 1Hz. The norm and the phase angle of interface stiffness were calculated using the method introduced in the section 4.1.

Figure 4.55 presents the norm of interface stiffness plotted against the displacement gap amplitude $\Delta u_{\theta z\_0}$. The norm of interface stiffness mostly varies between 270 MPa/mm to 500 MPa/mm, and the amplitude of displacement gap at the interface between 0.4 and 2.5 µm. As can be seen from Figure 4.55, the norm of interface stiffness decreases with the increase of displacement gap at the interface. This result aligns with what can be observed for bitumen and bituminous mixtures (Babadopulos, 2017; S. Mangiafico et al., 2018). Figure 4.55 also shows the linear regression lines for the norm of interface stiffness ($|K^*_{\theta z}|$) calculated at different interface displacement gap amplitude ($\Delta u_{\theta z\_0}$). From these linear regression lines, one can extrapolate the $|K^*_{\theta z}|$ of an interface, if the $\Delta u_{\theta z\_0}$ was nil. The figure demonstrates an example for extrapolated $|K^*_{\theta z}|$ of the sample SBS-2.

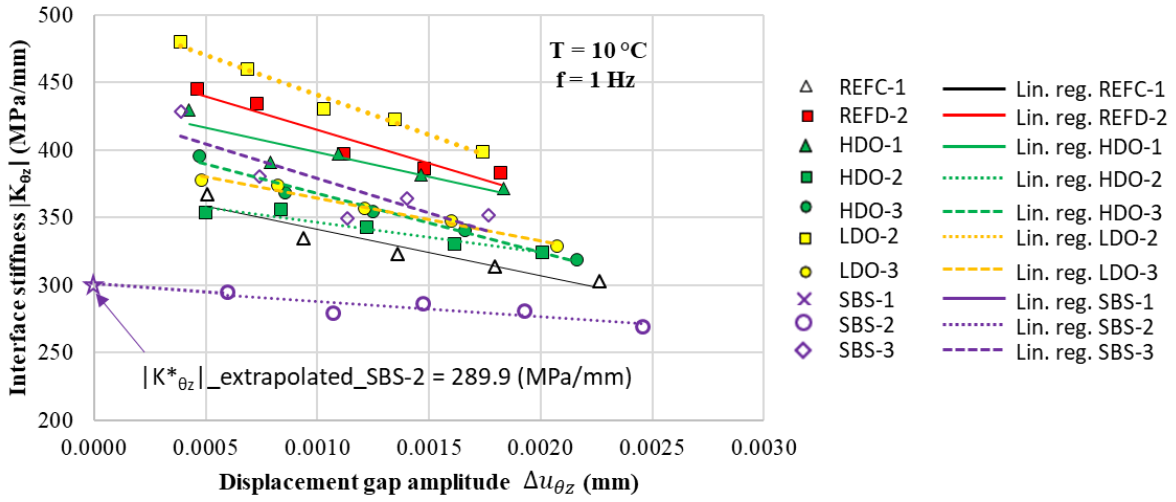

Figure 4.55: Evolution of norm of the interface stiffness $|K^*_{\theta z}|$ with the displacement gap amplitude at the interface ($\Delta u_{\theta z\_0}$) during the nonlinearity tests

Figure 4.56 depicts the evolution of phase angle of interface stiffness ($\varphi_{K\theta z}$) and the displacement gap at the interface amplitude ($\Delta u_{\theta z\_0}$) during the nonlinearity tests. The phase

angles $\varphi_{K\theta z}$ exhibit the variation in the range of 25° to 40°. As the displacement gap at the interface increases, the phase angle of interface stiffness increase. The linear regression lines for the phase angle of interface stiffness ($\varphi_{K\theta z}$) are also illustrated in Figure 4.56. These lines were calculated at various amplitudes of the interface displacement gap ($\Delta u_{\theta z\_0}$). It is possible to derive the $\varphi_{K\theta z}$ of an interface from these linear regression lines, when the applied $\Delta u_{\theta z\_0}$ was nil. The illustration showcases an instance of the extrapolated ($\varphi_{K\theta z}$) of the sample SBS-2.

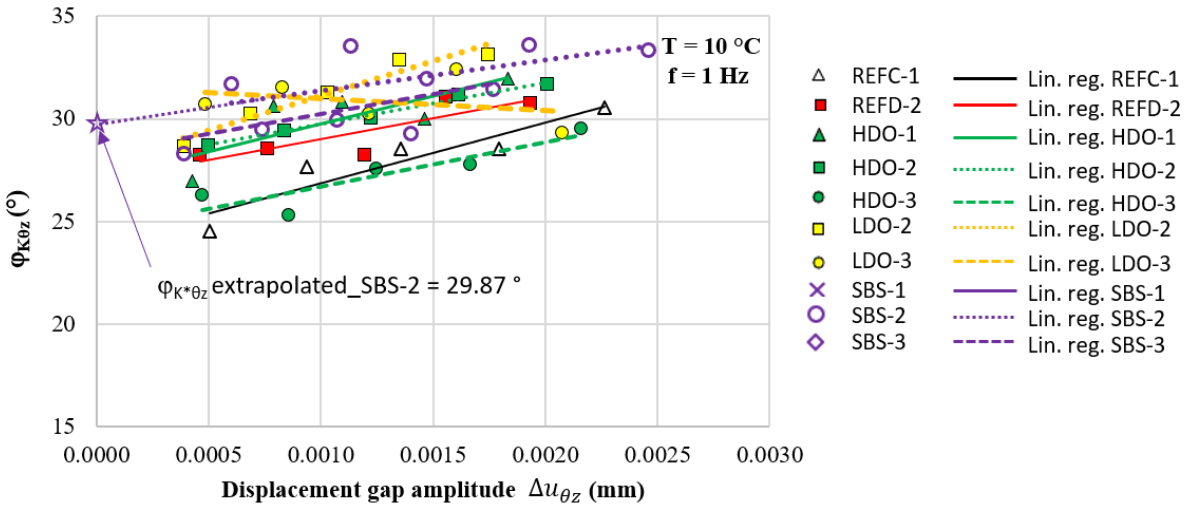

Figure 4.56: Evolution of phase angle of the interface stiffness ($\varphi_{K\theta z}$) with the displacement gap amplitude at the interface ($\Delta u_{\theta z\_0}$) during the nonlinearity tests

As it is introduced in the Chapter 3 that the global shear strain amplitude ($\varepsilon_{\theta zg\_0}$) used for the shear complex modulus and fatigue is 50 µm/m. Since the $\varepsilon_{\theta zg\_0}$ is the global value and calculated according to the relative displacement between the top and the bottom surfaces of a sample, the displacement gap is not constant for all samples. The averaged $\Delta u_{\theta z\_0}$ when samples were loaded with 50 µm/m is 8 µm. The interpolated values of $|K^*_{\theta z}|$, and $\varphi_{K\theta z}$ computed when $\Delta u_{\theta z\_0}$ is 8 µm presented on Table 4.11 alongside with the extrapolated values calculated when $\Delta u_{\theta z\_0}$ is nil. Furthermore, the effects of nonlinearity on the norm ($\Delta|K^*_{\theta z\_NL}|$) and the phase angle ($\Delta\varphi_{K^*_{\theta z\_NL}}$) of the complex interface stiffness when $\Delta u_{\theta z\_0} = 8$ µm are calculated by Equation (4.22), and (4.23), and the results are shown on Table 4.11. $|K^*_{\theta z}|_{(\Delta u_{\theta z\_0} = 8\ \mu m)}$, and $\varphi_{K\theta z(\Delta u_{\theta z\_0} = 8\ \mu m)}$ are the norm and phase angle of the interpolated complex interface stiffness when $\Delta u_{\theta z\_0} = 8$ µm. $|K^*_{\theta z}|_{(\Delta u_{\theta z\_0} = 0\ \mu m)}$, and $\varphi_{K\theta z(\Delta u_{\theta z\_0} = 0\ \mu m)}$ the norm and phase angle of the extrapolated complex interface stiffness when $\Delta u_{\theta z\_0} = 0$ µm. The results are also plotted

on Figure 4.57, and Figure 4.58, respectively, for the norm and phase angle of the complex interface stiffness.

$$\Delta|K^*_{\theta z\_NL}| = \frac{|K^*_{\theta z}|_{(\Delta u_{\theta z\_0} = 8\ \mu m)} - |K^*_{\theta z}|_{(\Delta u_{\theta z\_0} = 0\ \mu m)}}{|K^*_{\theta z}|_{(\Delta u_{\theta z\_0} = 8\ \mu m)}} \quad (4.22)$$

$$\Delta\varphi_{K^*_{\theta z\_NL}} = \varphi_{K\theta z(\Delta u_{\theta z\_0} = 8\ \mu m)} - \varphi_{K\theta z(\Delta u_{\theta z\_0} = 0\ \mu m)} \quad (4.23)$$

Table 4.11: Interpolated interface stiffness when interface displacement gap is 8 µm ($|K^*_{\theta z}|_{(\Delta u_{\theta z\_0} = 8\ \mu m)}$), extrapolated interface stiffness when interface displacement gap is 0 µm ($|K^*_{\theta z}|_{(\Delta u_{\theta z\_0} = 0\ \mu m)}$), and the effects of nonlinearity on the complex interface stiffness when $\Delta u_{\theta z\_0} = 8\ \mu m$

Sample	$K^*_{\theta z(\Delta u_{\theta z\_0} = 0\ \mu m)}$		$K^*_{\theta z(\Delta u_{\theta z\_0} = 8\ \mu m)}$		Effect of Nonlinearity	
	$\|K^*_{\theta z}\|$ (MPa/mm)	$\varphi_{K^*_{\theta z}}$ (°)	$\|K^*_{\theta z}\|$ (MPa/mm)	$\varphi_{K^*_{\theta z}}$ (°)	$\Delta\|K^*_{\theta z_{NL}}\|$ (%)	$\Delta\varphi_{K^*_{\theta z\_NL}}$ (°)
REFC-1	375.40	23.90	348.03	26.27	-7.29	2.37
REFD-2	465.60	27.02	426.07	28.63	-8.49	1.61
HDO-1	434.41	27.07	405.67	29.22	-6.62	2.15
HDO-2	369.07	27.73	351.24	29.34	-4.83	1.61
HDO-3	411.16	24.54	376.39	26.27	-8.46	1.74
LDO-2	500.13	27.77	452.81	30.46	-9.46	2.69
LDO-3	396.10	31.54	370.90	31.10	-6.36	-0.44
SBS-2	298.90	29.87	289.98	31.06	-2.99	1.20
SBS-3	430.17	28.29	389.44	29.86	-9.47	1.56
				Average:	7.11 % (± 2.05%)	1.86° (± 0.46 %)

From Table 4.11, it can be observed that $\Delta\varphi_{K^*_{\theta z\_NL}}$ for sample LDO-3 is not consistent with those of other samples, that can be errors during measurement. In general, nonlinearity reduces averagely 7.11 % (± 2.05%) of the interface stiffness, and increase averagely 1.86° (± 0.46 %) of phase angle when displacement gap at the interface ($\Delta u_{\theta z\_0}$) is 8 µm (corresponding to 50 µm/m global shear strain). The nonlinear tests were conducted at the temperature of 10 °C, and the frequency of 1 Hz. Under these experimental parameters, the interface behaviour

can be approximated as linear viscoelastic, as is hypothesised for the bituminous mixture. (Di Benedetto et al., 2011).

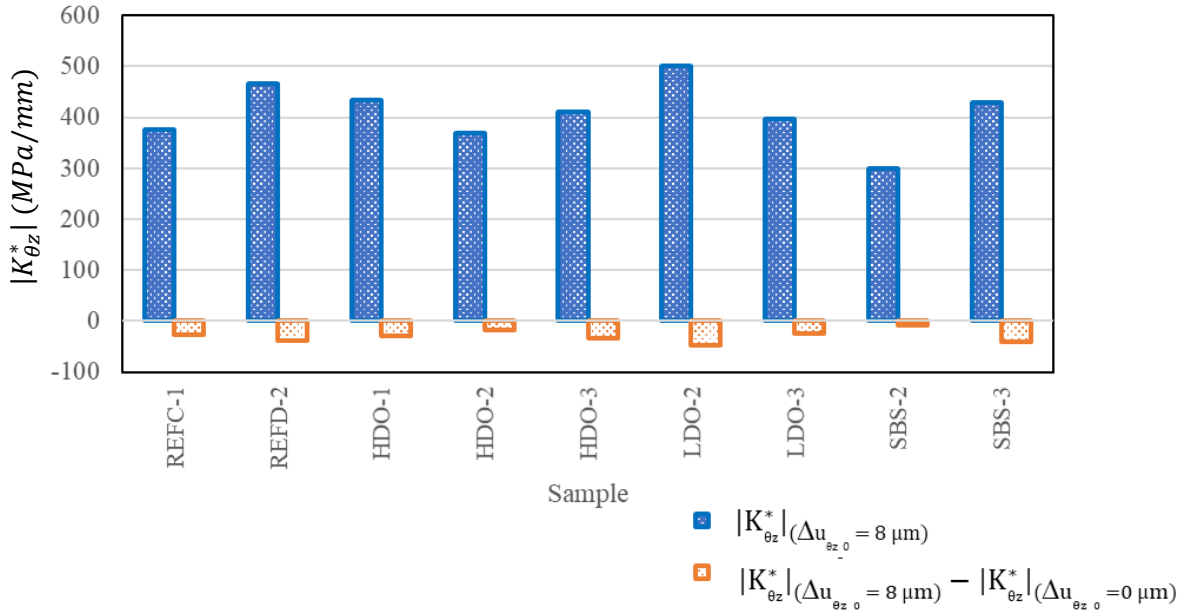

Figure 4.57:The norm of the interpolated complex interface stiffness ($|K^*_{\theta z(\Delta u_{\theta z\_0} = 8\ \mu m)}|$) interpolated when interface displacement gap ($\Delta u_{\theta z\_0}$) is 0 µm (at temperature:10 °C, frequency: 1 Hz), and the deduced reduction of interface stiffness due to nonlinearity ($\Delta|K^*_{\theta z\_NL}|$)

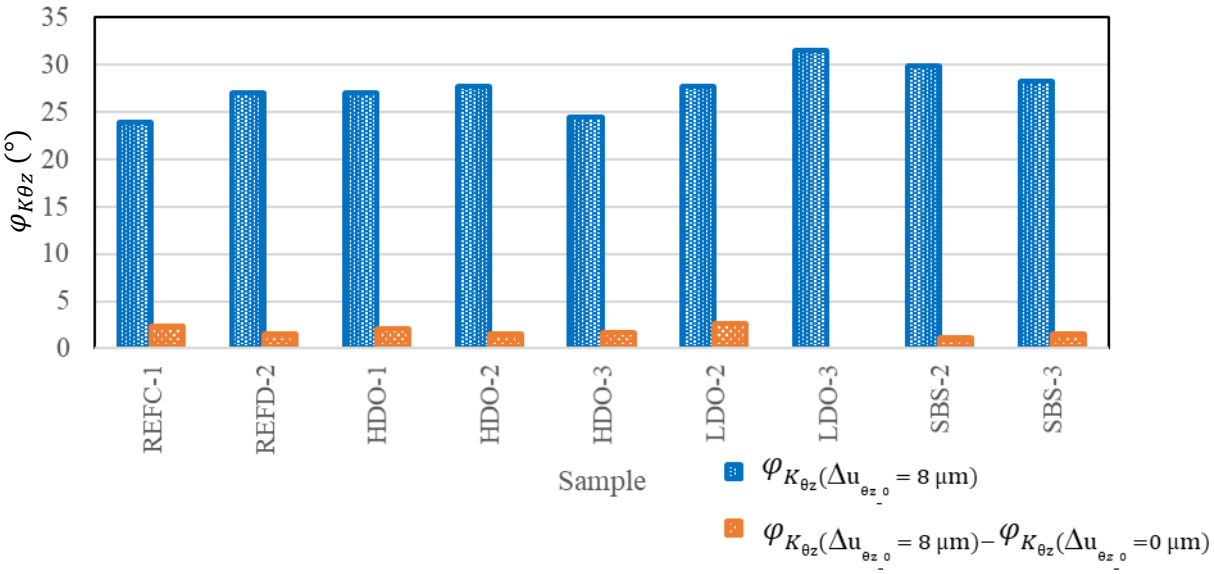

Figure 4.58: The phase angle of the interpolated complex interface stiffness ($|K^*_{\theta z(\Delta u_{\theta z\_0} = 8\ \mu m)}|$) interpolated when interface displacement gap ($\Delta u_{\theta z\_0}$) is 0 µm (at temperature:10 °C, frequency: 1 Hz), and the deduced increase of phase angle due to nonlinearity ($\Delta\varphi_{K^*_{\theta z\_NL}}$)

4.7 Conclusions

The complex shear modulus tests were successfully launched on 20 double-layered hollow cylinders using the 2T3C hollow cylinder apparatus. There are different combinations of loading parameters applied to the samples and there are some conclusions can be made:

For bituminous mixtures, the Time-Temperature Superposition Principle (TTSP) is validated. The LVE 2S2P1D model successfully models the thermomechanical behaviour of bituminous mixtures in layers in different combination of loading the experimental campaign. The mixture in the upper layer (BBSG3) shows more viscous behaviour in the medium temperature, while the aggregates in the mixture of lower layer (EME2) are interlocked better.

For the interfaces, the interfaces show the validation of the TTSP in all test results. For each combination of loading parameters, some behaviours can be observed:

- The global shear strain of 50 µm/m, combined with the axial stress of 0.026 MPa: The interface shown their LVE behaviour, and the LVE 2S2P1D model characterise successfully the thermomechanical of the interfaces.
- The global shear strain of 50 µm/m, combined with three axial stresses of - 0.026 MPa, - 0.125 MPa, and - 0.250 MPa: The interface shown their LVE behaviour, and the LVE 2S2P1D model characterise successfully the thermomechanical of the interfaces. However, the axial shear stresses have influences on the static modulus that is a 2S2P1D parameter used to describe the friction and adhesion of aggregate structure, more specifically the aggregates from two layers at the interfaces. The higher the axial stress is, the higher the static modulus observed.
- The global shear strain of 50 µm/m, combined with the axial stress of - 0.026 MPa on samples with different tack coat contents, and tack coat types: The variation of tack coat contents does not affect to the LVE behaviour of the interfaces. Similarly, the modification has really minor influences on the both the experimental results and LVE modelling.
- The global shear strain of 200 µm/m, combined with the axial stress of - 0.026 MPa: The interface shows plastic dissipation during cyclic test, and that the LVE 2S2P1D model underestimates the phase angle of complex interface stiffness in Black's space and the phase angle master curve. The Visco-Elasto-Plastic model DBN_{PDSC} with the addition of plastic dissipation into spring elements of a generalised Kelvin-Voigt model is introduced. This

model was used to describe the plastic dissipation and overcomes the underestimation for phase angle from an LVE model.

The nonlinearity tests reveal the influence on the complex shear interface stiffness, both in norm and phase angle. The increase of global shear strain amplitude (displacement gap at the interface) reduces norm and increase phase angle of the complex interface stiffness.

Chapter 5: RESULTS OF FATIGUE TESTS

Chapter 5 is devoted to the presentation of the outcomes obtained from fatigue tests. In the first section, the transient effect will be verified in order to confirm the reliability of the fatigue results derived from the suggested experimental procedure. In literature, measurements for the complex modulus on bituminous mixture are recommended to start from the third cycle depending on testing frequency and temperature (Gayte et al., 2016). With a specific testing procedure as described on Chapter 3, it is expected to measure for the complex shear moduli in layers and interface stiffness from the second cycle. After that, the results for fatigue tests at three different global shear strain amplitudes levels (50 µm/m, 150 µm/m, 200 µm/m) will be presented. Fatigue failure was observed exclusively at the interfaces, not within the layers. Six fatigue criteria are proposed to determine the fatigue life of an interface. As mentioned in Chapter 4, the axial stresses may influence the interlock between aggregates at interface, and improve the static modulus K_{00} (a parameter in 2S2P1D modelling). The same levels of axial stresses (-0.026 MPa, -0.125 MPa, -0.250 MPa) will be studied their influences to fatigue behaviour. In addition, there are three more configurations with a higher/lower residual bitumen, and with an SBS modified bitumen at interfaces. The results in Chapter 5 will reveal their effects on fatigue behaviour. Subsequently, the nonlinearity will be taken into consideration for fatigue tests at the interfaces. Finally, the shear fatigue behaviour of bituminous layer will be studied. By looking at the stability in evolutions of complex shear moduli, it is possible to know if a sample are already in failure at the interface.

5.1 Verification of transient effect

The testing procedure for a fatigue test was introduced in the section 3.2.2. Cycles controlled on the global shear strain applied on the samples are performed at 3 Hz during fatigue tests. As it is not possible to use the DIC device at this frequency, three cycles are performed at 1 Hz, regularly, in order to follow the evolution of the complex interface stiffness during fatigue tests. As explained in this section, the reduction of testing frequency is to meet the limitation of cameras frequency. There were three cycles applied in this measuring periods, and two last cycles will be considered for the complex modulus/stiffness calculation. Three cycles are expected to be sufficient to measure the interface stiffness, since the minimum number of cycles for sinusoidal signals approximation is two cycles. Furthermore, using more than three cycles during the measurement can modify interface fatigue behaviour or the bias effects during a continuous fatigue test, such as self-heating. Only two last cycles of the three are considered for calculation, in order to reduce the eventual error due to transient effect. The transient effect was observed at the really beginning of a complex modulus test, that makes the imperfection of

responding sinusoidal signal to the applying sinusoidal signal (Gayte et al., 2016). Gayte et al. propose to eliminate the first three to four cycles in the complex modulus test. However, Nguyen et al. (2019) propose to start the measurement from the second or the third cycle for the nonlinearity test on bitumen using Metravib equipment. The tests launched at four strain levels (2.5%, 5%, 7.5%, 10%), four frequencies (5 Hz, 10 Hz, 25 Hz, 50 Hz), combined with three temperature (10 °C, 30 °C, 50 °C). The transient effect depends on testing conditions such as frequency and temperature. It influences the measurement complex modulus in both norm and phase angle, and has clearer appearance at high frequency and high temperature. Hence, it is imperative to ascertain that the transient impact is negligible during the final two cycles of a three-cycle measurement under the specified loading condition. This section aims to provide information on the quality of recorded sinusoidal signals from a fatigue tests, and the reliability of the calculated data obtained from the cycles 2-3.

Figure 5.1 illustrates a representative instance of two-cycle signals, specifically the displacement gap at the interface and the torque, with the last two cycles being depicted out of the three cycles that were measured. It is evident that the measured signals exhibit sinusoidal characteristics and their approximation demonstrates a high level of accuracy. The fitting quality Q (calculated as Equation 4.8) are 4.44% and 5.76% for the displacement gap at the interface, and for the torque, respectively. They are both inferior to 15% which is the limit for an acceptable approximation.

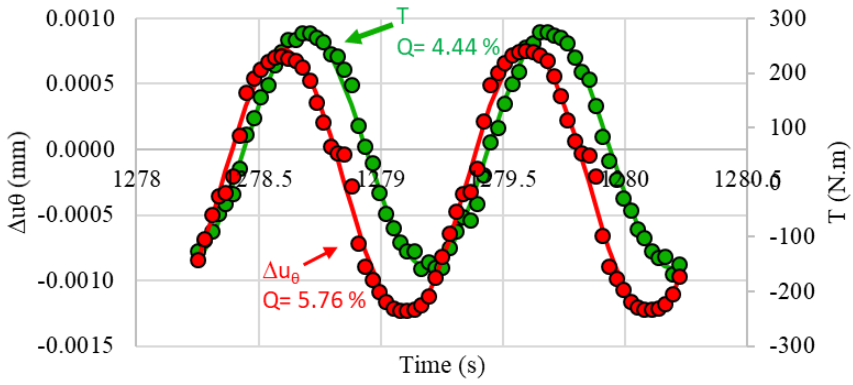

Figure 5.1: Example of two-cycles measurement and approximation using the least square method of displacement gap at the interface (Δu_θ) and Torque (T).

In order to verify that only the last two cycles of each three-cycle measurement could be used, a series of 27 cycles was launched at the fatigue loading conditions. The test was conducted on four samples from four interface configurations including the REF, HDO, LDO, SBS. The complex interface stiffness (norm and phase angle) was evaluated by a couple of two adjacent cycles; for example: cycles 1-2, 2-3, …, 26-27. In addition, the complex shear modulus

(norm and phase angle) in two layers were also calculated by the same strategy. The transient effect is influenced by the testing frequency, temperature. Therefore, this is important to know at the specific fatigue testing condition (f = 1Hz, T = 10°C), how the transient may affect the measurement. Figure 5.2 presents the evolution of the interface stiffness norm across 27 cycles for four different interface configurations. The stability of the norms can be observed in the figure, where it is evident that they remain consistent from the initial two cycles, and even more from the cycles 2-3. To get insight into the variability of the data in relation to the averages, the averaged norm is depicted for four different configurations. It is true that the from the cycles 2-3, the transient effect can be considerably neglected. The same observation can be found for the phase angle of interface stiffness in Figure 5.3. Table 5.1 presents the relative difference for norm ($\Delta|K^*_{\theta z}|_{cycles\ 2-3}(\%)$), and phase angle ($\Delta\varphi_{K\theta z_{cycles\ 2-3}}$) between the values obtained at cycles 2-3 ($|K^*_{\theta z}|_{cycles\ 2-3}$, $\varphi_{K\theta z_{cycles\ 2-3}}$) and the averaged values ($|K^*_{\theta z}|_{averg}$, and $\varphi_{K\theta z_{averg}}$) of all two adjacent cycles comprising 27 cycles. The Equation (4.1), (5.2) shows how to calculate relatively the relative difference of norm and phase angle. The largest relative difference of norm of interface stiffness is 2.34 % recorded for the configuration REFD-2, and the that of the phase angle is 1.49° seen for the sample SBS-3. Therefore, one can say that the transient effect can be negligible from the second cycle when interface stiffness is considered.

$$\Delta|K^*_{\theta z}|_{cycles\ 2-3}(\%) = \frac{|K^*_{\theta z}|_{cycles\ 2-3} - |K^*_{\theta z}|_{averg}}{|K^*_{\theta z}|_{averg}} \tag{5.1}$$

$$\varphi_{K\theta z_{cycles\ 2-3}} = \varphi_{K\theta z_{cycles\ 2-3}} - \varphi_{K\theta z_{averg}} \tag{5.2}$$

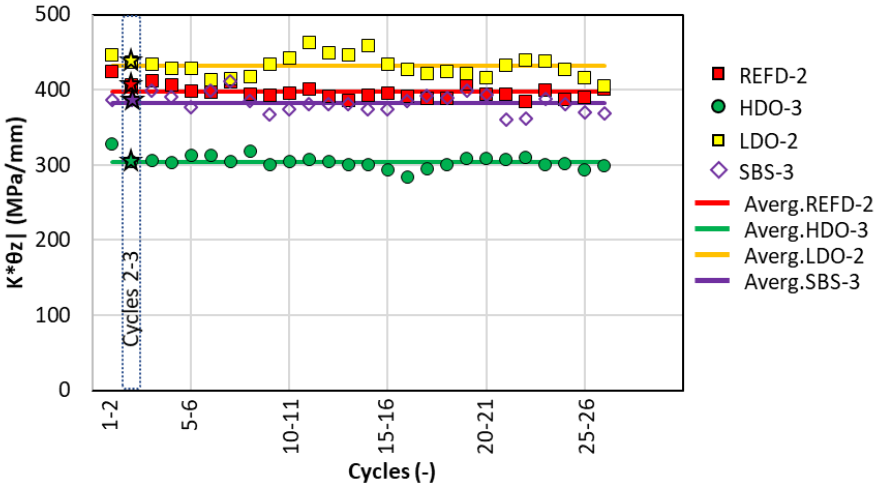

Figure 5.2: The variation of the norm of interface stiffness of four configurations during 27 cycles loaded with 1 Hz, 10 °C, and their averaged lines

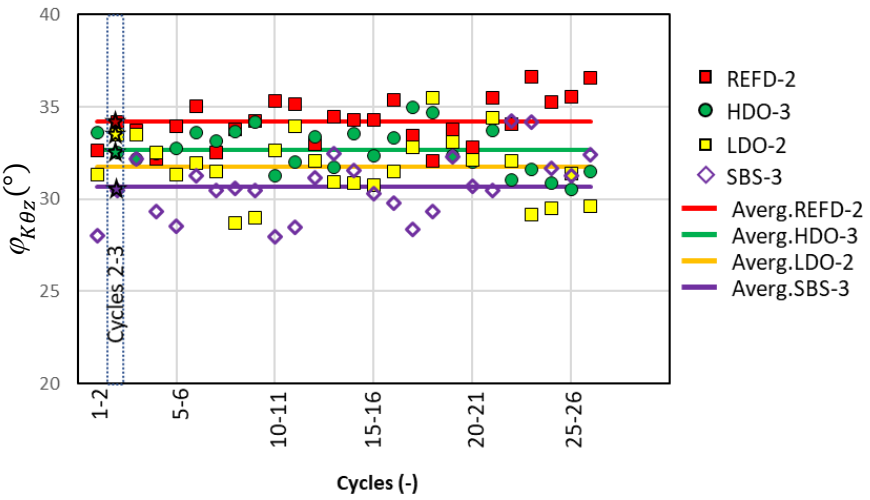

Figure 5.3: The variation of the phase angle of interface stiffness of four configurations during 27 cycles loaded with 1 Hz, 10 °C, and their averaged lines

Figure 5.4 and Figure 5.5 present the evolution of the norm and phase angle of the complex shear moduli of upper layers. The norm and phase angle exhibit stability over the duration of 27 cycles, with some discrepancies. Table 5.1 presents a comparison between the measurements obtained during cycles 2-3 in the upper layer and the corresponding averaged values. The relative difference in norm ($\Delta\left|G^*_{\theta z.up}\right|_{cycles\ 2-3}$) and phase angle ($\Delta\varphi_{G.up,cycles\ 2-3}$) between the values obtained at cycles 2-3 ($\left|G^*_{\theta z.up}\right|_{cycles\ 2-3}$, $\varphi_{G.up,cycles\ 2-3}$) and the averaged values ($\left|G^*_{\theta z.up}\right|_{averg}$, and $\varphi_{G.up,averg}$) of all two adjacent cycles in 27 cycles can be respectively calculated by Equation (5.3), and (5.4). The samples that exhibit the greatest discrepancies in terms of norm are the LDO-2 sample, which shows a relative difference of 3.07%, and the HDO-3 sample, which exhibits a difference of 2.54%. Additionally, upper layers of two other samples display the difference of approximately 0.1%. Sample SBS-3 exhibits the greatest disparity in phase angle, with a magnitude of 1.27°, whereas the remaining samples demonstrate disparities below 1°. Therefore, the measurements obtained during cycles 2-3 can be considered for calculation.

$$\Delta\left|G^*_{\theta z.up}\right|_{cycles\ 2-3}(\%) = \frac{\left|G^*_{\theta z.up}\right|_{cycles\ 2-3} - \left|G^*_{\theta z.up}\right|_{averg}}{\left|G^*_{\theta z.up}\right|_{averg}} \quad (5.3)$$

$$\Delta\varphi_{G.up,cycles\ 2-3} = \varphi_{G.up,cycles\ 2-3} - \varphi_{G.up,averg} \quad (5.4)$$

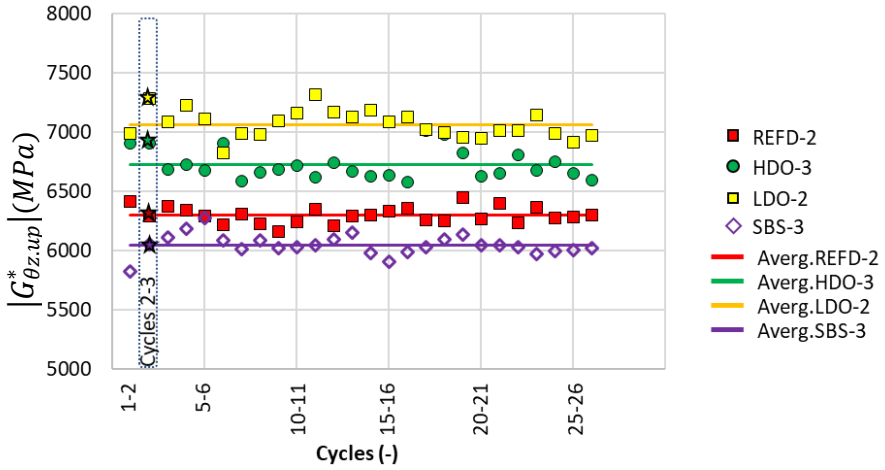

Figure 5.4: The variation of the norm of complex shear moduli of upper layer of four configurations during 27 cycles loaded with 1 Hz, 10 °C, and their averaged lines

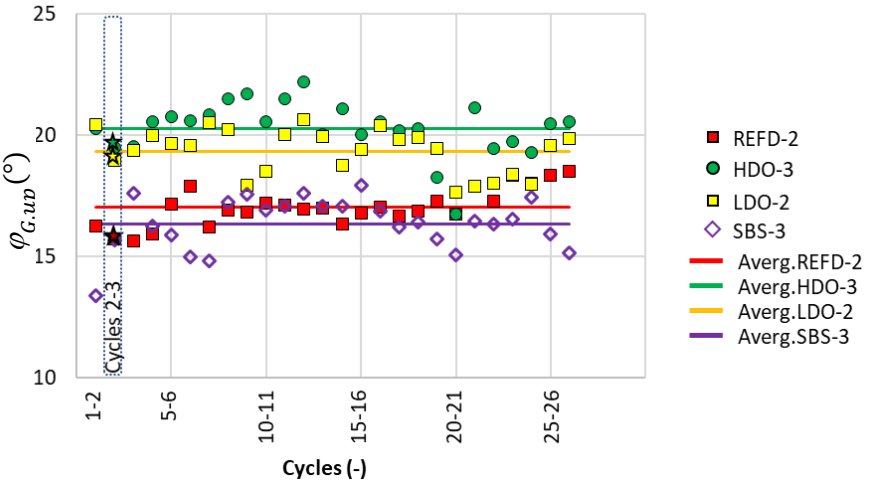

Figure 5.5: The variation of the phase angle of complex shear moduli of upper layer stiffness of four configurations during 27 cycles loaded with 1 Hz, 10 °C, and their averaged lines

Similar to the variation of norm and phase angle of complex shear moduli in the upper layer, those in the lower layer also observe the stability from the first cycle. Their variations are demonstrated on Figure 5.6 and Figure 5.7. The differences of norm and phase angle of complex shear modulus measured at the cycles 2-3 compared with the averaged values are shown on Table 5.1. And the calculation for the relative difference in norm ($\Delta|G^*_{\theta z.up}|_{cycles\ 2-3}$) and phase

angle ($\Delta\varphi_{G.low,cycles\ 2-3}$) are similar to those obtained for the upper layer. It can be said that the measurements at the cycles 2-3 can represent the property of materials.

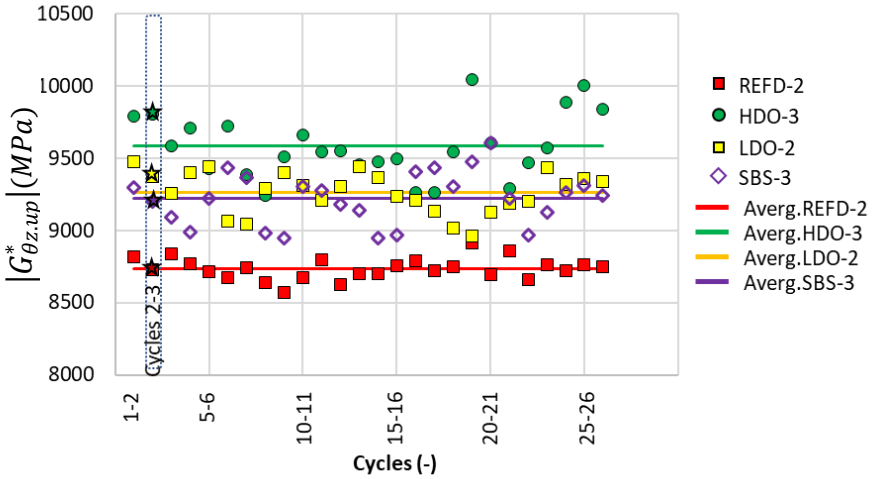

Figure 5.6: The variation of the norm of complex shear moduli of lower layer of four configurations during 27 cycles loaded with 1 Hz, 10 °C, and their averaged lines

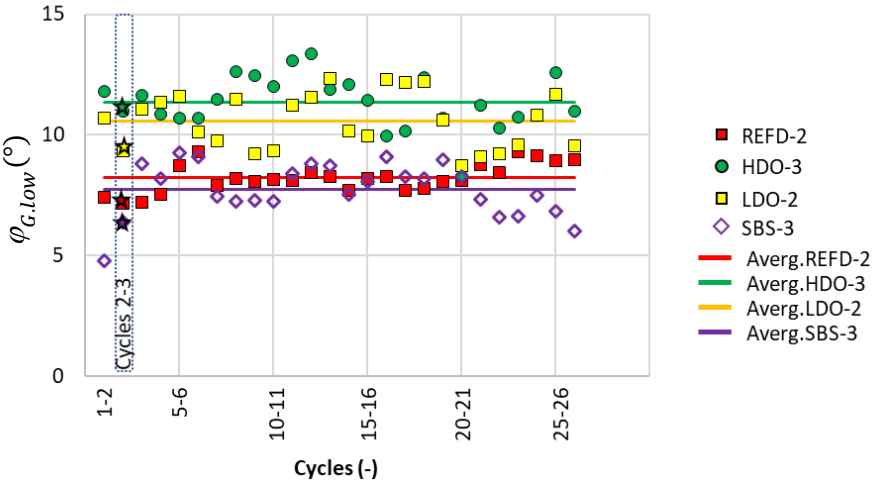

Figure 5.7: The variation of the phase angle of complex shear moduli of lower layer of four configurations during 27 cycles loaded with 1 Hz, 10 °C, and their averaged lines

Table 5.1: The relative difference in norm and phase angle of interface stiffness/complex shear moduli between the cycle 2-3 compared to the averaged value

	Configuration	Relative difference of norm (%)	Relative difference of phase angle (°)
Interface	REFD-2	2.34	0.47
	HDO-3	0.14	0.46
	LDO-2	1.25	1.75
	SBS-3	0.89	1.49
Upper layer	REFD-2	0.16	0.46
	HDO-3	2.64	0.73
	LDO-2	3.07	0.04
	SBS-3	0.11	1.27
Lower layer	REFD-2	0.10	1.00
	HDO-3	2.32	0.29
	LDO-2	1.18	0.49
	SBS-3	0.20	1.08

5.2 The influence of global shear strain amplitudes to the fatigue behaviour of the interface

The impact of global shear strain amplitude on the fatigue behaviour of the interface is examined in this section. Throughout the fatigue tests, the axial loading is kept at a uniform compression of -0.026 MPa across all samples. Three distinct levels of global shear strain amplitudes ($\varepsilon_{\theta zg\_0}$= 50, 150, 200 µm/m) were applied to each of the three samples. The fatigue results for sample REFA-1 (applied global shear strain amplitude $\varepsilon_{\theta zg\_0}$= 200 µm/m), sample REFA-3 ($\varepsilon_{\theta zg\_0}$= 150 µm/m), and sample REFD-2 ($\varepsilon_{\theta zg\_0}$= 50 µm/m) are illustrated in Figure 5.8, Figure 5.9, and Figure 5.10, respectively.

The evolution of the norm of the interface shear stiffness ($|K^*_{\theta z}|$) and the norms of the shear complex moduli of upper layer and lower layer ($\left|G^*_{\theta z.up}\right|$, and $|G^*_{\theta z.low}|$) are depicted in Figure 5.8(a), Figure 5.9(a), and Figure 5.10(a), respectively. The figures illustrate a significant decrease in the interface shear stiffness norm across all fatigue test. The rate of decline is greatest at the beginning of the experiments and diminishes as the number of cycles increases. Depending on the amplitude of the global shear strain amplitude (200, 150, or 50 µm/m), the interface shear stiffness diminishes by 50% of its initial value after 60, 165, or 46830 cycles. The shear moduli norms in both layers do not demonstrate substantial decreases.

In addition, the phase angle of complex moduli in upper and lower layers (respective $\varphi_{G.up}$, $\varphi_{G.low}$) and the evolution of the phase angle of complex interface stiffness ($\varphi_{K\theta z}$) are

illustrated in Figure 5.8(b), Figure 5.9(b), and Figure 5.10(b) throughout the fatigue tests. For the layers, they undergo a brief increase at the start of the tests, followed by a rather stable evolution. On the contrary, for the three examined global strain amplitudes (200, 150, 50 µm/m), the phase angle of complex interface stiffness exhibits an ascending trend during the experiments until it reaches its corresponding apexes (55°, 47°, and 44°). The aforementioned peaks are attained 120, 660, and 163470 cycles in order.

The evolution of the amplitude of the shear strain in upper and lower layers (respective $\varepsilon_{\theta z.\mathrm{up}\_0}$, $\varepsilon_{\theta z.\mathrm{low}\_0}$) and the amplitude of the displacement gap at the interface (Δu_{θ_0}) throughout the experiments for three different global shear strain amplitudes (200, 150, 50 µm/m) is illustrated in Figures Figure 5.8(c)Figure 5.9(c)Figure 5.10(c). In general, the displacement gap at the interface (Δu_{θ_0}) increases continuously, while the strain in the layers ($\varepsilon_{\theta z.\mathrm{up}\_0}$, $\varepsilon_{\theta z.\mathrm{low}\_0}$) decreases. This suggests that the concentrated global shear displacement (u_{θ_g}) occurs at the interface as the number of cycles increases. Additionally, there are two periods of growth observed in the evolution of the displacement gap amplitude at the interface (Δu_{θ_0}) of a sample performed with either 150 or 50 µm/m global shear strain. The second period of evolution is characterised by a steeper slope along two distinct linear regression lines. The number of cycles at which the two linear lines intersect is denoted by $N_{\mathrm{fslp.}\Delta u}$. Table 5.2 will contain the outcomes of the $N_{\mathrm{fslp.}\Delta u}$.

The evolution of dissipated energy at the interfaces throughout the fatigue tests is illustrated in Figure 5.8(d)Figure 5.9(d)Figure 5.10(d). Equation (*5.5*) determines the dissipated energy per interface surface unity (W_i) for the i^{th} loading cycle.

$$W_i = \pi \tau_{\theta \mathrm{z}\_0i} \Delta u_{\theta\_0i} \sin(\varphi_{K\theta z\_i}) \tag{5.5}$$

Where $\tau_{\theta \mathrm{z}\_0i}$ is the shear stress amplitude at cycle *i* (MPa), Δu_{θ_0i} is the displacement gap amplitude at cycle *i* (mm) and $\varphi_{K\theta z\_i}$ the phase lag at cycle *i*.

Data indicate that the dissipated energy per cycle experiences an initial increase, culminates in a peak value, and subsequently declines precipitously. The maximum dissipated energy occurs after a specified number of cycles: 30, 930, and 199920 cycles for samples subjected to 200, 150, and 50 µm/m, respectively. The data presented in the figures indicates that the dissipated energy (W) of samples subjected to 150 and 50 µm/m global shear strain experiences two distinct phases of growth. Two linear regression lines delineate the two periods of evolution, wherein the slope of the line representing the second period is greater. The number of cycles at which the two regression lines intersect is denoted by $N_{\mathrm{fslp.W}}$. The shear stress amplitude ($\tau_{\theta \mathrm{z}\_0}$) also undergoes two distinct phases of evolution, as depicted in the same

figures. The number of cycles at which the two linear regression lines intersect is denoted by $N_{fslp.\tau\theta z}$. $N_{fslp.W}$ and $N_{fslp.\tau\theta z}$ are detailed in Table 5.2.

Overall, the amplitudes of the dissipated energy (W_i), the displacement gap amplitude at the interface (Δu_{θ_0}), and the shear stress amplitude ($\tau_{\theta z\_0}$) exhibit two-stage evolutions. Further analysis reveals that the outcomes pertaining to $N_{fslp.\Delta u}$, $N_{fslp.W}$, and $N_{fslp.\tau\theta z}$ are remarkably comparable. Consequently, it is reasonable to hypothesise that material behaviour changes during the transitional zone between two phases.

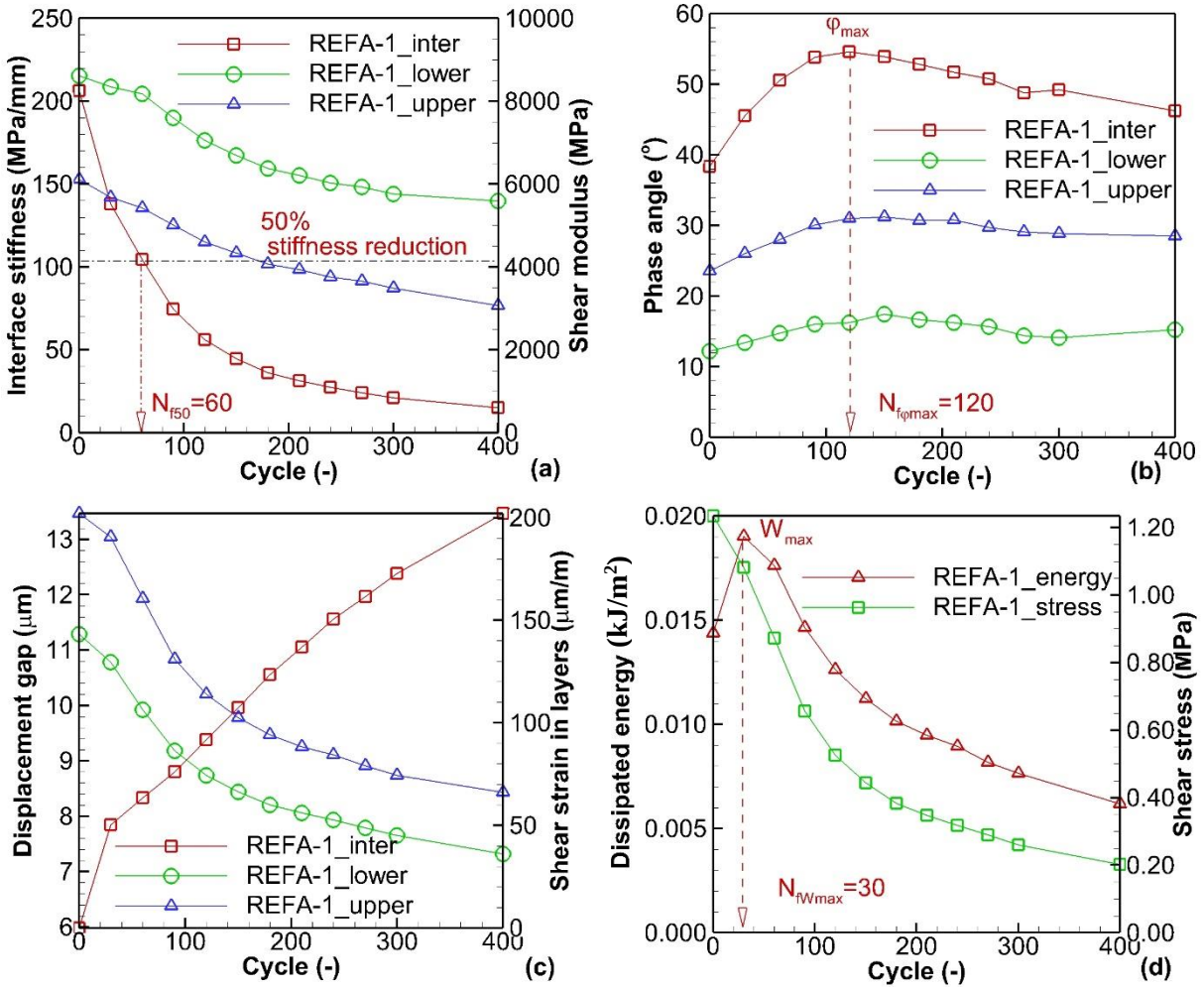

Figure 5.8: Fatigue test results for sample REFA-1 tested with $\varepsilon_{\theta zg\_0}$= 200 μm/m: (a) norm of interface shear stiffness ($|K^*_{\theta z}|$), and of complex shear moduli of upper and lower layers ($|G^*_{\theta z.up}|$, and$|G^*_{\theta z.low}|$(b) phase angle of interface complex shear stiffness ($\varphi_{K\theta z}$), and of complex shear moduli of layers ($\varphi_{G.up}$, $\varphi_{G.low}$); (c) amplitude of displacement gap at the interface (Δu_{θ_0}) and shear strains in layers ($\varepsilon_{\theta z.up\_0}$, $\varepsilon_{\theta z.low\_0}$), (d) dissipated energy at the interface (W) and shear stress amplitude ($\tau_{\theta z\_0}$)

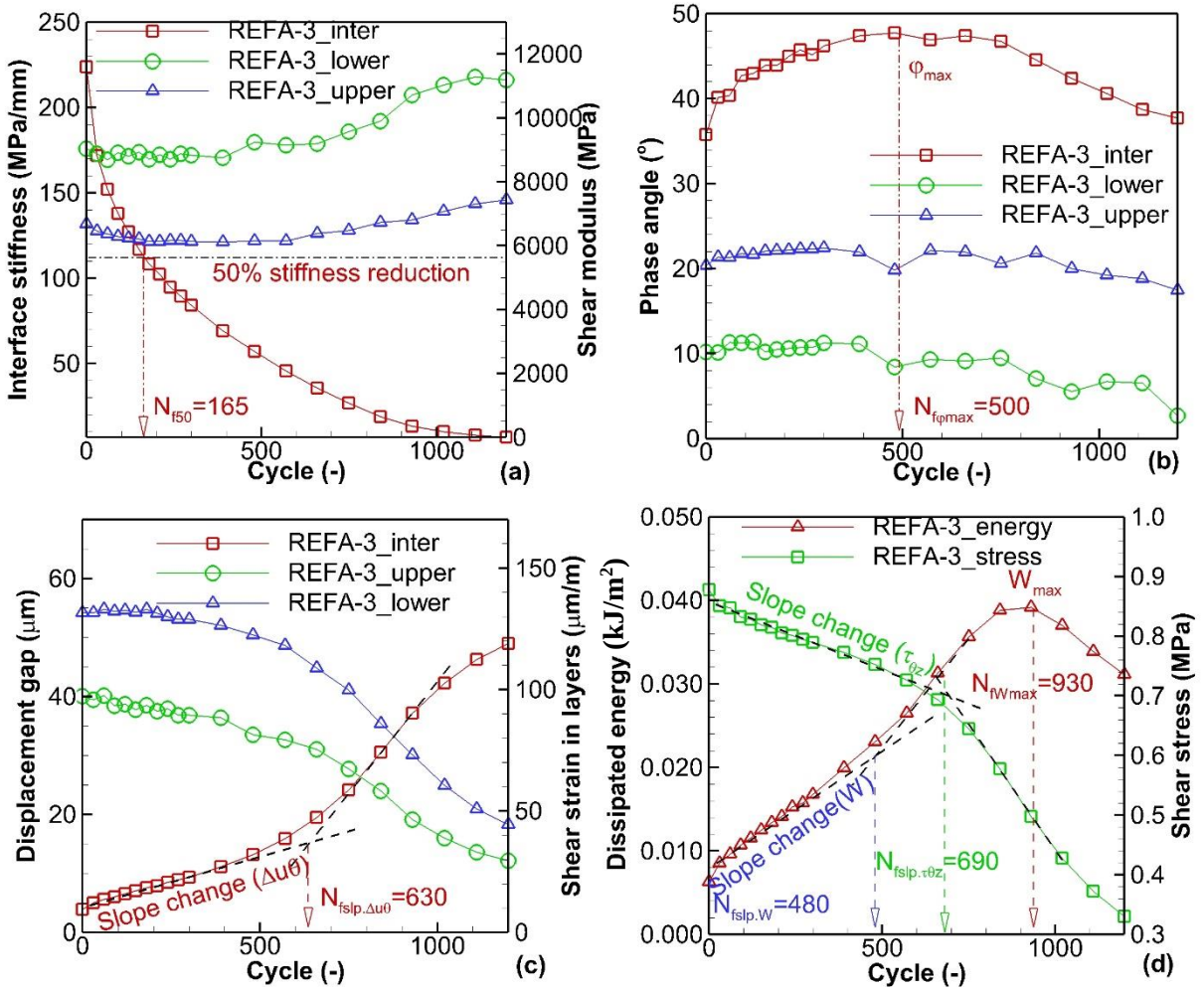

Figure 5.9: Fatigue test results for sample REFA-3 tested with $\varepsilon_{\theta zg\_0}$= 150 μm/m: (a) norm of interface shear stiffness ($|K^*_{\theta z}|$), and of complex shear moduli of upper and lower layers ($|G^*_{\theta z.up}|$, and$|G^*_{\theta z.low}|$(b) phase angle of interface complex shear stiffness ($\varphi_{K\theta z}$), and of complex shear moduli of layers ($\varphi_{G.up}$, $\varphi_{G.low}$); (c) amplitude of displacement gap at the interface (Δu_{θ_0}) and shear strains in layers ($\varepsilon_{\theta z.up\_0}, \varepsilon_{\theta z.low\_0}$), (d) dissipated energy at the interface (W) and shear stress amplitude ($\tau_{\theta z\_0}$)

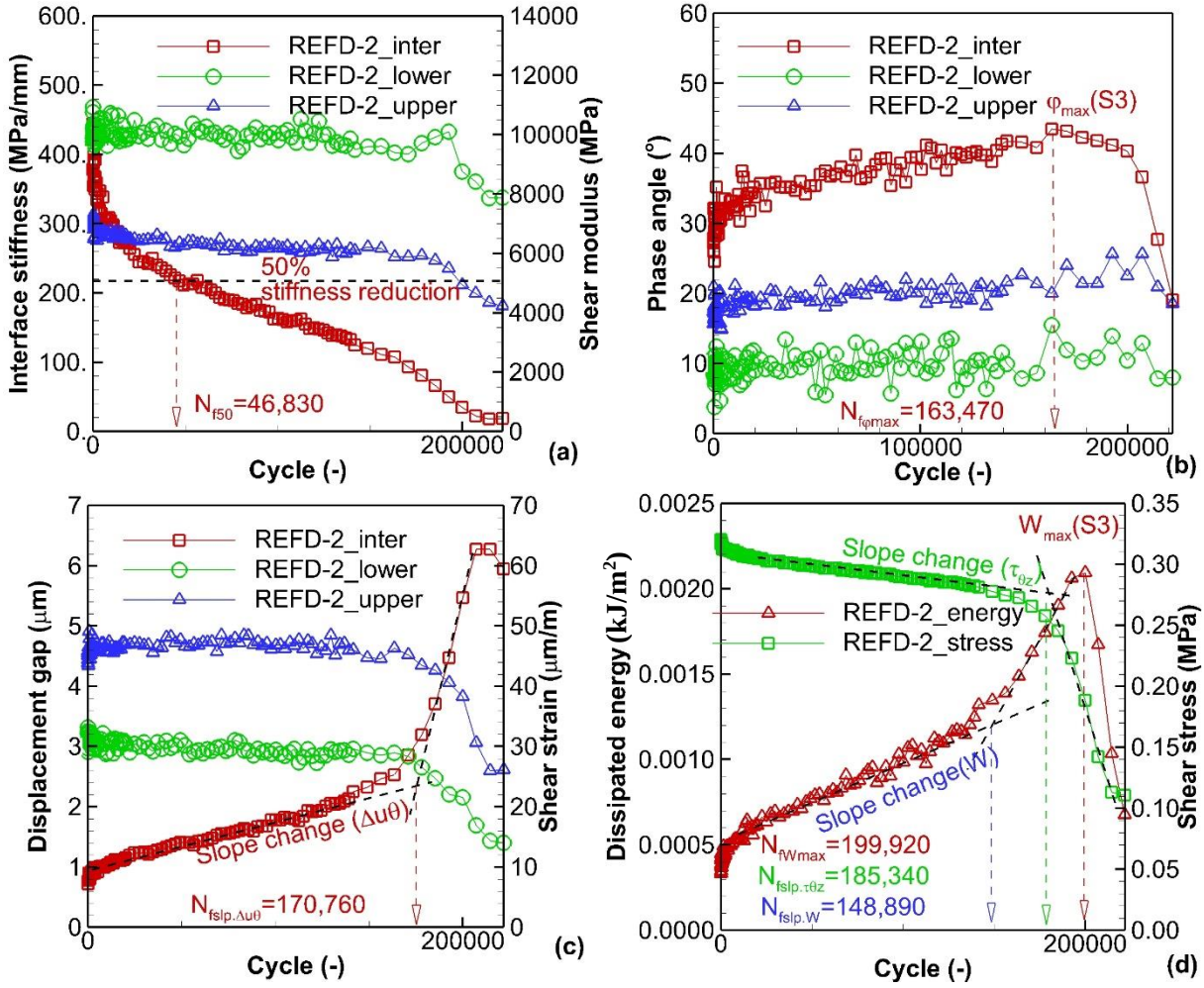

Figure 5.10: Fatigue test results for sample REFD-2 tested with $\varepsilon_{\theta zg\_0}$= 50 µm/m: (a) norm of interface shear stiffness ($|K^*_{\theta z}|$), and of complex shear moduli of upper and lower layers ($|G^*_{\theta z.up}|$, and$|G^*_{\theta z.low}|$(b) phase angle of interface complex shear stiffness ($\varphi_{K\theta z}$), and of complex shear moduli of layers ($\varphi_{G.up}$, $\varphi_{G.low}$); (c) amplitude of displacement gap at the interface (Δu_{θ_0}) and shear strains in layers ($\varepsilon_{\theta z.up\_0}, \varepsilon_{\theta z.low\_0}$), (d) dissipated energy at the interface (W) and shear stress amplitude ($\tau_{\theta z\_0}$)

5.2.1 Repeatability of the 2T3C hollow cylinder fatigue tests

To assess the test's repeatability, three replicates (REFD-2, REFB-1, and REFA-2) underwent testing under a global shear strain of 50 µm/m. Within this particular section, the fatigue characteristics of the interface are the focal point of the reproduction capacity test. The evolution of normalised interface stiffnesses for three samples (REFD-2, REFB-1, and REFA-2) is illustrated in Figure 5.11. Furthermore, the initial interface stiffness norms for each are as follows: 431 MPa/mm, 384 MPa/mm, and 324 MPa/mm. All three curves exhibit a consistent rate of reduction and nearly superimpose until they reach a stiffness decrease of 70-80 %. In

order to achieve a 50 % reduction in interface stiffness (N_{f50}), the corresponding cycles for the three samples (REFD-2, REFB-1, and REFA-2) are 46,830, 56,550, and 39,540, respectively.

The phase angle evolution of complex interface stiffness for three samples (REFD-2, REFB-1, and REFA-2) is illustrated in Figure 5.12. The number of cycles at which the phase angles reach their maximum values ($N_{f\varphi max}$) for samples REFD-2, REFB-1, and REFA-2 are 163470, 124590, and 221790 cycles, respectively, and the curves are close together. The evolution of dissipated energy (W) at the interface throughout the fatigue tests is depicted in Figure 5.13. At beginning of the experiments, the dissipated energy steadily increases until it reaches its maximum value. N_{fWmax} is the number of cycles at which the maximal dissipated energy is observed, which is comparable to the value obtained from phase angle curves. The explanation can be found in Equation (*5.5*), in which $\sin(\varphi_{K\theta z})$ significantly contributes. The numbers of cycles for the sample REFD-2, REFB-1, and REFA-2 are as follows: 199920, 114870, and 221790, respectively. Subsequently, displacement gap at the interface of the three samples are presented in Figure 5.14. The number of cycles at which there are slope changes in the displacement gap evolution curves are 170760, 127020, and 207210, respectively for the sample REFD-2, REFB-1, and REFA-2.

The proposed fatigue testing method and the 2T3C hollow cylinder apparatus enable extremely repeatable outcomes with regard to the evolution of interface stiffness norm, phase angle, and dissipated energy. A summary of the results for each sample examined is presented in Table 5.2.

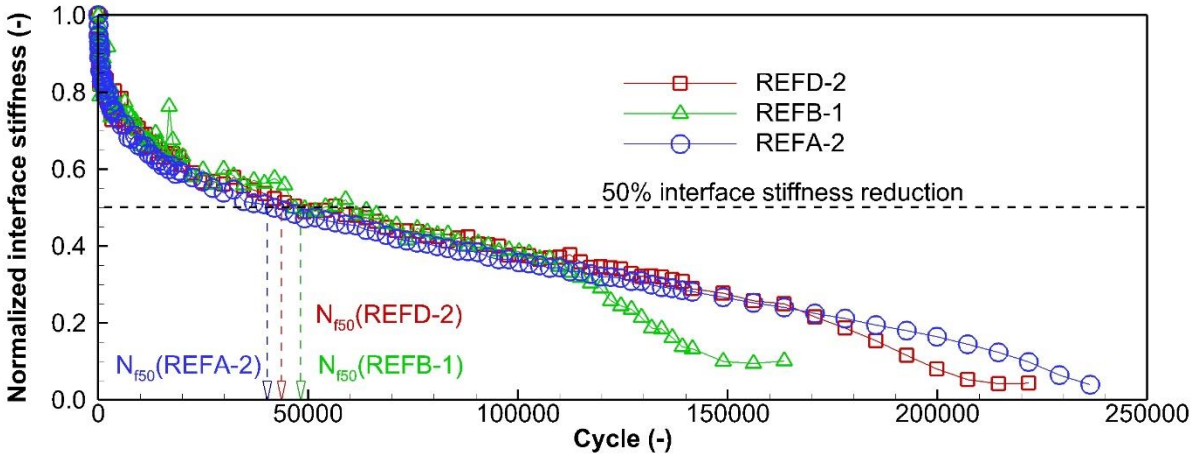

Figure 5.11: Evolution of normalized interface stiffnesses during fatigue tests of three samples REFD-2, REFB-1, REFA-2 tested with $\varepsilon_{\theta zg\_0} = 50\mu m/m$

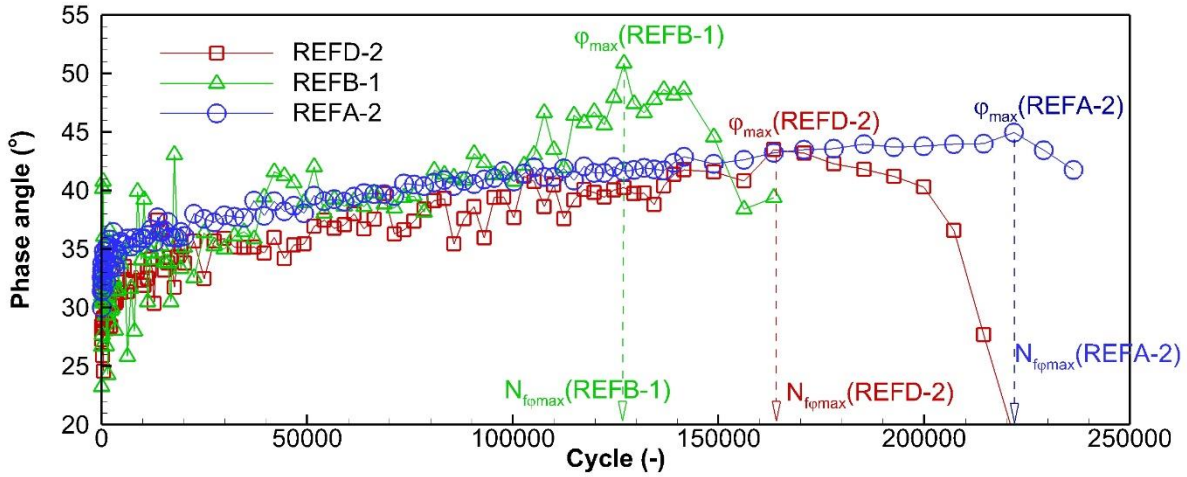

Figure 5.12: Evolution of phase angle of interface stiffnesses during fatigue tests of three samples REFD-2, REFB-1, REFA-2 tested with $\varepsilon_{\theta zg\_0} = 50\mu m/m$

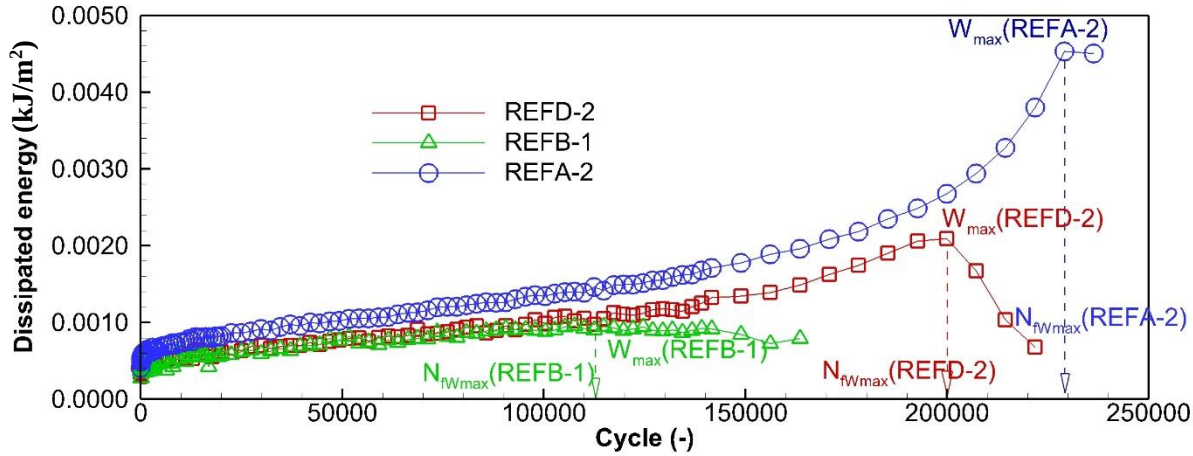

Figure 5.13: Evolution of dissipated energy at interfaces during fatigue tests of three samples REFD-2, REFB-1, REFA-2 tested with $\varepsilon_{\theta zg\_0} = 50\mu m/m$

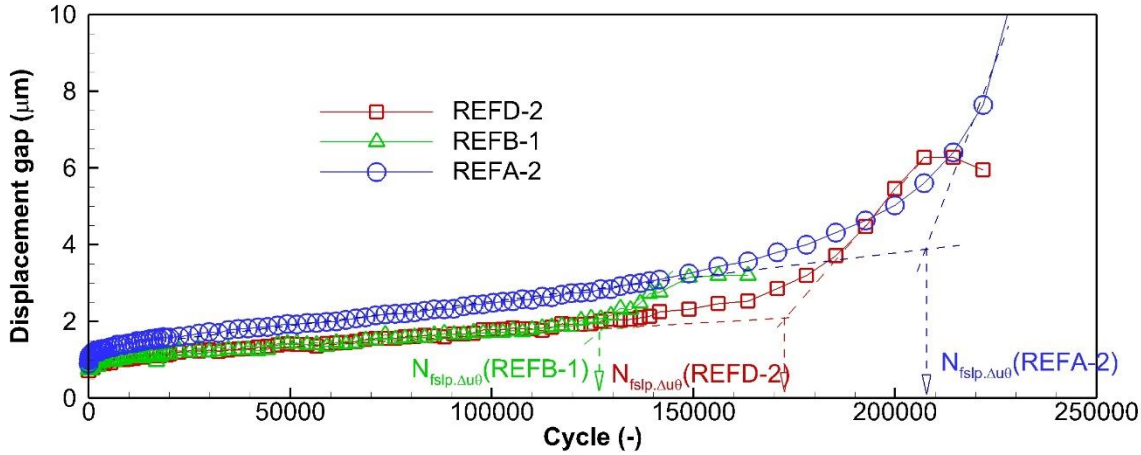

Figure 5.14: Evolution of displacement gap at interfaces during fatigue tests of three samples REFD-2, REFB-1, REFA-2 tested with $\varepsilon_{\theta zg\_0} = 50\mu m/m$

5.2.2 Fatigue life criteria for the interface

Based on the observations made on the five samples that were tested, fatigue failure is observed to occur at the interface as opposed to within the layers. Six criteria are proposed here for assessing the fatigue life of an interface based on criteria found in literature for mixtures (Di Benedetto et al., 2004; Tapsoba et al., 2013), and for interface (Isailović et al., 2017; Isailović & Wistuba, 2018; Ragni, Takarli, et al., 2020) : (1) the 50% reduction of stiffness criterion (N_{f50}); (2) the maximal phase angle criterion ($N_{f\varphi max}$), (3) maximal dissipated energy (N_{fWmax}) criterion , (4) slope change in the dissipated energy evolution curve ($N_{fslp.W}$) criterion, (5) slope change in the stress evolution curve ($N_{fslp.\tau\theta z}$) criterion, and (6) slope change in the displacement gap at the interface evolution curve ($N_{fslp.\Delta u\theta}$) criterion.

Wohler's fatigue lines can be deduced from fatigue tests performed at different strain amplitudes. Equation (5.6) represents a general Wohler's law with two parameters ε_6 and a2. ε_6 denotes the strain amplitude at which a material has accumulated 10^6 cycles of fatigue life, and a_2 represents the slope in the logarithmic Log ε_0 – Log N_f diagram (Di Benedetto et al., 2023). The number at failure N_f is expressed as function of the strain amplitude (ε_0):

$$N_f = 10^6 \left(\frac{\varepsilon_0}{\varepsilon_6}\right)^{-a_2} \quad (5.6)$$

Based on the fatigue failure observed at the interface and the utilisation of global shear displacement ($\varepsilon_{\theta zg\_0}$)) to monitor the fatigue tests in the 2T3C hollow cylinder apparatus, the controlled strain (ε_0) in the general Wohler's law can be adapted as the initial displacement gap at the interface (Δu_{θ_0}) for results obtained from the 2T3C hollow cylinder apparatus. It should be highlighted that the Δu_{θ_0} is not constant during a fatigue test, while ε_0 is. Moreover, ε_6 can be substituted with Δu_{θ_6}, which represents the initial displacement gap at the interface and yields a fatigue life of 10^6 cycles, respectively. In the Log Δu_{θ_0} – Log N_f diagram, a_2 represents the slope. Regarding this investigation, equation (5.7) can be derived from equation (5.6):

$$N_f = 10^6 \left(\frac{\Delta u_{\theta\_0}}{\Delta u_{\theta\_6}}\right)^{-a_2} \quad (5.7)$$

Using the six criteria, Table 5.2 displays the quantity of cycles that result in fatigue failure for each of the five samples. The number of fatigue tests is few to build Wohler's lines,

but it is a first attempt of fatigue analyse. Following this, the six Wohler's lines are utilised to graph this data in Figure 5.15. The parameters for Wohler's law are presented in Table 5.3 (a_2, Δu_{θ_6}). N_{f50} fatigue criterion is observed to be more conservative, indicating that when the other fatigue criteria are implemented, the fatigue lives of the double-layered hollow cylinder samples are prolonged. Moreover, fatigue lives determined using criteria derived from the maximal phase angle and slope-changing approaches yield results that are remarkably comparable. In comparison to the other criteria, the Wohler's law parameters (a_2, Δu_{θ_6}) for the maximum dissipated energy are greater. The slopes a_2 of fatigue curves found here (in a range of 3.34 – 3.52) are reasonable compared with those found in literature for bitumen. Sybilski et al. (2009) launched fatigue tests on three bitumen with similar stiffnesses (around 50 MPa at 10 Hz, and 10 °C) at 10 °C, 10 Hz, and three controlled shear strain levels (2.5 %, 1.8 %, 0.8 %). The authors found a_2 are in the range of 2.74 to 4.98.

Table 5.2: Fatigue lives at the interface loaded with three different global shear strain $\varepsilon_{\theta zg\_0}$ according to six proposed different fatigue criteria

Sample	Global shear strain $\varepsilon_{\theta zg\_0}$ (µm/m)	Initial displacement gap at interface Δu_{θ_0} (µm)	Number of cycles until failure according to six fatigue criteria (-)					
			50 % reduction of stiffness N_{f50}	Maximal phase angle $N_{f\varphi max}$	Maximal dissipated energy N_{fWmax}	Slope change in dissipated energy curve $N_{fslp.W}$	Slope change in stress curve $N_{fslp.\tau\theta z}$	Slope change in displacement gap curve $N_{fslp.\Delta u\theta}$
REFA-1	200	5.981	60	120	30	n/a	n/a	n/a
REFA-3	150	3.923	165	660	930	480	690	630
REFA-2	50	0.985	39,540	221,790	229,080	185,340	214,550	207,210
REFB-1	50	0.768	56,550	124,590	114,870	112,440	105,150	127,020
REFD-2	50	0.718	46,830	163,470	199,920	148,890	185,340	170,760

Table 5.3: Wöhler's law parameters for six proposed fatigue criteria

Wöhler's law	Parameter	Six fatigue criteria (-)					
		50 % reduction of stiffness	Maximal phase angle	Maximal dissipated energy	Slope change in dissipated energy curve	Slope change in stress curve	Slope change in displacement gap curve
$N_f = 10^6 \left(\frac{\Delta u_{\theta\_0}}{\Delta u_{\theta\_6}}\right)^{-a_2}$	a_2	3.397	3.521	3.927	3.504	3.339	3.414
	Δu_{θ_6} (µm)	0.327	0.484	0.526	0.464	0.465	0.474

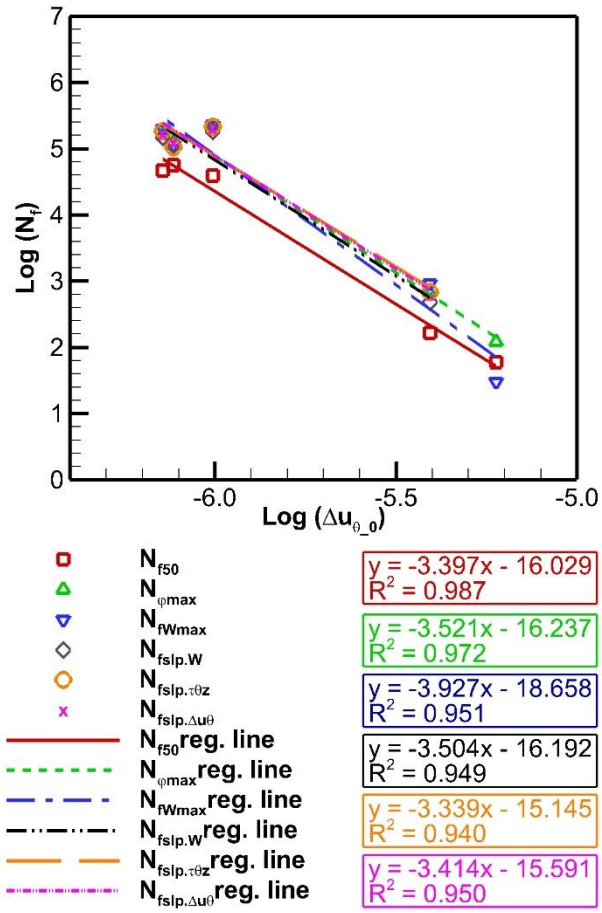

Figure 5.15: Fatigue curves from six fatigue criteria for the five samples tested with three different global strains 50, 150 and 200 µm/m presenting the fatigue law in Log Δu_{θ_0} – Log N_f diagram

5.3 The influence of axial loadings to shear fatigue behaviour of the interface

In order to investigate the influence of different axial loadings to shear fatigue behaviour of the interface, seven samples from the reference configuration (REF) were tested with the same global shear strain ($\varepsilon_{\theta zg\_0}$ = 50 µm/m) and three different axial loadings (σ_{zz}). Three of them were introduced in the section 5.2, with the axial stress amplitude of (σ_{zz}) -0.026 MPa. This axial stress is quite small and used to kept sample slightly in axial compression while shearing. Two other axial stresses (σ_{zz}) -0.125 MPa, and -0.250 (MPa) were imposed. Figure 5.16 illustrates the evolution of the normalised interface stiffness for each of the seven samples. At all levels of axial loading, the outcomes of the fatigue test indicate a very good repeatability. Throughout the results, the samples loaded with the higher axial stresses perform better in the fatigue tests. Considering the classical fatigue criterion of 50% stiffness reduction, the interface loaded with the constant -0.250 MPa axial stress shown the longest fatigue life of over 200000 cycles. While those loaded with the compression of -0.026 MPa withstand the repeated loading

during around 40000 cycles, before reaching the 50% reduction of interface stiffness. Details of their fatigue lives are demonstrated on Table 5.5. The results agree well with the those from a study of Isailović et al. (2017). The authors applied shear fatigue tests at the same shear strain amplitude for all samples, while maintaining three different axial stresses (0 MPa, 0.25 MPa, and 0.5 MPa). The better fatigue lives were observed from samples loaded with higher axial stresses. This can be explained by the better interlocking between aggregates at the interface when higher axial loading is applied. This complies with the observation for static modulus K_0 simulated with the LVE 2S2P1D model. In the chapter 4, the static moduli of samples tested with higher axial stress are higher than those tested with lower ones. It is convinced to say that the interlock between aggregates play a role in fatigue endurance of interface between two bituminous layers.

The evolution of phase angle of interface stiffness during fatigue tests are introduced on Figure 5.17. Figure 5.17 (a) shows the results for the samples REFC-1, and REFC-2 tested with the axial stress of -0.125 MPa, while Figure 5.17 (b) presents these for the samples REFB-2 and REFD-1 loaded with the axial stress of -0.250 MPa. The maximal phase angle cannot be witnessed in these tests applying high axial stresses. The phase angle keeps increasing when the tests go on and until they are finished. The results for phase angle are well repeated for samples tested with same testing parameters. Therefore, the maximal phase angle criterion cannot be considered in this evaluation, and this criterion can be applied with interface loaded with a small axial stress (for example σ_{zz}= -0.026 MPa).

Figure 5.18 (a) shows the evolution of dissipated energy calculated for two samples tested with the axial stress of -0.125 MPa. Results show that dissipated energy increases more and more until it reaches a peak. It was also observed in the evolution curves of samples tested with the really small axial stress (σ_{zz}= -0.026). However, they cannot be seen in the dissipated energy evolution curves for samples tested with the axial stress of -0.250 MPa. Therefore, the maximal dissipated energy criterion can be used for samples tested with the axial stresses of -0.026 MPa, and -0.125 MPa. Details of their fatigue lives according to the dissipated energy criteria can be found on Table 5.5.

Figure 5.19 demonstrates the evolution of displacement gap at the interface of two samples REFC-1 and REFC-2 tested with σ_{zz}= -0.125 MPa (a), and (b) two samples REFB-2 and REFD-1 tested with σ_{zz}= -0.250 MPa. It can be seen that the displacement gap evolution in two samples tested with σ_{zz}= -0.125 MPa has the change in slope which cannot be seen the two tested with σ_{zz}= -0.250 MPa. Figure 5.20 (a) and (b) shows the evolutions shear stresses during

the fatigue tests in those samples. The similar slope change is also observed in stress evolutions. The fatigue lives of interfaces considering the criteria of displacement gap and shear stress are listed on Table 5.5.

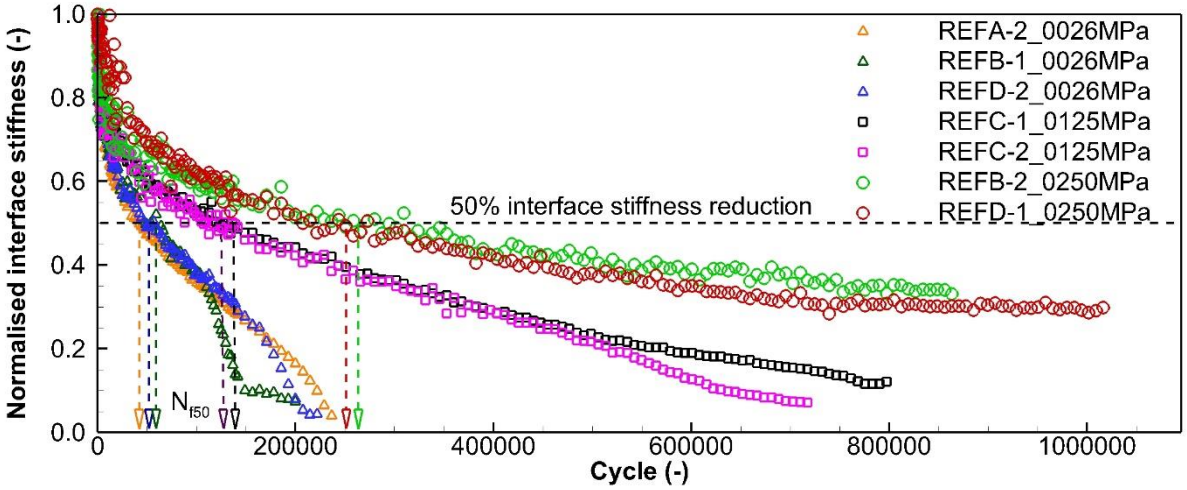

Figure 5.16: Evolution of normalized interface stiffnesses during fatigue tests of seven samples tested with $\varepsilon_{\theta zg\_0}$= 50µm/m, three different axial stress σ_{zz}= -0.026, -0.125, -0.250 MPa

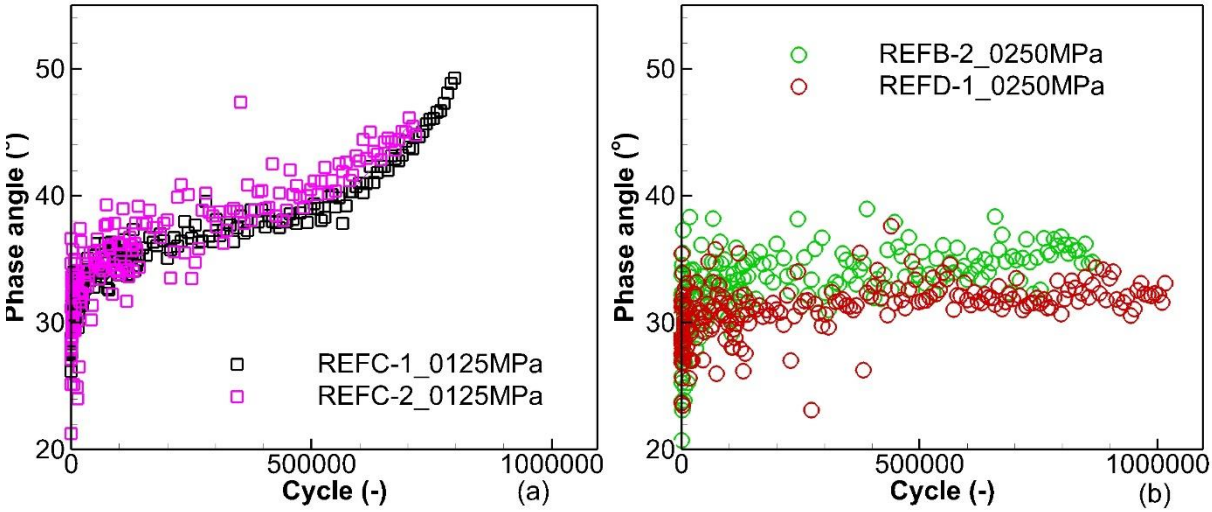

Figure 5.17: Evolution of phase angle of interface stiffnesses during fatigue tests of (a) two samples REFC-1 and REFC-2 tested with σ_{zz}= -0.125 MPa, (b) two samples REFB-2 and REFD-1 tested with σ_{zz}= -0.250 MPa

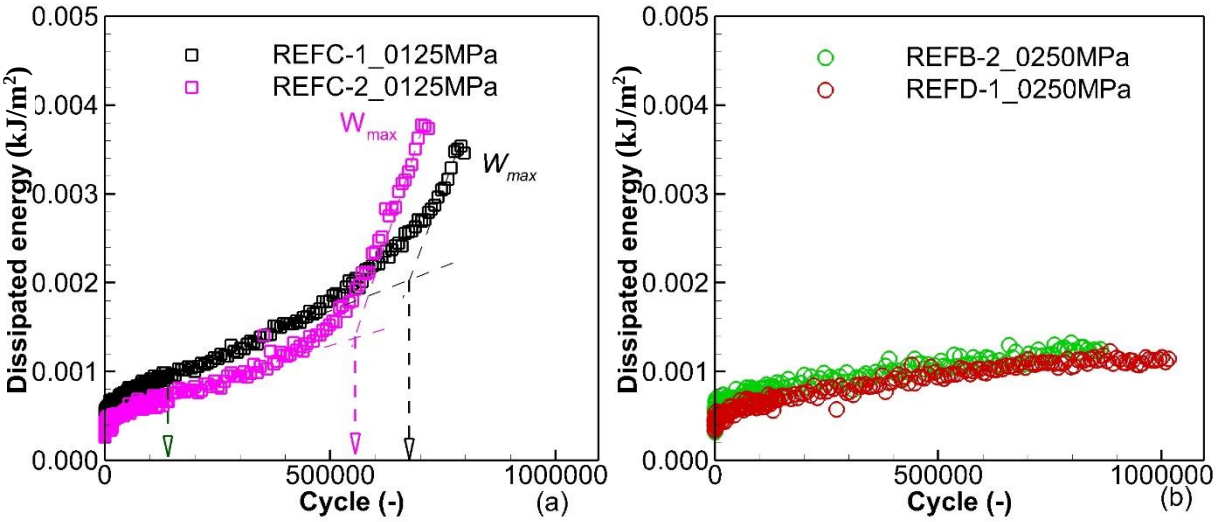

Figure 5.18: Evolution of dissipated energy during fatigue tests of (a) two samples REFC-1 and REFC-2 tested with σ_{zz}= -0.125 MPa, (b) two samples REFB-2 and REFD-1 tested with σ_{zz}= -0.250 MPa

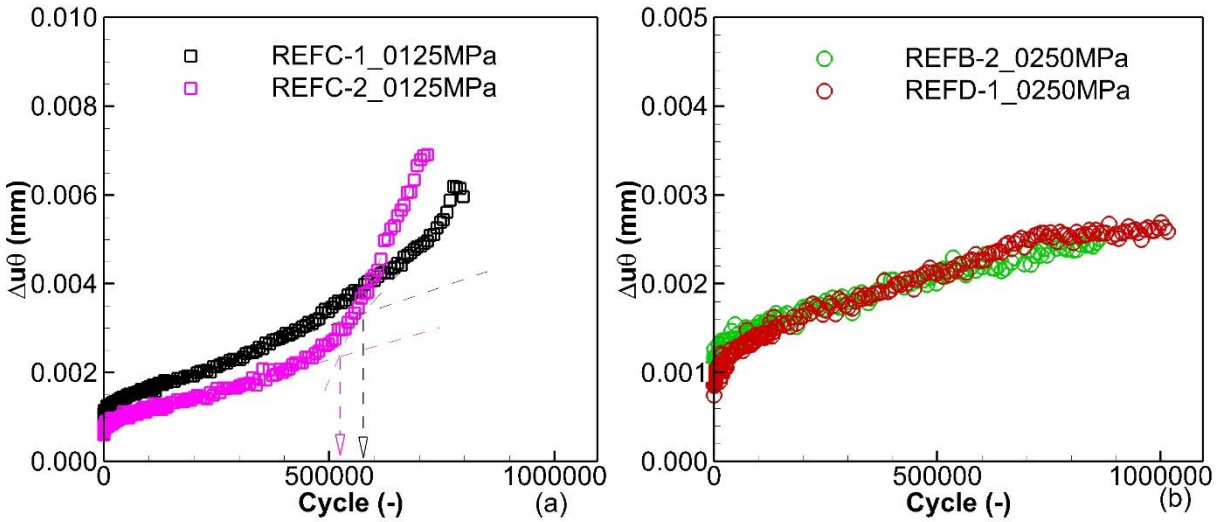

Figure 5.19: Evolution of displacement gap at the interface during fatigue tests of (a) two samples REFC-1 and REFC-2 tested with σ_{zz}= -0.125 MPa, (b) two samples REFB-2 and REFD-1 tested with σ_{zz}= -0.250 MPa

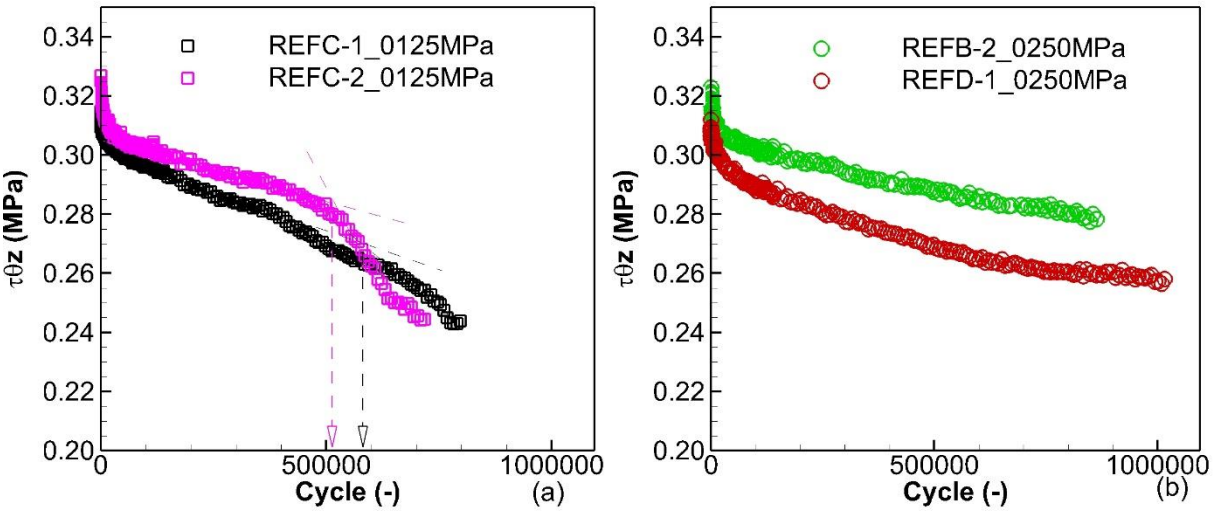

Figure 5.20: Evolution of shear stress during fatigue tests of (a) two samples REFC-1 and REFC-2 tested with σ_{zz} = -0.125 MPa, (b) two samples REFB-2 and REFD-1 tested with σ_{zz} = -0.250 MPa

5.4 The influence of residual emulsified-bitumen doses to shear fatigue behaviour of the interface

To examine the impact of dosages of residual bitumen on the fatigue behaviour of the interface, five additional samples containing two distinct residual bituminous dosages at the interface were tested alongside the reference samples with σ_{zz}= -0.026 MPa and $\varepsilon_{\theta zg\_0}$ = 50µm/m. A total of three concentrations, namely 250 g/m2 (LDO), 350 g/m2 (REF), and 450 g/m2 (HDO), were evaluated.

The normalised interface stiffnesses of eight samples from the three distinct configurations (REF, LDO, HDO) were depicted in Figure 5.21. The figure illustrates that, of the eight samples examined, the evolution of six normalised interface stiffness curves follow a comparable trajectory and exhibits equivalent fatigue lives. Six samples are comprised of one out of three samples from the high dosage configuration (HDO), all samples from the REF configuration, and all samples from the low dosage configuration (LDO). It might be due to the presence of 450 g/m2 of residual bitumen at the interface, the fatigue test results are not replicated precisely. Conversely, alterations in the quantity of bitumen introduced at the interface have no apparent impact on the fatigue characteristics of the interface.

Figure 5.22 demonstrates the evolutions of the phase angle of interface stiffness. The evolutions of all samples made with three different residual bitumen dosages of tack coat are comparable. The peaks of phase angle can be observed in all curves, and generally are reached

after 200000 cycles. The fatigue lives of all samples are listed on Table 5.5 considering the maximal phase angle criterion.

Figure 5.23 shows the evolution of the dissipated energy during fatigue tests of samples made of two different residual bitumen dosages at the interface: (a) 250 g/m^2 (LDO), and (b) 450 g/m^2 (HDO). From the results, one can see on one hand that the results for the LDO configuration are well repeated, and on the other hand these for HDO configuration are not overlapped. The same observation can be found for the evolution of shear stress ($\tau_{\theta z}$) during fatigue tests of these samples in Figure 5.24. In general, the fatigue lives of samples made with three different residual dosages do not show any clear changing in withstanding fatigue loading considering dissipated energy criteria (the maximal dissipated energy, and the change of slope in dissipated energy evolution curves). Details about their fatigue lives can be found on Table 5.5.

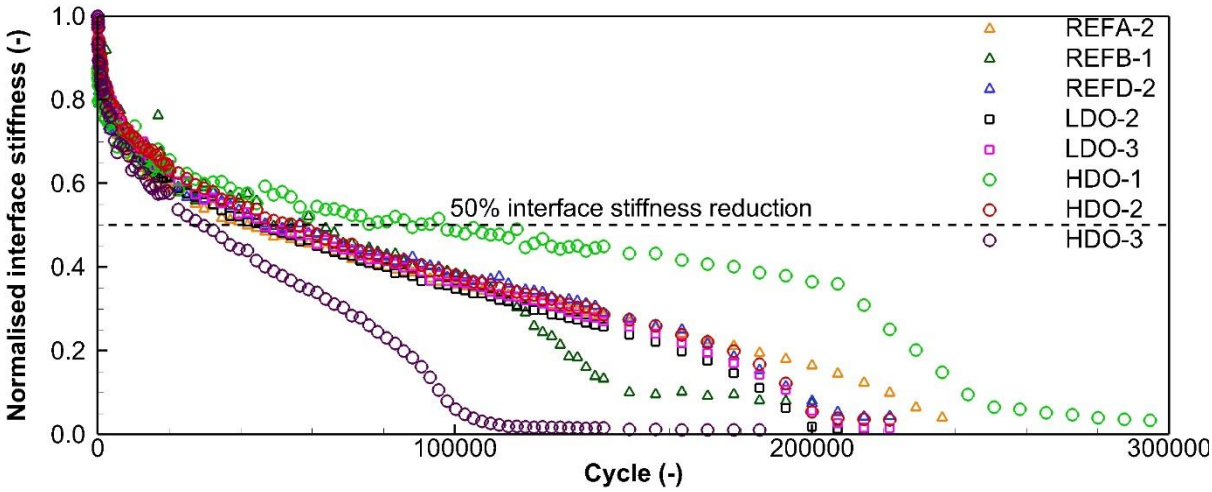

Figure 5.21: Evolution of normalized interface stiffnesses during fatigue tests of eight samples tested with $\varepsilon_{\theta zg\_0}$= 50µm/m, σ_{zz}= 0.0026 MPa, three different dosages of tack coat: 350 g/m^2 (REF), 250 g/m^2 (LDO), 450 g/m^2 (HDO)

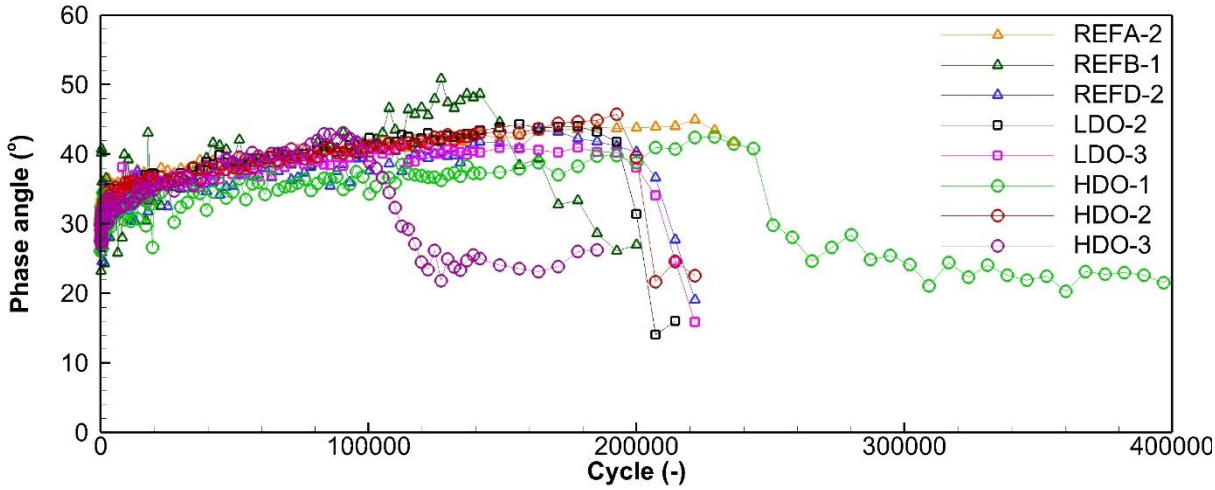

Figure 5.22: Evolution of phase angle during fatigue tests of eight samples tested with $\varepsilon_{\theta zg\_0}$= 50µm/m, σ_{zz}= 0.0026 MPa, three different dosages of tack coat: 350 g/m^2 (REF), 250 g/m^2 (LDO), 450 g/m^2 (HDO)

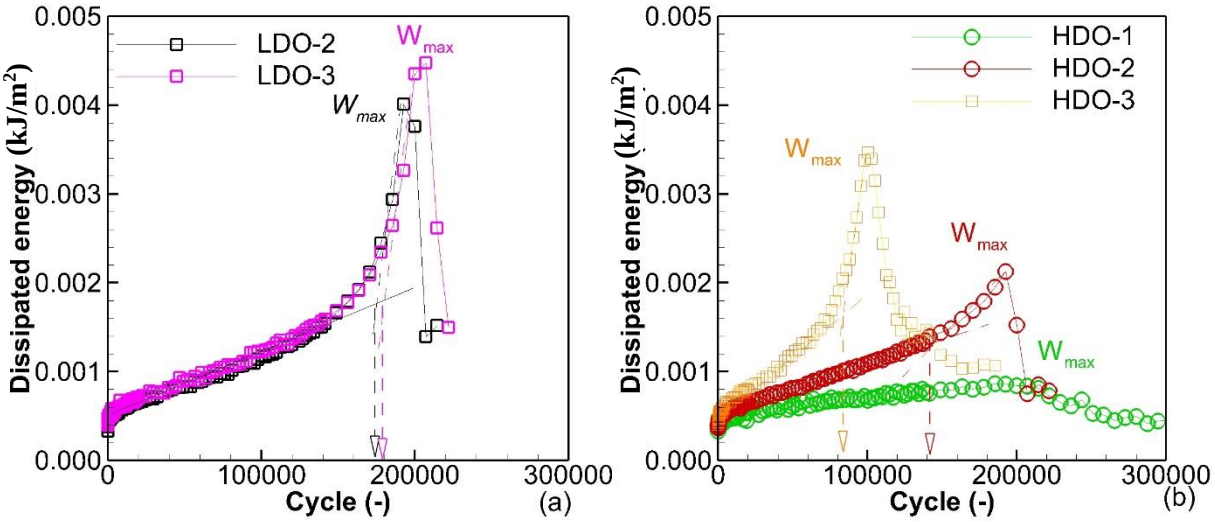

Figure 5.23: Evolution of dissipated energy during fatigue tests of seven tested with $\varepsilon_{\theta zg\_0}$= 50µm/m, σ_{zz}= 0.0026 MPa, two different dosages of tack coat: (a) 250 g/m^2 (LDO), (b) 450 g/m^2 (HDO)

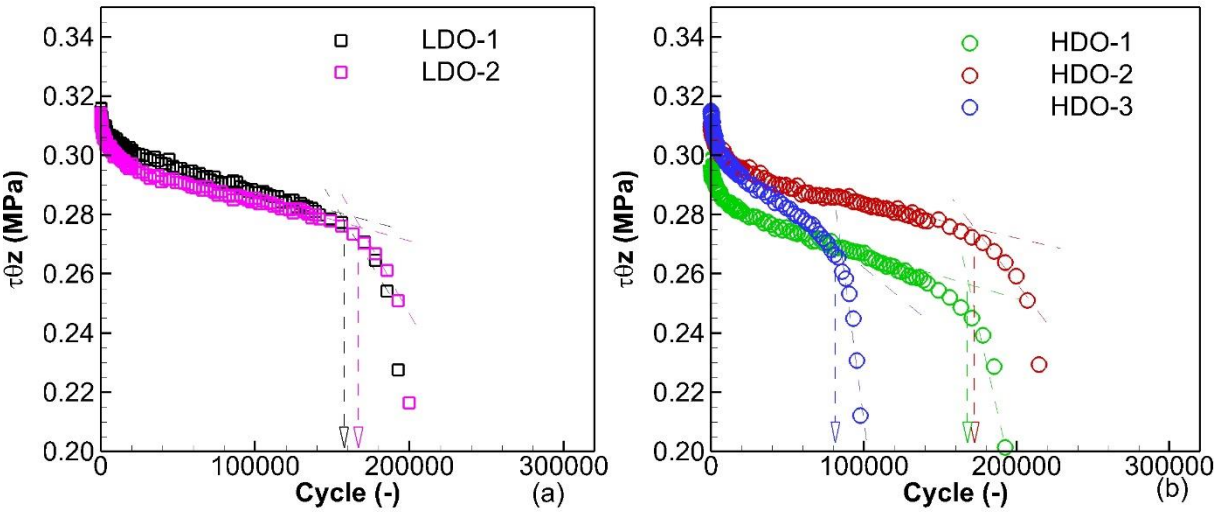

Figure 5.24: Evolution of shear stress ($\tau_{\theta z}$) during fatigue tests of seven tested with $\varepsilon_{\theta zg\_0}$= 50µm/m, σ_{zz}= 0.0026 MPa, two different dosages of tack coat: (a) 250 g/m^2 (LDO), (b) 450 g/m^2 (HDO)

5.5 The influence of emulsified bitumen types to shear fatigue behaviour of the interface

To study the influence of bitumen types used for the tack coat at the interface, a configuration of polymer modified bitumen (SBS) is added. The modification was made on the pure bitumen of 160/220 pen which are the same with the reference configurations (REF).

Figure 5.25 presents the evolutions of normalised interface stiffness of samples from the two configurations (REF and SBS). It can be seen that the fatigue results of interface made of polymer modified bitumen are well repeated. In comparison with the normalised interface stiffness curves of REF configuration samples, those of SBS configuration samples follow the comparable in the first 40% of reduction in the interface stiffness. Consequently, the interfaces made with polymer modified bitumen endure more significantly compared with those without the modification. The norm of interface stiffness of interface of bitumen with the modification witness the slower drop when the tests go on. Therefore, when considering the fatigue lives of interface by their 50% reduction of their norms of interface stiffness, those of interface with polymer modification are higher than those without the modification. Their fatigue lives are listed on Table 5.5.

Figure 5.26 shows the evolution of phase angle of interface stiffness during the fatigue tests of samples with the interface made with two different bitumen: the 160/220 pen bitumen and the 160/220 pen bitumen with the polymer modification. As can be seen from the figure, the evolutions of phase angle are quite similar in the beginning of the fatigue tests. However, curves for interface without modification early reach the maximal phase angle, and the curves

for interface with polymer modification do not. Considering the maximal phase angle criterion, the fatigue lives of samples with the modification are about twice compared to those without the modification. However, their maximal phase angles are quite similar which is around 45°. The fatigue lives of all samples with the interface made with polymer modification are introduced on Table 5.5. One can say that the modification with polymer in the tack coat improve the fatigue endurance of the interface.

Figure 5.27 depicts the progression of dissipated energy throughout fatigue tests conducted on interfaces composed of two distinct types of bitumen. The outcomes depicted in this figure validate that interfaces composed of polymer-modified bitumen have a greater resistance to repeated load than those not modified. The evolution of dissipated energy of the interfaces made of polymer-modified bitumen have clear peaks, but only that of the sample SBS-2 has a clear slope change zone before reaching the maximal value. The interface of the sample SBS-1 does not show a really clear transition zone between two slopes, and that of the sample SBS-3 does not have the slope change. The same observation can be found for the evolutions of displacement gap at the interfaces (Figure 5.28) of the three samples. More details about the fatigue lives of the interfaces regarding the maximal dissipated energy and the slope change in the dissipated energy evolution curves are introduced on Table 5.5.

The evolutions of shear stress inside three samples with the interfaces made of the polymer-modified bitumen are shown in Figure 5.29. The change of slope can be seen from three evolution curves. Their fatigue lives regarding the slope change in shear stress evolution curves can be found on Table 5.5.

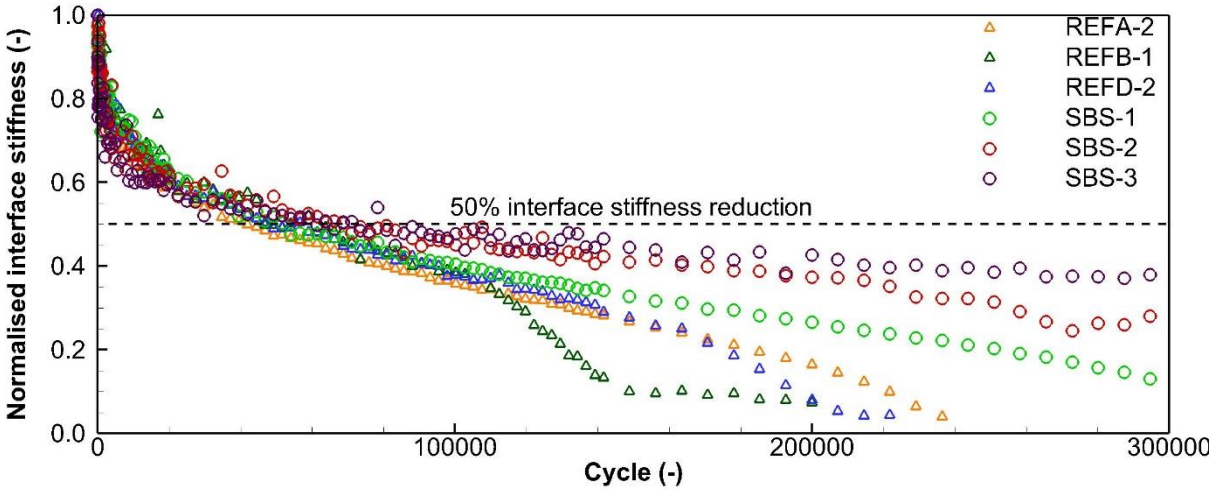

Figure 5.25: Evolution of normalized interface stiffnesses during fatigue tests of six samples tested with $\varepsilon_{\theta zg\_0}$= 50µm/m, σ_{zz}= 0.0026 MPa, two different types of tack coat: REF, SBS

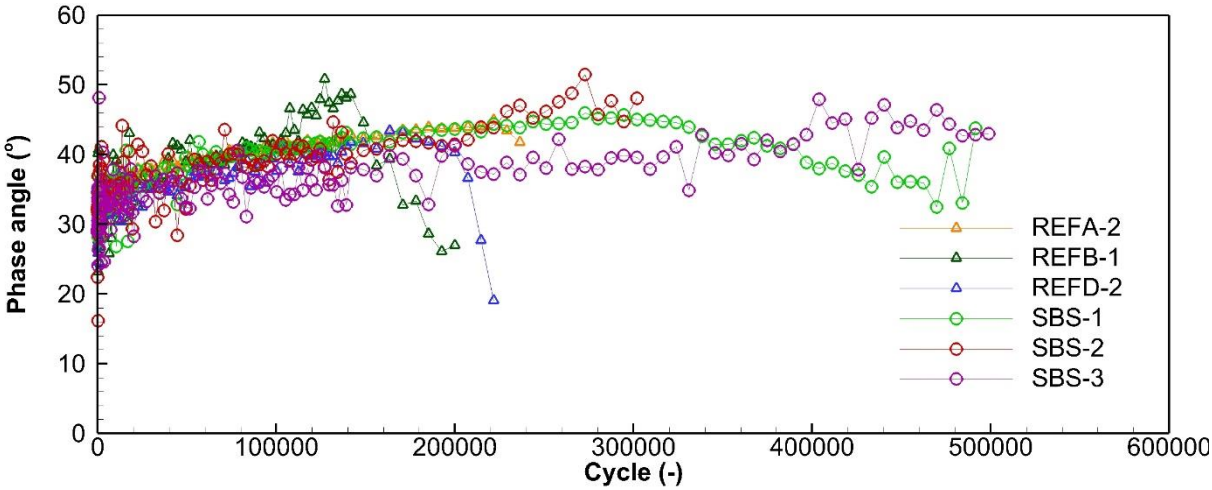

Figure 5.26: Evolution of phase angle of interface stiffnesses during fatigue tests of six samples tested with $\varepsilon_{\theta zg\_0}$= 50µm/m, σ_{zz}= 0.0026 MPa, two different types of tack coat: REF, SBS

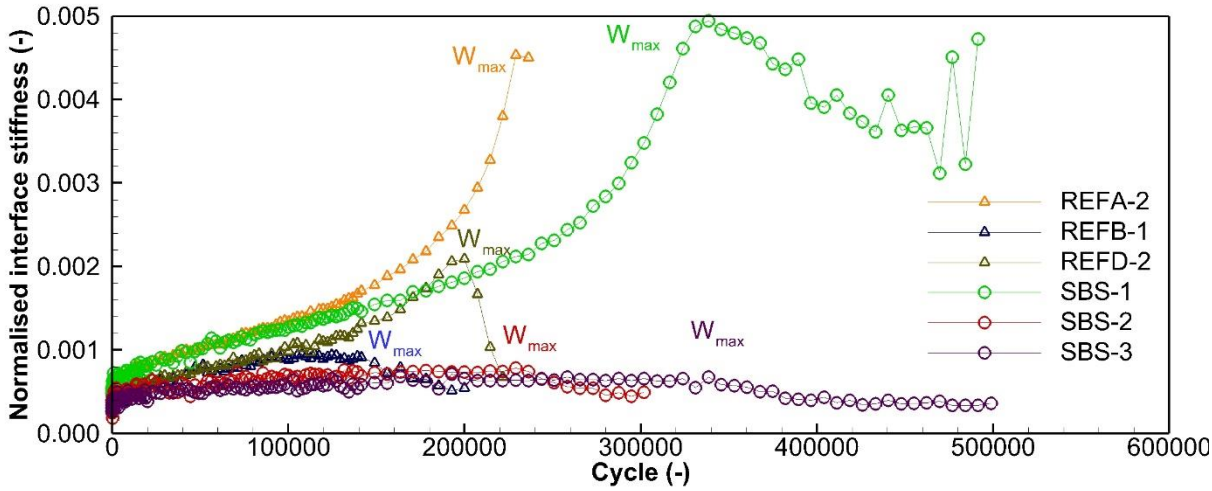

Figure 5.27: Evolution of dissipated energy during fatigue tests of six samples tested with $\varepsilon_{\theta zg\_0}$= 50µm/m, σ_{zz}= 0.0026 MPa, two different types of tack coat: REF, SBS

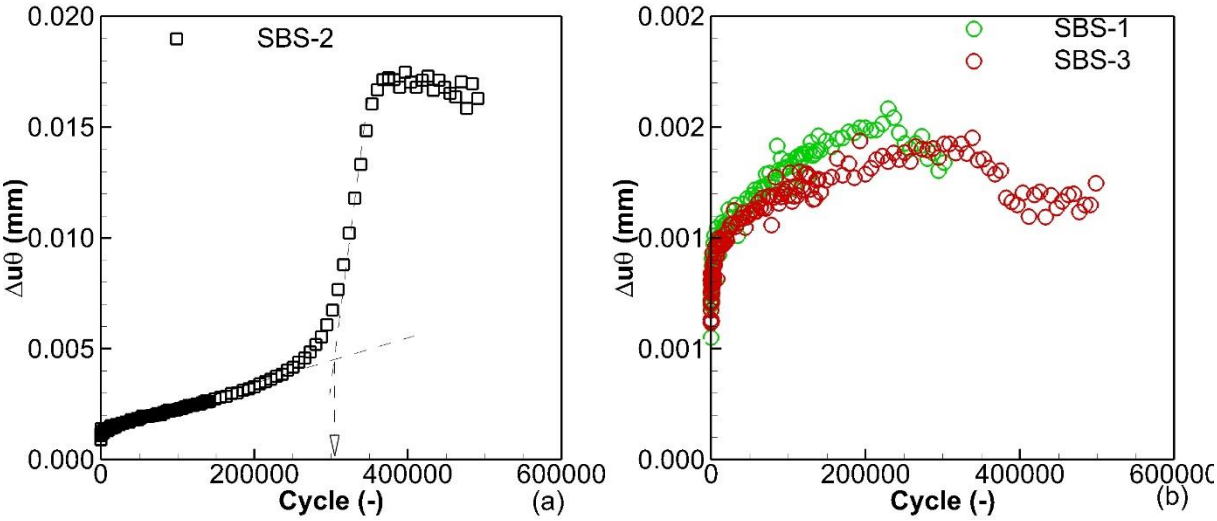

Figure 5.28: Evolution of displacement gap at the interfaces during fatigue tests of three samples tested with $\varepsilon_{\theta zg\_0}$= 50µm/m, σ_{zz}= 0.0026 MPa: (a) SBS-2; (b) SBS-1 and SBS-3

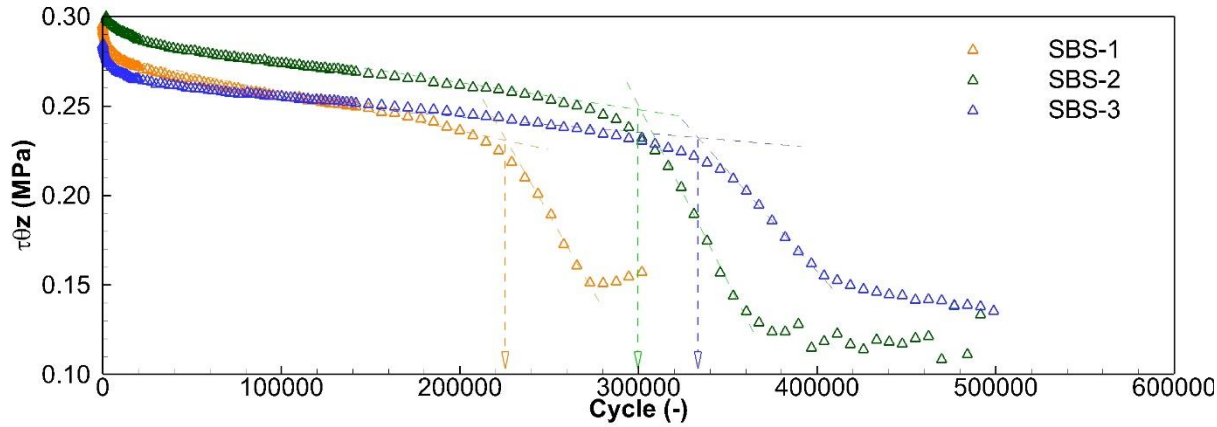

Figure 5.29: Evolution of shear stresses during fatigue tests of three samples with the interface using polymer-modified bitumen tested with $\varepsilon_{\theta zg\_0}$= 50µm/m, σ_{zz}= 0.0026 MPa

5.6 Summary of fatigue lives of different interface configurations

The summarization of fatigue lives for different interface configuration are shown in Figure 5.30 considering six fatigue criteria ((1) the 50% reduction of stiffness criterion (N_{f50}); (2) the maximal phase angle criterion ($N_{f\varphi max}$), (3) maximal dissipated energy (N_{fWmax}) criterion , (4) slope change in the dissipated energy evolution curve ($N_{fslp.W}$) criterion, (5) slope change in the stress evolution curve ($N_{fslp.\tau\theta z}$) criterion, and (6) slope change in the displacement gap at the interface evolution curve ($N_{fslp.\Delta u\theta}$) criterion). These samples were tested with the same global shear strain amplitude ($\varepsilon_{\theta zg\_0}$) of 50 µm/m, the same axial stress (σ_{zz}) of -0.026 MPa, and at the same temperature 10 °C. The summarization from Table 5.4, and Figure 5.30 show that results from different criteria are quite similar except the 50% reduction of stiffness criterion (N_{f50}), which is more conservative. The addition and the reduction of tack coat contents using at the

interface do not influence much the fatigue endurance of the interfaces. With too much tack coat at the interface, the repeatability is negatively influenced. However, more samples should be tested to confirm that statement. The modification with polymer (SBS) improves significantly the fatigue endurance of the interfaces. Table 5.5, and Figure 5.31 summarise the interface fatigue lives of 15 samples loaded with a global shear strain ($\varepsilon_{\theta zg\_0}$) amplitude of 50 µm/m. The results were presented by averaged values for all the samples in the same configurations, and their standard deviations (SD). It can be seen clearly the influence of axial stresses as well as the modification with SBS of bitumen on shear fatigue lives of interfaces. Since results were well repeated within a limit number of samples, there should have more fatigue tests to check the repeatability of each configuration.

Table 5.4: Summarization of fatigue lives of different interface configurations according to six proposed fatigue criteria

Configuration		Criterion					
		N_{f50}	N_{fjmax}	N_{fWmax}	$N_{fslp.W}$	$N_{fslp.\tau\theta z}$	$N_{fslp.\Delta u\theta}$
REF	N_f (cycles)	47640	169950	181290	148890	168347	168330
	SD (± cycles)	6968	39945	48451	29761	46251	32782
LDO	N_f (cycles)	44400	181340	203565	174405	188985	185340
	SD (± cycles)	2430	11290	3645	3645	3645	0
HDO	N_f (cycles)	53310	170760	160230	122160	159420	165090
	SD (± cycles)	19874	58623	40774	41310	47342	56410
SBS	N_f (cycles)	65460	323850	292230	253380	282540	284940
	SD (± cycles)	9787	57402	65273	18184	39632	44639

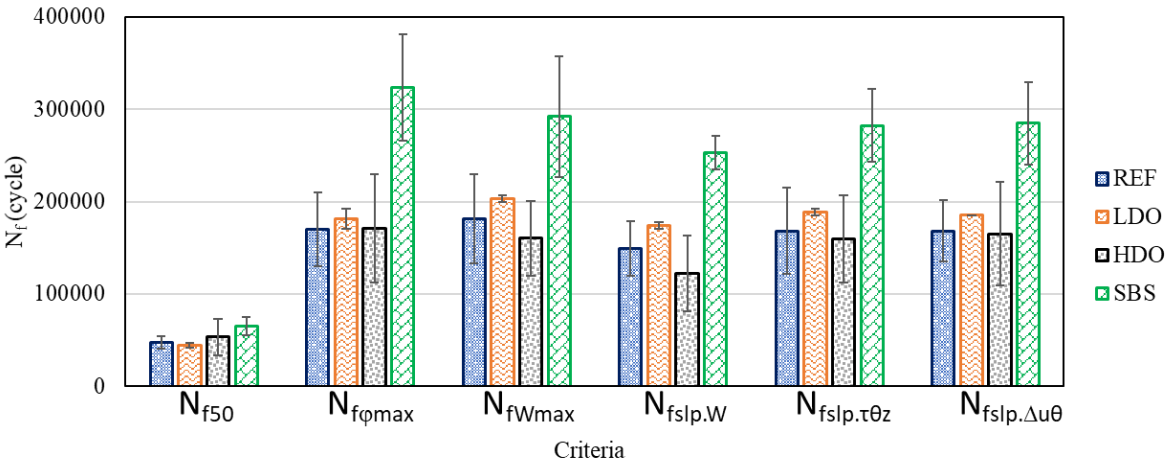

Figure 5.30: Summarization of fatigue lives of different interface configurations according to six proposed fatigue criteria

Table 5.5: Fatigue lives at the interfaces of 15 samples loaded with a global shear strain ($\varepsilon_{\theta zg\_0}$) amplitude of 50 µm/m according to six proposed different fatigue criteria

Sample	Axial stress σ_{zz} (MPa)	Initial displacement gap at interface Δu_{θ_0} (µm)	Number of cycles until failure according to six fatigue criteria (-)					
			50 % reduction of stiffness N_{f50}	Maximal phase angle $N_{f\varphi max}$	Maximal dissipated energy N_{fWmax}	Slope change in dissipated energy curve $N_{fslp.W}$	Slope change in stress curve $N_{fslp.\tau\theta z}$	Slope change in displacement gap curve $N_{fslp.\Delta u\theta}$
REFA-2	-0.026	0.985	39,540	221,790	229,080	185,340	214,550	207,210
REFB-1	-0.026	0.768	56,550	124,590	114,870	112,440	105,150	127,020
REFD-2	-0.026	0.718	46,830	163,470	199,920	148,890	185,340	170,760
REFC-1	-0.125	0.883	110,010	-	790,410	637,320	586,290	659,190
REFC-2	-0.125	0.613	114,870	-	702,930	513,390	520,680	513,390
REFB-2	-0.250	0.965	272,820	-	-	-	-	-
REFD-1	-0.250	0.745	207,210	-	-	-	-	-
LDO-2	0.026	0.74	41,970	170,050	199,920	170,760	185,340	185,340
LDO-3	0.026	0.855	46,830	192,630	207,210	178,050	192,630	185,340
HDO-1	0.026	0.768	78,420	229,080	185,340	-	199,920	221,790
HDO-2	0.026	0.801	51,690	192,630	192,630	163,470	185,340	185,340
HDO-3	0.026	0.887	29,820	90,570	102,720	80,850	93,000	88,140
SBS-1	0.026	0.697	73,560	272,820	199,920	229,080	229,080	229,080
SBS-2	0.026	0.897	51,690	294,690	338,430	272,820	294,690	287,400
SBS-3	0.026	0.887	71,130	404,040	338,340	258,240	323,850	338,340

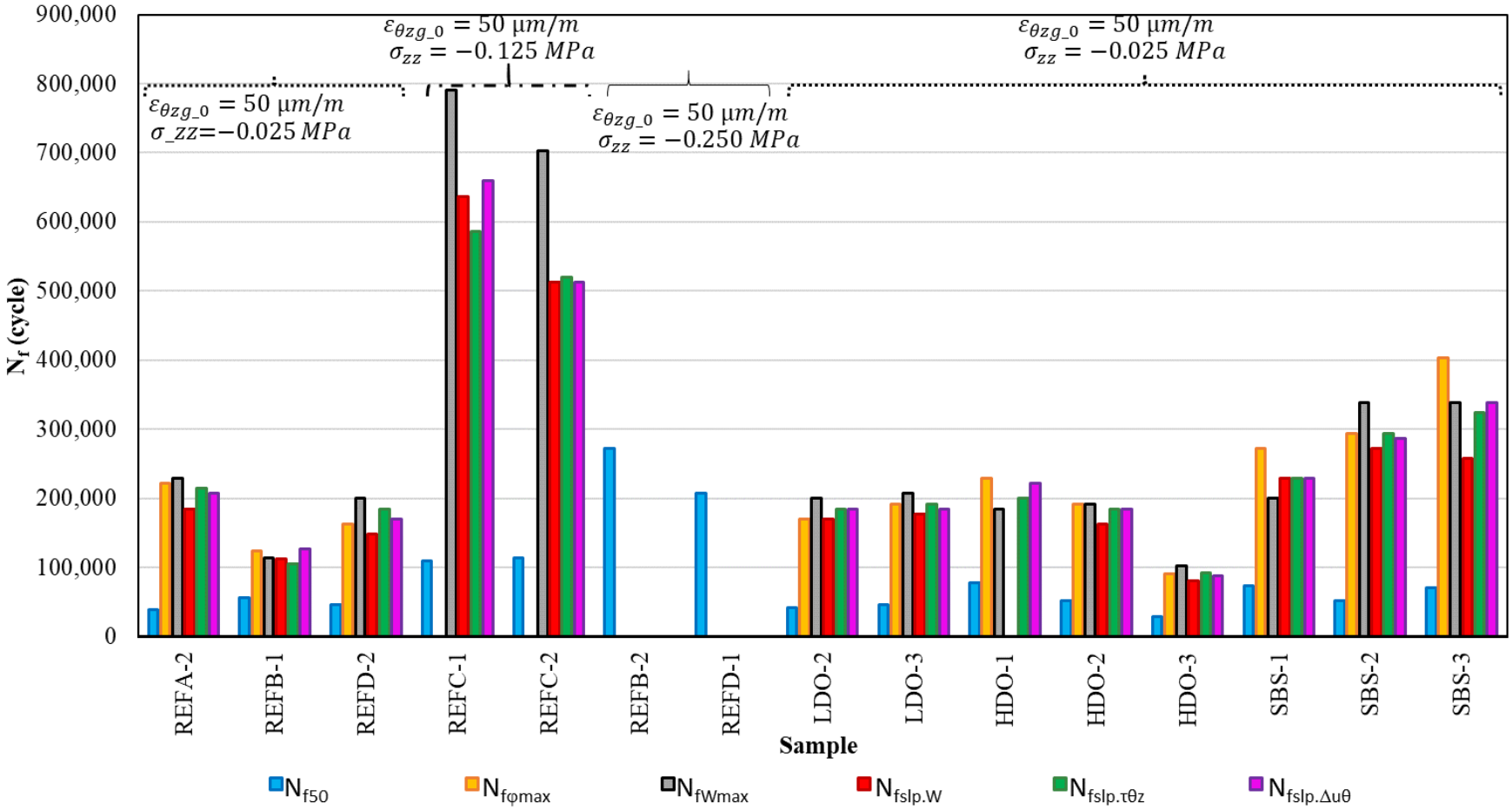

Figure 5.31: Fatigue lives at the interfaces of 15 samples loaded with a global shear strain ($\varepsilon_{\theta zg\_0}$) amplitude of 50 µm/m according to six proposed different fatigue criteria

5.7 The fatigue behaviour of interface considering the nonlinearity

In order to quantify the nonlinearity that make the reduction of interface stiffness during a cyclic test, the nonlinearity test is conducted at 5 different global shear strain amplitude from 30 µm/m to 110 µm/m with steps of 20 µm/m. These tests were done before and analysed in Chapter 4 (section 4.6.6). Figure 5.32 shows the results of the sample REFD-2 for norm and phase of complex interface stiffness plotted against their obtained displacement gap at the interface. It can be seen from the figure; the increase of displacement gap at the interface leads to the decrease of norm and the rise of phase angle. As shown before, the displacement gap at interface varies during fatigue tests. Nonlinearity may be responsible for one part of the decrease in norm and the increase in phase angle of the complex interface stiffness during fatigue tests. In order to qualify this influence, Equations obtained from two linear regression lines in Figure 5.32 are introduced respectively into the evolution curves of norm and phase angle of complex interface stiffness during the fatigue test. It is hypothesized that nonlinearity effects stay the same during the fatigue test before the fracture at the interface. The fracture is considered in this example when the phase angle reaches its maximal value.

Figure 5.33 illustrates the impact of nonlinearity during a fatigue test. It can be seen that the influence gets more significantly with the increase of number of cycles. Right before the fracture, the nonlinearity reduces 25% norm of interface stiffness, and increase almost 6° in phase angle.

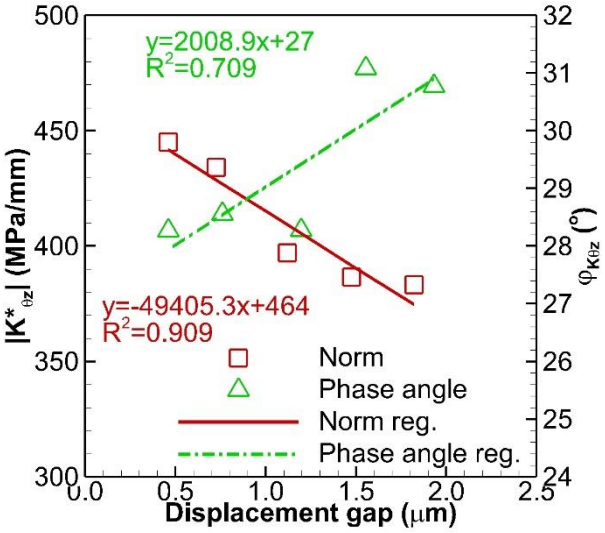

Figure 5.32 The nonlinearity test results for sample REFD-2: evolution of norm and phase angle of complex interface stiffness versus their corresponding displacement gap at the interface (data and regression lines)

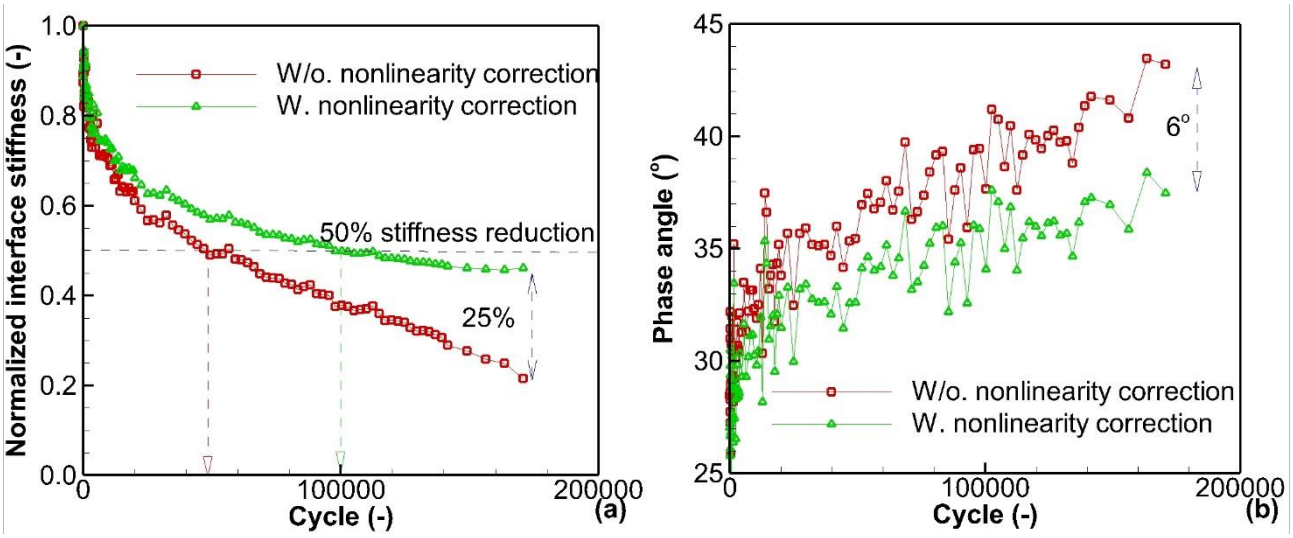

Figure 5.33: Influence of nonlinearity to (a) norm and (b) phase angle of complex interface stiffness during fatigue test on the sample REFD-2: data plotted without (w/o) and with (w) correction from equation in Figure 5.32

Equation of nonlinearity effect on the complex interface stiffness for other samples can be found on Table 5.6. Figure 5.34, Figure 5.35, and Figure 5.36 correspondingly shows the influence of the nonlinearity on the fatigue behaviour of the interfaces in the samples HDO-3, LDO-2, and SBS-2 represented by their norm and phase angle of interface stiffness. It can be seen from these figures that the nonlinearity plays an important role in reducing the norm and increase the phase angle during fatigue tests. If the criterion of 50% norm of interface stiffness reduction is considered, the nonlinearity reduce roughly 50% fatigue lives of all interfaces tested. In the other side, if the maximal phase angle criterion is considered, the nonlinearity increases 6°- 9° in the phase angle.

Table 5.6: Equation of nonlinearity effect on the complex interface stiffness for samples REFD-2, HDO-3, LDO-2, SBS-2

Samples	Equation of nonlinearity effect on $K^*_{\theta z}$	
	$\|K^*_{\theta z}\|$ (MPa)	$\varphi_{K\theta z}$ (°)
REFD-2	$\|K^*_{\theta z}\|$ = -49405.3Δu_{θ_0} + 464	$\varphi_{K\theta z}$= 2008.9Δu_{θ_0} + 27
HDO-3	$\|K^*_{\theta z}\|$ = -43467.1Δu_{θ_0} + 411	$\varphi_{K\theta z}$= 2172.8Δu_{θ_0} + 24
LDO-2	$\|K^*_{\theta z}\|$ = -59146.9Δu_{θ_0} + 500	$\varphi_{K\theta z}$= 3358.7Δu_{θ_0} + 28
SBS-2	$\|K^*_{\theta z}\|$ = -11152.8Δu_{θ_0} + 299	$\varphi_{K\theta z}$= 1493.9Δu_{θ_0} + 30

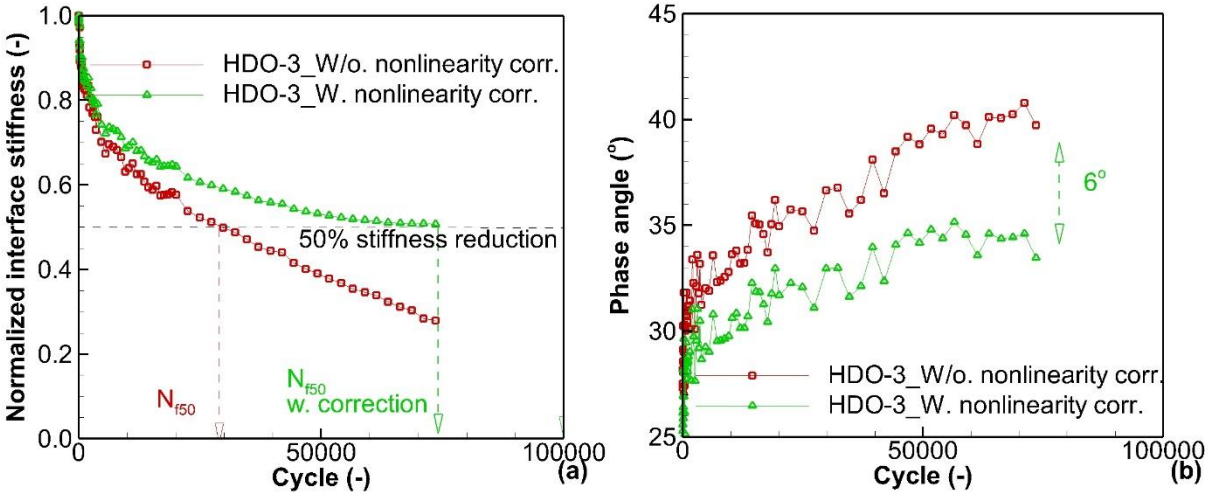

Figure 5.34: The influence of nonlinearity to (a) norm and (b) phase angle of complex interface stiffness during a fatigue test of the sample HDO-3

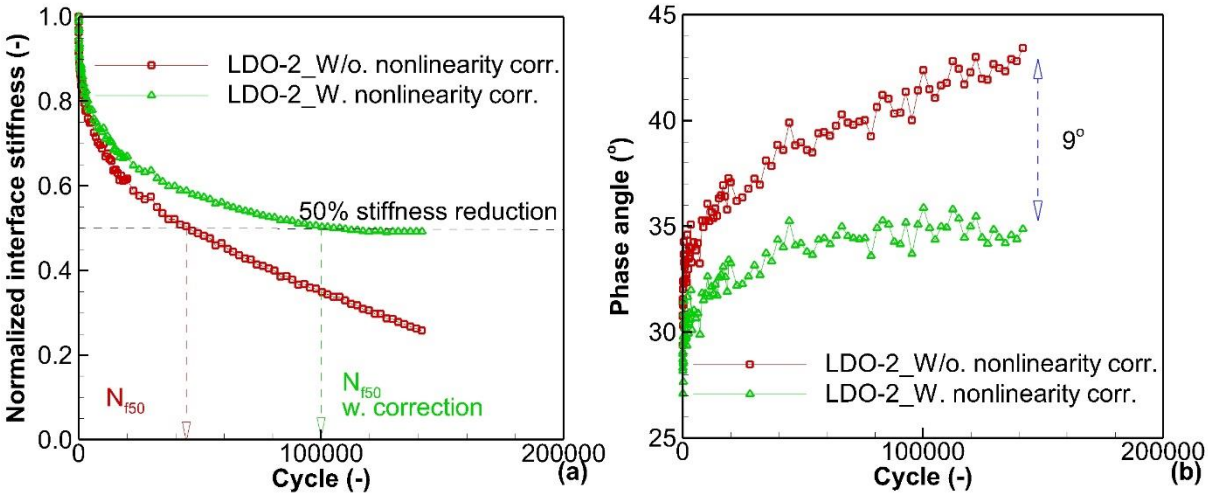

Figure 5.35: The influence of nonlinearity to (a) norm and (b) phase angle of complex interface stiffness during a fatigue test of the sample LDO-2

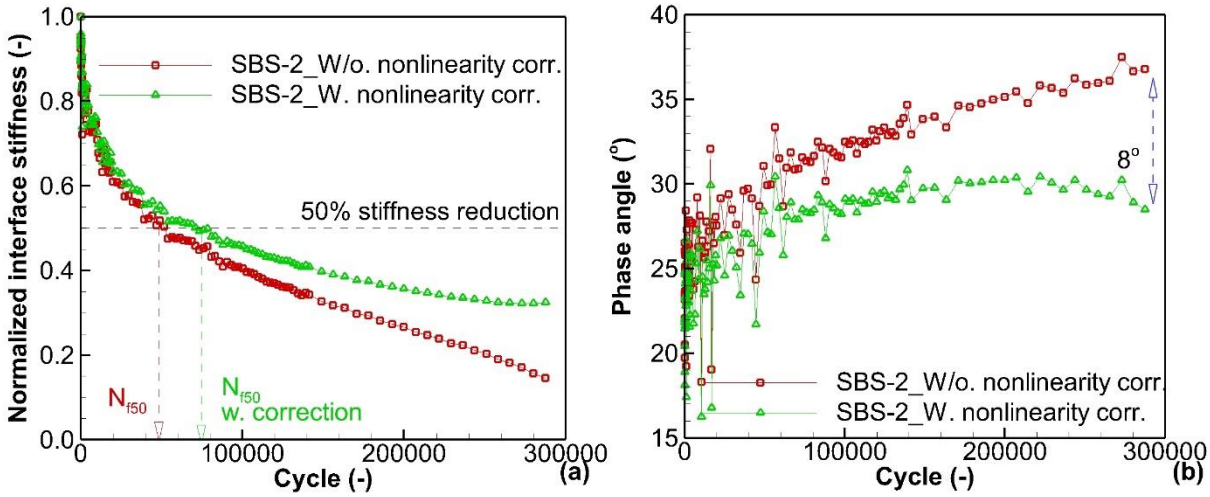

Figure 5.36: The influence of nonlinearity to (a) norm and (b) phase angle of complex interface stiffness during a fatigue test of the sample SBS-2

5.8 The behaviour of bituminous layers during fatigue tests

In the previous section of this chapter, the focus was on the fatigue lives of interfaces from different loading types on the samples of the reference configuration, and of interface from different configurations. The interface of each configuration varies according to the dosage and sort of residual bitumen utilised. However, the materials used in layers are kept the same throughout the study. They are BBSG3 for the upper layer, and EME2 for the lower layer as presented in the Chapter 3. A concise conclusion was reached in section 5.2 that the fatigue behaviour of two layers was not substantially affected by cyclic torsion. The fatigue behaviour of the two bituminous layers are represented by the evolution of their complex shear moduli.

The evolution of the norm and phase angle ($|G^*_{\theta z.up}|$, and $\varphi_{G.up}$) of complex shear moduli in the upper layers of four distinct samples, which correspond to the four configurations (REF, HDO, LDO, SBS), is illustrated in Figure 5.37 and Figure 5.38, respectively. The figures illustrate that the evolutions consist of three distinct stages:

- Stage 1: An initial slight decrease in the norm and an accompanying slight increase in the phase angle.
- Stage 2: A steady phase angle and norm. This phase persists for nearly the entire duration of a fatigue test.
- Stage 3: During this phase, the norm and phase angle of complex moduli begin to evolve unpredictably. The evolution of the norm and phase angle of complex shear moduli ($|G^*_{\theta z.low}|$, and $\varphi_{G.low}$) in the lower layer layers (EME2) of the aforementioned samples are illustrated in Figure 5.39 and Figure 5.40,

respectively. In the same way that the complex shear moduli of upper layers undergo fatigue testing, they develop through the three distinct phases that have been described.

It is evident that neither the upper nor lower layers demonstrate fatigue failure. Nevertheless, when stage 3 commences, the recorded number of cycles is in close proximity to the number of cycles attained at the point of maximum phase angle and dissipated energy. Fatigue failures at the interfaces occurs around that number of cycles. Therefore, the results indicate that the measurement in layers is erroneous. The subsequent figures illustrate the initiations of instabilities observed during the measurement of the norm and phase angle of complex shear moduli in both layers. By locating the point of instability in layer measurements, fatigue failures at the interface can be identified. Hence, the starting of instability observed during the assessment of layers can be regarded as a fatigue criterion at their interfaces.

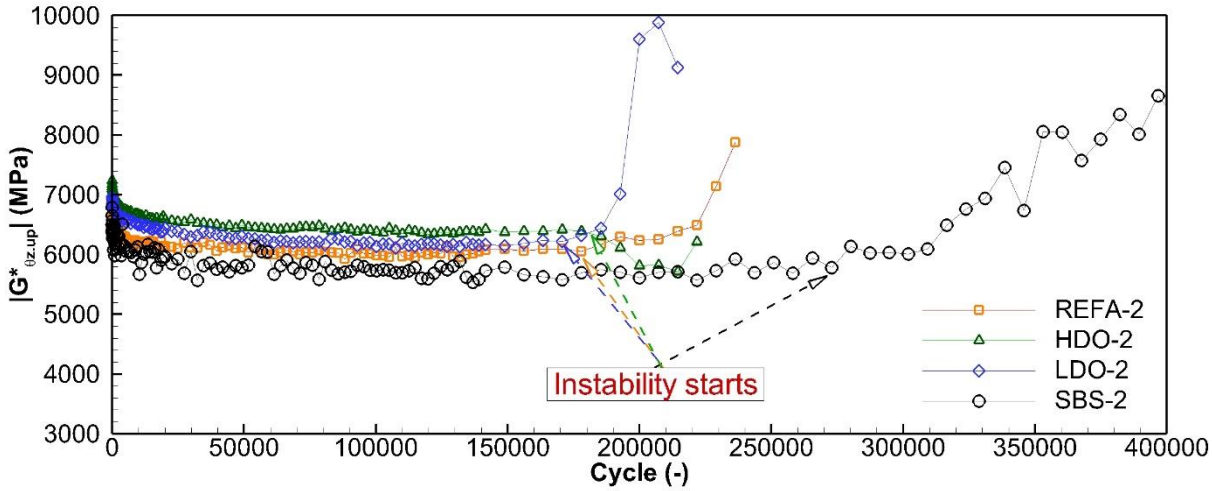

Figure 5.37: The evolution of the norm of complex shear moduli ($\left|G^*_{\theta z.up}\right|$)of the upper layer (BBSG3) during fatigue tests (represented by four upper layers in four distinct configurations REF, HDO, LDO, and SBS)

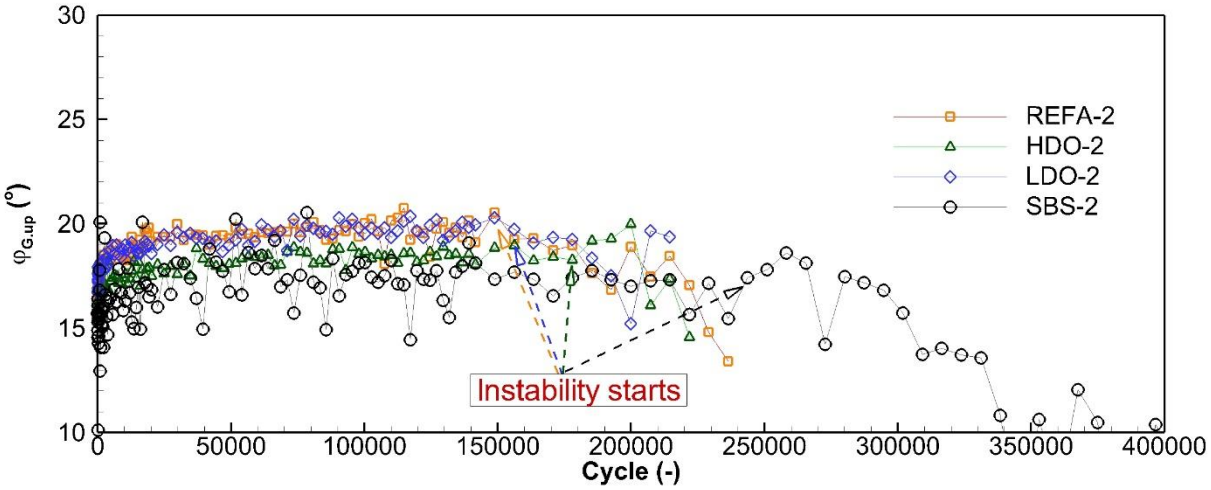

Figure 5.38: The evolution of the phase angle of complex shear moduli ($\varphi_{G.up}$) of upper layer (BBSG3) during fatigue tests (represented by four upper layers in four distinct configurations REF, HDO, LDO, and SBS)

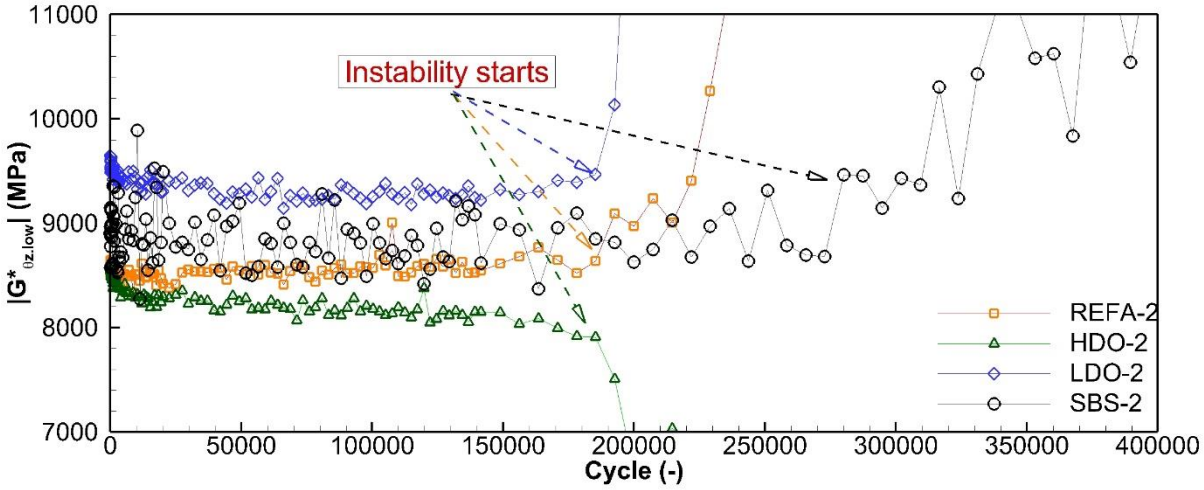

Figure 5.39: The evolution of the norm of complex shear moduli ($|G^*_{\theta z.low}|$)of the lower layer (EME2) during fatigue tests (represented by four upper layers in four distinct configurations REF, HDO, LDO, and SBS)

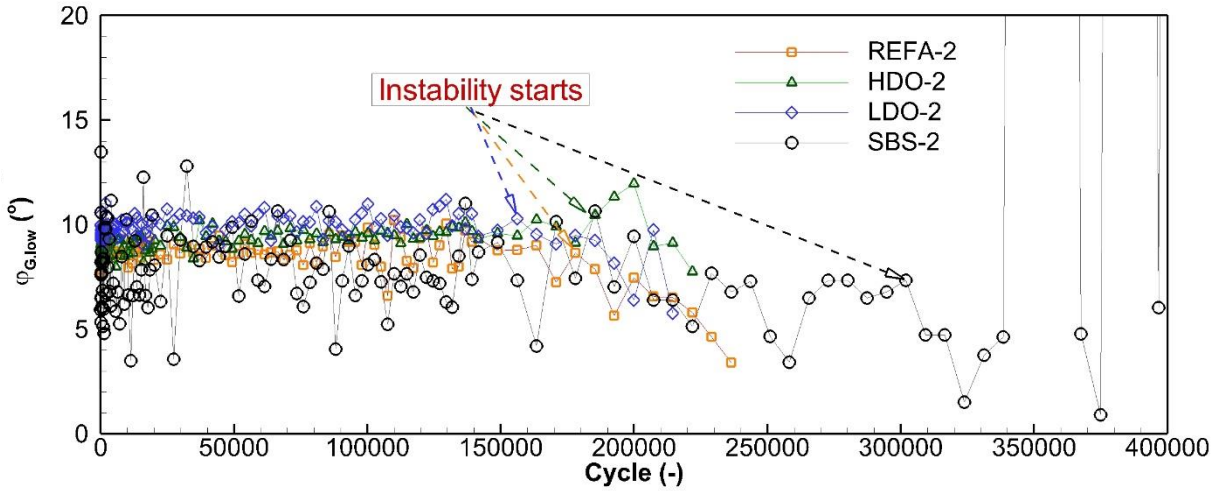

Figure 5.40: The evolution of the phase angle of complex shear moduli ($\varphi_{G.low}$) of lower layer (EME2) during fatigue tests (represented by four upper layers in four distinct configurations REF, HDO, LDO, and SBS)

5.9 Conclusions

The fatigue tests were launched on 20 double-layered hollow cylinders using the 2T3C hollow cylinder apparatus. Fatigue tests of three samples failed because of the power cut and overloaded data acquisition to the computer's memory. They are the samples REFC-3, REFD-3, and LDO-1. From the remaining 17 successful fatigue tests, there are different combinations of loading parameters applied to the samples with different interface configurations, some

conclusions can be made:

- Three levels of the global shear strain amplitudes 50 µm/m, 150 µm/m, and 200 µm/m, combined with the axial stress of -0.026 MPa: There are six proposed criteria for assessing the fatigue life of an interface: (1) the 50% reduction of stiffness criterion (N_{f50}); (2) the maximal phase angle criterion ($N_{f\varphi max}$), (3) maximal dissipated energy (N_{fWmax}) criterion , (4) slope change in the dissipated energy evolution curve ($N_{fslp.W}$) criterion, (5) slope change in the stress evolution curve ($N_{fslp.\tau\theta z}$) criterion, and (6) slope change in the displacement gap at the interface evolution curve ($N_{fslp.\Delta u\theta}$) criterion. Thanks to the six criteria, there are six Wohler's lines were drawn in the Log Δu_{θ_0} – Log N_f diagram.
- Global shear strain of 50 µm/m, combined with the axial stress of -0.026 MPa: three samples from the reference configuration were tested with the same loading parameter. The results show a good repetition.
- The global shear strain of 50 µm/m, combined with three axial stresses of -0.026 MPa, -0.125 MPa, and -0.250 MPa: The higher the axial stress applied, the higher fatigue life the interface shows.
- The global shear strain of 50 µm/m, combined with the axial stress of -0.026 MPa on samples with different tack coat contents, and tack coat types: The increase of tack coat content at the interface does not increase the fatigue life. However, the results from three sample with highest tack coat use of 450 g/m^2 did not well repeated.
- The global shear strain of 50 µm/m, combined with the axial stress of -0.026 MPa on samples with the tack coat modified with polymer: The fatigue life of interface using modified bitumen for tack coat were incredibly improved.

The nonlinearity bias was incorporated into fatigue results with a great influence.

The shear complex moduli of bituminous mixture in layers does not notably affected during fatigue tests. However, by observing the stability of the measurement of the complex shear moduli (norm and phase angle) of bituminous mixture in layers during fatigue tests, it is possible to know when there is fatigue failure at their interface. Therefore, this observation may be considered as a fatigue criterion.

CONCLUSIONS AND PERSPECTIVES

The purpose of this thesis is to investigate the thermomechanical behaviour of the interfaces between two bituminous layers, as well as that within the two layers, using the 2T3C hollow cylinder apparatus. Various combinations of loading parameters were utilised to investigate the Linear ViscoElastic (LVE), nonlinear ViscoElastic (non-LVE), fatigue, and nonlinearity behaviours of the interface and the two layers of bituminous mixture.

The 2T3C hollow cylinder apparatus, developed at the Laboratoire de Tribologie et Dynamique des Système (LTDS, URM 5513) of the University of Lyon/Ecole Nationale des Travaux Publics de l'Etat (ENTPE), permits the application of stress and displacement gaps at the interface and quasi-homogeneous stress and strain fields in two mixture layers. The apparatus is capable of applying cyclic loading in tension/compression and/or torsion modes to samples. The device incorporates with four cameras, a 3D Digital Image Correlation (3D-DIC) technology system, and a unique analysis method that differentiates interface behaviour from that of two layers.

A total of 21 samples were obtained from seven slabs; one of these samples was broken during the coring process from the reference slab. As a result, 20 samples were tested for this thesis. Upper layers of every double-layered hollow cylinder are composed of a BBSG3 mixture, while lower layers are composed of an EME2 mixture. The reference samples are determined by selecting samples that have a tack coat composed of pure 160/220 bitumen at the interface, with a residual content of 350 g/m^2. Two amplitudes of global shear strain (50 and 200 µm/m), and three constant axial stresses (-0.026, -0.125, -0.250 MPa) were combined in shear complex modulus tests in order to investigate the effects of these stresses on the thermomechanical behaviour of interfaces. The shear complex modulus tests were conducted

at five frequencies ranging from 0.01 Hz to 1 Hz and five temperatures ranging from 0°C to 40°C. Experiments at 40 °C are absent for shear complex modulus tests combined with an axial stress exceeding -0.026 MPa (-0.125 MPa and -0.250 MPa) in order to mitigate the potential creep effect at the elevated temperature. Two of the samples underwent non-linearity testing (REFC-1 and REFD-2). Fatigue tests were launched at a temperature of 10 °C and a frequency of 3 Hz (with measurements at 1 Hz). The effects of three additional interface configurations, including a different tack coat type (SBS-modified bitumen for tack coat) and residual bitumen contents of tack coat (250 and 450 g/m2), were determined through the shear complex modulus test and shear fatigue test. Non-linearity tests were also performed on samples made of different interface configurations. The samples underwent testing with axial stress of -0.026 MPa and global shear strain of 50 µm/m for these configurations. Other parameters of temperatures and frequencies were kept the same with the reference samples.

Twenty double-layered hollow cylinders were utilised for the complex shear modulus experiments with the 2T3C hollow cylinder apparatus. Various loading parameter combinations are implemented on the samples, leading to the following conclusions:

The Time-Temperature Superposition Principle (TTSP) is verified in the case of bituminous mixtures. The LVE 2S2P1D model effectively reproduces the thermomechanical characteristics of the bituminous mixture layers.

In regard to the interfaces, the validation of the TTSP is confirmed in every test result. As the loading parameters are combined, the following behaviours can be observed:

- When the axial stress of 0.026 MPa is combined with the global shear strain of 50 µm/m: The interfaces have demonstrated their LVE behaviour, and the LVE 2S2P1D model accurately describes their thermomechanical properties.
- In combination with three axial stresses of -0.026 MPa, -0.125 MPa, and -0.250 MPa, and a global shear strain of 50 µm/m. The interfaces have demonstrated their LVE behaviour, and the LVE 2S2P1D model accurately describes their thermomechanical behaviour. Nevertheless, the static modulus, a 2S2P1D parameter utilised to characterise the friction and adhesion of aggregate structures, particularly aggregates composed of two layers at interfaces, is affected by axial stresses. The higher the axial stress is applied; the higher static modulus is obtained.
- An axial stress of -0.026 MPa and a global shear strain amplitude of 50 µm/m were applied to samples with varying tack coat contents and types. It was observed that the variation in tack coat contents had no significant impact on the LVE behaviour of the

interfaces. Similarly, the modification of bitumen has negligible effects on both the experimental results and LVE modelling.

- When the axial stress of 0.026 MPa is combined with the global shear strain of 200 µm/m: during cyclic testing, there is plastic dissipation at the interface, and it is determined that the LVE 2S2P1D model significantly underestimates the phase angle of complex interfaces stiffness observing in the Black's space and the phase angle master curve plots. The DBN_{PDSC} model, which incorporates plastic dissipation into the spring elements of a generalised Kelvin-Voigt model, is a visco-elasto-plastic model. The plastic dissipation was described by this model, which also overcomes the phase angle underestimation introduced by the LVE model.

The nonlinearity tests provide insights into the norm and phase angle effects on the complex shear modulus. When the amplitude of the global shear strain (and consequently the displacement gap at the interface) increases, the phase angle of the complex interface stiffness rises while the norm decreases.

Twenty double-layered hollow cylinders were subjected to fatigue testing utilising the 2T3C hollow cylinder apparatus. The shear fatigue tests were launched at 3Hz, while the shear complex interface stiffness, and shear complex moduli in layers measurements were recorded at 1Hz during 3 cycles. Several conclusions can be drawn from the remaining 17 successful fatigue experiments in which various combinations of loading parameters were applied to samples with distinct interface configurations:

- In conjunction with an axial stress of -0.026 MPa and a global shear strain amplitude of 50 µm/m, three samples were subjected to testing using the reference configuration samples under identical loading conditions. The outcomes demonstrate effective repetition.
- A combination of three levels of global shear strain amplitudes—50 µm/m, 150 µm/m, and 200 µm/m—and an axial stress of -0.026 MPa were utilised: There are six proposed criteria for assessing the fatigue life of an interface: (1) the 50% reduction of stiffness criterion (N_{f50}); (2) the maximal phase angle criterion ($N_{f\varphi max}$), (3) maximal dissipated energy (N_{fWmax}) criterion , (4) slope change in the dissipated energy evolution curve ($N_{fslp.W}$) criterion, (5) slope change in the stress evolution curve ($N_{fslp.\tau\theta z}$) criterion, and (6) slope change in the displacement gap at the interface evolution curve ($N_{fslp.\Delta u\theta}$) criterion. Thanks to the six criteria, Wöhler's lines were drawn in the Log Δu_{θ_0} – Log Nf diagram.

- In conjunction with three axial stresses of -0.026 MPa, -0.125 MPa, and -0.250 MPa, the global shear strain amplitude is 50 µm/m. As axial stress increases, the fatigue life of the interface also increases.
- The samples varying tack coat contents and types tested with a global shear strain amplitude of 50 µm/m and an axial stress of -0.026 MPa. Increasing the amount of tack coat at the interface has no effect on the fatigue life. The outcomes, however, did not replicate accurately for the three samples with the maximum tack coat application of 450 g/m2. The fatigue resistance of interfaces made of the tack coat with the modified bitumen was significantly enhanced. This observation shows that the polymer modification in bitumen has a long-term effect, rather than in the short-term.

Significantly, the nonlinearity bias was incorporated into the fatigue results with an assumption that the nonlinearity laws are unchanged. It was observed that the nonlinearity plays an important role in reducing norm and increasing phase angle of the complex interface stiffness.

During fatigue tests, the shear complex moduli of bituminous mixtures in layers are not significantly altered. Nevertheless, fatigue failure at the interface of bituminous mixtures can be identified by monitoring the stability of the complex shear moduli (especially the phase angle and norm) measurements as the tests progress. Consequently, this observation could be regarded as a criterion for fatigue behaviour.

Some perspectives and future research can be considered as below:

- Only three samples were cored and tested from one slab in this thesis. There should have more tests, especially fatigue tests, to be done to validate the Wöhler's curves found. That requires surely a long experimental campaign in term of duration. Double-layered hollow cylinder samples cored from real pavements are also interesting for testing.
- It is possible to implement the results obtained from the shear complex modulus test, and the LVE modelling on the interface, and fatigue results to a finite element model for a pavement structure. This allows to predict a more realistic service life of pavement, improving design methods.
- It is possible to perform fatigue tests with rest periods with the 2T3C Hollow Cylinder Apparatus to quantify biasing effects involved during a cyclic test. In addition, the fatigue test with rest periods procedure for mixture developed at the laboratory LTDS the University of Lyon/ENTPE can be used for double-layered hollow cylinder samples.

- The recent shear fatigue tests can be improved. Higher speed cameras will be useful to study thermomechanical behaviour of interfaces at higher frequencies, and fatigue behaviour of interface at 10Hz.
- By applying creep/recovery test, it is possible to distinguish the permanent displacement gap (plastic displacement gap) from the total displacement gap at the interface in the shearing mode.

REFERENCES

Attia, T. (2020). *Interfaces between pavement layers in bituminous mixtures*. University of Lyon/ENTPE. [Doctoral dissertation]. https://theses.hal.science/tel-02860819.

Attia, T., Benedetto, H. Di, Sauzéat, C., & Pouget, S. (2021). Behaviour of an interface between pavement layers obtained using Digital Image Correlation. *Materials and Structures*, *54*(38), 1–14. https://doi.org/10.1617/s11527-021-01625-w

Attia, T., Di Benedetto, H., Sauzéat, C., & Pouget, S. (2020). 2T3C HCA, a new hollow cylinder device using Digital Image Correlation to measure properties of interfaces between asphalt layers. *Construction and Building Materials*, *247*, 118499. https://doi.org/10.1016/j.conbuildmat.2020.118499

Attia, T., Di Benedetto, H., Sauzéat, C., & Pouget, S. (2021). Behaviour of an interface between pavement layers obtained using Digital Image Correlation. *Materials and Structures/Materiaux et Constructions*, *54*(1). https://doi.org/10.1617/s11527-021-01625-w

Babadopulos, L. (2017). *Phenomena occurring during cyclic loading and fatigue tests on bituminous materials : Identification and quantification*. University of Lyon/ENTPE. [Doctoral dissertation]. https://tel.archives-ouvertes.fr/tel-01599933.

Canestrari, F., & Santagata, E. (2005). Temperature effects on the shear behaviour of tack coat emulsions used in flexible pavements. *International Journal of Pavement Engineering*, *6*(1), 39–46. https://doi.org/10.1080/10298430500068720

Canestrari, Francesco, Attia, T., Di Benedetto, H., Graziani, A., Jaskula, P., Kim, Y. R., Maliszewski, M., Pais, J. C., Petit, C., Raab, C., Ragni, D., Rys, D., Sangiorgi, C., Sauzéat, C., & Zofka, A. (2022). *Interlaboratory Test to Characterize the Cyclic Behavior of Bituminous Interlayers: An Overview of Testing Equipment and Protocols BT - Proceedings of the RILEM International Symposium on Bituminous Materials* (Hervé Di Benedetto, H. Baaj, E. Chailleux, G. Tebaldi, C. Sauzéat, & S. Mangiafico (eds.); pp. 29–36). Springer International Publishing.

Canestrari, Francesco, Belogi, L., Ferrotti, G., & Graziani, A. (2015). Shear and flexural characterization of grid-reinforced asphalt pavements and relation with field distress evolution. *Materials and Structures*, *48*(4), 959–975. https://doi.org/10.1617/s11527-013-0207-1

Canestrari, Francesco, Ferrotti, G., & Graziani, A. (2016). Shear failure characterization of time–temperature sensitive interfaces. *Mechanics of Time-Dependent Materials*, *20*(3), 405–419. https://doi.org/10.1007/s11043-016-9299-7

Canestrari, Francesco, Ferrotti, G., Lu, X., Millien, A., Partl, M. N., Petit, C., Phelipot-Mardelé, A., Piber, H., & Raab, C. (2013). Mechanical testing of interlayer bonding in asphalt pavements. In *RILEM State-of-the-Art Reports* (Vol. 9). https://doi.org/10.1007/978-94-007-5104-0_6

Canestrari, Francesco, Ferrotti, G., Partl, M. N., & Santagata, E. (2005). Advanced testing and characterization of interlayer shear resistance. *Transportation Research Record*, *1929*, 69–78. https://doi.org/10.3141/1929-09

Collop, A. C., Sutanto, M. H., Airey, G. D., & Elliott, R. C. (2009). Shear bond strength between asphalt layers for laboratory prepared samples and field cores. *Construction and Building Materials*, *23*(6), 2251–2258. https://doi.org/https://doi.org/10.1016/j.conbuildmat.2008.11.017

Collop, A. C., Sutanto, M. H., Airey, G. D., & Elliott, R. C. (2011). Development of an automatic torque test to measure the shear bond strength between asphalt. *Construction and Building Materials*, *25*(2), 623–629. https://doi.org/10.1016/j.conbuildmat.2010.07.030

Csanyi, L. H. (1962). Funtions of fillers in bituminous mixes. *Symposium on Mineral Fillers for Bituminous Mixtures*, 1–5.

D'Andrea, A., Loprencipe, G., & Xhixha, E. (2012). Vibration Induced by Rail Traffic: Evaluation of Attenuation Properties in a Bituminous Sub-ballast Layer. *Procedia - Social and Behavioral Sciences*, *53*, 245–255. https://doi.org/10.1016/j.sbspro.2012.09.877

D'Andrea, A., Russo, S., & Tozzo, C. (2013). Interlayer shear testing under combined state of stress. *Advanced Materials Research*, *723*, 381–388. https://doi.org/10.4028/www.scientific.net/AMR.723.381

D'Andrea, A., & Tozzo, C. (2016). Dynamic tests on bituminous layers interface. *Materials and Structures/Materiaux et Constructions*, *49*(3), 917–928. https://doi.org/10.1617/s11527-015-0548-z

Di Benedetto, H., & Corté, J.-F. (2004). Matériaux routiers bitumineux: constitution et propriétés thermomécaniques des mélanges. In *Hermés Lavoisier*. https://doi.org/10.2143/REA.28.1.505102

Di Benedetto, H, de La Roche, C., Baaj, H., Pronk, A., & Lundström, R. (2004). Fatigue of bituminous mixtures. *Materials and Structures*, *37*(3), 202–216. https://doi.org/10.1007/BF02481620

Di Benedetto, Hervé, Mondher, N., Sauzéat, C., & Olard, F. (2007). Three-dimensional thermo-viscoplastic behaviour of bituminous materials: The DBN model. *Road Materials and Pavement Design*, *8*(2), 285–315. https://doi.org/10.3166/rmpd.8.285-315

Di Benedetto, Hervé, Nguyen, Q. T., & Sauzéat, C. (2011). Nonlinearity, heating, fatigue and thixotropy during cyclic loading of asphalt mixtures. *Road Materials and Pavement Design*, *12*(1), 129–158. https://doi.org/10.3166/RMPD.12.129-158

Di Benedetto, Hervé, Perraton, D., Lamothe, S., & Boussabnia, M. M. (2023). Rational relationship between the fatigue curves of asphalt mixes obtained from tension/compression and 4-point bending tests. *Road Materials and Pavement Design*, *24*(S1), 192–208. https://doi.org/10.1080/14680629.2023.2180303

Diakhaté, M., Millien, A., Petit, C., Phelipot-Mardelé, A., & Pouteau, B. (2011). Experimental investigation of tack coat fatigue performance: Towards an improved lifetime assessment of pavement structure interfaces. *Construction and Building Materials*, *25*(2), 1123–1133. https://doi.org/10.1016/j.conbuildmat.2010.06.064

Duttine, A., Di Benedetto, H., Pham Van Bang, D., & Ezaoui, A. (2007). Anisotropic Small Strain Elastic Properties of Sands and Mixture of Sand-clay Measured by Dynamic and Static Methods. *Soils and Foundations*, *47*(3), 457–472.

https://doi.org/https://doi.org/10.3208/sandf.47.457

EN 13924-2. (2014). *Bitumen and bituminous binders — Specification framework for special paving grade bitumen — Part 2: Multigrade paving grade bitumens*.

EN NF 13108-1. (2017). *Mélanges bitumineux —Spécifications pour le matériau — Partie 1 :Enrobés bitumineux*.

Ferrotti, G., Canestrari, F., Pasquini, E., & Virgili, A. (2012). Experimental evaluation of the influence of surface coating on fiberglass geogrid performance in asphalt pavements. *Geotextiles and Geomembranes*, *34*, 11–18. https://doi.org/10.1016/j.geotexmem.2012.02.011

Freire, A. R. (2020). *Use of fiberglass geogrids to the reinforcement of bituminous mixtures layers* [ENTPE/Université de Lyon]. https://theses.hal.science/tel-03249370

Freire, A. R., Di Benedetto, H., Sauzéat, C., Pouget, S., & Lesueur, D. (2022). Linear viscoelastic behaviours of bituminous mixtures and fiberglass geogrids interfaces. *Geotextiles and Geomembranes*, *50*(5), 961–969. https://doi.org/10.1016/j.geotexmem.2022.06.003

Freire, R. A., Di Benedetto, H., Sauzéat, C., Pouget, S., & Lesueur, D. (2021). Crack propagation analysis in bituminous mixtures reinforced by different types of geogrids using digital image correlation. *Construction and Building Materials*, *303*(July). https://doi.org/10.1016/j.conbuildmat.2021.124522

G.Speight, J. (2016). Asphalt Chemistry. In *Asphalt Materials Science and Technology*. https://doi.org/10.1016/B978-0-12-800273-5.00006-4

Gayte, P. (2016). *Modélisation du comportement thermo-viscoplastique des enrobés bitumineux Pierre Gayte HAL Id : tel-02134154* (Issue May).

Gayte, P., Di Benedetto, H., Sauzéat, C., & Nguyen, Q. T. (2016). Influence of transient effects for analysis of complex modulus tests on bituminous mixtures. *Road Materials and Pavement Design*, *17*(2), 271–289. https://doi.org/10.1080/14680629.2015.1067246

Gharbi, M., Broutin, M., Schneider, T., Stephane, M., & Chabot, A. (2020). Towards an adapted ovalization system for flexible airfield pavement interface characterization using rolling-wheel or HWD loads. *Lecture Notes in Civil Engineering*, *96 LNCE*, 516–525. https://doi.org/10.1007/978-3-030-55236-7_53

Graziani, A., Canestrari, F., Cardone, F., & Ferrotti, G. (2017). Time–temperature superposition principle for interlayer shear strength of bituminous pavements. *Road Materials and Pavement Design*, *18*(March), 12–25. https://doi.org/10.1080/14680629.2017.1304247

Hight, D. W., Gens, A., & Symes, M. J. (1983). The development of a new hollow cylinder apparatus for investigating the effects of principal stress rotation in soils. *Géotechnique*, *33*(4), 355–383. https://doi.org/10.1680/geot.1983.33.4.355

Hristov, B. (2018). Master Function for Analytical Determination of the Interlayer Bond Shear Stiffness and Fatigue Functions for Asphalt Pavements. *MATEC Web of Conferences*, *251*. https://doi.org/10.1051/matecconf/201825101001

Isailović, I., Falchetto, A. C., & Wistuba, M. (2017). Fatigue investigation on asphalt mixture layers' interface. *Road Materials and Pavement Design*, *18*, 514–534.

https://doi.org/10.1080/14680629.2017.1389087

Isailović, I., & Wistuba, M. P. (2018). Asphalt mixture layers' interface bonding properties under monotonic and cyclic loading. *Construction and Building Materials*, *168*, 590–597. https://doi.org/10.1016/j.conbuildmat.2018.02.149

Jelagin, D., Olsson, E., Raab, C., & Partl, M. N. (2023). Experimental and numerical modelling of shear bonding between asphalt layers. *Road Materials and Pavement Design*, *24*(S1), 176–191. https://doi.org/10.1080/14680629.2023.2180298

Leutner, R. (1979). Untersuchung des Schichtenverbundes beim bituminösen Oberbau. *Bitumen*, *41*(3), 84–91.

Lévenard, F., Gaudefroy, V., Capron, I., Petiteau, C., Chailleux, E., & Bujoli, B. (2023). Alternative bio-based emulsifiers for road materials. *Road Materials and Pavement Design*, 1–9. https://doi.org/10.1080/14680629.2023.2202257

Liquidlabswa. (n.d.). *Asphalt Core Sampling*. Retrieved December 8, 2023, from https://www.liquidlabswa.com.au/asphalt-core-sampling/

Liu, Z., Yang, Q., & Gu, X. (2023). Assessment of Pavement Structural Conditions and Remaining Life Combining Accelerated Pavement Testing and Ground-Penetrating Radar. *Remote Sensing*, *15*(18). https://doi.org/10.3390/rs15184620

Mandel, J. (1969). Aperçu sur les principaux comportements rhéologique. In *La Réologie* (pp. 1–17). Masson.

Mangiafico, S., Babadopulos, L. F. A. L., Sauzéat, C., & Benedetto, H. Di. (2018). Nonlinearity of bituminous mixtures. *Mechanics of Time-Dependent Materials Volume*, *22*, 29–49. https://doi.org/https://doi.org/10.1007/s11043-017-9350-3

Mangiafico, Salvatore. (2014). *Linear viscoelastic properties and fatigue of bituminous mixtures produced with Reclaimed Asphalt Pavement and corresponding binder blends*. University of Lyon/ENTPE. [Doctoral dissertation].

Mohammad, L. N., Raqib, M. A., & Huang, B. (2002). Influence of asphalt tack coat materials on interface shear strength. *Transportation Research Record*, *1789*, 56–65. https://doi.org/10.3141/1789-06

Needham, D. (1996). *Developtments in bitumen emulsion mixtures for roads*. University of Nottingham.

NF EN 12607-1. (2014). *Bitumen and bituminous binders — Determination of the resistance to hardening under the influence of heat and air — Part 1: RTFOT method*.

NF EN 13043. (2003). *Aggregates for bituminous mixtures and surface treatments for roads, airfields and other trafficked areas*.

NF EN 1426. (2018). *Bitumen and bituminous binders - Determination of needle penetration*.

NF EN 1427. (2018). *Bitumen and bituminous binders - Determination of the softening point - Ring and Ball method*.

NF P 98-150-1. (2010). *Exécution des assises de chaussées, couches de liaison et couches de roulement. Partie 1 : Enrobé s hydrocarbonés à chaud — Constituants, formulation, fabrication, transport, mise en œuvre et cont rôle sur chantier*.

NF P 98-203-1. (1997). *Essais relatifs aux chaussées - Déformations dans les couches de chaussées - Partie 1 : essai d'ovalisation.*

Nguyen, Q. T. (2011). *Comportement thermomécanique des enrobés bitumineux sous sollicitations cycliques dans les domaines linéaire et non-linéaire [Thermomechanical behavior of bituminous mixtures under cyclic loading in the linear and non-linear domains]*.

Nguyen, Q. T., Di Benedetto, H., & Sauzéat, C. (2015). Linear and nonlinear viscoelastic behaviour of bituminous mixtures. *Materials and Structures/Materiaux et Constructions*, *48*(7), 2339–2351. https://doi.org/10.1617/s11527-014-0316-5

Nguyen, Q. T., Nguyen, M. L., Di Benedetto, H., Sauzéat, C., Chailleux, E., & Hoang, T. T. N. (2019). Nonlinearity of bituminous materials for small amplitude cyclic loadings. *Road Materials and Pavement Design*, *20*(7), 1571–1585. https://doi.org/10.1080/14680629.2018.1465452

Olard, F., & Di Benedetto, H. (2003). General "2S2P1D" Model and Relation Between the Linear Viscoelastic Behaviours of Bituminous Binders and Mixes. *Road Materials and Pavement Design*, *4*(2), 185–224. https://doi.org/10.1080/14680629.2003.9689946

Pasquini, E., Bocci, M., Ferrotti, G., & Canestrari, F. (2013). Laboratory characterisation and field validation of geogrid-reinforced asphalt pavements. *Road Materials and Pavement Design*, *14*(1), 17–35. https://doi.org/10.1080/14680629.2012.735797

Raab, C., & Partl, M. N. (2004a). Interlayer shear performance: Experience with different pavement structures. *Proceedings of the 3rd Eurasphalt & Eurobitmen Congress*.

Raab, C., & Partl, M. N. (2004b). Effect of tack coats on interlayer shear bond of pavements. *In: Road - the Arteries of Africa. 8th Conference on Asphalt Pavements for Southern Africa (CAPSA'04)*, 847–855.

Raab, Christiane, Abd El Halim, A. O., & Partl, M. N. (2012). Interlayer bond testing using a model material. *Construction and Building Materials*, *26*(1), 190–199. https://doi.org/10.1016/j.conbuildmat.2011.06.009

Raab, Christiane, & Partl, M. N. (2009). Interlayer bonding of binder, base and subbase layers of asphalt pavements: Long-term performance. *Construction and Building Materials*, *23*(8), 2926–2931. https://doi.org/10.1016/j.conbuildmat.2009.02.025

Ragni, D., Ferrotti, G., Petit, C., & Canestrari, F. (2020). Analysis of shear-torque fatigue test for bituminous pavement interlayers. *Construction and Building Materials*, *254*, 119309. https://doi.org/10.1016/j.conbuildmat.2020.119309

Ragni, D., Sudarsanan, N., Canestrari, F., & Kim, Y. R. (2021). Investigation into fatigue life of interface bond between asphalt concrete layers. *International Journal of Pavement Engineering*, *0*(0), 1–15. https://doi.org/10.1080/10298436.2021.1894420

Ragni, D., Takarli, M., Petit, C., Graziani, A., & Canestrari, F. (2020). Use of acoustic techniques to analyse interlayer shear-torque fatigue test in asphalt mixtures. *International Journal of Fatigue*, *131*(October 2019). https://doi.org/10.1016/j.ijfatigue.2019.105356

Raposeiras, A. C., Vega-Zamanillo, Á., Calzada-Pérez, M. Á., & Castro-Fresno, D. (2012). Influence of surface macro-texture and binder dosage on the adhesion between

bituminous pavement layers. *Construction and Building Materials*, *28*(1), 187–192. https://doi.org/10.1016/j.conbuildmat.2011.08.029

Raschia, S., Di Benedetto, H., Lamothe, S., Carter, A., Graziani, A., & Perraton, D. (2021). Thermo-rheological modelling of cement-bitumen treated materials in the small strain domain. *Transportation Geotechnics*, *31*(September). https://doi.org/10.1016/j.trgeo.2021.100647

Read, J., & Whiteoak, D. (2003). The Shell bitumen handbook. In *Read, J., & Whiteoak, D. (2003). The Shell bitumen handbook. Thomas Telford.* (p. 29). https://doi.org/10.1680/sbh.32200

Romanoschi, S. A., & Metcalf, J. B. (2001). Characterization of asphalt concrete layer interfaces. *Transportation Research Record*, *1778*, 132–139. https://doi.org/10.3141/1778-16

Roussel, J. M., Sauzéat, C., Di Benedetto, H., & Broutin, M. (2019). Numerical simulation of falling/heavy weight deflectometer test considering linear viscoelastic behaviour in bituminous layers and inertia effects. *Road Materials and Pavement Design*, *20*(sup1), S64–S78. https://doi.org/10.1080/14680629.2019.1587491

Salençon. (1983). *Visoélasticsité*. l'Ecole Nationale des Ponts et Chaussées.

Sauterey, R., Bonnot, J., Mucci, A., & de Boissoudy, A. (1972). Sollicitations Mécaniques Des Enrobés Dans Les Chaussées. *Journées d'information. Paris: Ministère de l'Equipement et Du Logement*, 7–20.

Sauzéat, C. (2003). *Comportement Du Sable Dans Le Domaine Des Petites et Moyennes Déformations: Rotations "d'axes" et Effets Visqueux*. Institut National des Sciences Appliquées de Lyon.

Sayao, A., & Vaid, Y. P. (1991). Critical assessment of stress nonuniformities in hollow cylinder test specimens. *Soils and Foundations*, *31*(1), 60–72. https://doi.org/10.3208/sandf1972.31.60

SETRA-LCPC. (1994). *Conception et dimensionnement des structures de chaussée*.

Somé, S. C., Feeser, A., Jaoua, M., & Le Corre, T. (2020). Mechanical characterization of asphalt mixes inter-layer bonding based on reptation theory. *Construction and Building Materials*, *242*. https://doi.org/10.1016/j.conbuildmat.2020.118063

Song, W., Shu, X., Huang, B., & Woods, M. (2016). Laboratory investigation of interlayer shear fatigue performance between open-graded friction course and underlying layer. *Construction and Building Materials*, *115*, 381–389. https://doi.org/10.1016/j.conbuildmat.2016.04.060

Speight, J. G. (2016a). Asphalt Technology. In *Asphalt Materials Science and Technology*. https://doi.org/10.1016/b978-0-12-800273-5.00009-x

Speight, J. G. (2016b). Test Methods for Aggregate and Asphalt Concrete. In *Asphalt Materials Science and Technology*. https://doi.org/10.1016/b978-0-12-800273-5.00005-2

Sybilski, D., Gajewski, M., Bankowski, W., Soenen, H., Chailleux, E., & Gauthier, G. (2009). Binder fatigue properties and the results of the Rilem Round Robin Test. *Advanced Testing and Characterization of Bituminous Materials, August 2015*. https://doi.org/10.1201/9780203092989.ch118

Tapsoba, N., Sauzéat, C., & Di Benedetto, H. (2013). Analysis of Fatigue Test for Bitumen Mixtures. *Journal of Materials in Civil Engineering, ASCE*, *25*(6), 701–710. https://doi.org/https://doi.org/10.1061/(ASCE)MT.1943-5533.0000636

Tapsoba, Nouffou. (2012). *Comportement des enrobés bitumineux à base de matériaux recyclés et / ou fabriqués à température réduite*. 266.

Tozzo, C., Fiore, N., & D'Andrea, A. (2014). Dynamic shear tests for the evaluation of the effect of the normal load on the interface fatigue resistance. *Construction and Building Materials*, *61*, 200–205. https://doi.org/10.1016/j.conbuildmat.2014.03.010

Tran, T. Nhan, Mangiafico, S., Sauzéat, C., & Di Benedetto, H. (2022a). Bituminous Interlayers Thermomechanical Behaviour under Small Shear Strain Loading Cycles with 2T3C Apparatus: Hollow Cylinder and Digital Image Correlation. *The Proceedings of The 1st International Online Conference on Infrastructures*, 26. https://doi.org/10.3390/engproc2022017026

Tran, T. Nhan, Mangiafico, S., Sauzéat, C., & Di Benedetto, H. (2022b). Characterization of interface between bituminous layers under shear loading cycles using 2T3C apparatus. *Eleventh International Conference on the Bearing Capacity of Roads, Railways and Airfields, Volume 2*, *2*, 477–486. https://doi.org/10.1201/9781003222897-44

Tran, Thien Nhan, Mangiafico, S., Attia, T., Sauzéat, C., & Benedetto, H. Di. (2023). Linear and nonlinear thermomechanical behaviour of interface between bituminous mixtures layers : results from 2T3C apparatus and modelling. *Road Materials and Pavement Design*, *24*(sup1), S521–S537. https://doi.org/10.1080/14680629.2023.2181009

West, R. C., Zang, J., & Moore, J. (2005). *Evaluation of bond strength between pavement layers (NCAT Report 05-08)*. https://rosap.ntl.bts.gov/view/dot/27815

Williams, M. L., Landel, R. F., & Ferry, J. D. (1955). The Temperature Dependence of Relaxation Mechanisms in Amorphous Polymers and Other Glass-forming Liquids. *Journal of the American Chemical Society*, *77*(14), 3701–3707. https://doi.org/10.1021/ja01619a008

Yarranton, H. (2000). Asphaltene deposition. In *Canadian International Petroleum Conference 2000, CIPC 2000*. https://doi.org/10.1016/b978-0-12-800273-5.00007-6

LIST OF FIGURES

LIST OF TABLES

Appendix A: COMPLEX MODULI FOR BITUMINOUS MIXTURES AND COMPLEX INTERFACE STIFFNESS

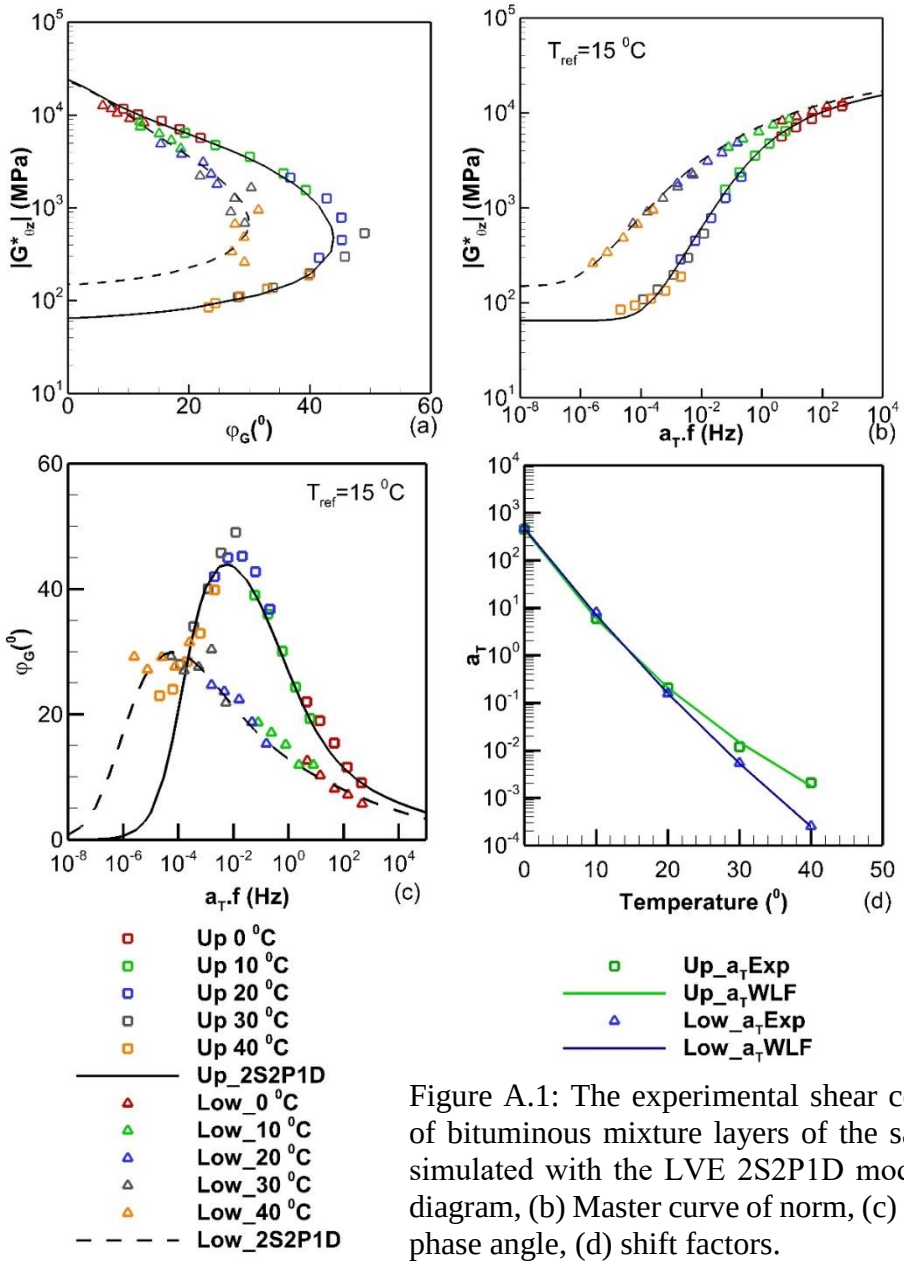

Figure A.1: The experimental shear complex moduli of bituminous mixture layers of the sample REFA-2 simulated with the LVE 2S2P1D model: (a) Black's diagram, (b) Master curve of norm, (c) master curve of phase angle, (d) shift factors.

Table A.1: The calibrating parameters for the 2S2P1D model and WLF modelling of bituminous mixture layers of the sample REFA-2

Layer	$G_{\theta z\_00}$ (MPa)	$G_{\theta z\_0}$ (MPa)	k	h	δ	τ_G (s)	β	C1	C2 (°C)
Upper	65	24000	0.17	0.57	2.10	0.033	150	11.70	81.15
Lower	150	23200	0.18	0.50	3.50	3.14	550	29.87	182.23

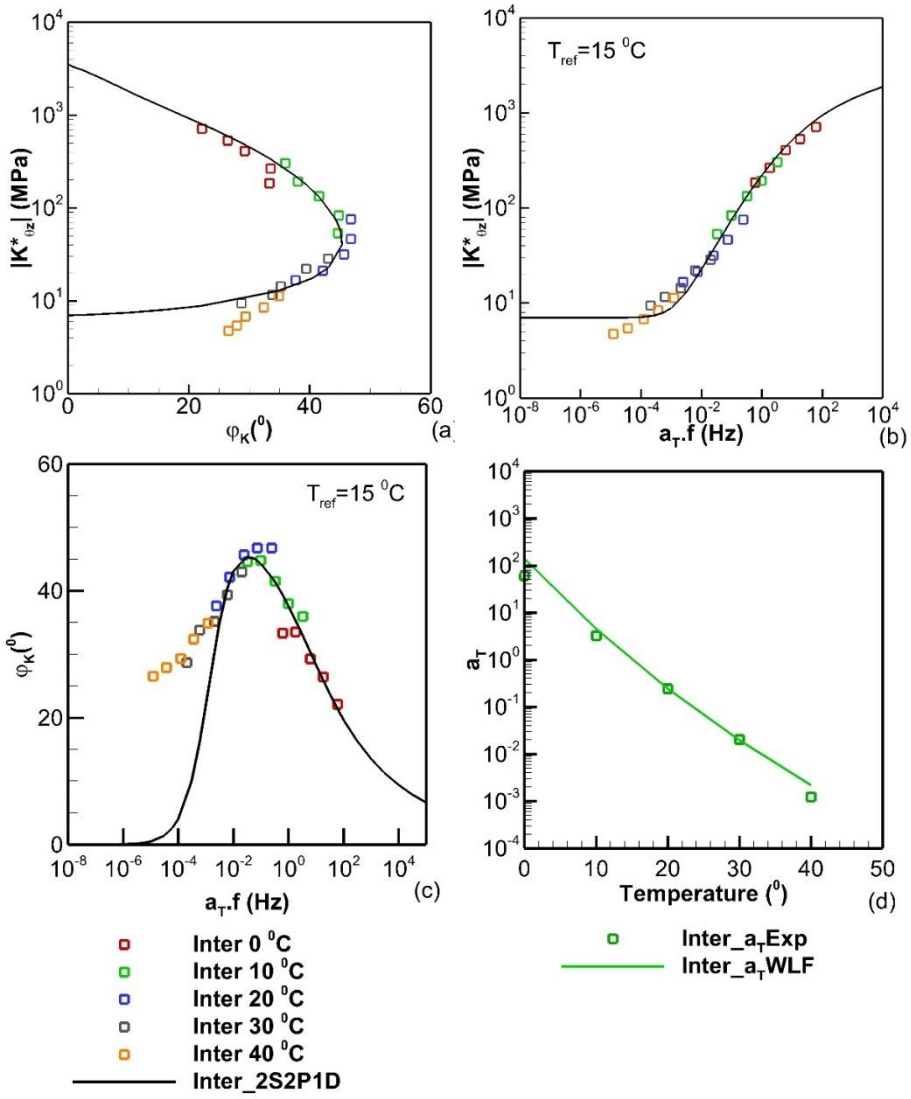

Figure A.2: The experimental shear complex interface stiffness of the sample REFA-2 simulated with the LVE 2S2P1D model: (a) Black's diagram, (b) Master curve of norm, (c) master curve of phase angle, (d) shift factors.

Table A.2: The calibrating parameters for the 2S2P1D model and WLF modelling of the interface of the sample REFA-2

Sample	$K_{\theta z\_00}$ (MPa/mm)	$K_{\theta z\_0}$ (MPa/mm)	k	h	δ	τ_K (s)	β	C1	C2 (°C)
REFA-2	7.0	3500	0.20	0.56	2.30	0.0024	120	16.61	131.00

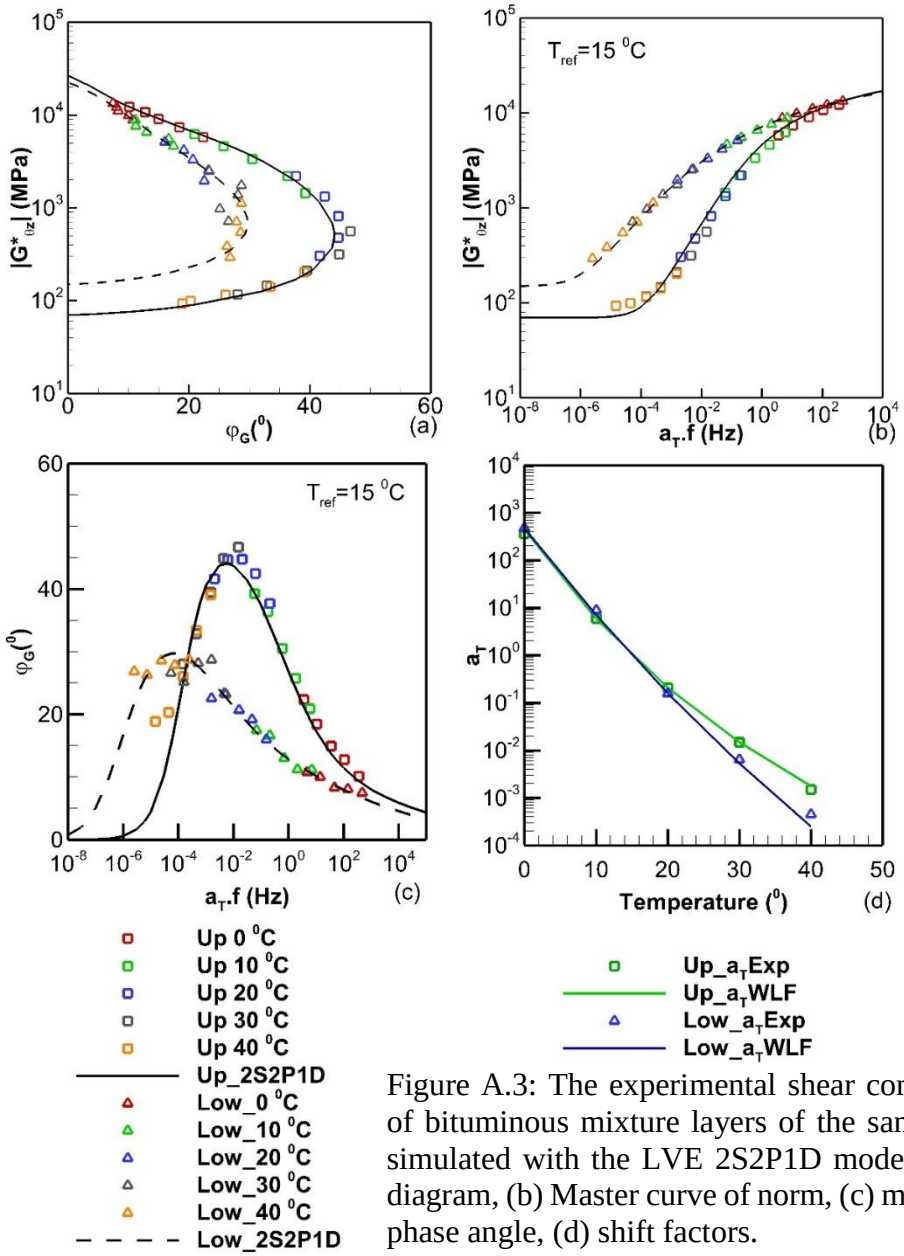

Figure A.3: The experimental shear complex moduli of bituminous mixture layers of the sample REFA-3 simulated with the LVE 2S2P1D model: (a) Black's diagram, (b) Master curve of norm, (c) master curve of phase angle, (d) shift factors.

Table A.3: The calibrating parameters for the 2S2P1D model and WLF modelling of the two bituminous mixtures of the sample REFA-3

Layer	$G_{\theta z\_00}$ (MPa)	$G_{\theta z\_0}$ (MPa)	k	h	δ	τ_G (s)	β	C1	C2 (°C)
Upper	70	26500	0.17	0.57	2.10	0.033	150	11.70	81.15
Lower	150	22500	0.18	0.50	3.50	3.14	550	29.87	182.23

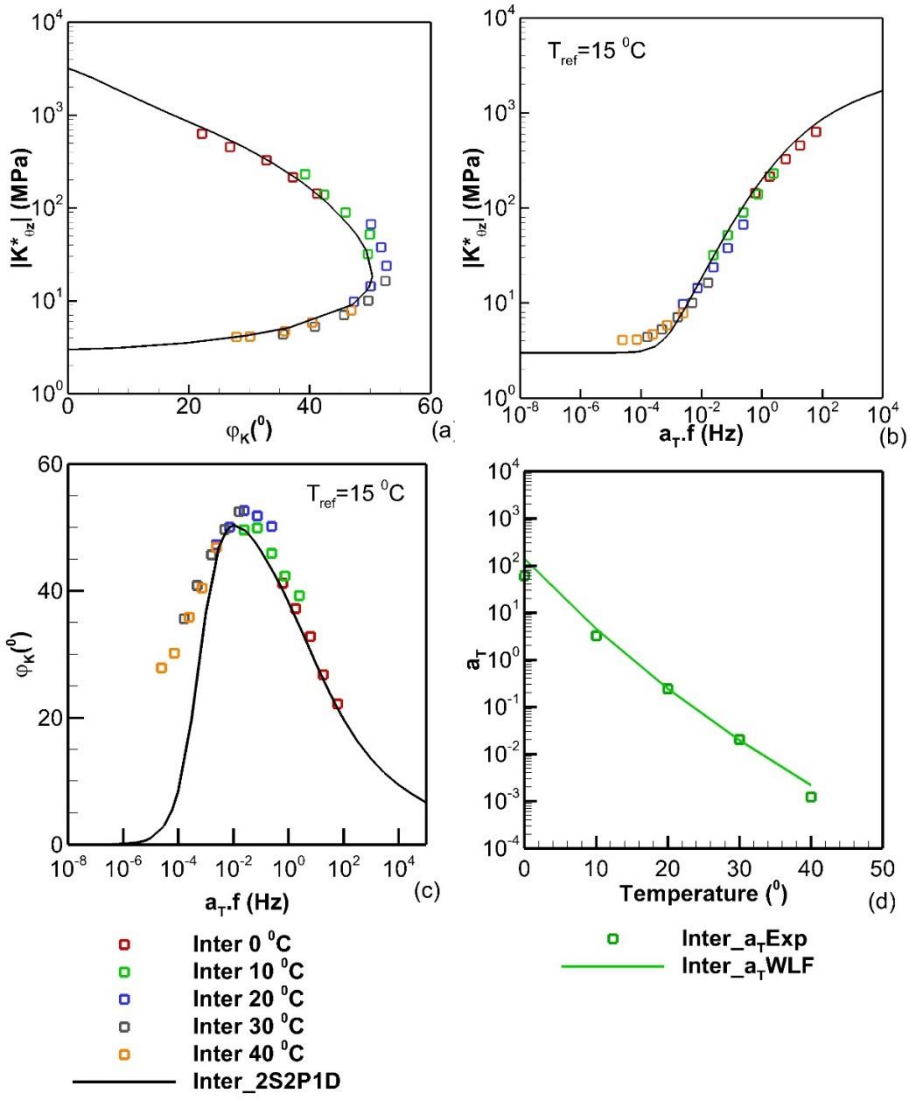

Figure A.4: The experimental shear complex interface stiffness of the sample REFA-3 simulated with the LVE 2S2P1D model: (a) Black's diagram, (b) Master curve of norm, (c) master curve of phase angle, (d) shift factors.

Table A.4: The calibrating parameters for the 2S2P1D model and WLF modelling of the interface of the sample REFA-3

Sample	$K_{\theta z\_00}$ (MPa/mm)	$K_{\theta z\_0}$ (MPa/mm)	k	h	δ	τ_K (s)	β	C1	C2 (°C)
REFA-3	3.0	3200	0.20	0.56	2.30	0.0024	120	16.61	131.00

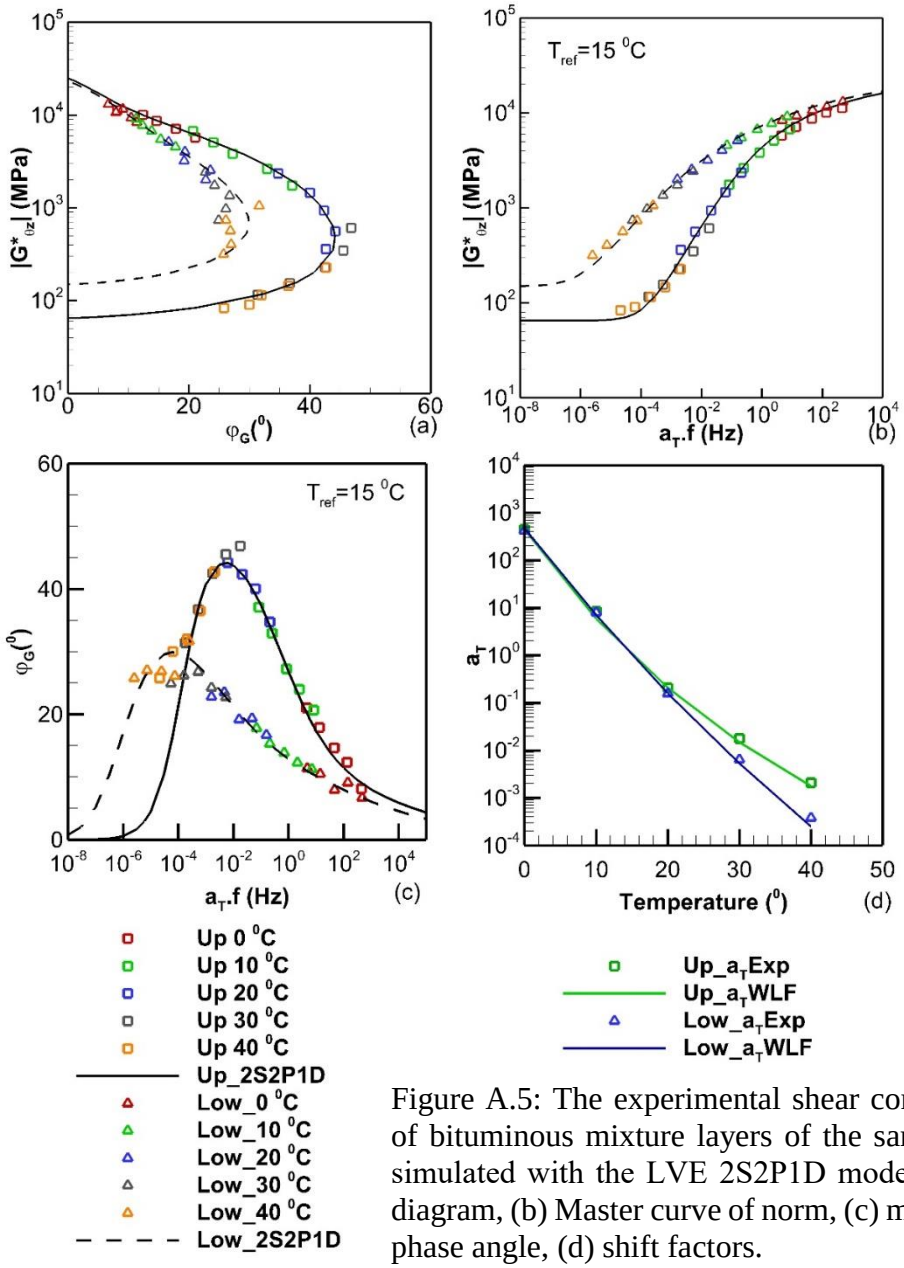

Figure A.5: The experimental shear complex moduli of bituminous mixture layers of the sample REFB-1 simulated with the LVE 2S2P1D model: (a) Black's diagram, (b) Master curve of norm, (c) master curve of phase angle, (d) shift factors.

Table A.5: The calibrating parameters for the 2S2P1D model and WLF modelling of the two bituminous mixtures of the sample REFB-1

Layer	$G_{\theta z\_00}$ (MPa)	$G_{\theta z\_0}$ (MPa)	k	h	δ	τ_G (s)	β	C1	C2 (°C)
Upper	65	25000	0.17	0.57	2.10	0.033	150	11.70	81.15
Lower	150	23200	0.18	0.50	3.50	3.14	550	29.87	182.23

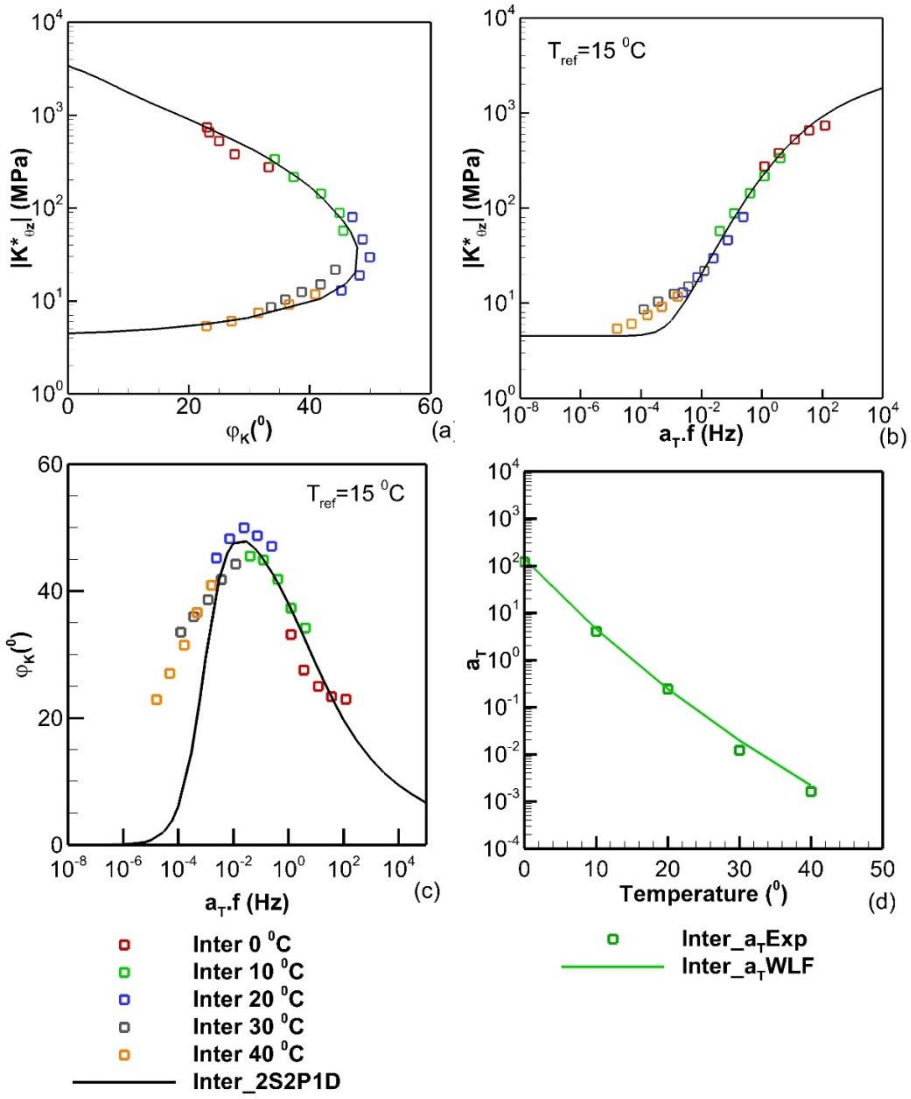

Figure A.6: The experimental shear complex interface stiffness of the sample REFB-1 simulated with the LVE 2S2P1D model: (a) Black's diagram, (b) Master curve of norm, (c) master curve of phase angle, (d) shift factors.

Table A.6: The calibrating parameters for the 2S2P1D model and WLF modelling of the interface of the sample REFB-1

Sample	$K_{\theta z\_00}$ (MPa/mm)	$K_{\theta z\_0}$ (MPa/mm)	k	h	δ	τ_K (s)	β	C1	C2 (°C)
REFB-1	4.5	3400	0.20	0.56	2.30	0.0024	120	16.61	131.00

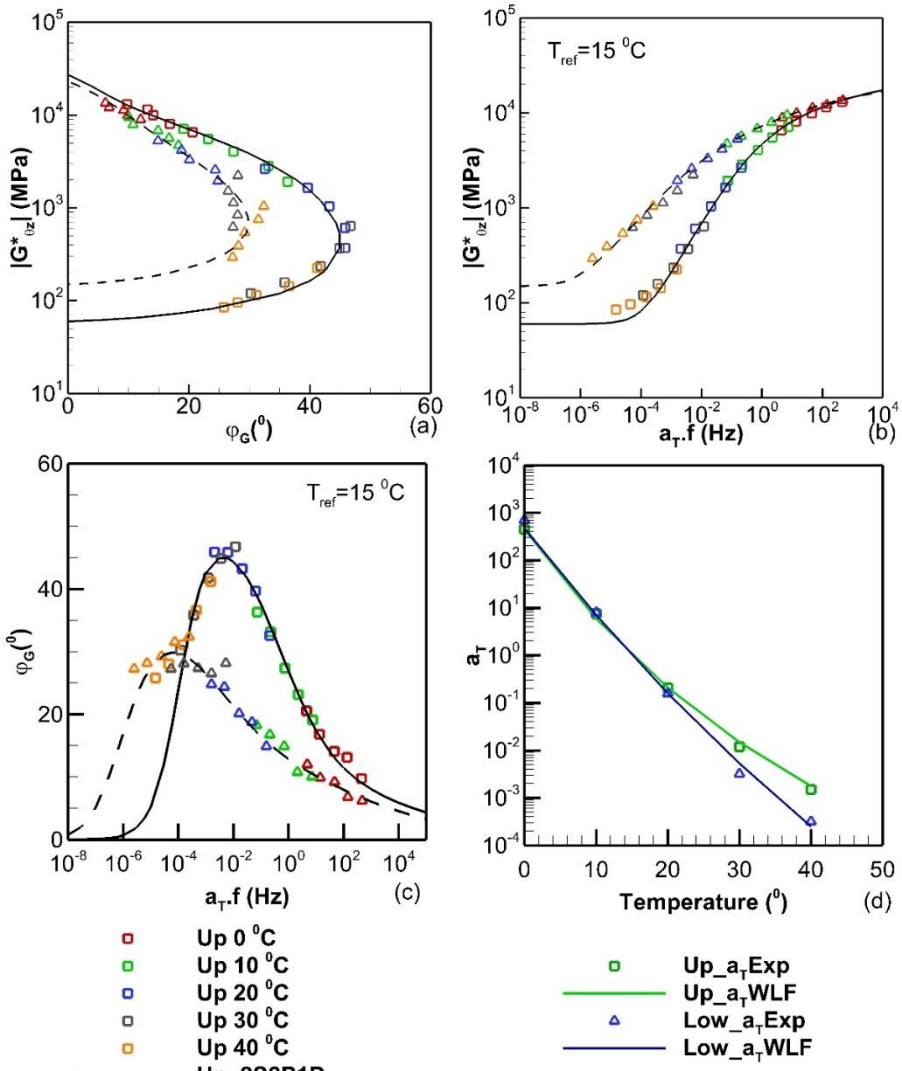

Figure A.7: The experimental shear complex moduli of bituminous mixture layers of the sample REFB-2 simulated with the LVE 2S2P1D model: (a) Black's diagram, (b) Master curve of norm, (c) master curve of phase angle, (d) shift factors.

Table A.7: The calibrating parameters for the 2S2P1D model and WLF modelling of the two bituminous mixtures of the sample REFB-2

Layer	$G_{\theta z\_00}$ (MPa)	$G_{\theta z\_0}$ (MPa)	k	h	δ	τ_G (s)	β	C1	C2 (°C)
Upper	60	27000	0.17	0.57	2.10	0.033	150	11.70	81.15
Lower	150	23000	0.18	0.50	3.50	3.14	550	29.87	182.23

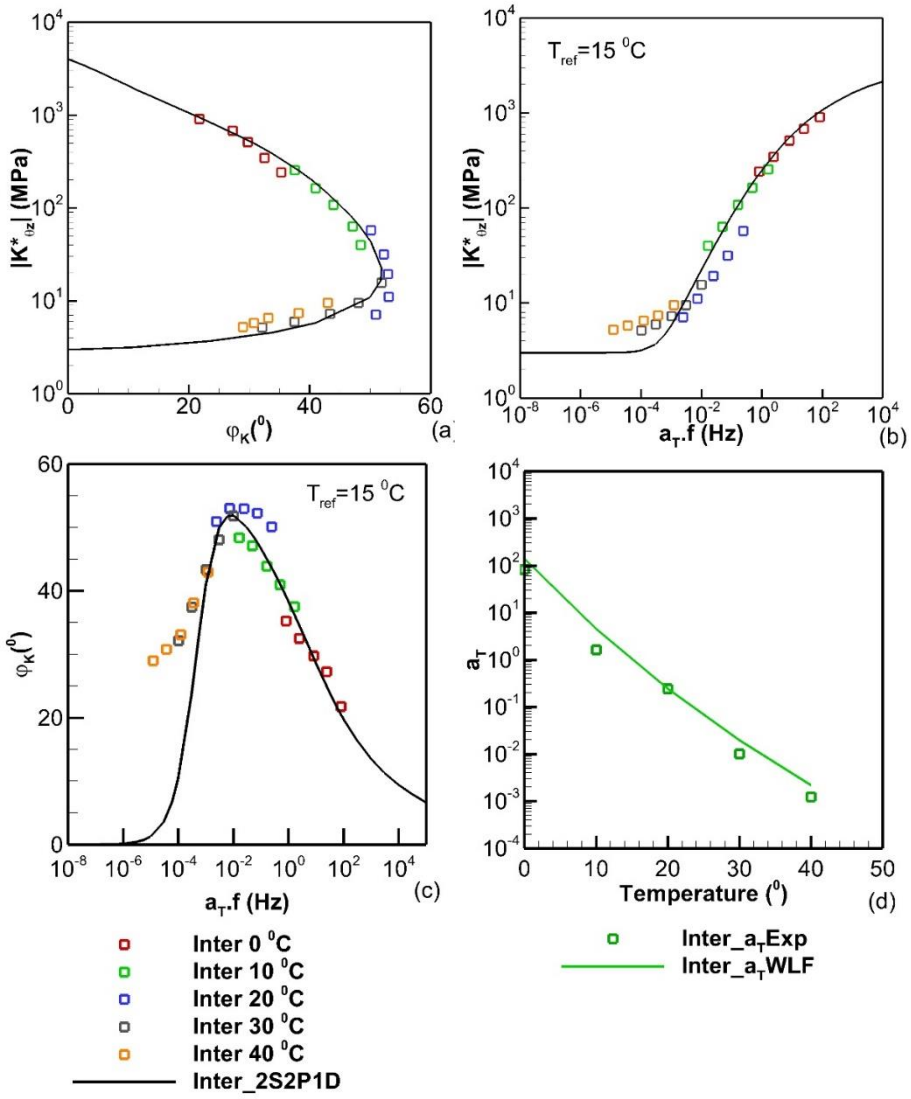

Figure A.8: The experimental shear complex interface stiffness of the sample REFB-2 simulated with the LVE 2S2P1D model: (a) Black's diagram, (b) Master curve of norm, (c) master curve of phase angle, (d) shift factors.

Table A.8: The calibrating parameters for the 2S2P1D model and WLF modelling of the interface of the sample REFB-2

Sample	$K_{\theta z\_00}$ (MPa/mm)	$K_{\theta z\_0}$ (MPa/mm)	k	h	δ	τ_K (s)	β	C1	C2 (°C)
REFB-2	3.0	4000	0.20	0.56	2.30	0.0024	120	16.61	131.00

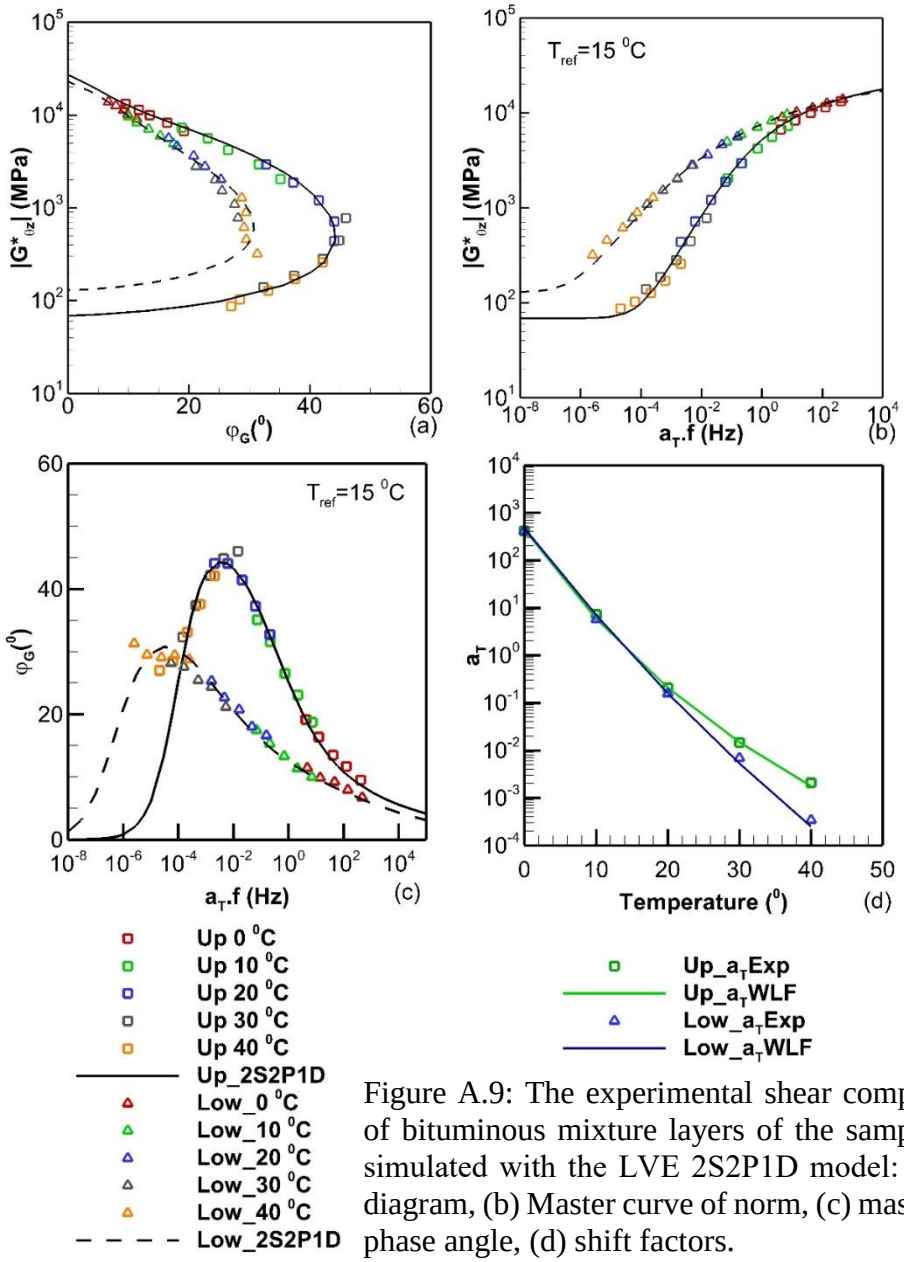

Figure A.9: The experimental shear complex moduli of bituminous mixture layers of the sample REFC-1 simulated with the LVE 2S2P1D model: (a) Black's diagram, (b) Master curve of norm, (c) master curve of phase angle, (d) shift factors.

Table A.9: The calibrating parameters for the 2S2P1D model and WLF modelling of the two bituminous mixtures of the sample REFC-1

Layer	$G_{\theta z\_00}$ (MPa)	$G_{\theta z\_0}$ (MPa)	k	h	δ	τ_G (s)	β	C1	C2 (°C)
Upper	69	27000	0.17	0.57	2.10	0.033	150	11.70	81.15
Lower	130	23000	0.18	0.50	3.50	3.14	550	29.87	182.23

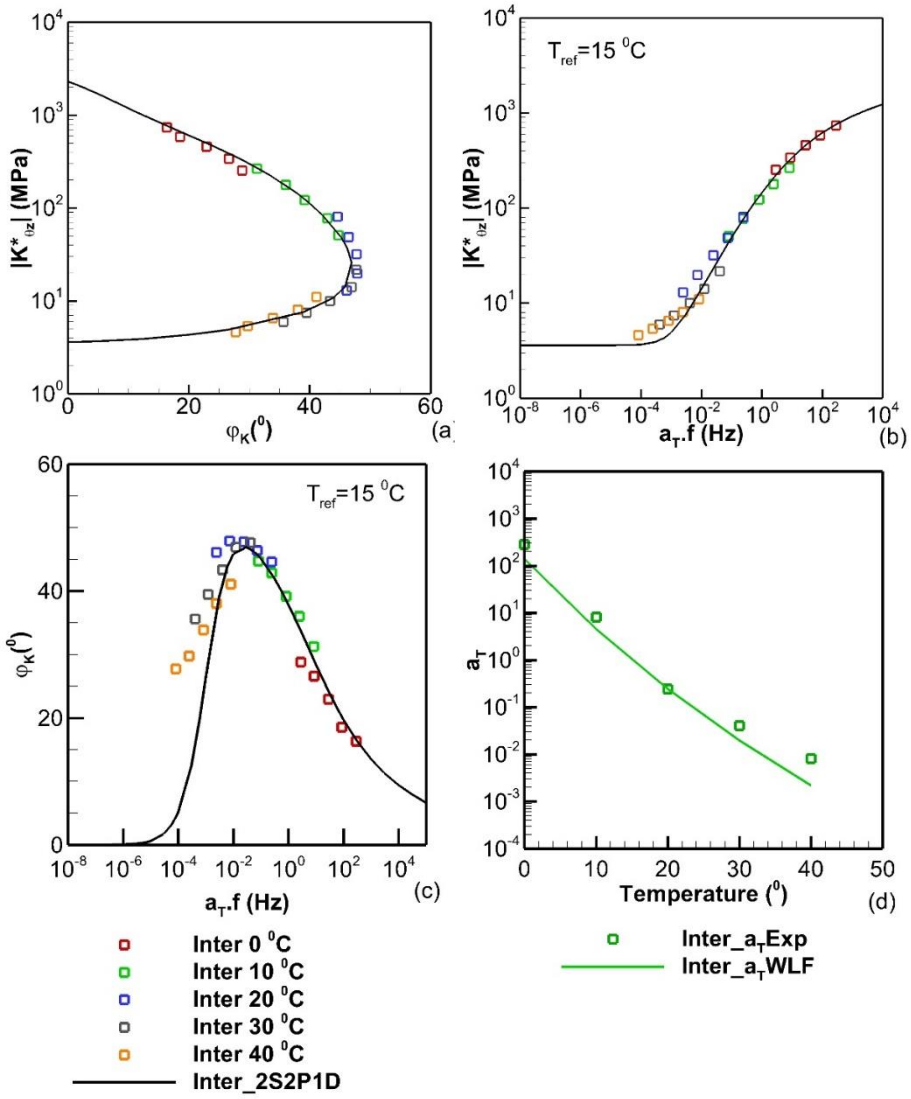

Figure A.10: The experimental shear complex interface stiffness of the sample REFC-1 simulated with the LVE 2S2P1D model: (a) Black's diagram, (b) Master curve of norm, (c) master curve of phase angle, (d) shift factors.

Table A.10: The calibrating parameters for the 2S2P1D model and WLF modelling of the interface of the sample REFC-1

Sample	$K_{\theta z\_00}$ (MPa/mm)	$K_{\theta z\_0}$ (MPa/mm)	k	h	δ	τ_K (s)	β	C1	C2 (°C)
REFC-1	3.6	2300	0.20	0.56	2.30	0.0024	120	16.61	131.00

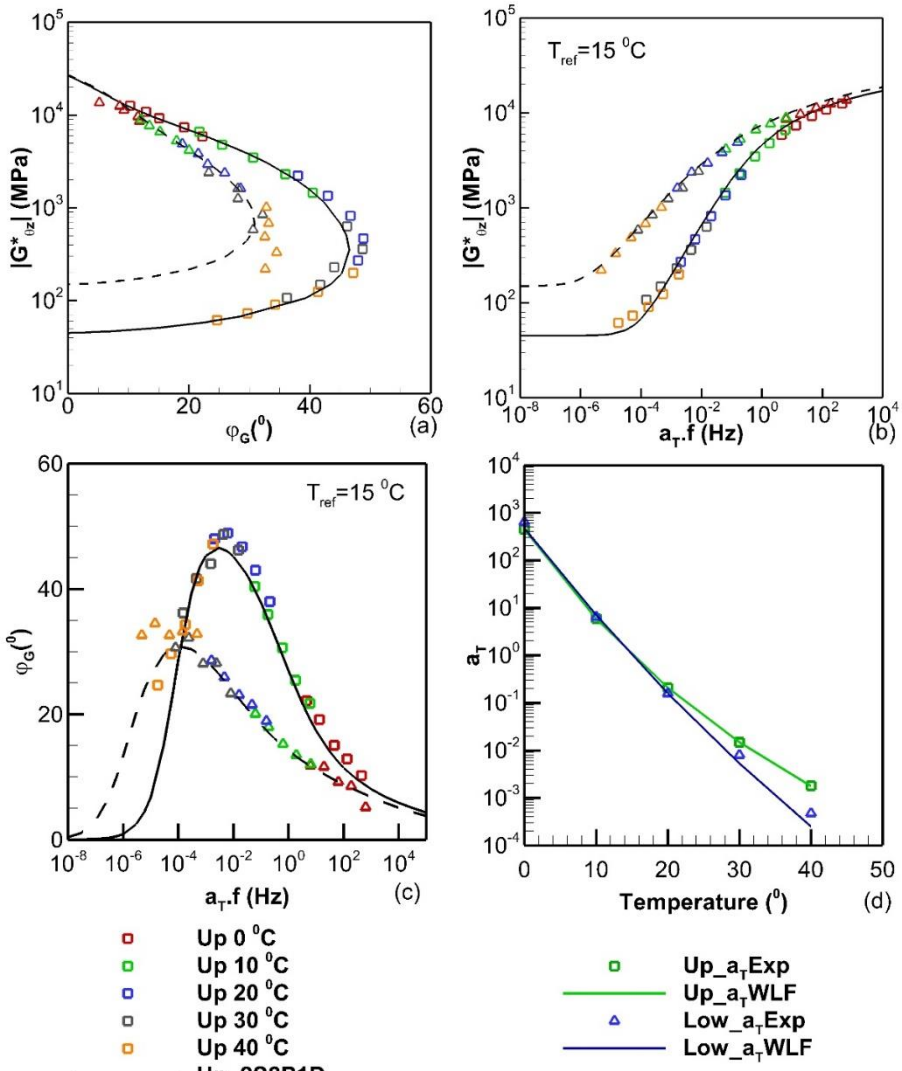

Figure A.11: The experimental shear complex moduli of bituminous mixture layers of the sample REFC-2 simulated with the LVE 2S2P1D model: (a) Black's diagram, (b) Master curve of norm, (c) master curve of phase angle, (d) shift factors.

Table A.11: The calibrating parameters for the 2S2P1D model and WLF modelling of the two bituminous mixtures of the sample REFC-2

Layer	$G_{\theta z\_00}$ (MPa)	$G_{\theta z\_0}$ (MPa)	k	h	δ	τ_G (s)	β	C1	C2 (°C)
Upper	45	26500	0.17	0.57	2.10	0.033	150	11.70	81.15
Lower	150	27000	0.18	0.50	3.50	3.14	550	29.87	182.23

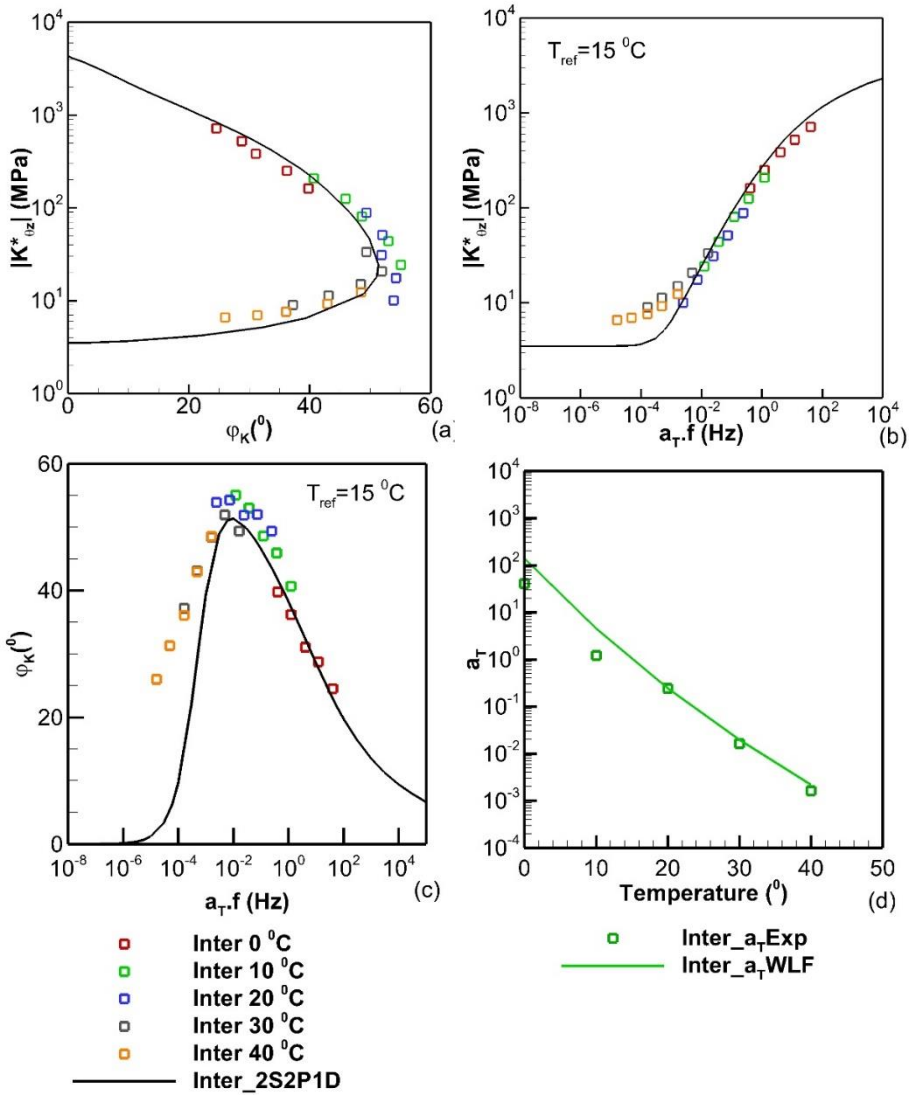

Figure A.12: The experimental shear complex interface stiffness of the sample REFC-2 simulated with the LVE 2S2P1D model: (a) Black's diagram, (b) Master curve of norm, (c) master curve of phase angle, (d) shift factors.

Table A.12: The calibrating parameters for the 2S2P1D model and WLF modelling of the interface of the sample REFC-2

Sample	$K_{\theta z\_00}$ (MPa/mm)	$K_{\theta z\_0}$ (MPa/mm)	k	h	δ	τ_K (s)	β	C1	C2 (°C)
REFC-2	3.5	4300	0.20	0.56	2.30	0.0024	120	16.61	131.00

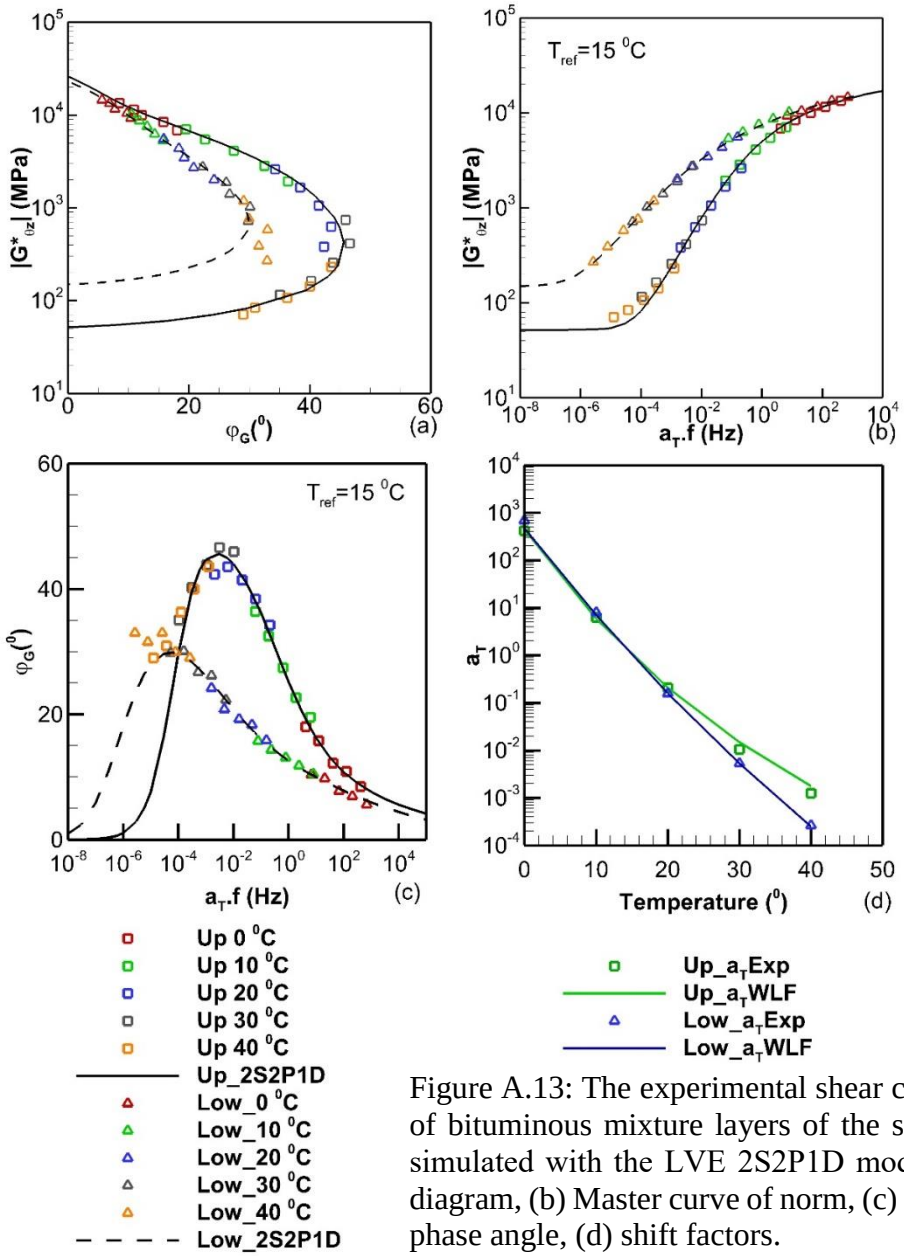

Figure A.13: The experimental shear complex moduli of bituminous mixture layers of the sample REFC-3 simulated with the LVE 2S2P1D model: (a) Black's diagram, (b) Master curve of norm, (c) master curve of phase angle, (d) shift factors.

Table A.13: The calibrating parameters for the 2S2P1D model and WLF modelling of the two bituminous mixtures of the sample REFC-3

Layer	$G_{\theta z\_00}$ (MPa)	$G_{\theta z\_0}$ (MPa)	k	h	δ	τ_G (s)	β	C1	C2 (°C)
Upper	52	26000	0.17	0.57	2.10	0.033	150	11.70	81.15
Lower	150	23000	0.18	0.50	3.50	3.14	550	29.87	182.23

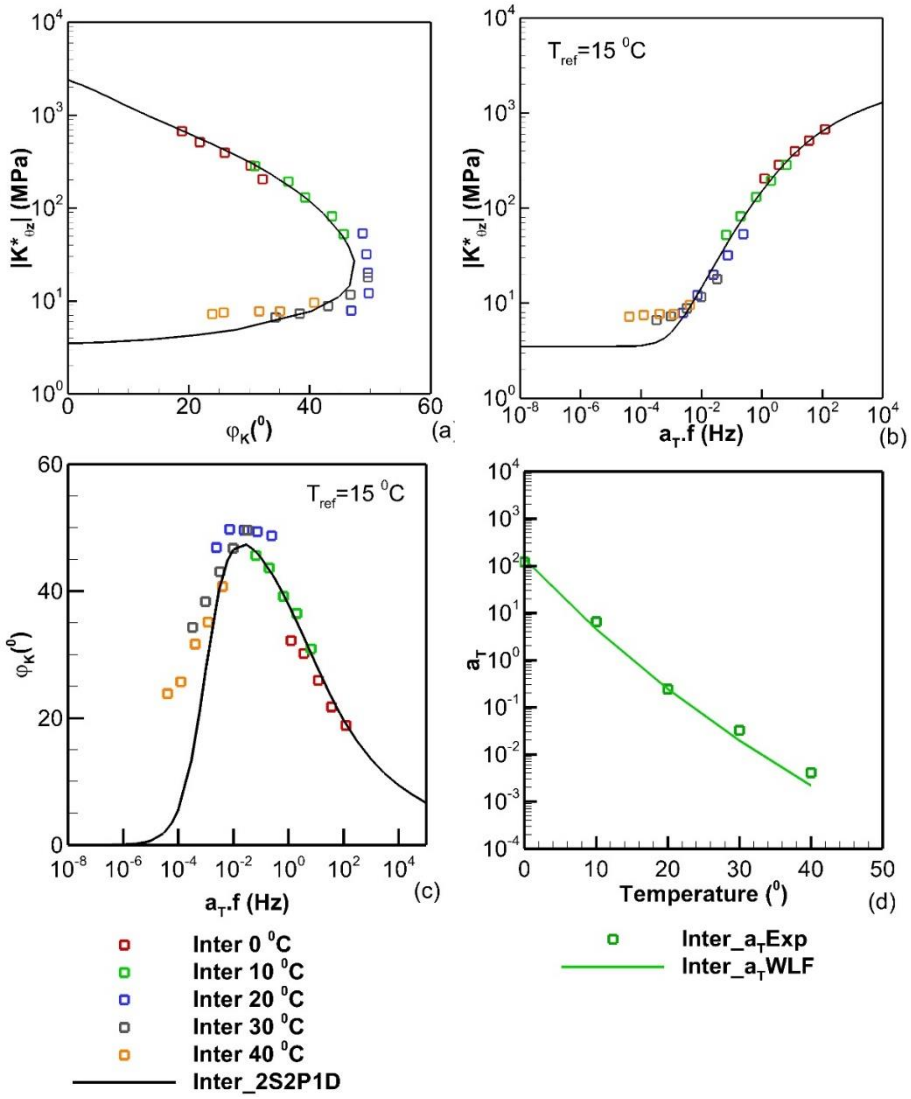

Figure A.14: The experimental shear complex interface stiffness of the sample REFC-3 simulated with the LVE 2S2P1D model: (a) Black's diagram, (b) Master curve of norm, (c) master curve of phase angle, (d) shift factors.

Table A.14: The calibrating parameters for the 2S2P1D model and WLF modelling of the interface of the sample REFC-3

Sample	$K_{\theta z\_00}$ (MPa/mm)	$K_{\theta z\_0}$ (MPa/mm)	k	h	δ	τ_K (s)	β	C1	C2 (°C)
REFC-3	3.5	2400	0.20	0.56	2.30	0.0024	120	16.61	131.00

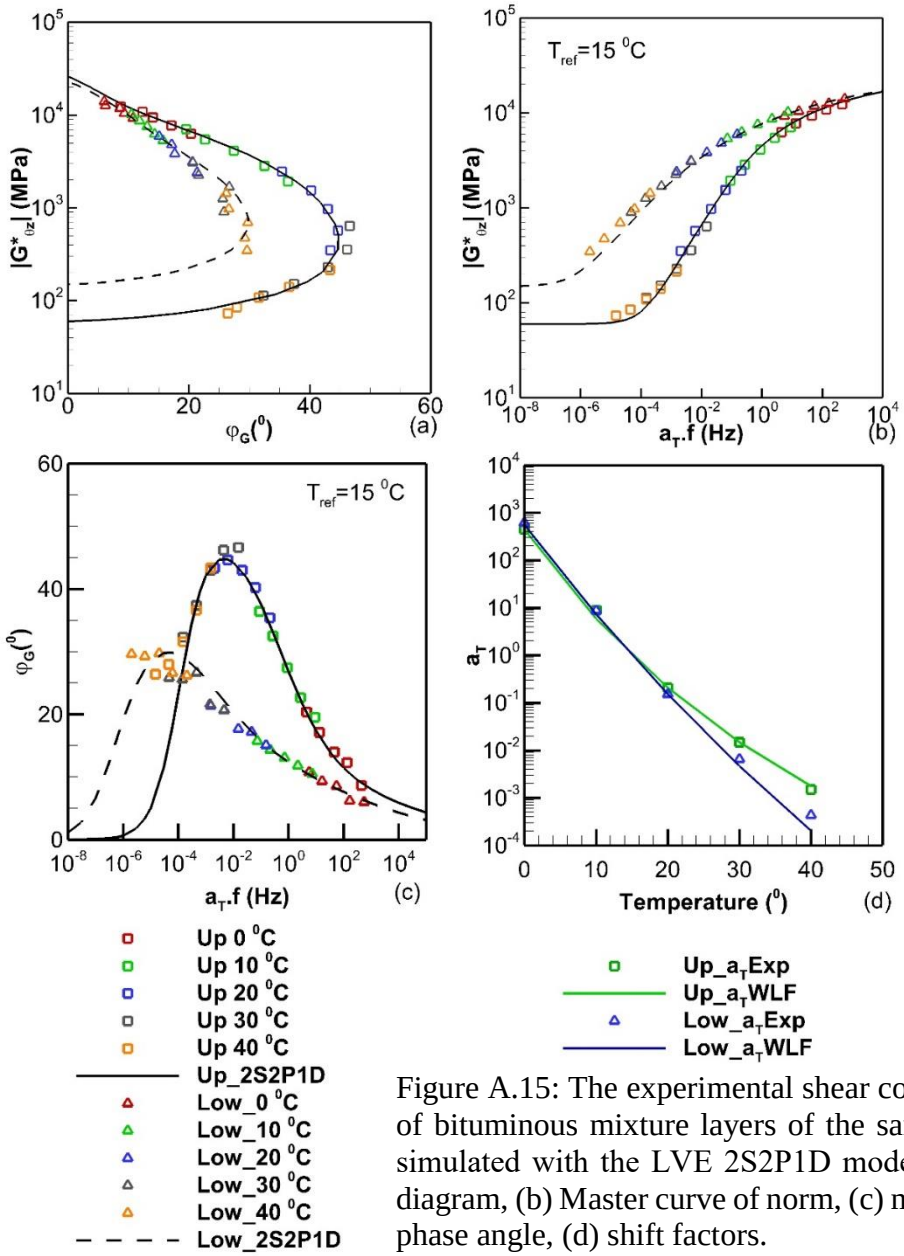

Figure A.15: The experimental shear complex moduli of bituminous mixture layers of the sample REFD-1 simulated with the LVE 2S2P1D model: (a) Black's diagram, (b) Master curve of norm, (c) master curve of phase angle, (d) shift factors.

Table A.15: The calibrating parameters for the 2S2P1D model and WLF modelling of the two bituminous mixtures of the sample REFD-1

Layer	$G_{\theta z\_00}$ (MPa)	$G_{\theta z\_0}$ (MPa)	k	h	δ	τ_G (s)	β	C1	C2 (°C)
Upper	60	26000	0.17	0.57	2.10	0.033	150	11.70	81.15
Lower	150	23000	0.18	0.50	3.50	3.14	550	29.87	182.23

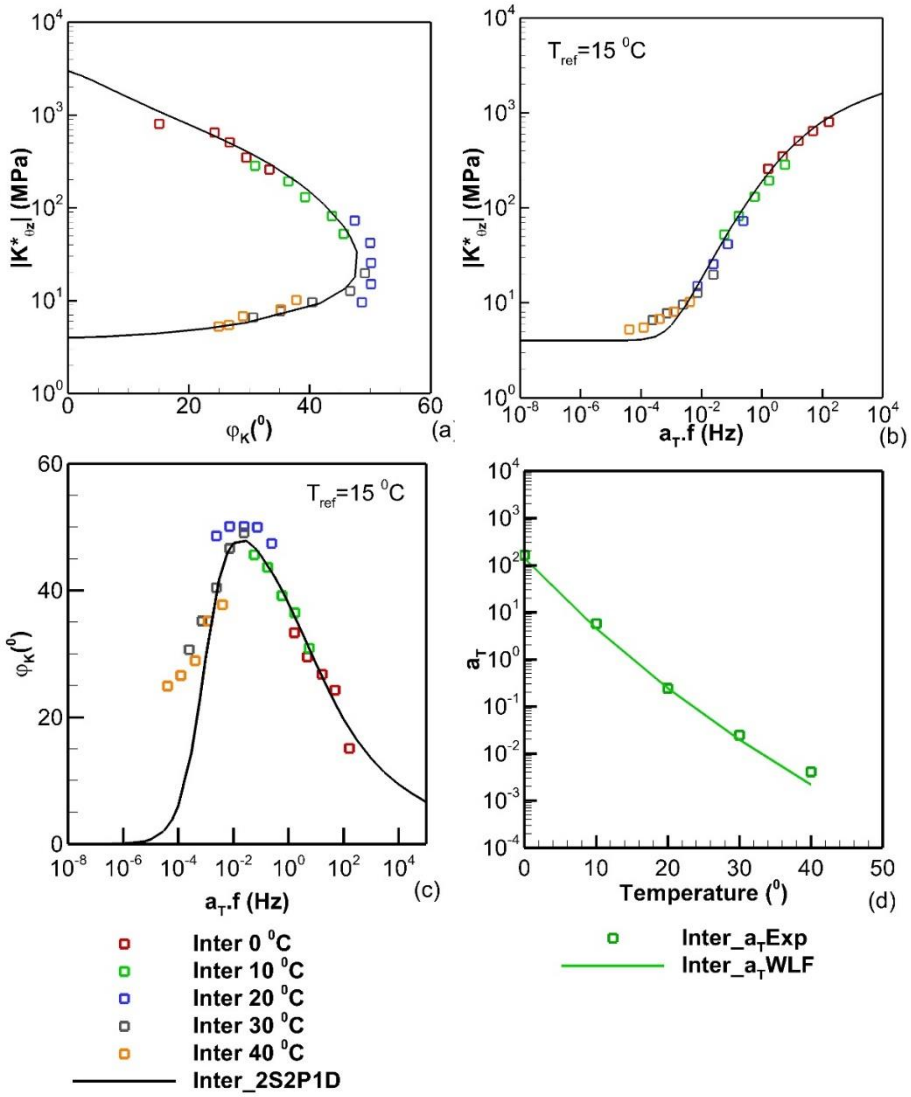

Figure A.16: The experimental shear complex interface stiffness of the sample REFD-1 simulated with the LVE 2S2P1D model: (a) Black's diagram, (b) Master curve of norm, (c) master curve of phase angle, (d) shift factors.

Table A.16: The calibrating parameters for the 2S2P1D model and WLF modelling of the interface of the sample REFD-1

Sample	$K_{\theta z\_00}$ (MPa/mm)	$K_{\theta z\_0}$ (MPa/mm)	k	h	δ	τ_K (s)	β	C1	C2 (°C)
REFD-1	4.0	3000	0.20	0.56	2.30	0.0024	120	16.61	131.00

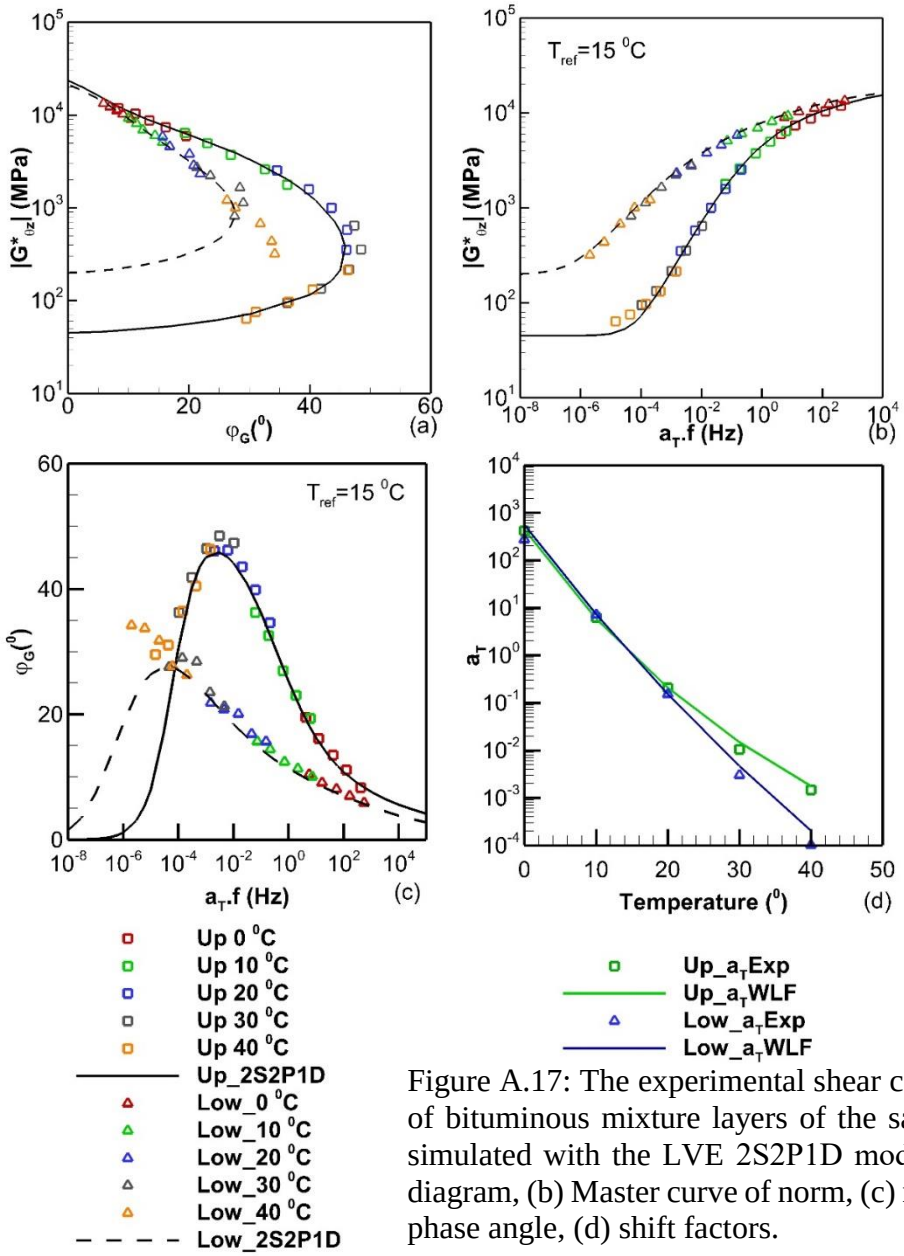

Figure A.17: The experimental shear complex moduli of bituminous mixture layers of the sample REFD-2 simulated with the LVE 2S2P1D model: (a) Black's diagram, (b) Master curve of norm, (c) master curve of phase angle, (d) shift factors.

Table A.17: The calibrating parameters for the 2S2P1D model and WLF modelling of the two bituminous mixtures of the sample REFD-2

Layer	$G_{\theta z\_00}$ (MPa)	$G_{\theta z\_0}$ (MPa)	k	h	δ	τ_G (s)	β	C1	C2 (°C)
Upper	45	23500	0.17	0.57	2.10	0.033	150	11.70	81.15
Lower	200	21300	0.18	0.50	3.50	3.14	550	29.87	182.23

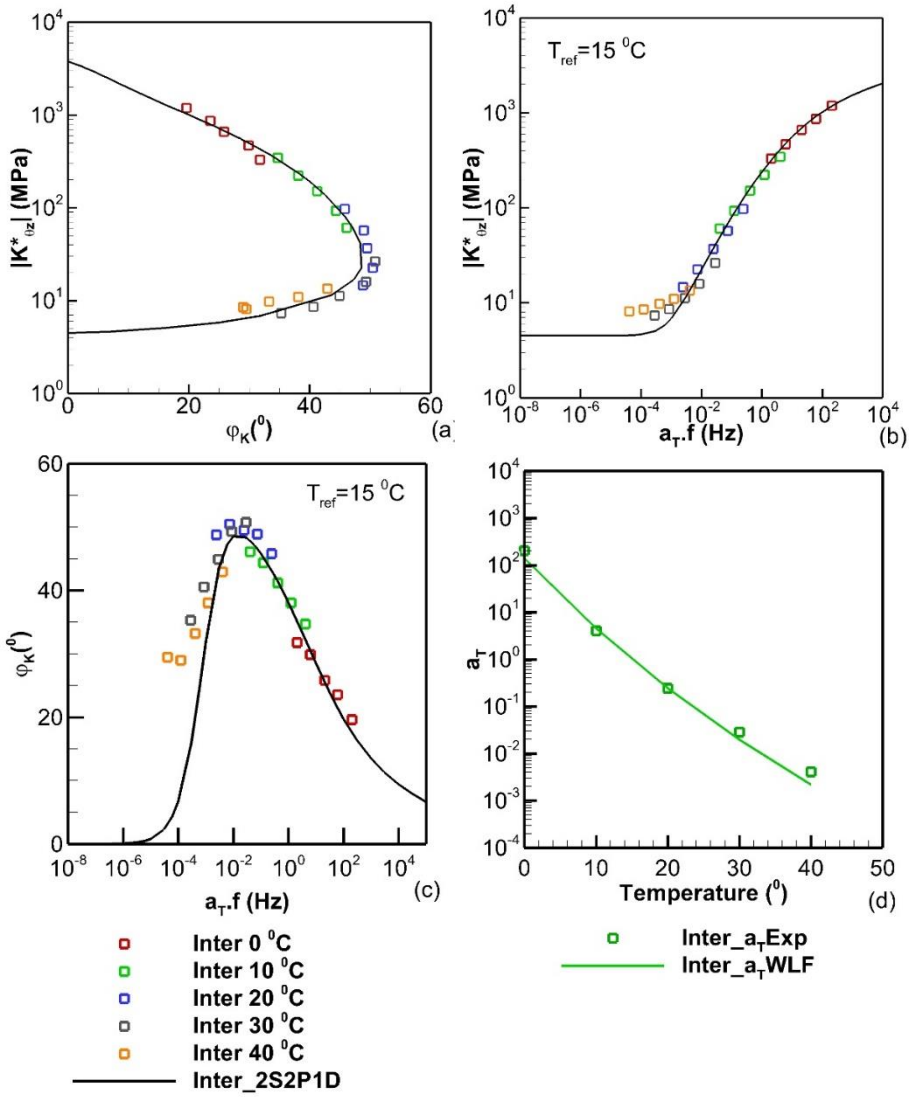

Figure A.18: The experimental shear complex interface stiffness of the sample REFD-2 simulated with the LVE 2S2P1D model: (a) Black's diagram, (b) Master curve of norm, (c) master curve of phase angle, (d) shift factors.

Table A.18: The calibrating parameters for the 2S2P1D model and WLF modelling of the interface of the sample REFD-2

Sample	$K_{\theta z\_00}$ (MPa/mm)	$K_{\theta z\_0}$ (MPa/mm)	k	h	δ	τ_K (s)	β	C1	C2 (°C)
REFD-2	4.5	3800	0.20	0.56	2.30	0.0024	120	16.61	131.00

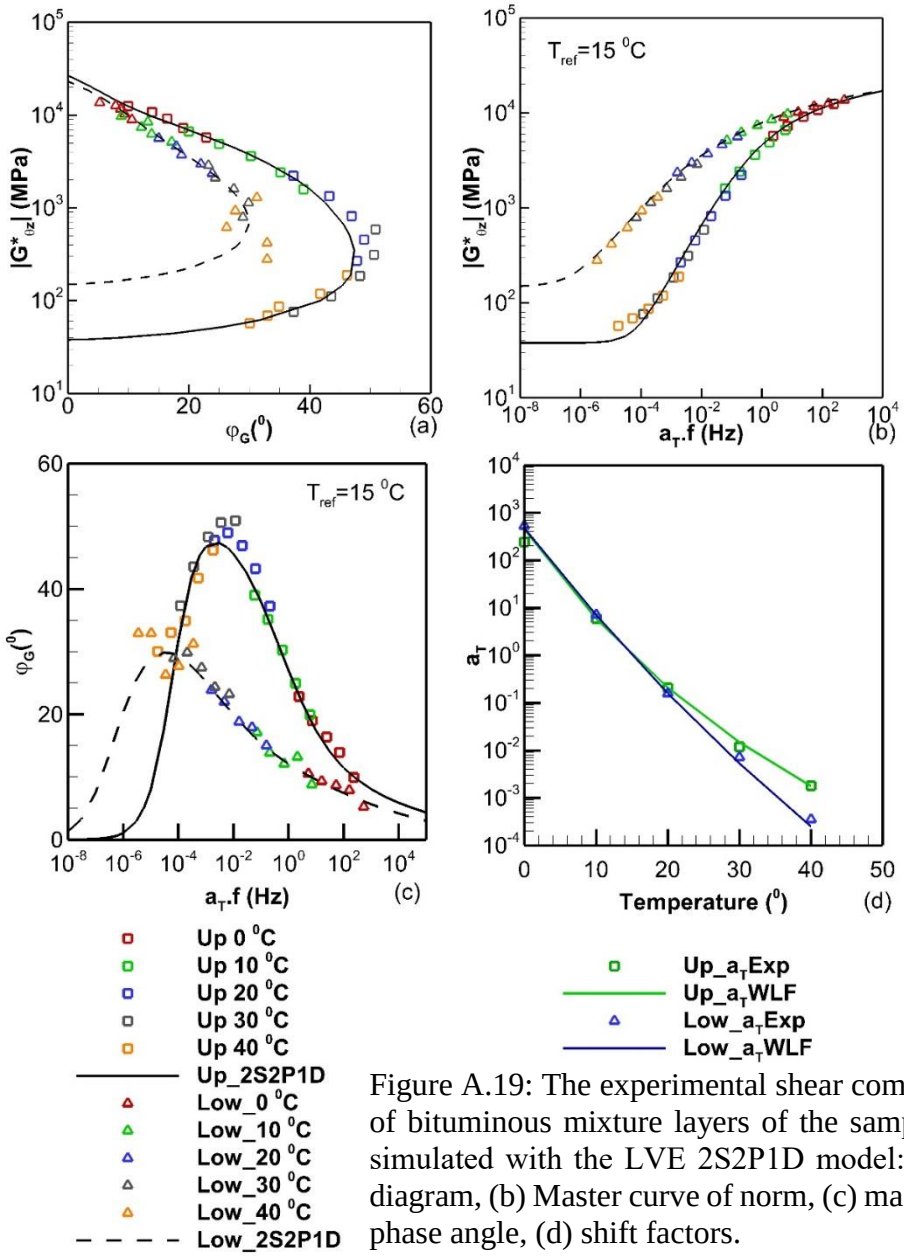

Figure A.19: The experimental shear complex moduli of bituminous mixture layers of the sample REFD-3 simulated with the LVE 2S2P1D model: (a) Black's diagram, (b) Master curve of norm, (c) master curve of phase angle, (d) shift factors.

Table A.19: The calibrating parameters for the 2S2P1D model and WLF modelling of the two bituminous mixtures of the sample REFD-3

Layer	$G_{\theta z\_00}$ (MPa)	$G_{\theta z\_0}$ (MPa)	k	h	δ	τ_G (s)	β	C1	C2 (°C)
Upper	38	26500	0.17	0.57	2.10	0.033	150	11.70	81.15
Lower	150	23000	0.18	0.50	3.50	3.14	550	29.87	182.23

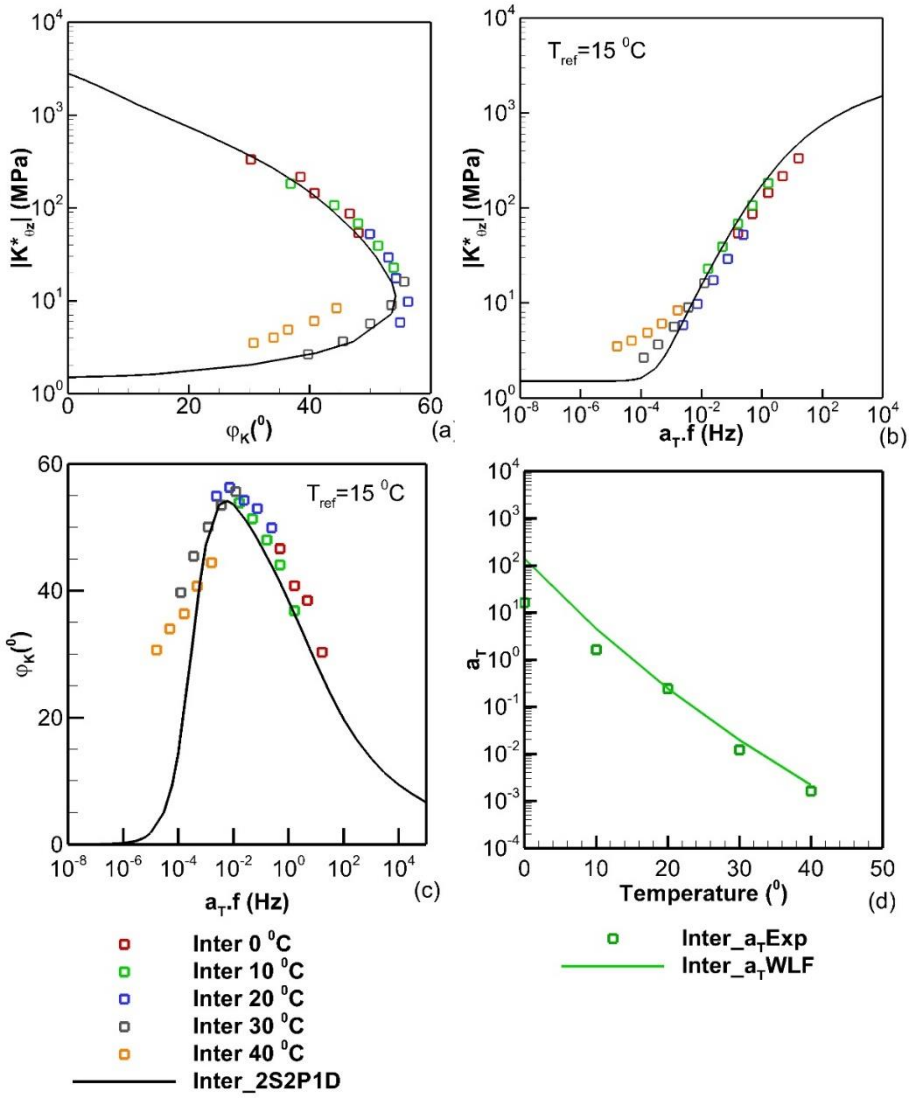

Figure A.20: The experimental shear complex interface stiffness of the sample REFD-3 simulated with the LVE 2S2P1D model: (a) Black's diagram, (b) Master curve of norm, (c) master curve of phase angle, (d) shift factors.

Table A.20: The calibrating parameters for the 2S2P1D model and WLF modelling of the interface of the sample REFD-3

Sample	$K_{\theta z\_00}$ (MPa/mm)	$K_{\theta z\_0}$ (MPa/mm)	k	h	δ	τ_K (s)	β	C1	C2 (°C)
REFD-3	1.5	2800	0.20	0.56	2.30	0.0024	120	16.61	131.00

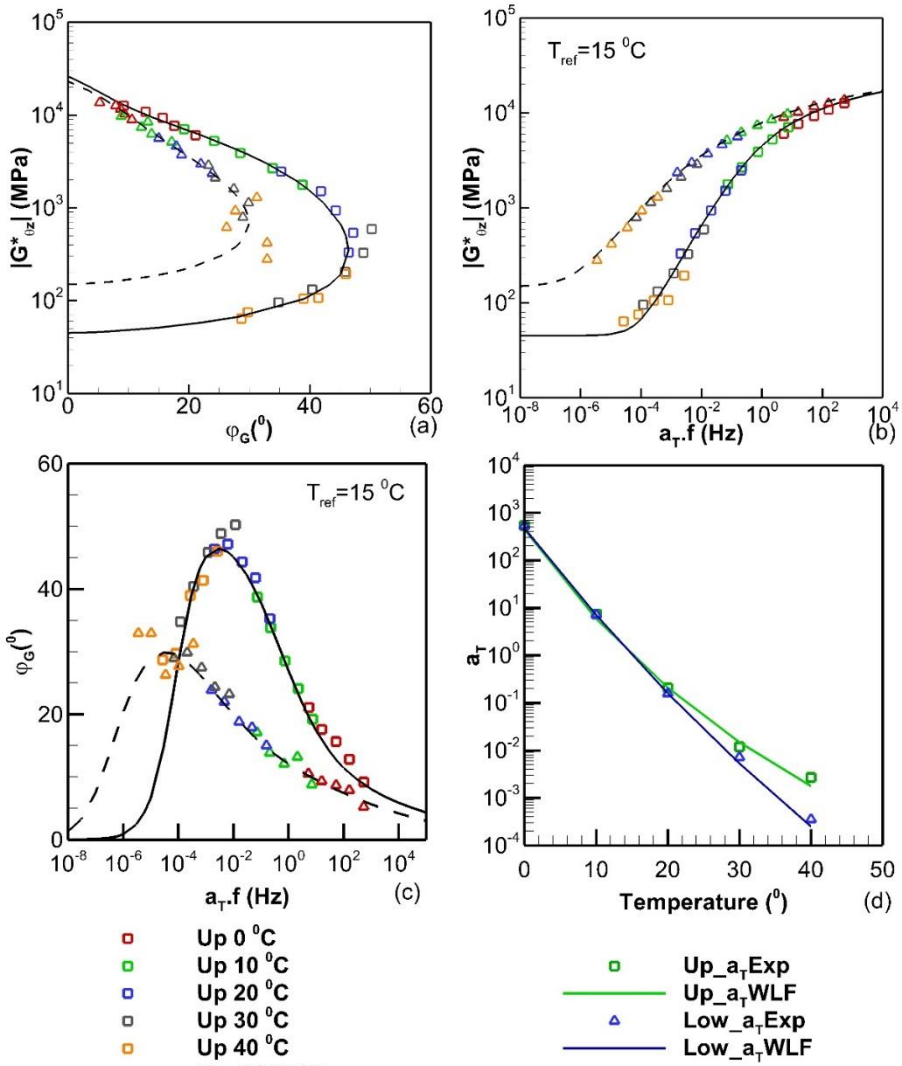

Figure A.21: The experimental shear complex moduli of bituminous mixture layers of the sample HDO-1 simulated with the LVE 2S2P1D model: (a) Black's diagram, (b) Master curve of norm, (c) master curve of phase angle, (d) shift factors.

Table A.21: The calibrating parameters for the 2S2P1D model and WLF modelling of the two bituminous mixtures of the sample HDO-1

Layer	$G_{\theta z\_00}$ (MPa)	$G_{\theta z\_0}$ (MPa)	k	h	δ	τ_G (s)	β	C1	C2 (°C)
Upper	45	26000	0.17	0.57	2.10	0.033	150	11.70	81.15
Lower	120	23000	0.18	0.50	3.50	3.14	550	29.87	182.23

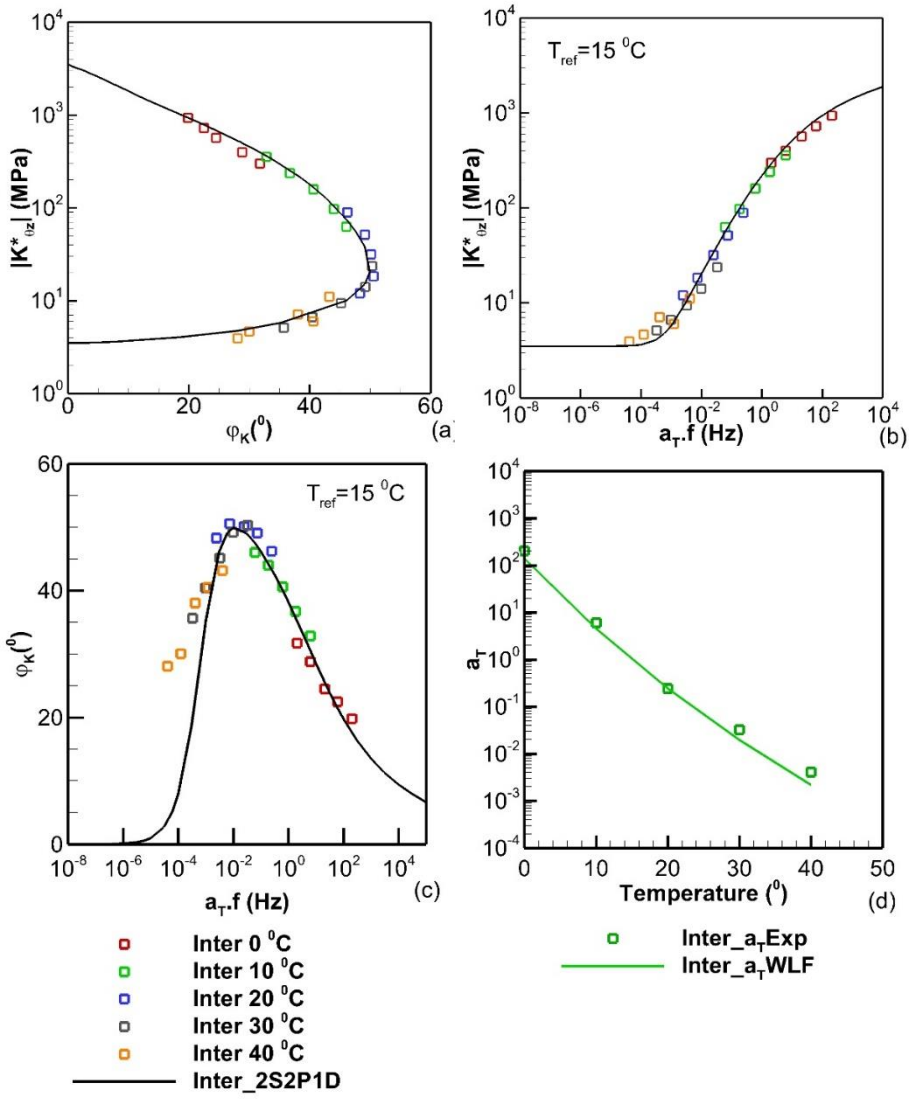

Figure A.22: The experimental shear complex interface stiffness of the sample HDO-1 simulated with the LVE 2S2P1D model: (a) Black's diagram, (b) Master curve of norm, (c) master curve of phase angle, (d) shift factors.

Table A.22: The calibrating parameters for the 2S2P1D model and WLF modelling of the interface of the sample HDO-1

Sample	$K_{\theta z\_00}$ (MPa/mm)	$K_{\theta z\_0}$ (MPa/mm)	k	h	δ	τ_K (s)	β	C1	C2 (°C)
HDO-1	3.5	3500	0.20	0.56	2.30	0.0024	120	16.61	131.00

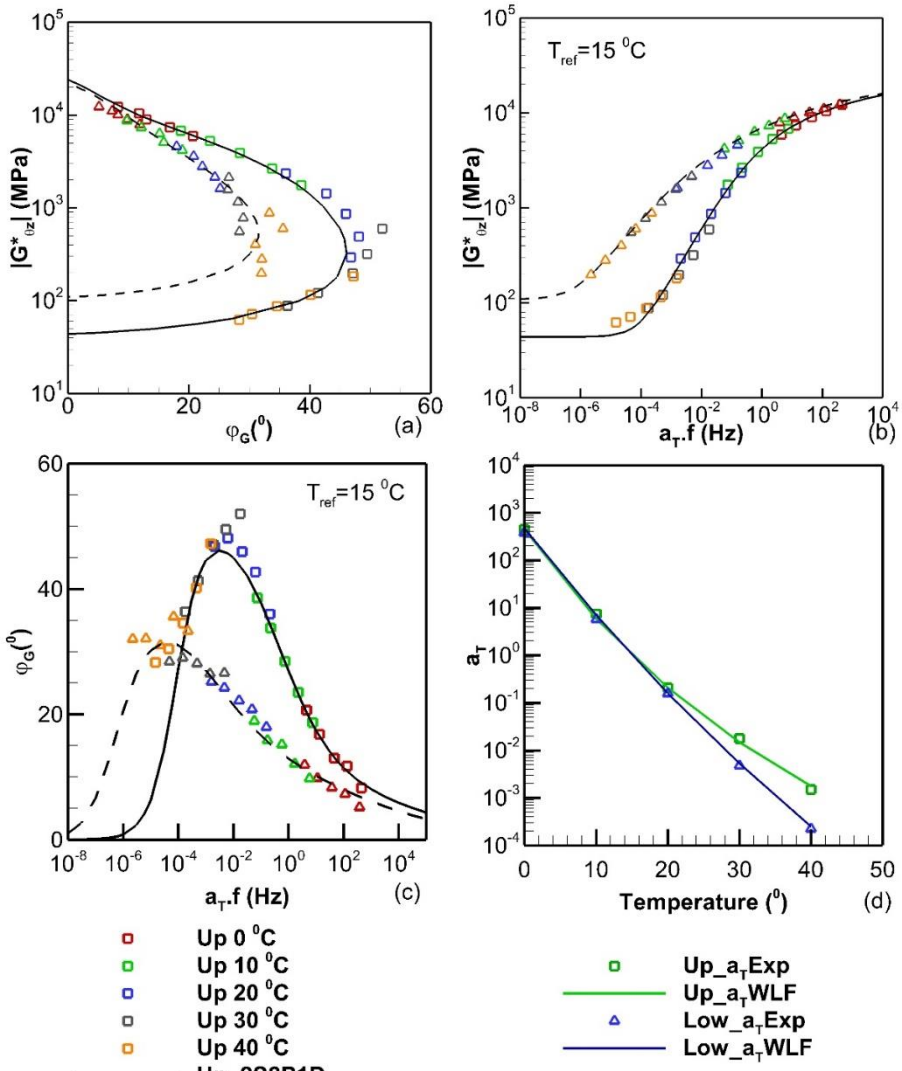

Figure A.23: The experimental shear complex moduli of bituminous mixture layers of the sample HDO-2 simulated with the LVE 2S2P1D model: (a) Black's diagram, (b) Master curve of norm, (c) master curve of phase angle, (d) shift factors.

Table A.23: The calibrating parameters for the 2S2P1D model and WLF modelling of the two bituminous mixtures of the sample HDO-2

Layer	$G_{\theta z\_00}$ (MPa)	$G_{\theta z\_0}$ (MPa)	k	h	δ	τ_G (s)	β	C1	C2 (°C)
Upper	44	24000	0.17	0.57	2.10	0.033	150	11.70	81.15
Lower	110	22000	0.18	0.50	3.50	3.14	550	29.87	182.23

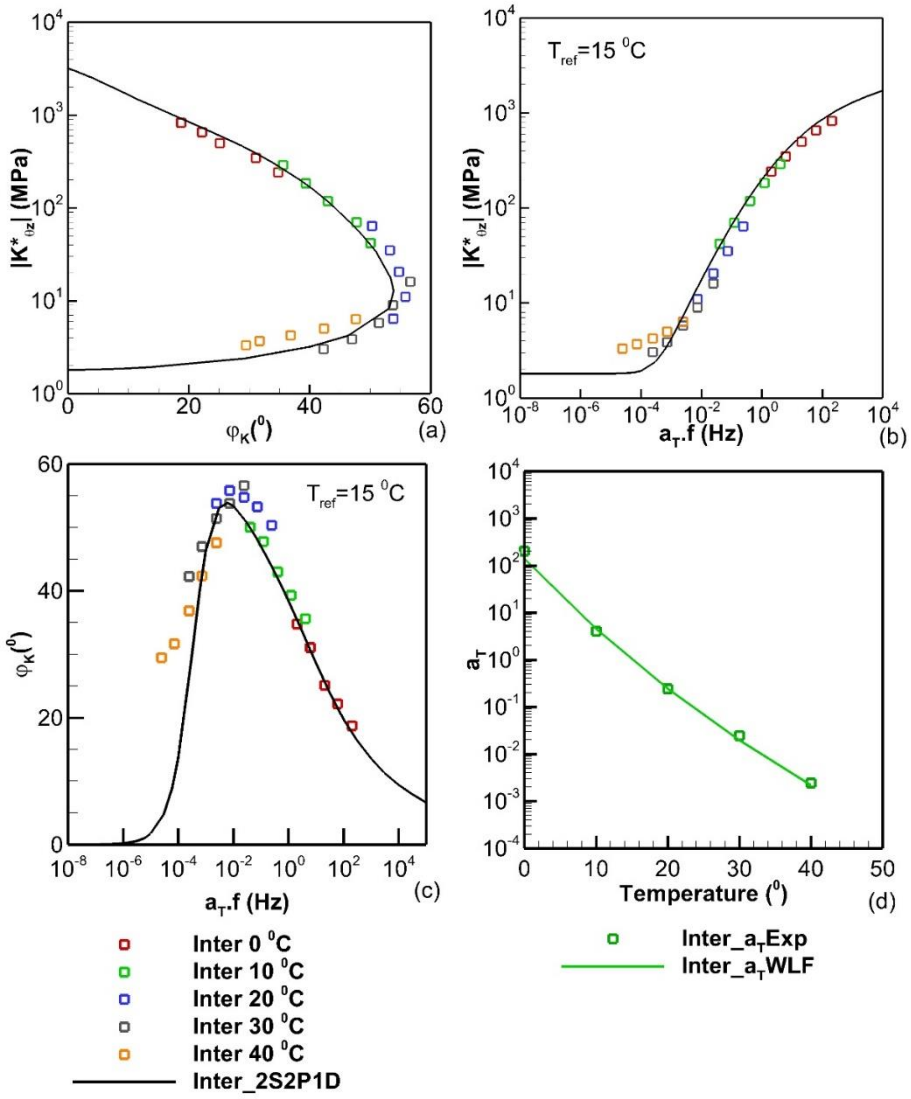

Figure A.24: The experimental shear complex interface stiffness of the sample HDO-2 simulated with the LVE 2S2P1D model: (a) Black's diagram, (b) Master curve of norm, (c) master curve of phase angle, (d) shift factors.

Table A.24: The calibrating parameters for the 2S2P1D model and WLF modelling of the interface of the sample HDO-2

Sample	$K_{\theta z\_00}$ (MPa/mm)	$K_{\theta z\_0}$ (MPa/mm)	k	h	δ	τ_K (s)	β	C1	C2 (°C)
HDO-2	1.8	3200	0.20	0.56	2.30	0.0024	120	16.61	131.00

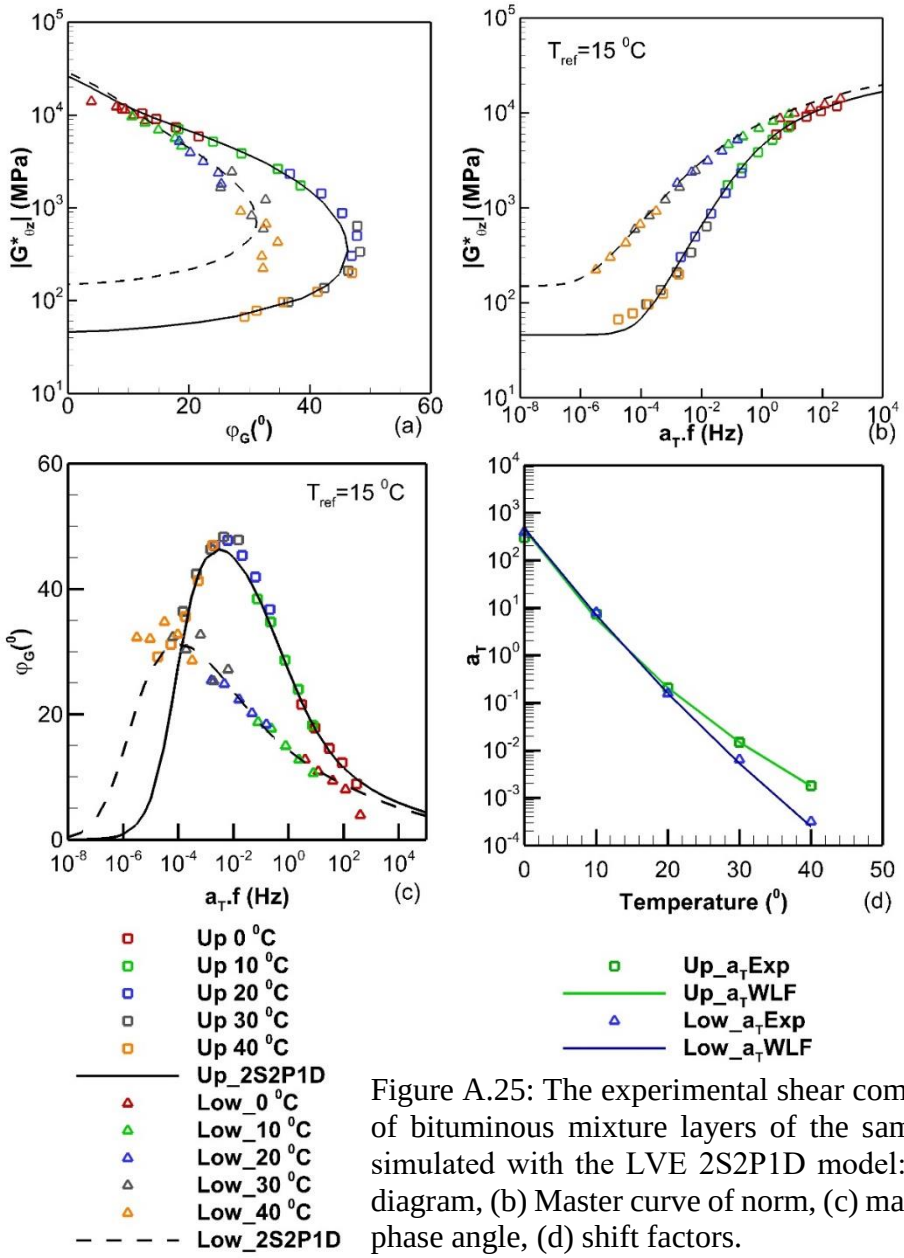

Figure A.25: The experimental shear complex moduli of bituminous mixture layers of the sample HDO-3 simulated with the LVE 2S2P1D model: (a) Black's diagram, (b) Master curve of norm, (c) master curve of phase angle, (d) shift factors.

Table A.25: The calibrating parameters for the 2S2P1D model and WLF modelling of the two bituminous mixtures of the sample HDO-3

Layer	$G_{\theta z\_00}$ (MPa)	$G_{\theta z\_0}$ (MPa)	k	h	δ	τ_G (s)	β	C1	C2 (°C)
Upper	46	26000	0.17	0.57	2.10	0.033	150	11.70	81.15
Lower	150	28500	0.18	0.50	3.50	3.14	550	29.87	182.23

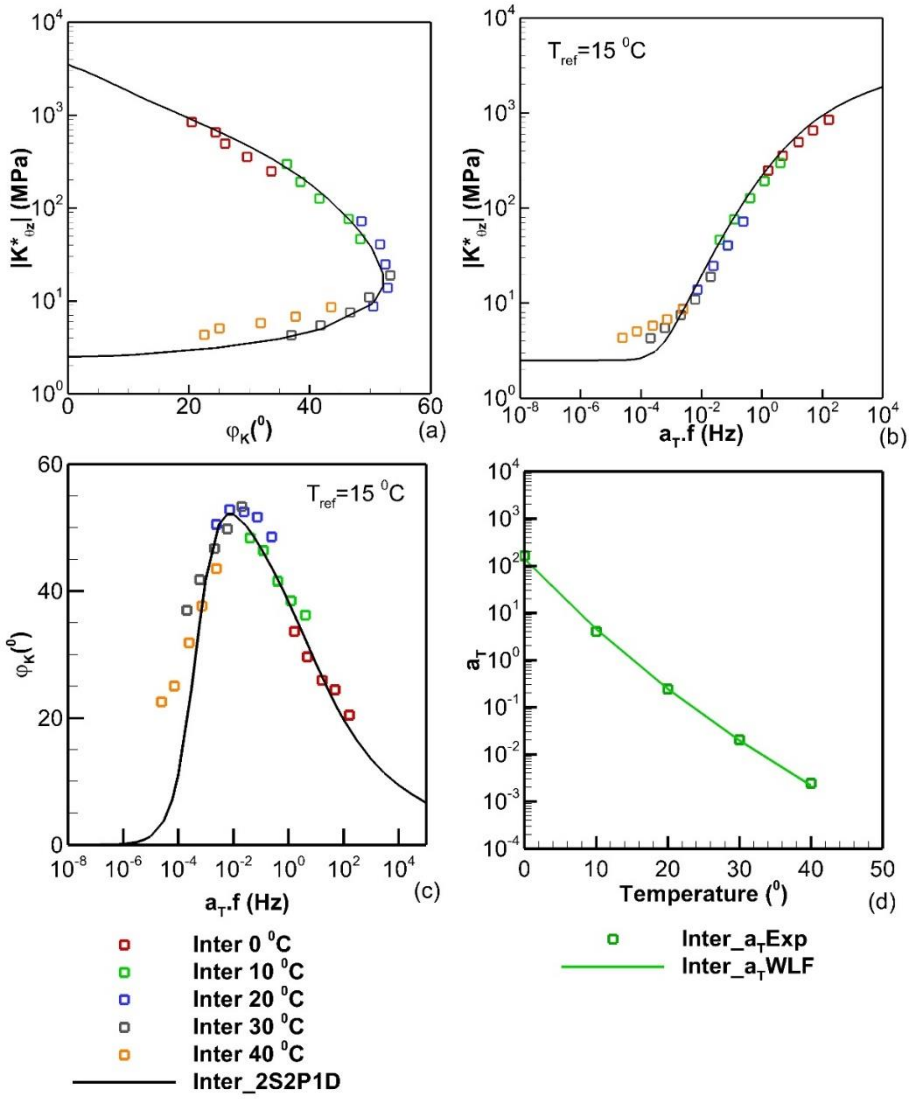

Figure A.26: The experimental shear complex interface stiffness of the sample HDO-3 simulated with the LVE 2S2P1D model: (a) Black's diagram, (b) Master curve of norm, (c) master curve of phase angle, (d) shift factors.

Table A.26: The calibrating parameters for the 2S2P1D model and WLF modelling of the interface of the sample HDO-3

Sample	$K_{\theta z\_00}$ (MPa/mm)	$K_{\theta z\_0}$ (MPa/mm)	k	h	δ	τ_K (s)	β	C1	C2 (°C)
HDO-3	2.5	3500	0.20	0.56	2.30	0.0024	120	16.61	131.00

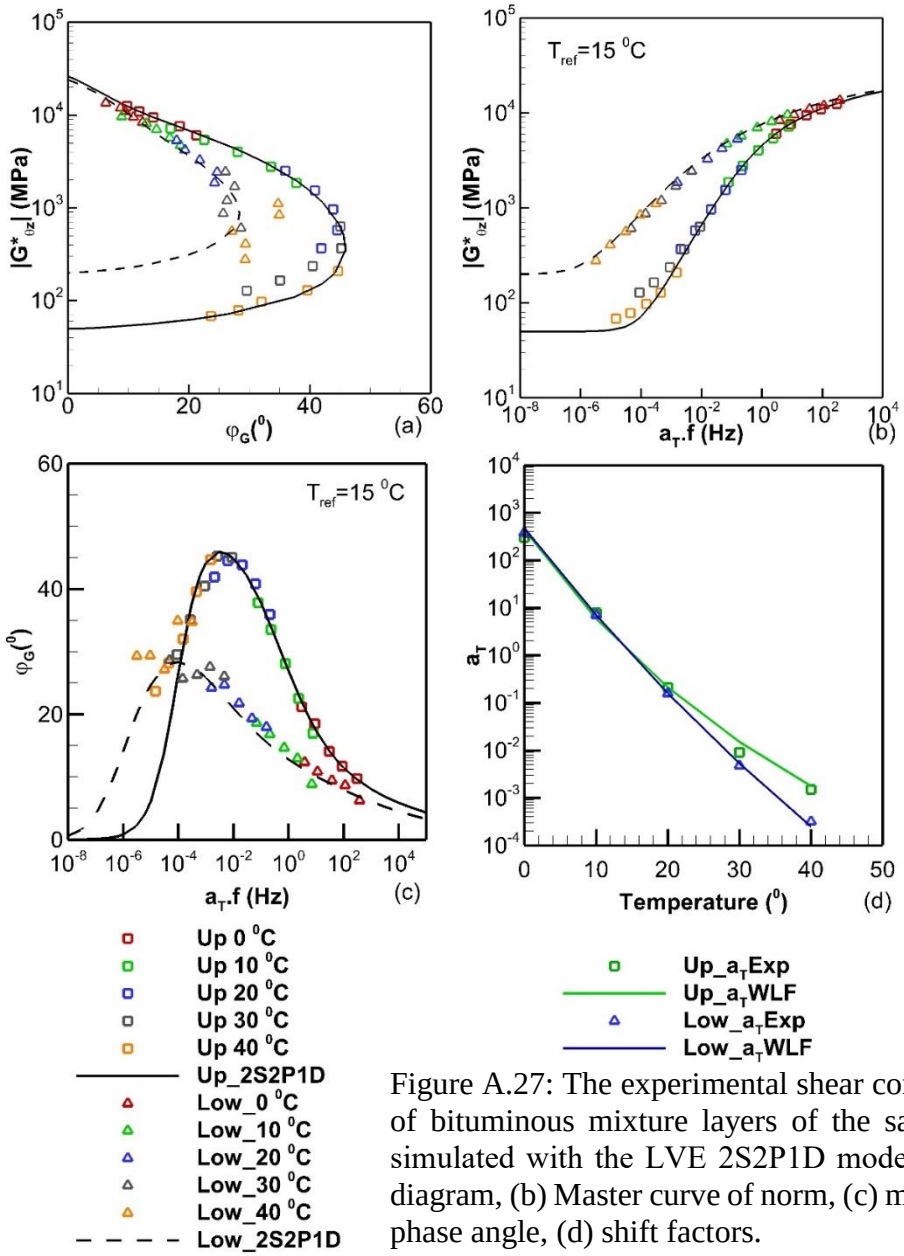

Figure A.27: The experimental shear complex moduli of bituminous mixture layers of the sample LDO-1 simulated with the LVE 2S2P1D model: (a) Black's diagram, (b) Master curve of norm, (c) master curve of phase angle, (d) shift factors.

Table A.27: The calibrating parameters for the 2S2P1D model and WLF modelling of the two bituminous mixtures of the sample LDO-1

Layer	$G_{\theta z\_00}$ (MPa)	$G_{\theta z\_0}$ (MPa)	k	h	δ	τ_G (s)	β	C1	C2 (°C)
Upper	50	26200	0.17	0.57	2.10	0.033	150	11.70	81.15
Lower	200	24000	0.18	0.50	3.50	3.14	550	29.87	182.23

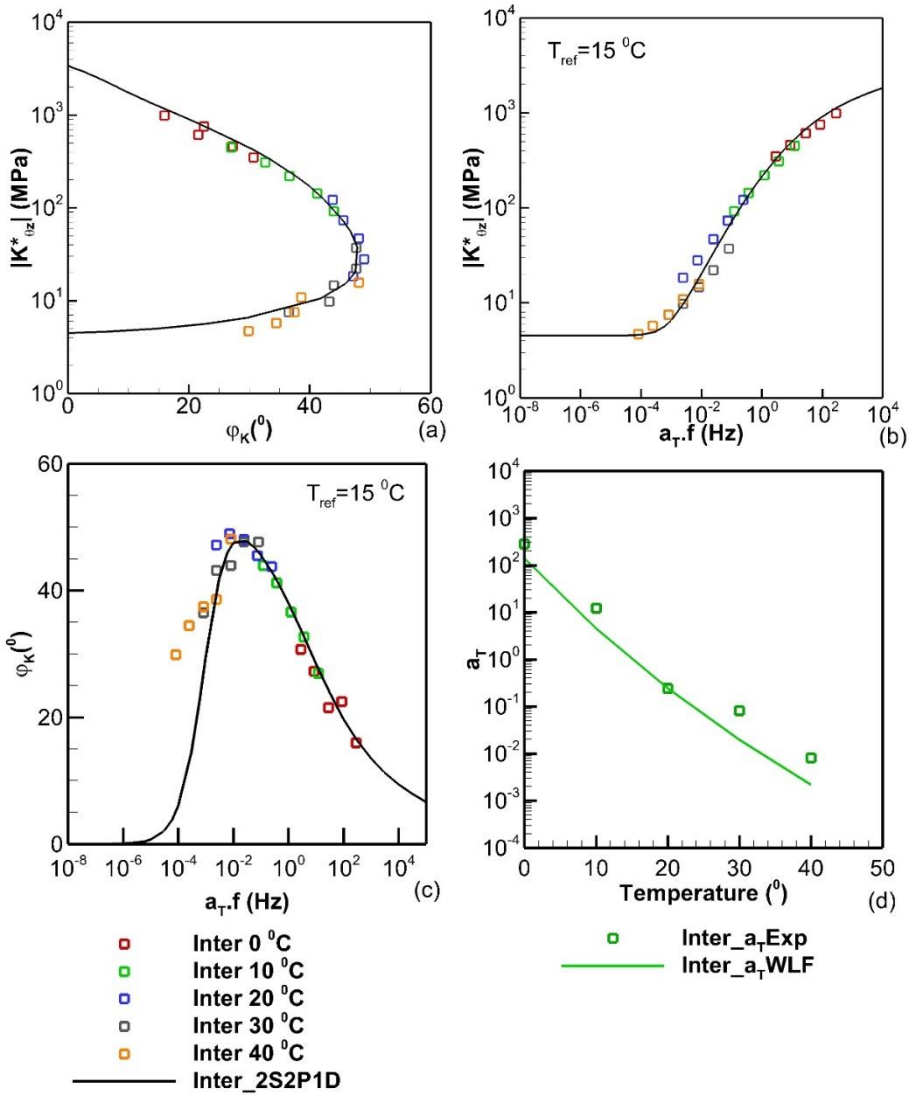

Figure A.28: The experimental shear complex interface stiffness of the sample LDO-1 simulated with the LVE 2S2P1D model: (a) Black's diagram, (b) Master curve of norm, (c) master curve of phase angle, (d) shift factors.

Table A.28: The calibrating parameters for the 2S2P1D model and WLF modelling of the interface of the sample LDO-1

Sample	$K_{\theta z\_00}$ (MPa/mm)	$K_{\theta z\_0}$ (MPa/mm)	k	h	δ	τ_K (s)	β	C1	C2 (°C)
LDO-1	4.5	3400	0.20	0.56	2.30	0.0024	120	16.61	131.00

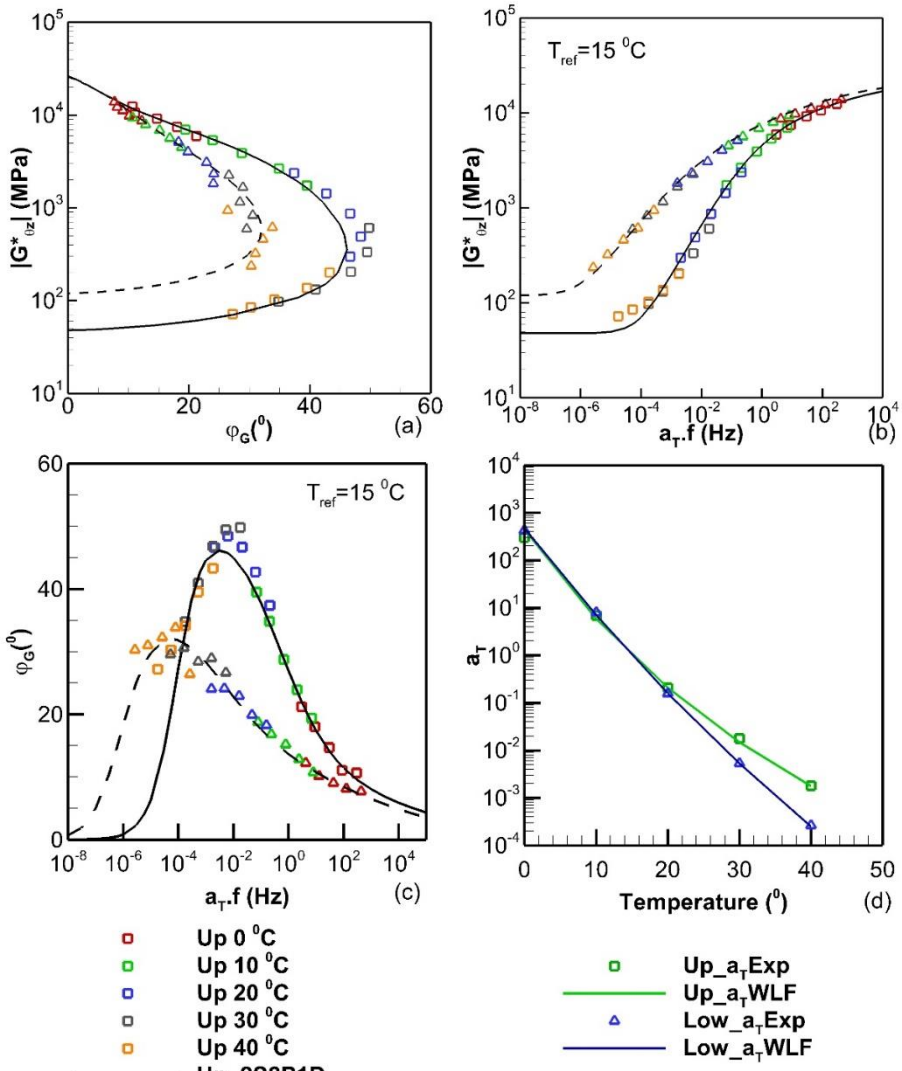

Figure A.29: The experimental shear complex moduli of bituminous mixture layers of the sample LDO-2 simulated with the LVE 2S2P1D model: (a) Black's diagram, (b) Master curve of norm, (c) master curve of phase angle, (d) shift factors.

Table A.29: The calibrating parameters for the 2S2P1D model and WLF modelling of the two bituminous mixtures of the sample LDO-2

Layer	$G_{\theta z\_00}$ (MPa)	$G_{\theta z\_0}$ (MPa)	k	h	δ	τ_G (s)	β	C1	C2 (°C)
Upper	48	26300	0.17	0.57	2.10	0.033	150	11.70	81.15
Lower	120	26000	0.18	0.50	3.50	3.14	550	29.87	182.23

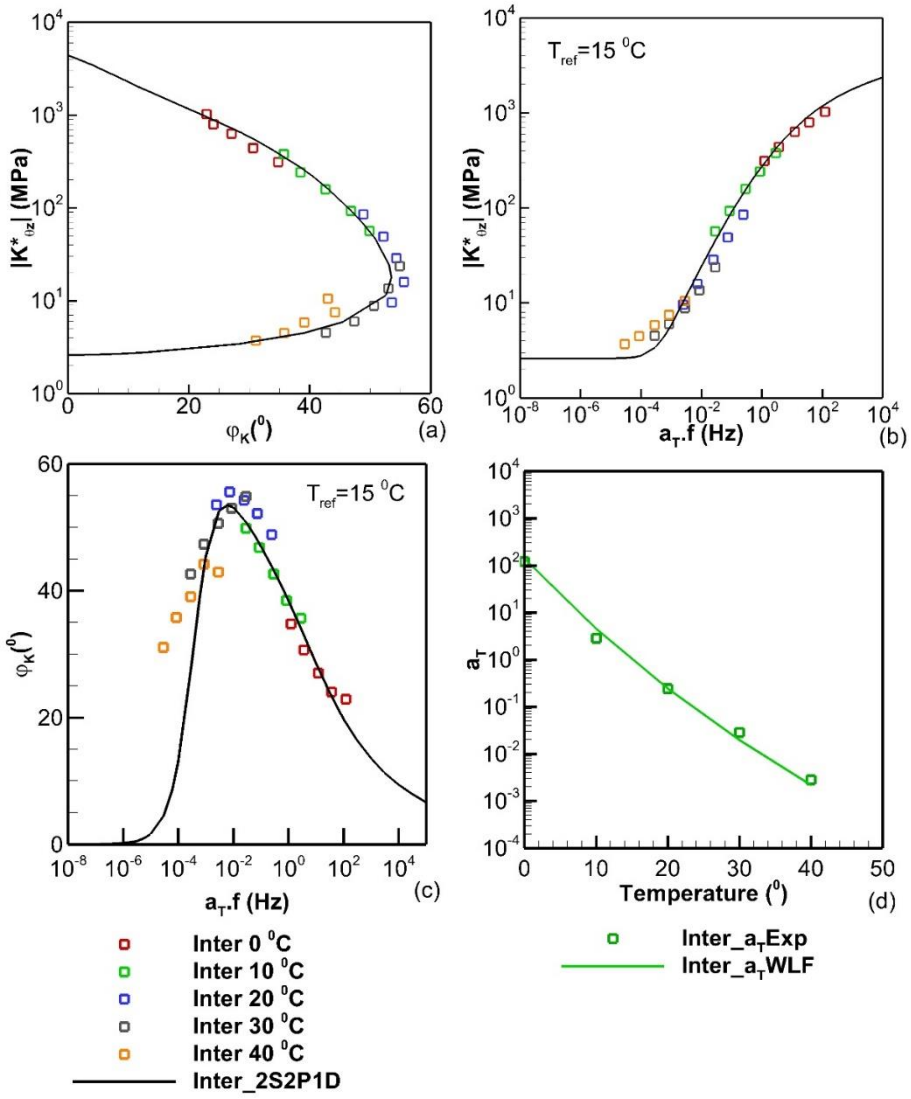

Figure A.30: The experimental shear complex interface stiffness of the sample LDO-2 simulated with the LVE 2S2P1D model: (a) Black's diagram, (b) Master curve of norm, (c) master curve of phase angle, (d) shift factors.

Table A.30: The calibrating parameters for the 2S2P1D model and WLF modelling of the interface of the sample LDO-2

Sample	$K_{\theta z\_00}$ (MPa/mm)	$K_{\theta z\_0}$ (MPa/mm)	k	h	δ	τ_K (s)	β	C1	C2 (°C)
LDO-2	2.6	4400	0.20	0.56	2.30	0.0024	120	16.61	131.00

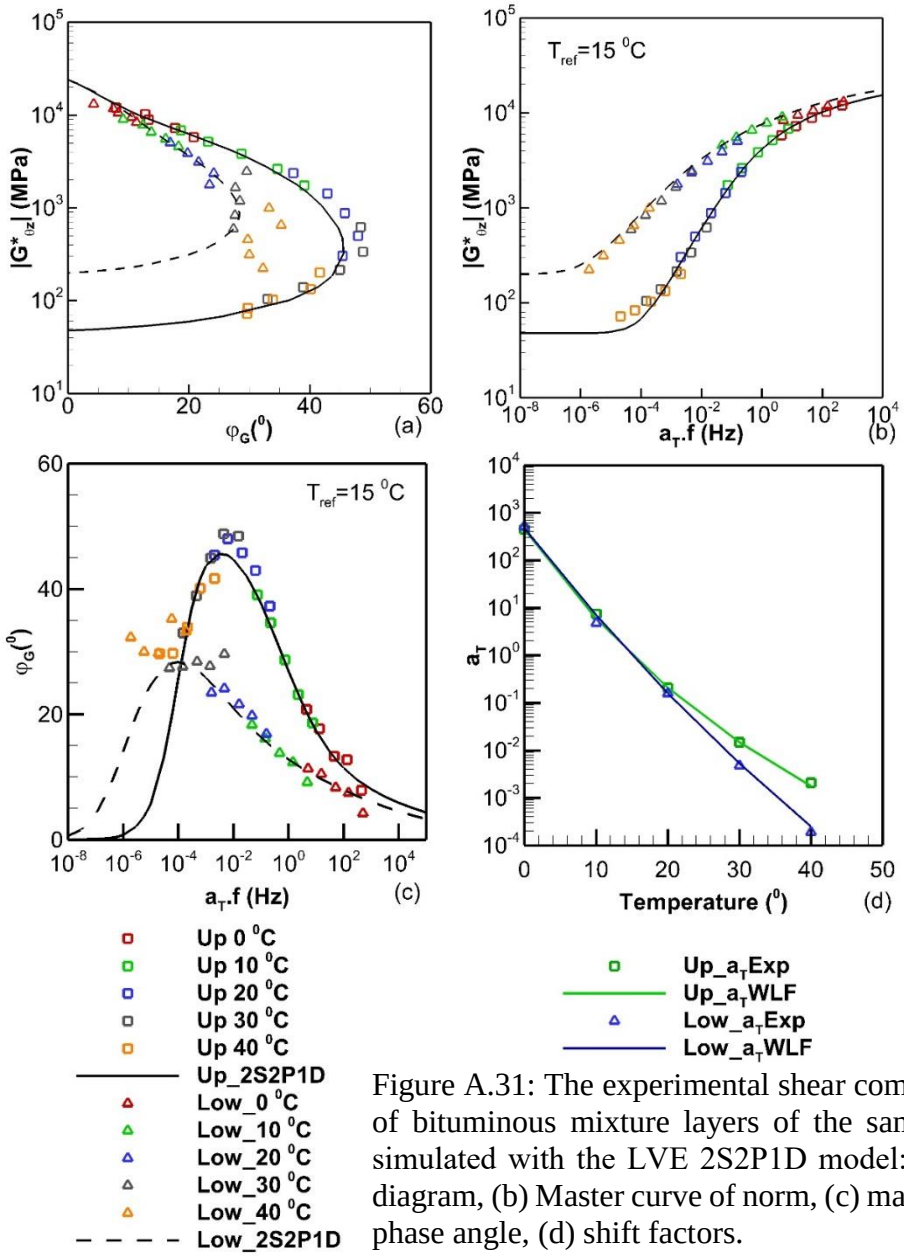

Figure A.31: The experimental shear complex moduli of bituminous mixture layers of the sample LDO-3 simulated with the LVE 2S2P1D model: (a) Black's diagram, (b) Master curve of norm, (c) master curve of phase angle, (d) shift factors.

Table A.31: The calibrating parameters for the 2S2P1D model and WLF modelling of the two bituminous mixtures of the sample LDO-3

Layer	$G_{\theta z\_00}$ (MPa)	$G_{\theta z\_0}$ (MPa)	k	h	δ	τ_G (s)	β	C1	C2 (°C)
Upper	48	24000	0.17	0.57	2.10	0.033	150	11.70	81.15
Lower	200	24000	0.18	0.50	3.50	3.14	550	29.87	182.23

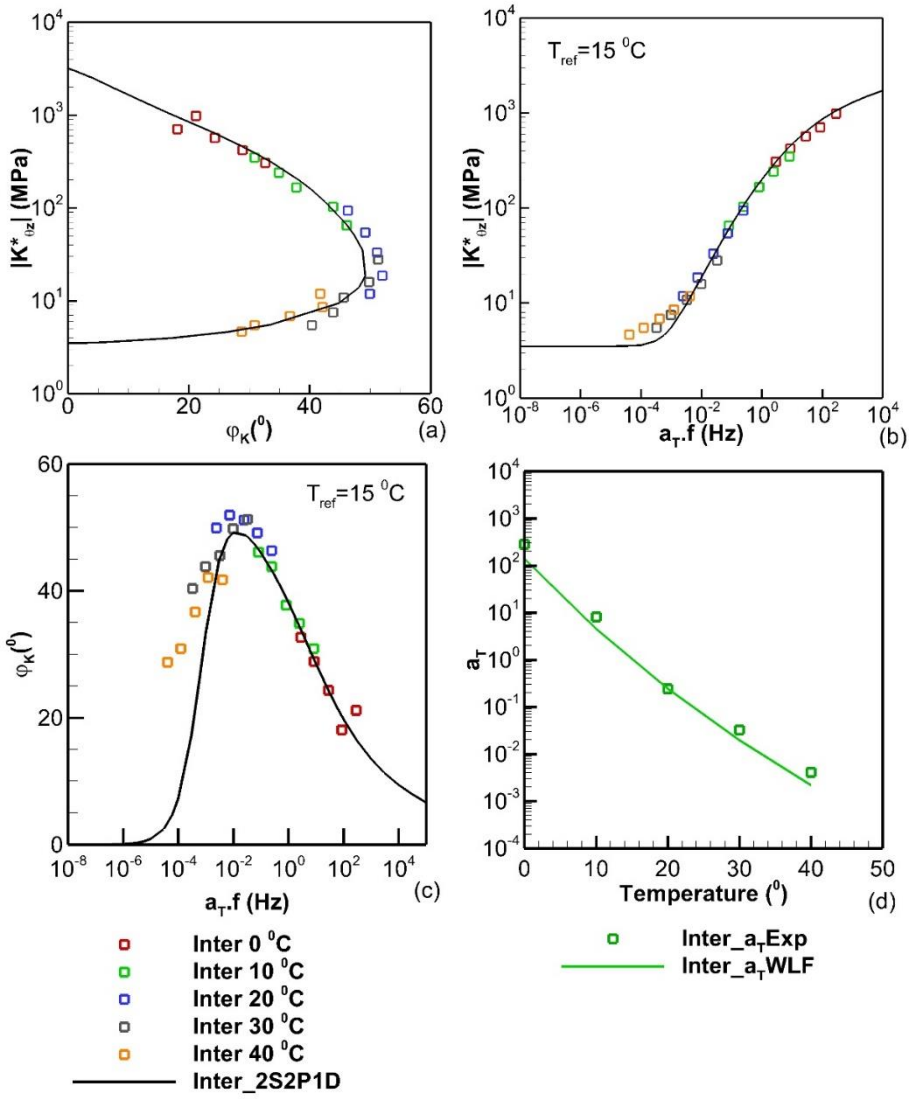

Figure A.32: The experimental shear complex interface stiffness of the sample LDO-3 simulated with the LVE 2S2P1D model: (a) Black's diagram, (b) Master curve of norm, (c) master curve of phase angle, (d) shift factors.

Table A.32: The calibrating parameters for the 2S2P1D model and WLF modelling of the interface of the sample LDO-3

Sample	$K_{\theta z\_00}$ (MPa/mm)	$K_{\theta z\_0}$ (MPa/mm)	k	h	δ	τ_K (s)	β	C1	C2 (°C)
LDO-3	3.5	3200	0.20	0.56	2.30	0.0024	120	16.61	131.00

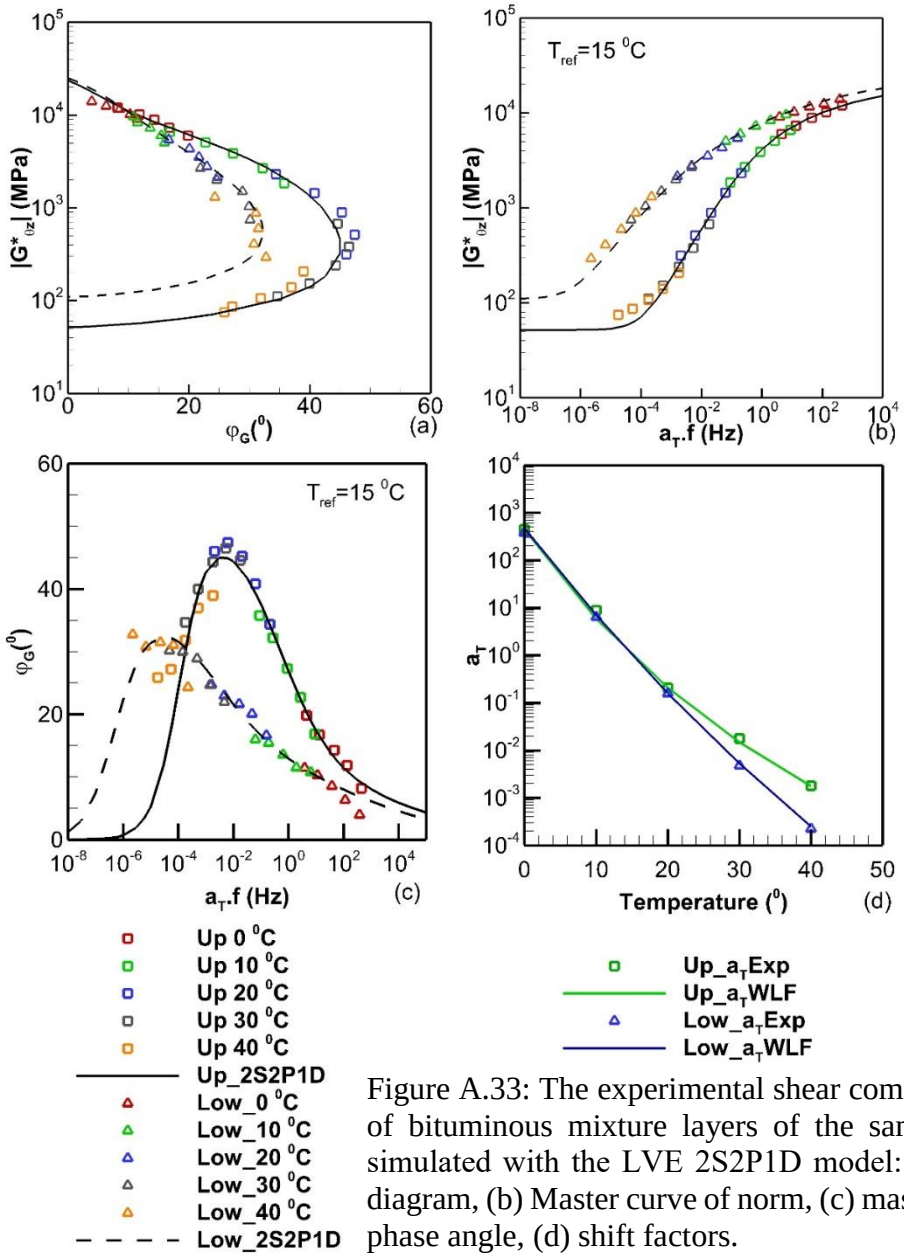

Figure A.33: The experimental shear complex moduli of bituminous mixture layers of the sample SBS-1 simulated with the LVE 2S2P1D model: (a) Black's diagram, (b) Master curve of norm, (c) master curve of phase angle, (d) shift factors.

Table A.33: The calibrating parameters for the 2S2P1D model and WLF modelling of the two bituminous mixtures of the sample SBS-1

Layer	$G_{\theta z\_00}$ (MPa)	$G_{\theta z\_0}$ (MPa)	k	h	δ	τ_G (s)	β	C1	C2 (°C)
Upper	52	23600	0.17	0.57	2.10	0.033	150	11.70	81.15
Lower	110	25000	0.18	0.50	3.50	3.14	550	29.87	182.23

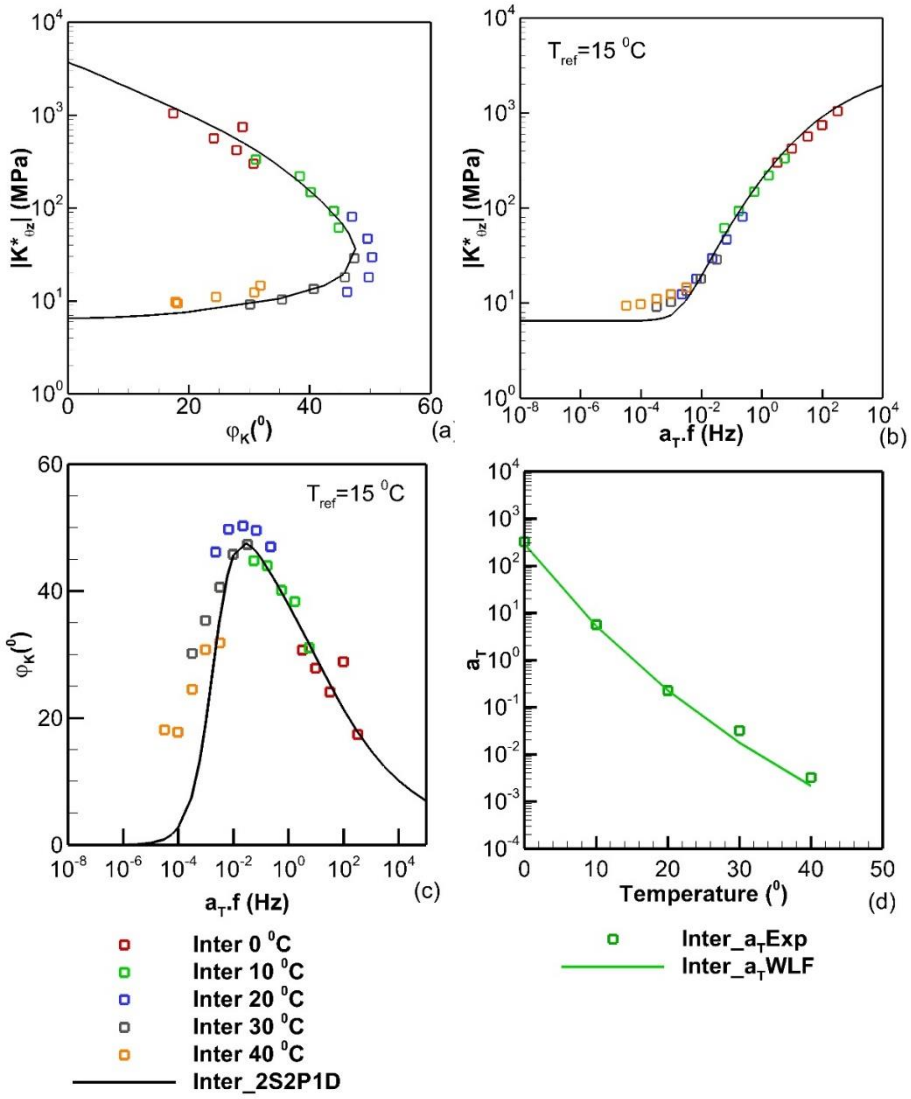

Figure A.34: The experimental shear complex interface stiffness of the sample SBS-1 simulated with the LVE 2S2P1D model: (a) Black's diagram, (b) Master curve of norm, (c) master curve of phase angle, (d) shift factors.

Table A.34: The calibrating parameters for the 2S2P1D model and WLF modelling of the interface of the sample SBS-1

Sample	$K_{\theta z\_00}$ (MPa/mm)	$K_{\theta z\_0}$ (MPa/mm)	k	h	δ	τ_K (s)	β	C1	C2 (°C)
SBS-1	6.5	3700	0.20	0.52	2.00	0.0012	120	12.16	89.14

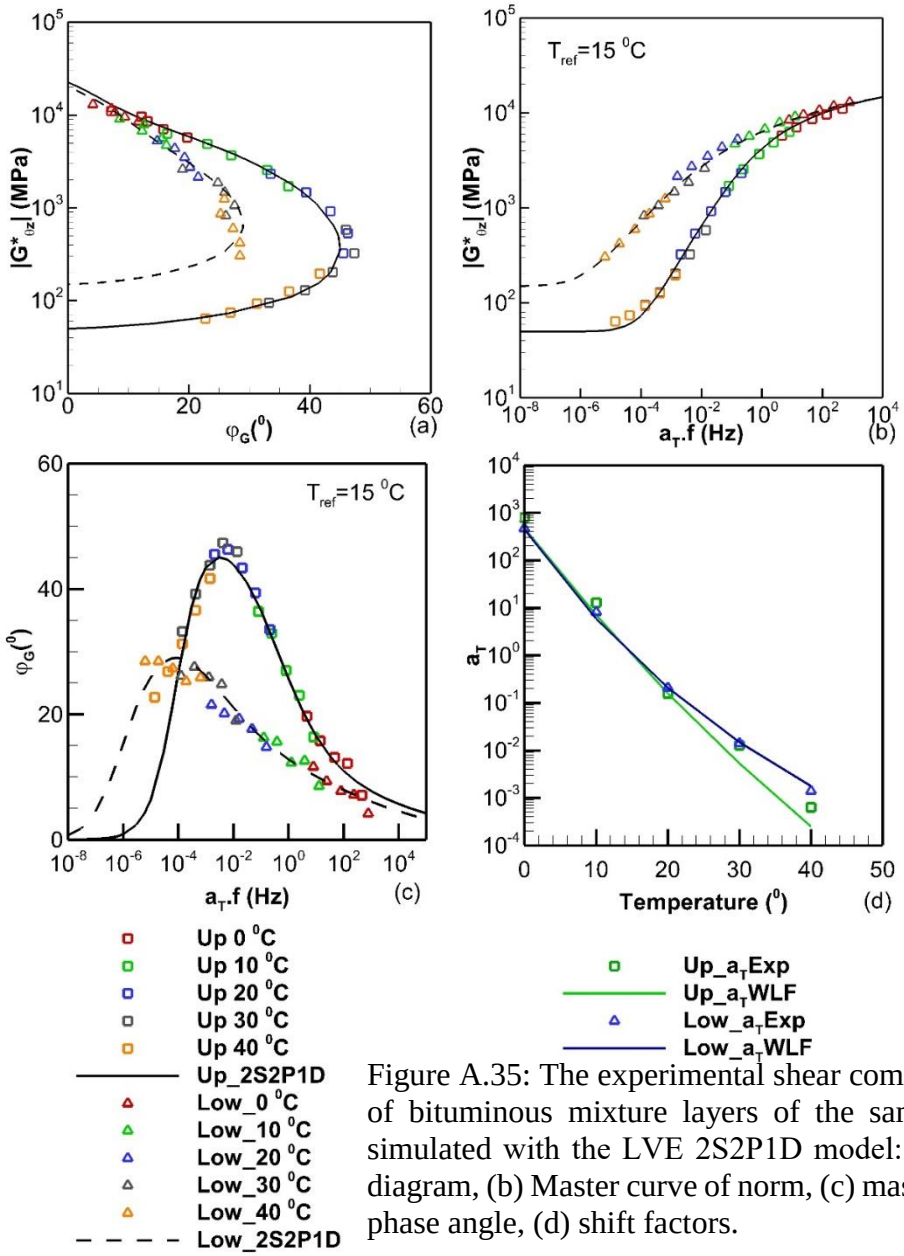

Figure A.35: The experimental shear complex moduli of bituminous mixture layers of the sample SBS-2 simulated with the LVE 2S2P1D model: (a) Black's diagram, (b) Master curve of norm, (c) master curve of phase angle, (d) shift factors.

Table A.35: The calibrating parameters for the 2S2P1D model and WLF modelling of the two bituminous mixtures of the sample SBS-2

Layer	$G_{\theta z\_00}$ (MPa)	$G_{\theta z\_0}$ (MPa)	k	h	δ	τ_G (s)	β	C1	C2 (°C)
Upper	50	22500	0.17	0.57	2.10	0.033	150	11.70	81.15
Lower	150	20000	0.18	0.50	3.50	3.14	550	29.87	182.23

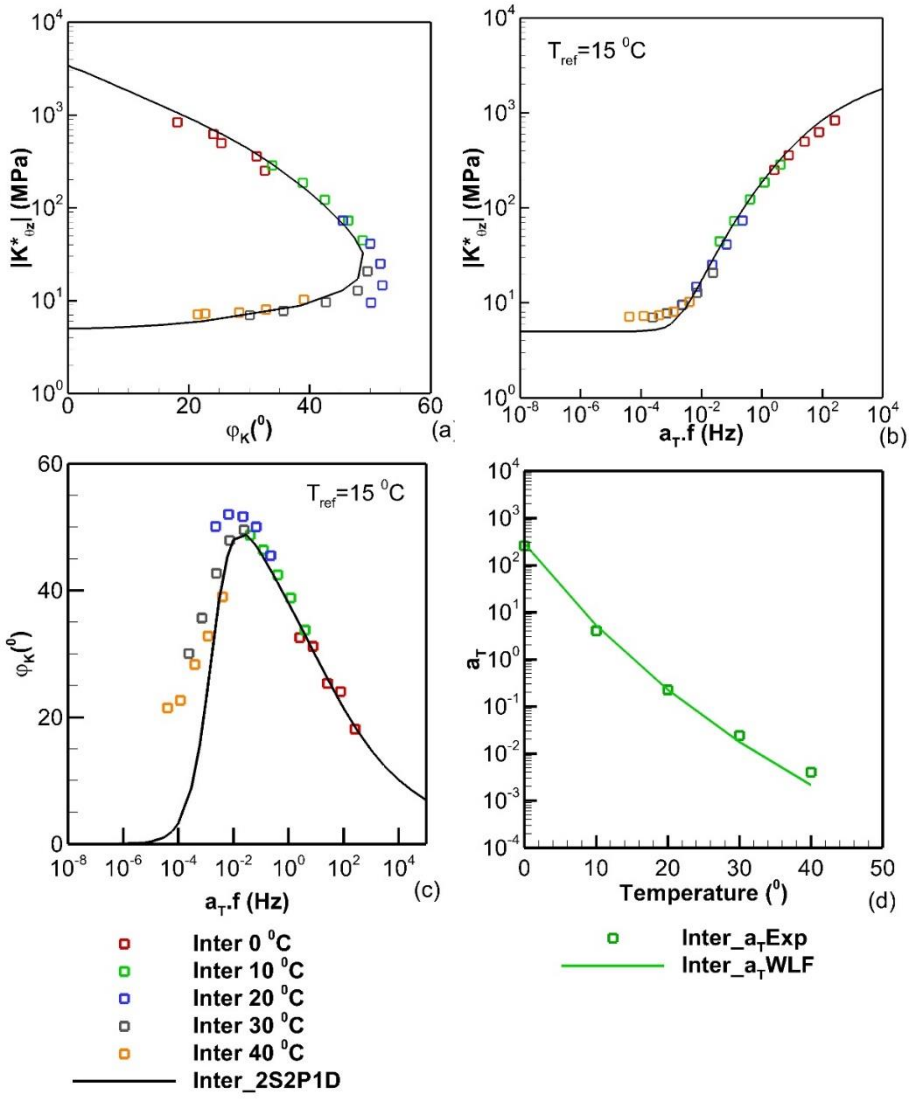

Figure A.36: The experimental shear complex interface stiffness of the sample SBS-2 simulated with the LVE 2S2P1D model: (a) Black's diagram, (b) Master curve of norm, (c) master curve of phase angle, (d) shift factors.

Table A.36: The calibrating parameters for the 2S2P1D model and WLF modelling of the interface of the sample SBS-2

Sample	$K_{\theta z\_00}$ (MPa/mm)	$K_{\theta z\_0}$ (MPa/mm)	k	h	δ	τ_K (s)	β	C1	C2 (°C)
SBS-2	5.0	3400	0.20	0.52	2.00	0.0012	120	12.16	89.14

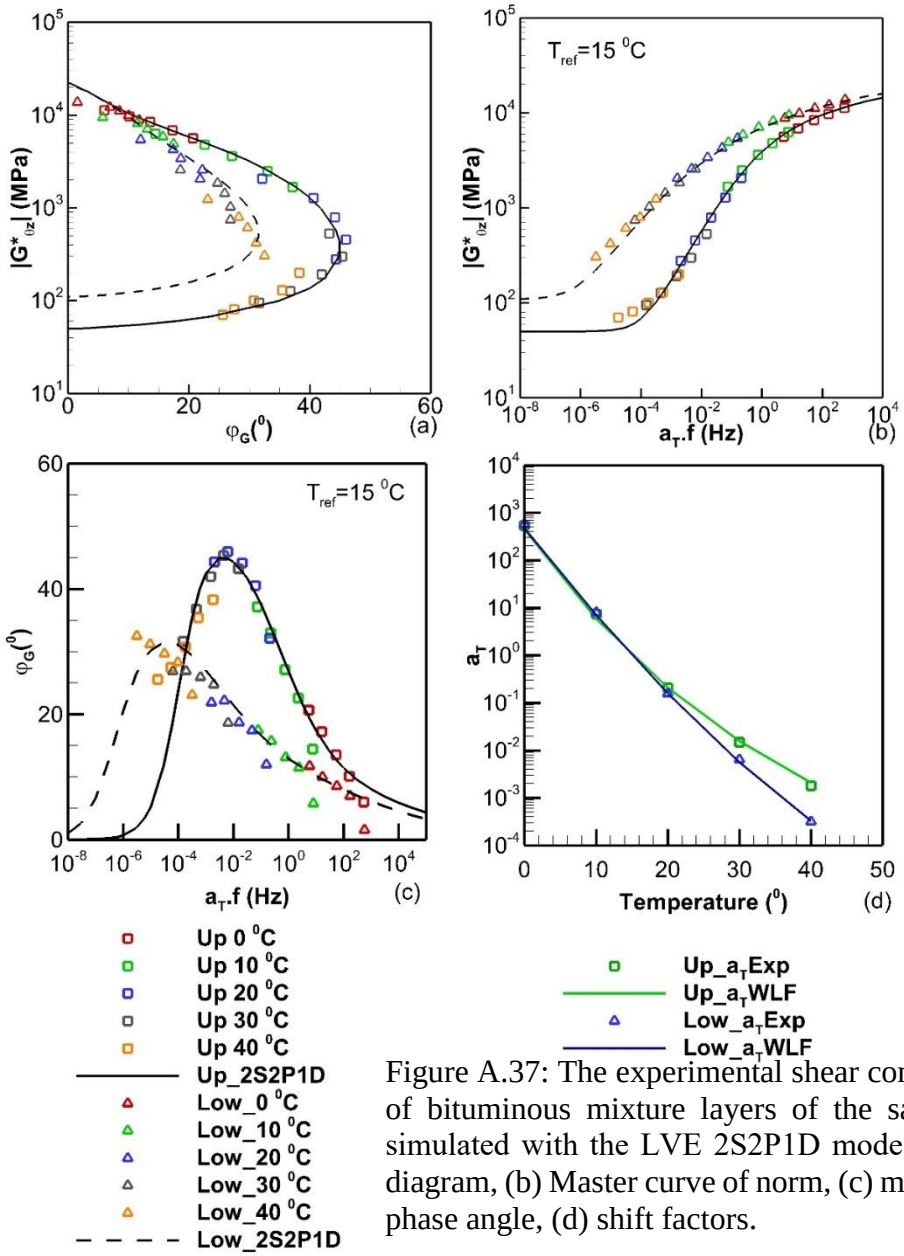

Figure A.37: The experimental shear complex moduli of bituminous mixture layers of the sample SBS-3 simulated with the LVE 2S2P1D model: (a) Black's diagram, (b) Master curve of norm, (c) master curve of phase angle, (d) shift factors.

Table A.37: The calibrating parameters for the 2S2P1D model and WLF modelling of the two bituminous mixtures of the sample SBS-3

Layer	$G_{\theta z\_00}$ (MPa)	$G_{\theta z\_0}$ (MPa)	k	h	δ	τ_G (s)	β	C1	C2 (°C)
Upper	50	22400	0.17	0.57	2.10	0.033	150	11.70	81.15
Lower	110	22000	0.18	0.50	3.50	3.14	550	29.87	182.23

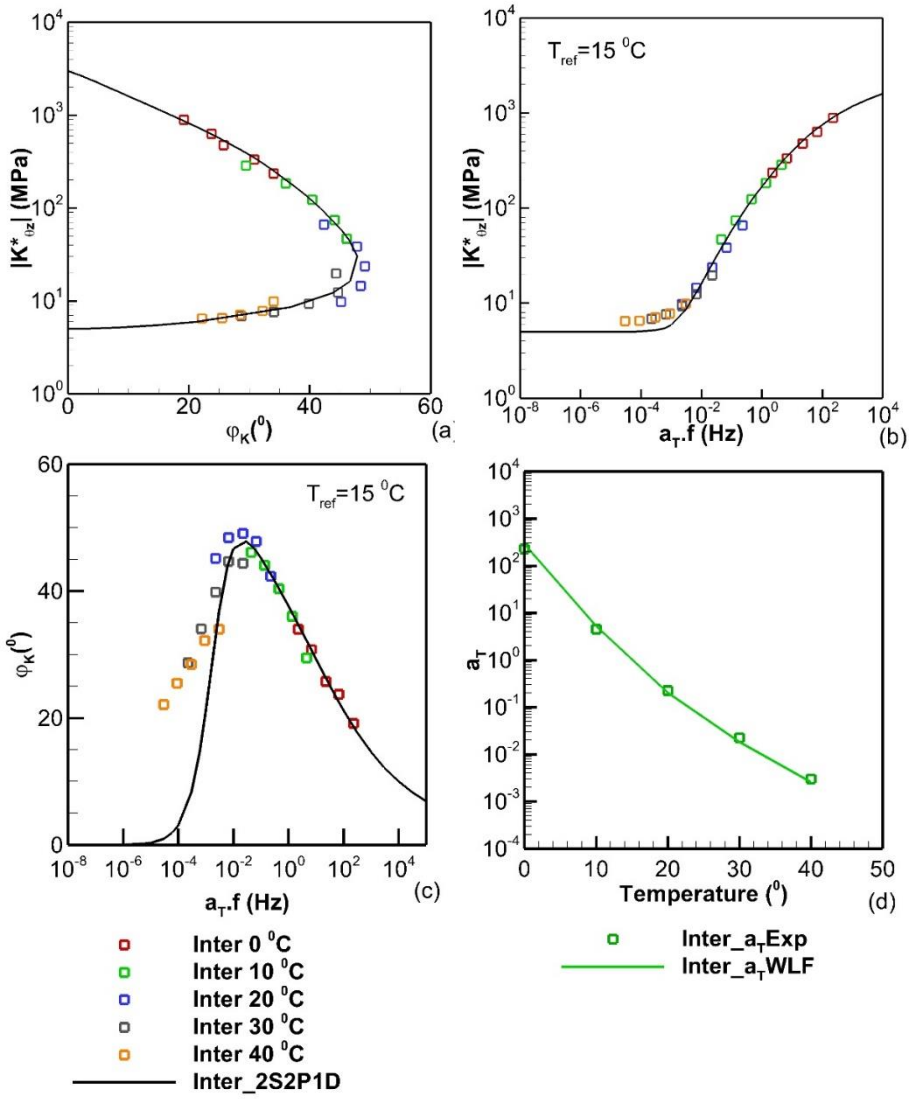

Figure A.38: The experimental shear complex interface stiffness of the sample SBS-3 simulated with the LVE 2S2P1D model: (a) Black's diagram, (b) Master curve of norm, (c) master curve of phase angle, (d) shift factors.

Table A.38: The calibrating parameters for the 2S2P1D model and WLF modelling of the interface of the sample SBS-3

Sample	$K_{\theta z\_00}$ (MPa/mm)	$K_{\theta z\_0}$ (MPa/mm)	k	h	δ	τ_K (s)	β	C1	C2 (°C)
SBS-3	5.0	3000	0.20	0.52	2.00	0.0012	120	12.16	89.14

Appendix B: FATIGUE BEHAVIOUR OF INTERFACE AND BITUMINOUS LAYERS

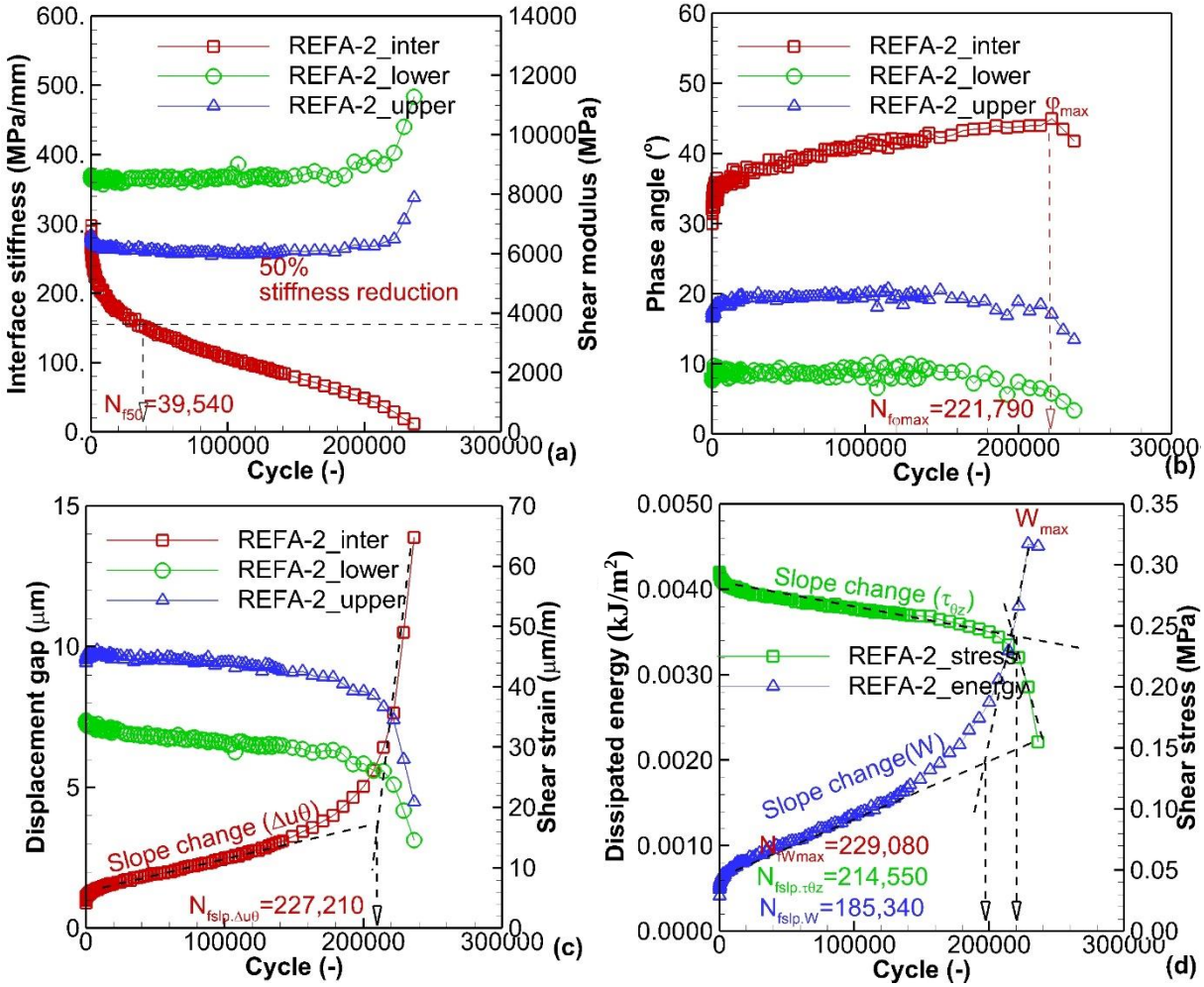

Figure B.1: Fatigue evolution for sample REFA-2 tested with $\varepsilon_{\theta zg\_0}$= 50 μm/m, σ_{zz} = -0.026 MPa: (a) norm of interface shear stiffness ($|K^*_{\theta z}|$), and of complex shear moduli of upper and lower layers ($|G^*_{\theta z.up}|$, and $|G^*_{\theta z.low}|$(b) phase angle of interface complex shear stiffness ($\varphi_{K\theta z}$), and of complex shear moduli of layers ($\varphi_{G.up}$, $\varphi_{G.low}$); (c) amplitude of displacement gap at the interface (Δu_{θ_0}) and shear strains in layers ($\varepsilon_{\theta z1\_0}$, $\varepsilon_{\theta z2\_0}$), (d) dissipated energy at the interface (W) and shear stress amplitude ($\tau_{\theta z\_0}$)

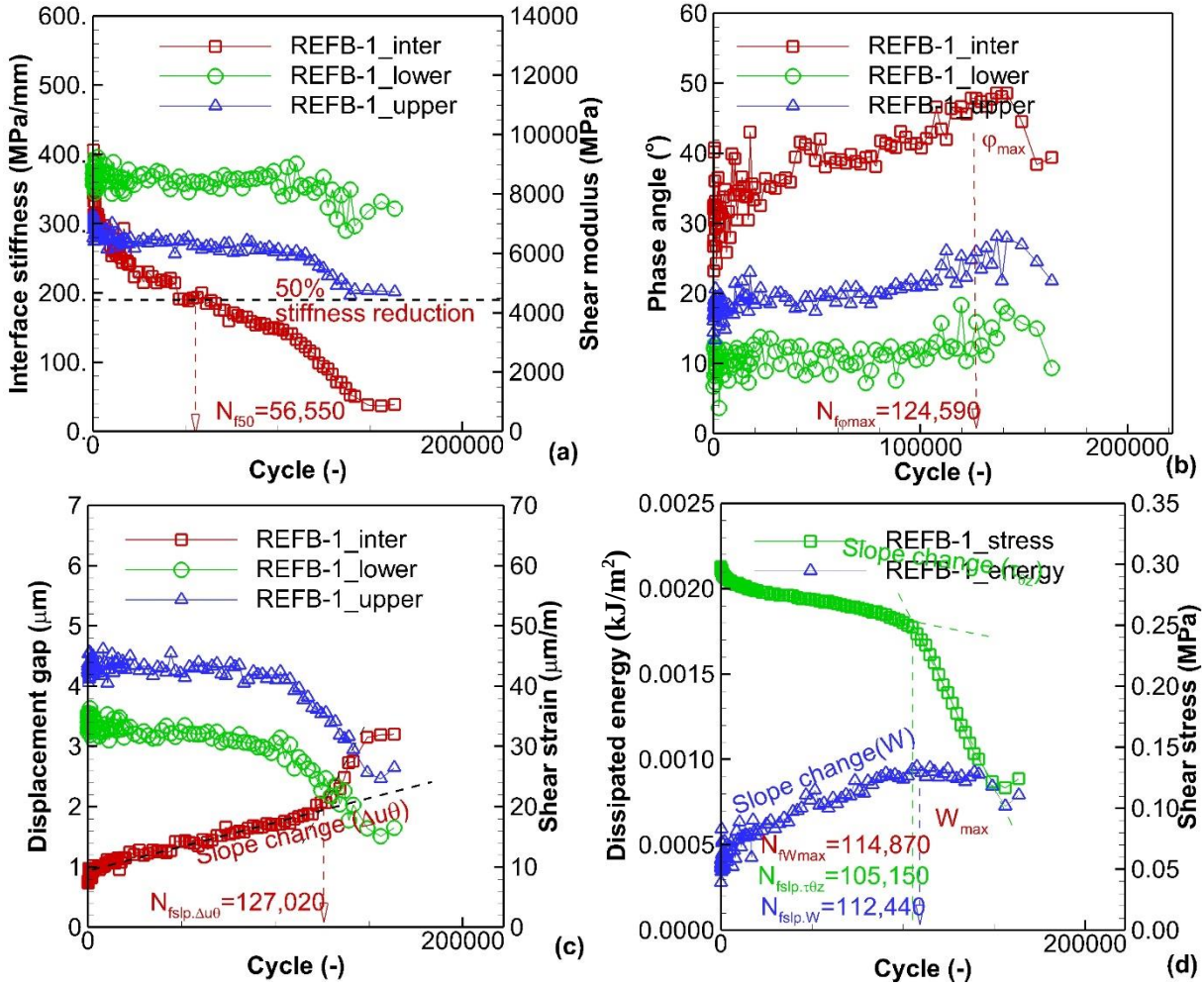

Figure B.2: Fatigue evolution for sample REFB-1 tested with $\varepsilon_{\theta zg\_0}$= 50 μm/m, σ_{zz} = -0.026 MPa: (a) norm of interface shear stiffness ($|K^*_{\theta z}|$), and of complex shear moduli of upper and lower layers ($|G^*_{\theta z.up}|$, and $|G^*_{\theta z.low}|$(b) phase angle of interface complex shear stiffness ($\varphi_{K\theta z}$), and of complex shear moduli of layers ($\varphi_{G.up}$, $\varphi_{G.low}$); (c) amplitude of displacement gap at the interface (Δu_{θ_0}) and shear strains in layers ($\varepsilon_{\theta z.up\_0}$, $\varepsilon_{\theta z.low\_0}$), (d) dissipated energy at the interface (W) and shear stress amplitude ($\tau_{\theta z\_0}$)

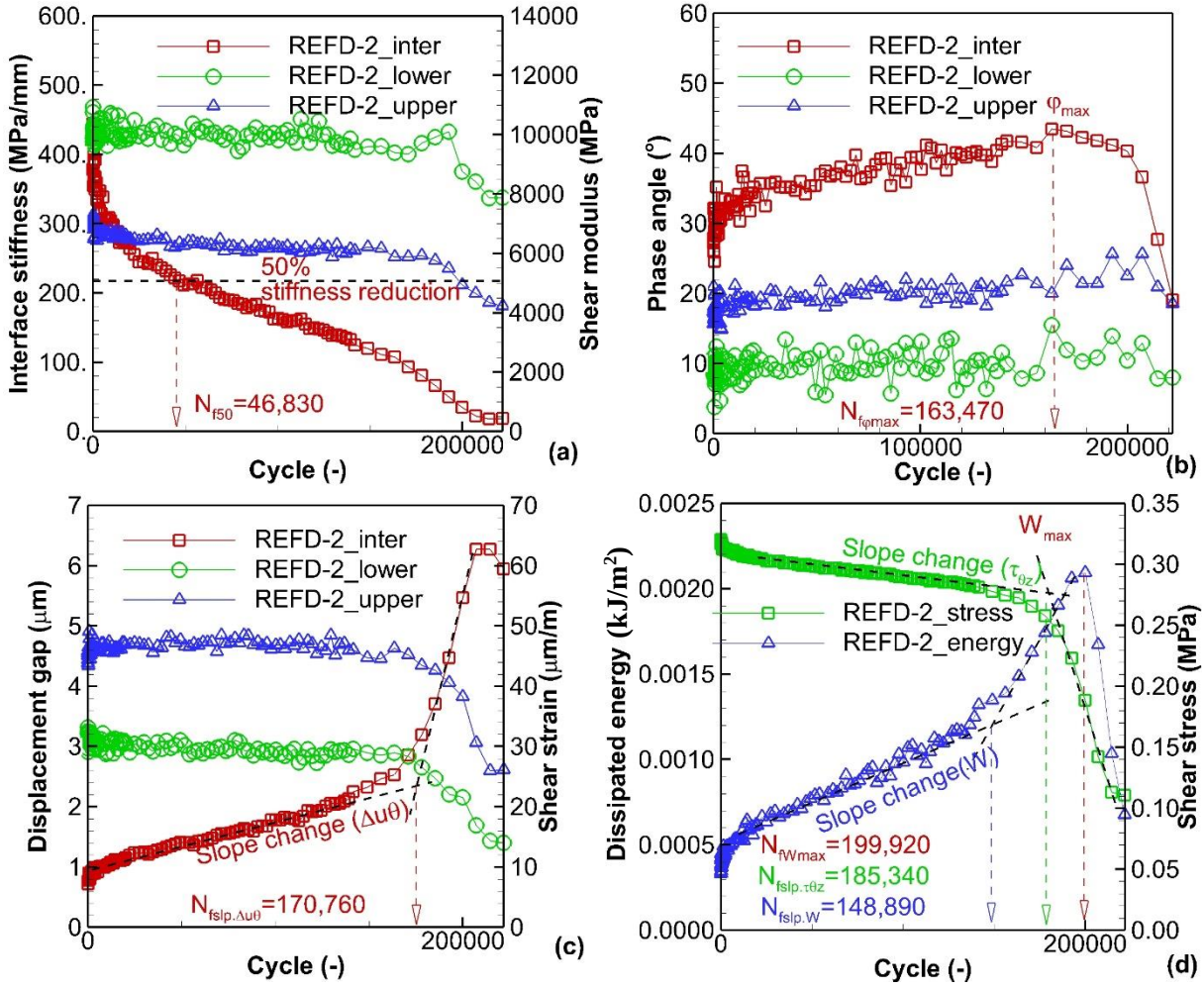

Figure B.3: Fatigue evolution for sample REFD-2 tested with $\varepsilon_{\theta zg\_0}$= 50 μm/m, σ_{zz} = -0.026 MPa: (a) norm of interface shear stiffness ($|K^*_{\theta z}|$), and of complex shear moduli of upper and lower layers ($|G^*_{\theta z.up}|$, and $|G^*_{\theta z.low}|$(b) phase angle of interface complex shear stiffness ($\varphi_{K\theta z}$), and of complex shear moduli of layers ($\varphi_{G.up}$, $\varphi_{G.low}$); (c) amplitude of displacement gap at the interface (Δu_{θ_0}) and shear strains in layers ($\varepsilon_{\theta z.up\_0}$, $\varepsilon_{\theta z.low\_0}$), (d) dissipated energy at the interface (W) and shear stress amplitude ($\tau_{\theta z\_0}$)

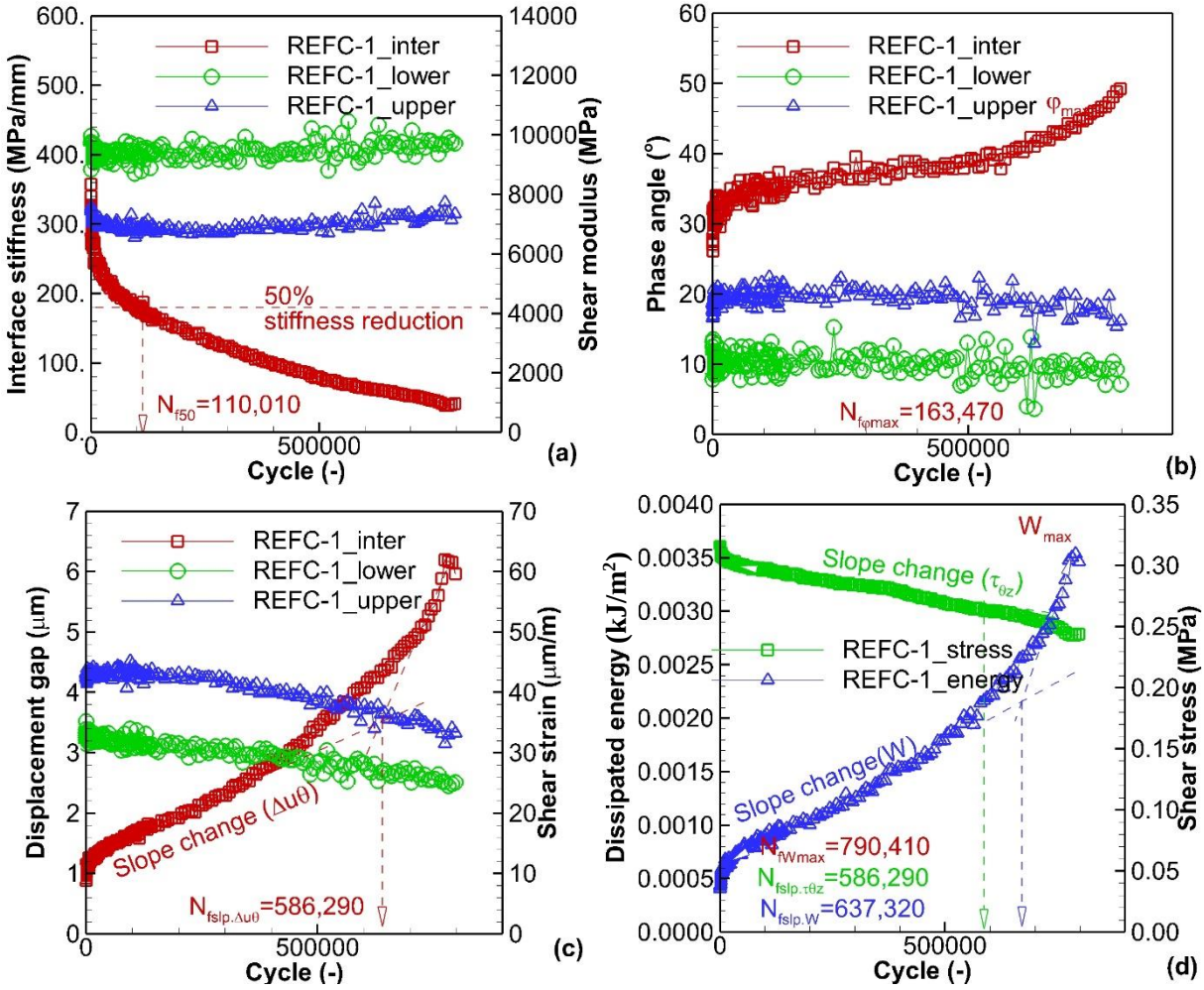

Figure B.4: Fatigue evolution for sample REFC-1 tested with $\varepsilon_{\theta zg\_0}$= 50 μm/m, , σ_{zz} = -0.125 MPa: (a) norm of interface shear stiffness ($|K^*_{\theta z}|$), and of complex shear moduli of upper and lower layers ($|G^*_{\theta z.up}|$, and $|G^*_{\theta z.low}|$(b) phase angle of interface complex shear stiffness ($\varphi_{K\theta z}$), and of complex shear moduli of layers ($\varphi_{G.up}$, $\varphi_{G.low}$); (c) amplitude of displacement gap at the interface (Δu_{θ_0}) and shear strains in layers ($\varepsilon_{\theta z.up\_0}$, $\varepsilon_{\theta z.low\_0}$), (d) dissipated energy at the interface (W) and shear stress amplitude ($\tau_{\theta z\_0}$)

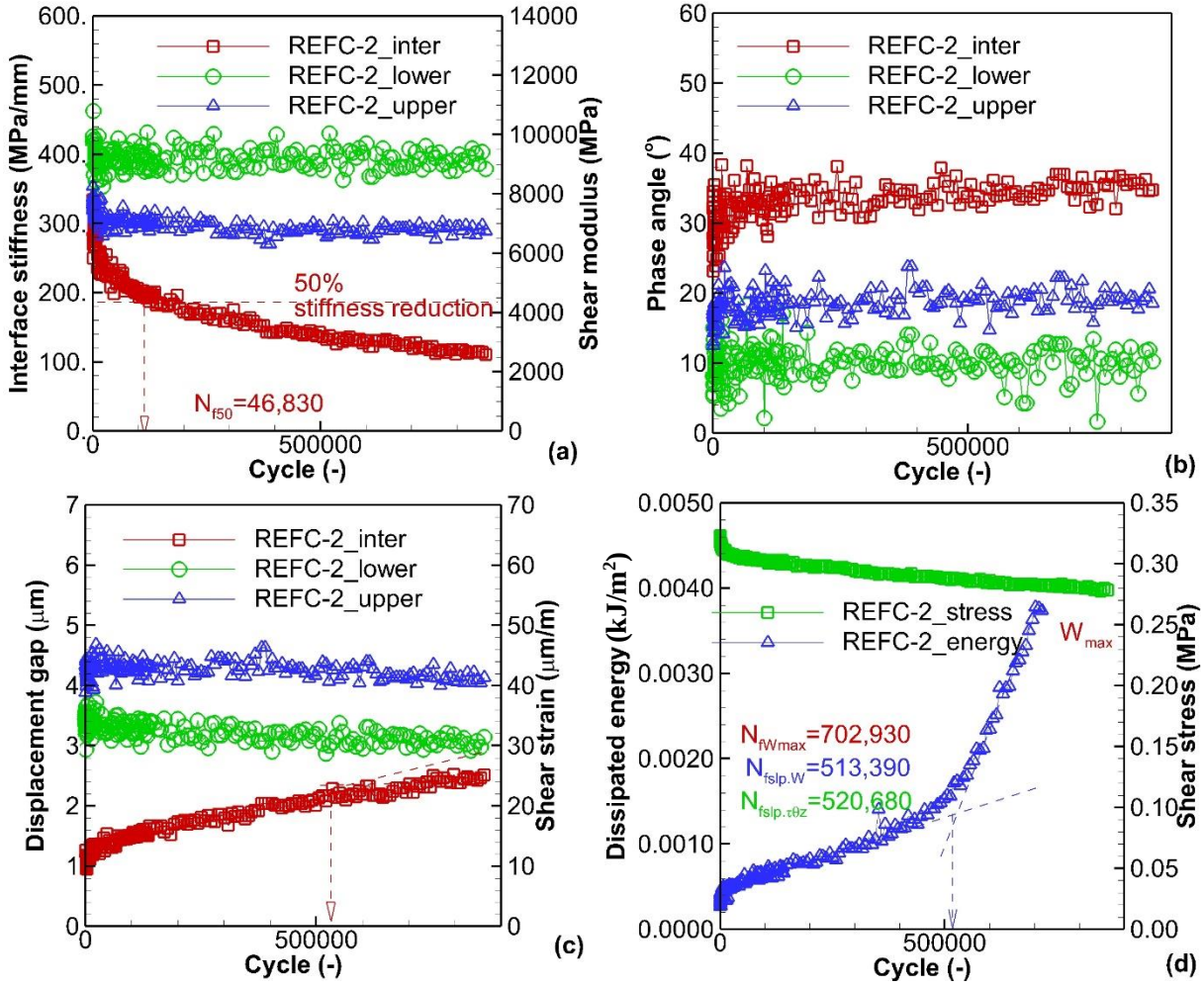

Figure B.5: Fatigue evolution for sample REFC-2 tested with $\varepsilon_{\theta zg\_0}$= 50 μm/m, , σ_{zz} = -0.125 MPa: (a) norm of interface shear stiffness ($|K^*_{\theta z}|$), and of complex shear moduli of upper and lower layers ($|G^*_{\theta z.up}|$, and$|G^*_{\theta z.low}|$(b) phase angle of interface complex shear stiffness ($\varphi_{K\theta z}$), and of complex shear moduli of layers ($\varphi_{G.up}$, $\varphi_{G.low}$); (c) amplitude of displacement gap at the interface (Δu_{θ_0}) and shear strains in layers ($\varepsilon_{\theta z.up\_0}$, $\varepsilon_{\theta z.low\_0}$), (d) dissipated energy at the interface (W) and shear stress amplitude ($\tau_{\theta z\_0}$)

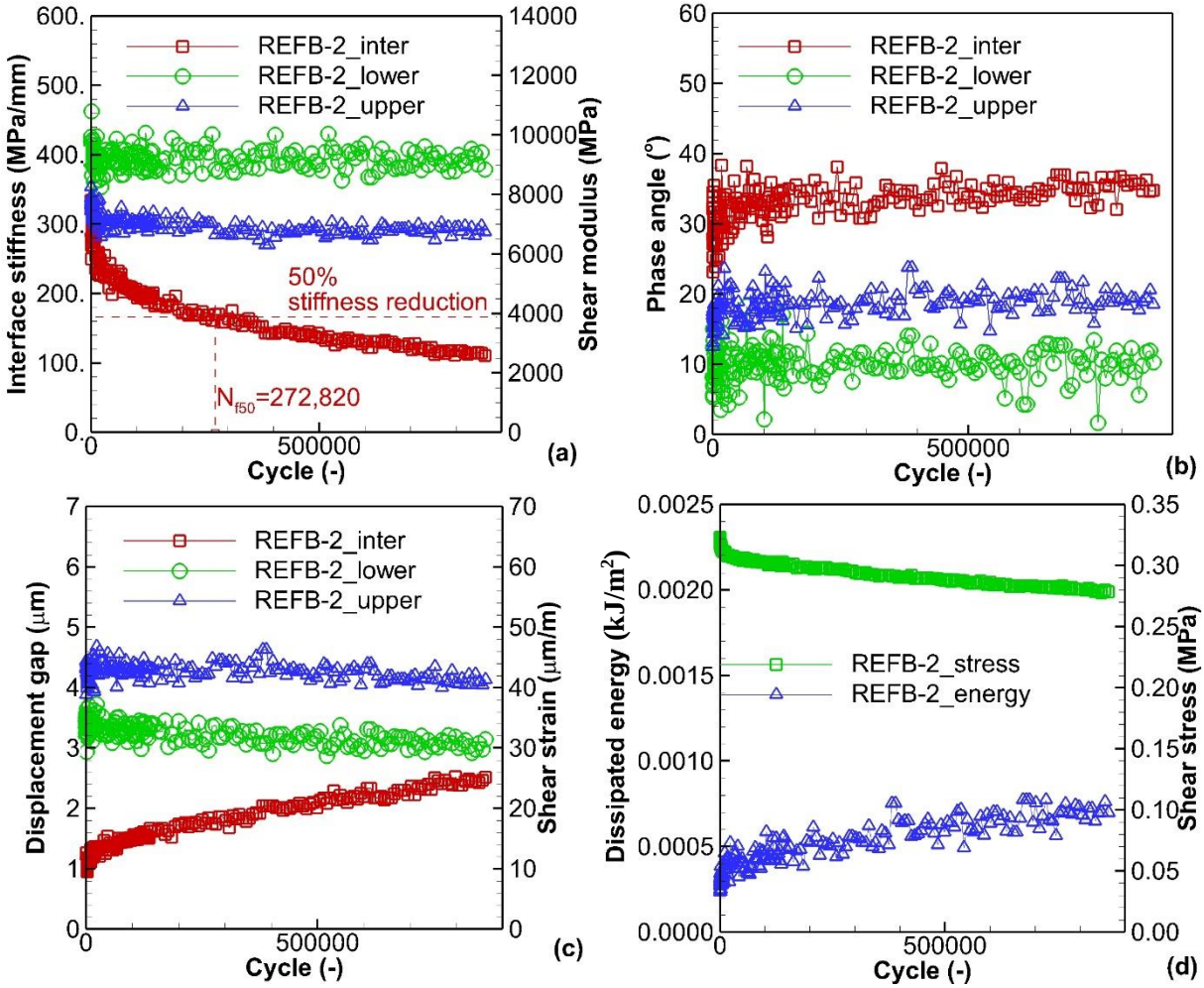

Figure B.6: Fatigue evolution for sample REFB-2 tested with $\varepsilon_{\theta zg\_0}$= 50 μm/m, , σ_{zz} = -0.250 MPa: (a) norm of interface shear stiffness ($|K^*_{\theta z}|$), and of complex shear moduli of upper and lower layers ($|G^*_{\theta z.up}|$, and $|G^*_{\theta z.low}|$(b) phase angle of interface complex shear stiffness ($\varphi_{K\theta z}$), and of complex shear moduli of layers ($\varphi_{G.up}$, $\varphi_{G.low}$); (c) amplitude of displacement gap at the interface (Δu_{θ_0}) and shear strains in layers ($\varepsilon_{\theta z.up\_0}$, $\varepsilon_{\theta z.low\_0}$), (d) dissipated energy at the interface (W) and shear stress amplitude ($\tau_{\theta z\_0}$)

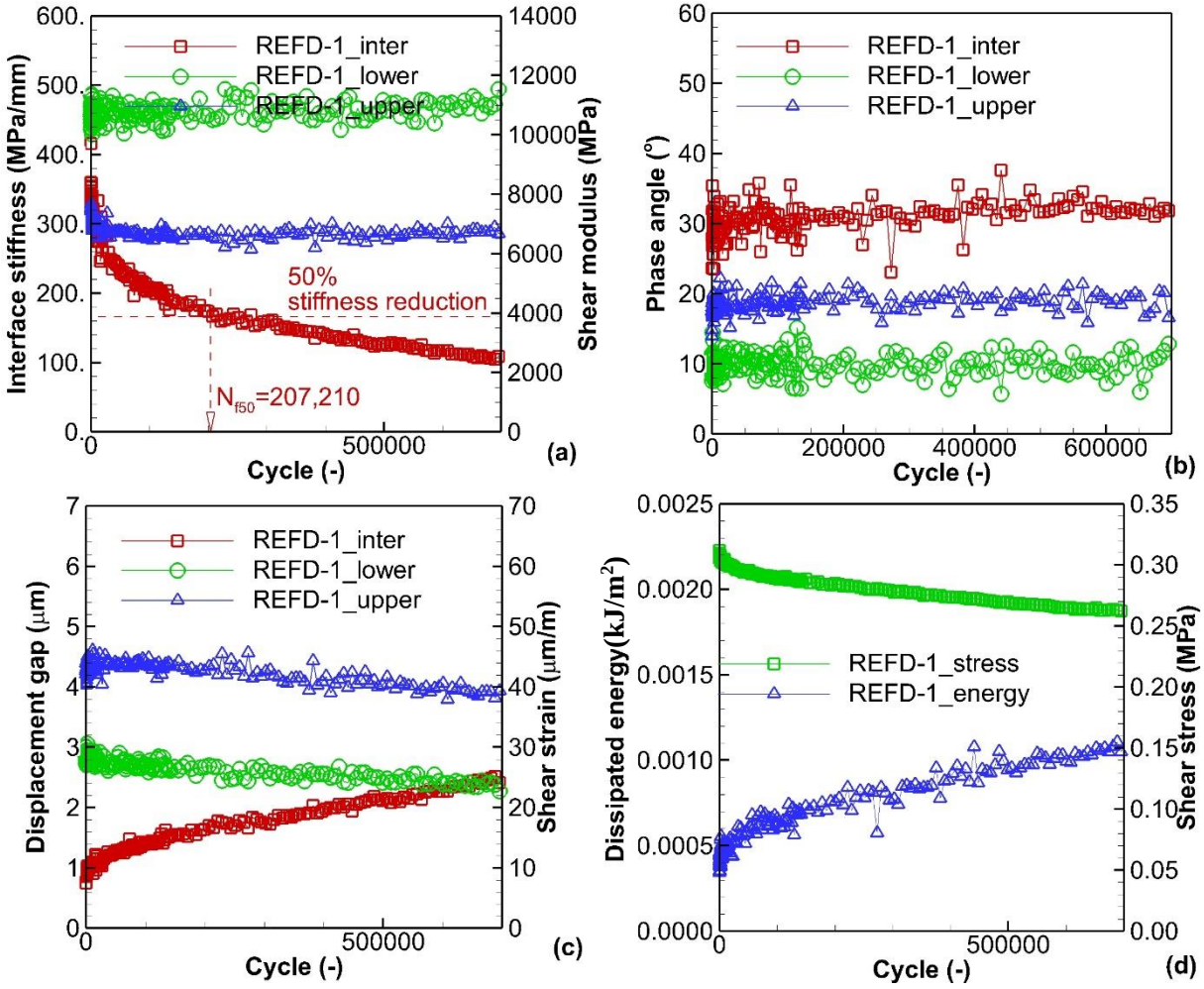

Figure B.7: Fatigue evolution for sample REFD-1 tested with $\varepsilon_{\theta zg\_0}$= 50 μm/m, , σ_{zz} = -0.250 MPa: (a) norm of interface shear stiffness ($|K^*_{\theta z}|$), and of complex shear moduli of upper and lower layers ($|G^*_{\theta z.up}|$, and$|G^*_{\theta z.low}|$(b) phase angle of interface complex shear stiffness ($\varphi_{K\theta z}$), and of complex shear moduli of layers ($\varphi_{G.up}$, $\varphi_{G.low}$); (c) amplitude of displacement gap at the interface (Δu_{θ_0}) and shear strains in layers ($\varepsilon_{\theta z.up\_0}$, $\varepsilon_{\theta z.low\_0}$), (d) dissipated energy at the interface (W) and shear stress amplitude ($\tau_{\theta z\_0}$)

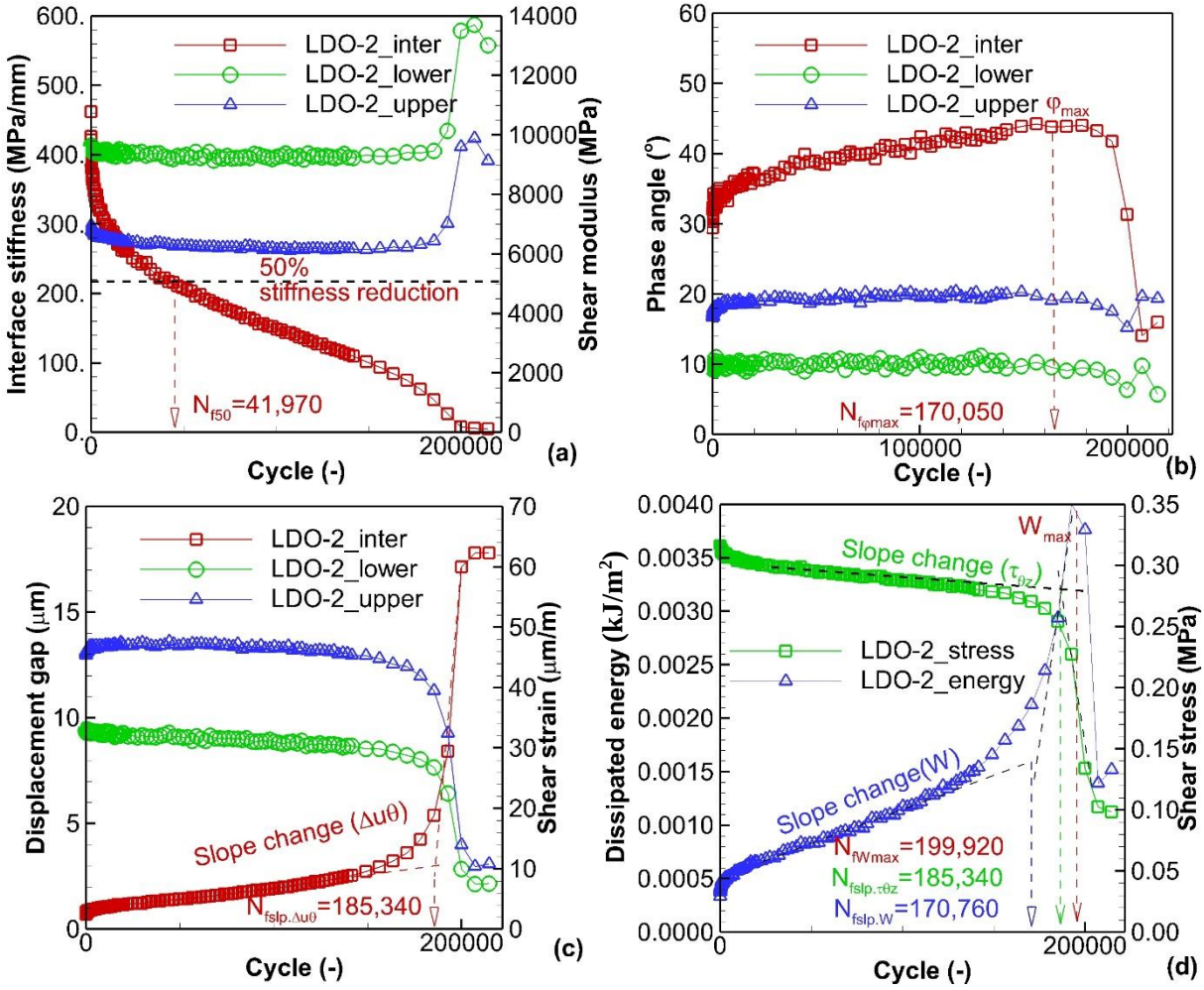

Figure B.8: Fatigue evolution for sample LDO-2 tested with $\varepsilon_{\theta zg\_0}$= 50 µm/m, , σ_{zz} = -0.026 MPa: (a) norm of interface shear stiffness ($|K^*_{\theta z}|$), and of complex shear moduli of upper and lower layers ($|G^*_{\theta z.up}|$, and$|G^*_{\theta z.low}|$(b) phase angle of interface complex shear stiffness ($\varphi_{K\theta z}$), and of complex shear moduli of layers ($\varphi_{G.up}$, $\varphi_{G.low}$); (c) amplitude of displacement gap at the interface (Δu_{θ_0}) and shear strains in layers ($\varepsilon_{\theta z.up\_0}$, $\varepsilon_{\theta z.low\_0}$), (d) dissipated energy at the interface (W) and shear stress amplitude ($\tau_{\theta z\_0}$)

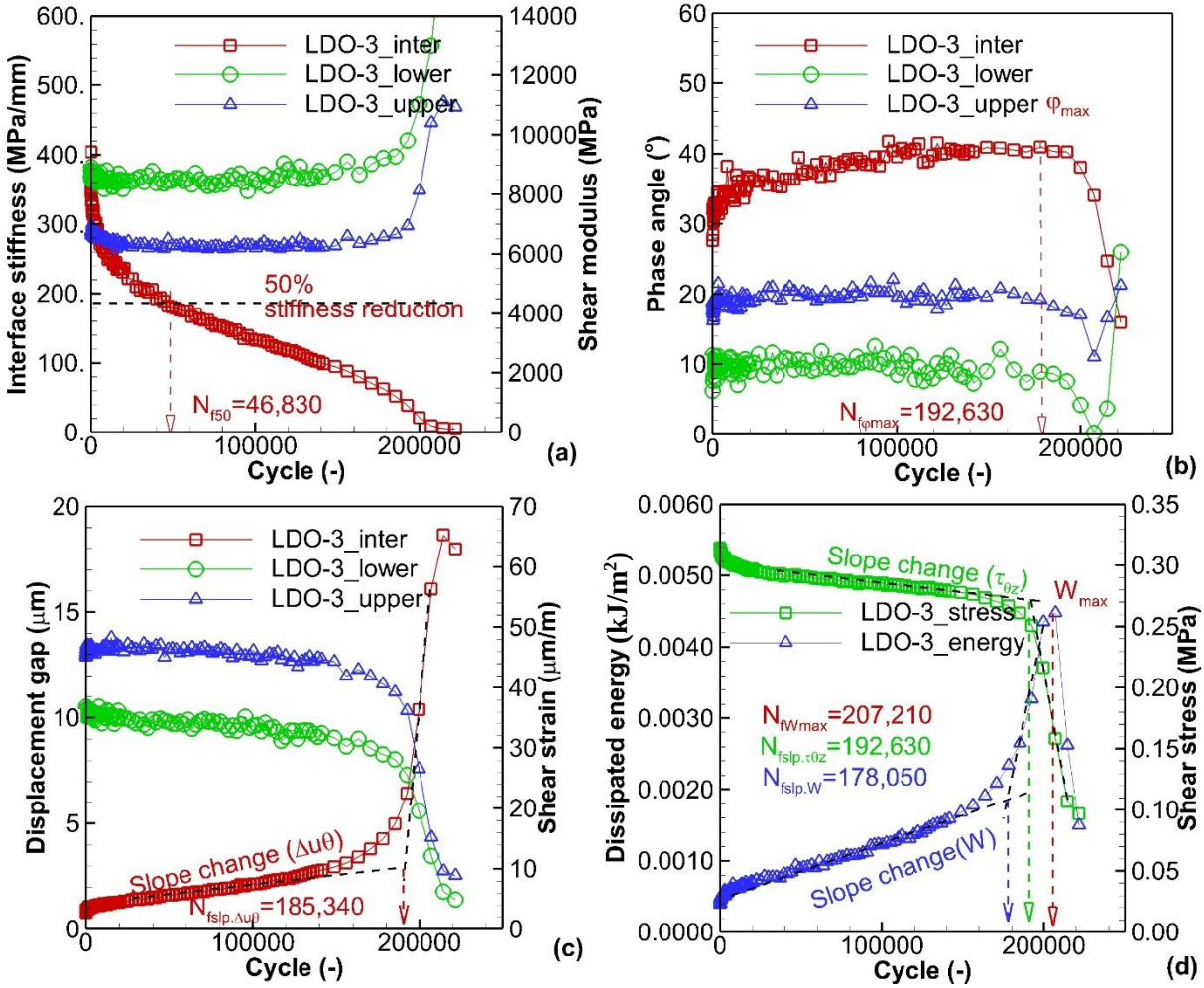

Figure B.9: Fatigue evolution for sample LDO-3 tested with $\varepsilon_{\theta zg\_0}$= 50 µm/m, , σ_{zz} = -0.026 MPa: (a) norm of interface shear stiffness ($|K^*_{\theta z}|$), and of complex shear moduli of upper and lower layers ($|G^*_{\theta z.up}|$, and$|G^*_{\theta z.low}|$(b) phase angle of interface complex shear stiffness ($\varphi_{K\theta z}$), and of complex shear moduli of layers ($\varphi_{G.up}$, $\varphi_{G.low}$); (c) amplitude of displacement gap at the interface (Δu_{θ_0}) and shear strains in layers ($\varepsilon_{\theta z.up\_0}$, $\varepsilon_{\theta z.low\_0}$), (d) dissipated energy at the interface (W) and shear stress amplitude ($\tau_{\theta z\_0}$)

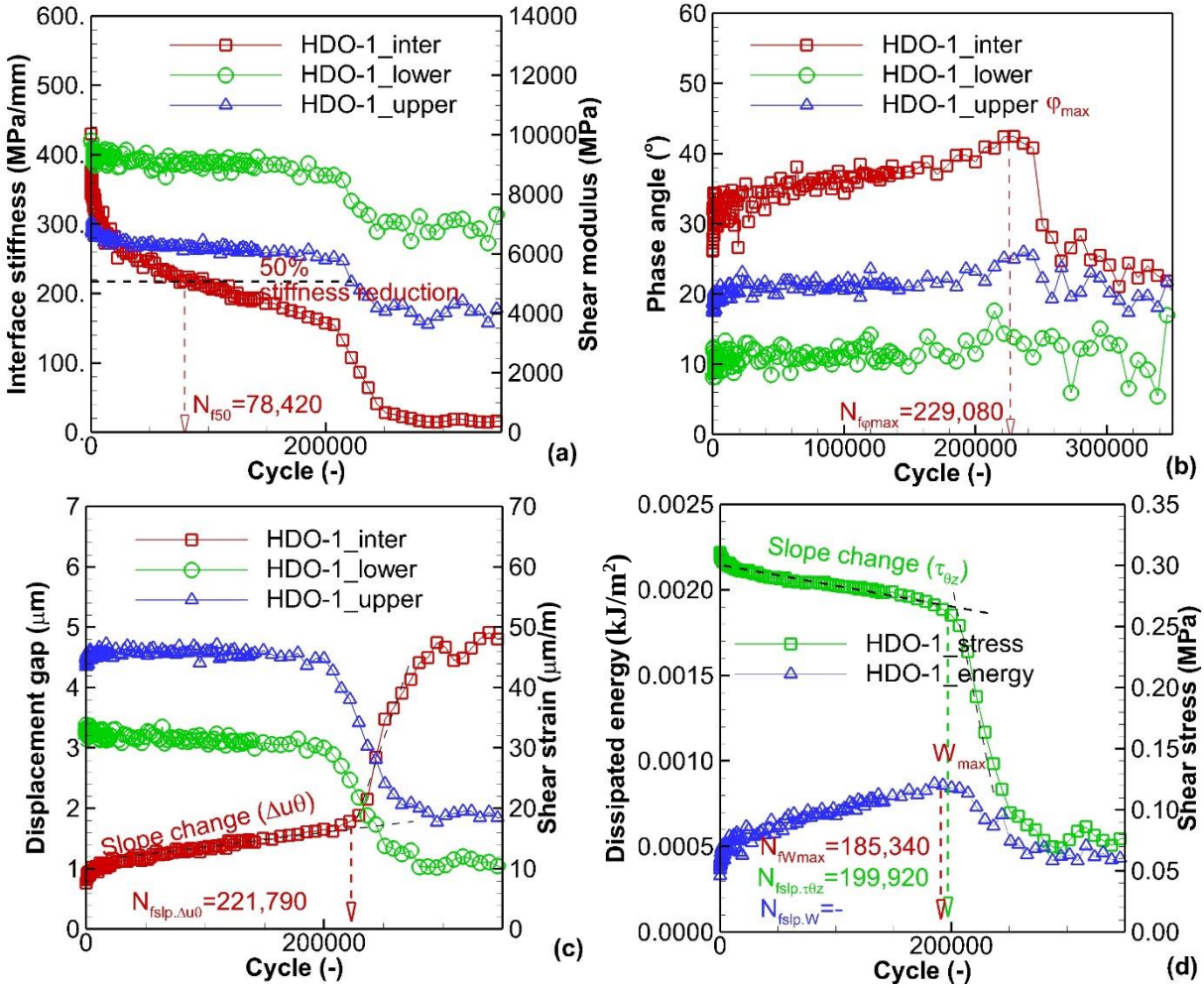

Figure B.10: Fatigue evolution for sample HDO-1 tested with $\varepsilon_{\theta zg\_0}$= 50 μm/m, , σ_{zz} = -0.026 MPa: (a) norm of interface shear stiffness ($|K^*_{\theta z}|$), and of complex shear moduli of upper and lower layers ($|G^*_{\theta z.up}|$, and$|G^*_{\theta z.low}|$(b) phase angle of interface complex shear stiffness ($\varphi_{K\theta z}$), and of complex shear moduli of layers ($\varphi_{G.up}$, $\varphi_{G.low}$); (c) amplitude of displacement gap at the interface (Δu_{θ_0}) and shear strains in layers ($\varepsilon_{\theta z.up\_0}$, $\varepsilon_{\theta z.low\_0}$), (d) dissipated energy at the interface (W) and shear stress amplitude ($\tau_{\theta z\_0}$)

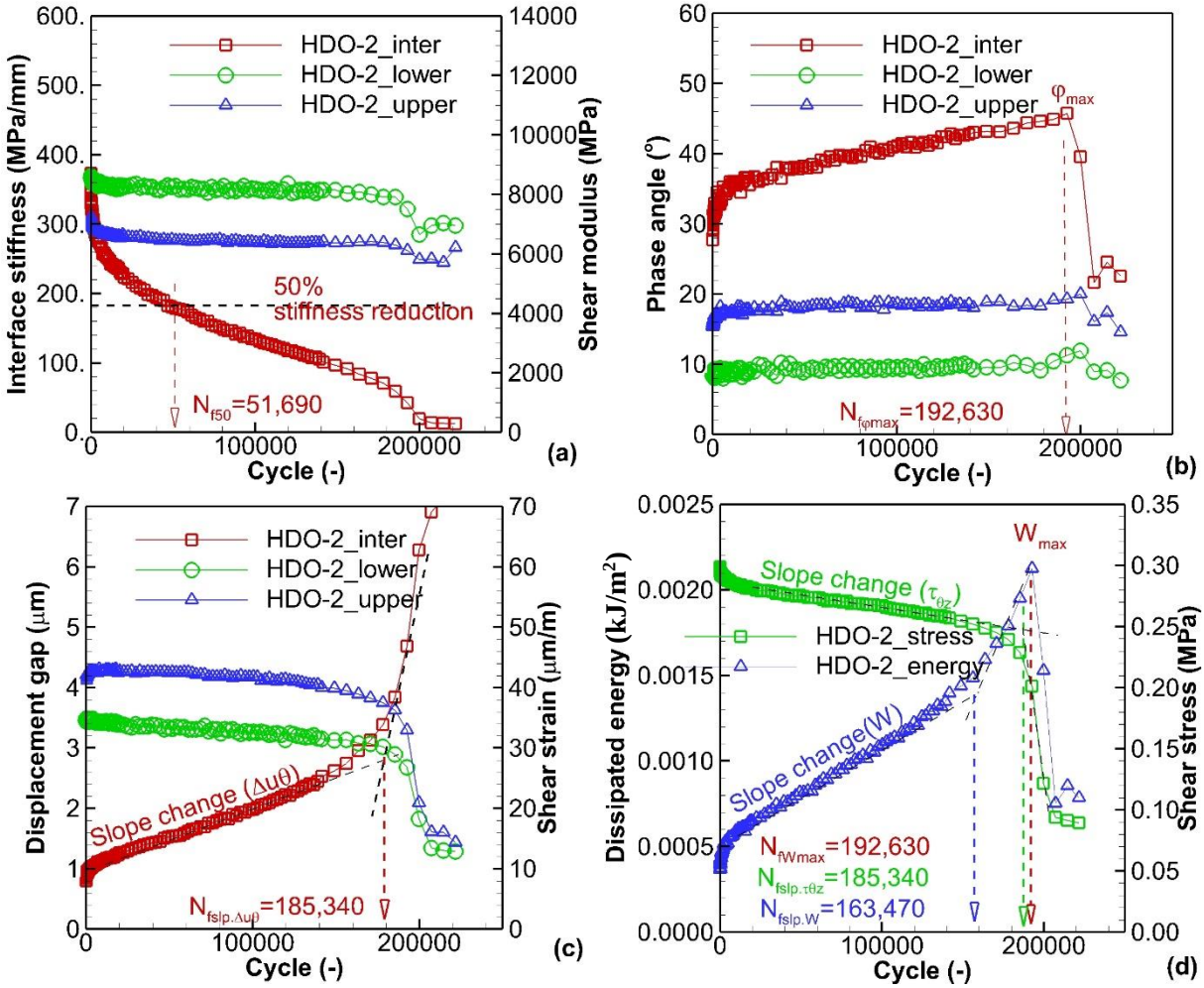

Figure B.11: Fatigue evolution for sample HDO-2 tested with $\varepsilon_{\theta zg\_0}$= 50 μm/m, , σ_{zz} = -0.026 MPa: (a) norm of interface shear stiffness ($|K^*_{\theta z}|$), and of complex shear moduli of upper and lower layers ($|G^*_{\theta z.up}|$, and$|G^*_{\theta z.low}|$(b) phase angle of interface complex shear stiffness ($\varphi_{K\theta z}$), and of complex shear moduli of layers ($\varphi_{G.up}$, $\varphi_{G.low}$); (c) amplitude of displacement gap at the interface (Δu_{θ_0}) and shear strains in layers ($\varepsilon_{\theta z.up\_0}$, $\varepsilon_{\theta z.low\_0}$), (d) dissipated energy at the interface (W) and shear stress amplitude ($\tau_{\theta z\_0}$)

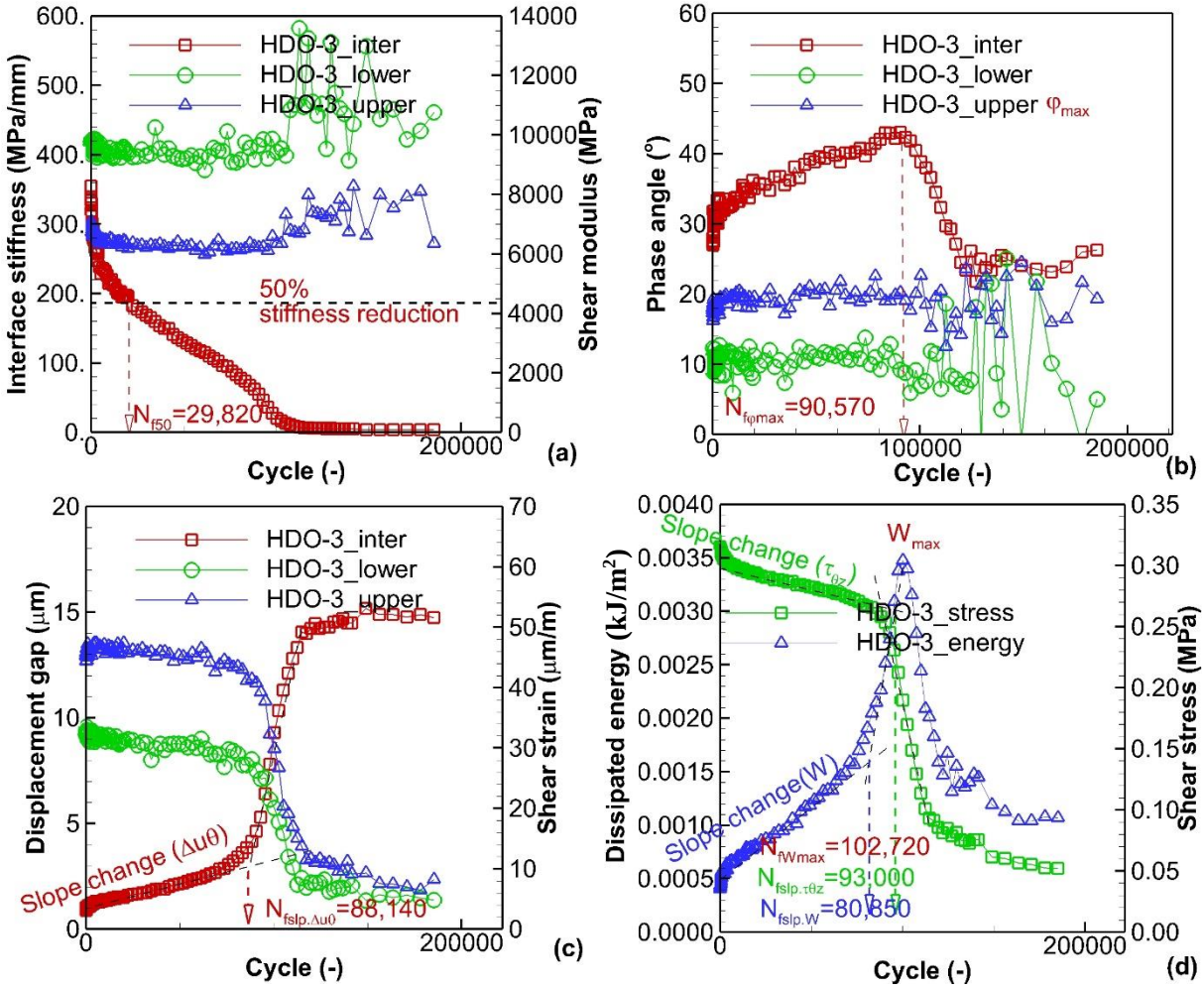

Figure B.12: Fatigue evolution for sample HDO-3 tested with $\varepsilon_{\theta zg\_0}$= 50 μm/m, , σ_{zz} = -0.026 MPa: (a) norm of interface shear stiffness ($|K^*_{\theta z}|$), and of complex shear moduli of upper and lower layers ($|G^*_{\theta z.up}|$, and $|G^*_{\theta z.low}|$(b) phase angle of interface complex shear stiffness ($\varphi_{K\theta z}$), and of complex shear moduli of layers ($\varphi_{G.up}$, $\varphi_{G.low}$); (c) amplitude of displacement gap at the interface (Δu_{θ_0}) and shear strains in layers ($\varepsilon_{\theta z.up\_0}$, $\varepsilon_{\theta z.low\_0}$), (d) dissipated energy at the interface (W) and shear stress amplitude ($\tau_{\theta z\_0}$)

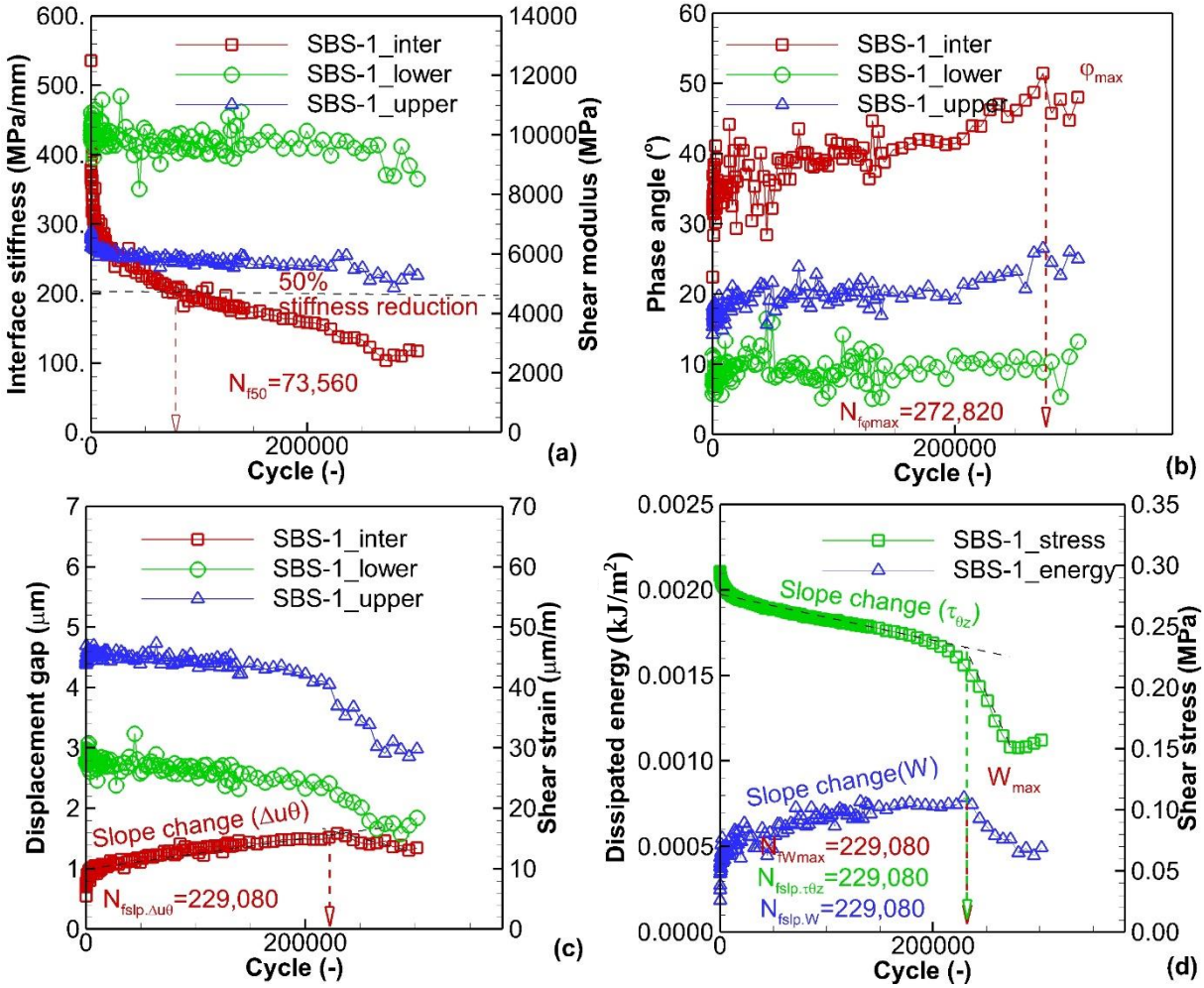

Figure B.13: Fatigue evolution for sample SBS-1 tested with $\varepsilon_{\theta zg\_0}$= 50 µm/m, , σ_{zz} = -0.026 MPa: (a) norm of interface shear stiffness ($|K^*_{\theta z}|$), and of complex shear moduli of upper and lower layers ($|G^*_{\theta z.up}|$, and$|G^*_{\theta z.low}|$(b) phase angle of interface complex shear stiffness ($\varphi_{K\theta z}$), and of complex shear moduli of layers ($\varphi_{G.up}$, $\varphi_{G.low}$); (c) amplitude of displacement gap at the interface (Δu_{θ_0}) and shear strains in layers ($\varepsilon_{\theta z.up\_0}$, $\varepsilon_{\theta z.low\_0}$), (d) dissipated energy at the interface (W) and shear stress amplitude ($\tau_{\theta z\_0}$)

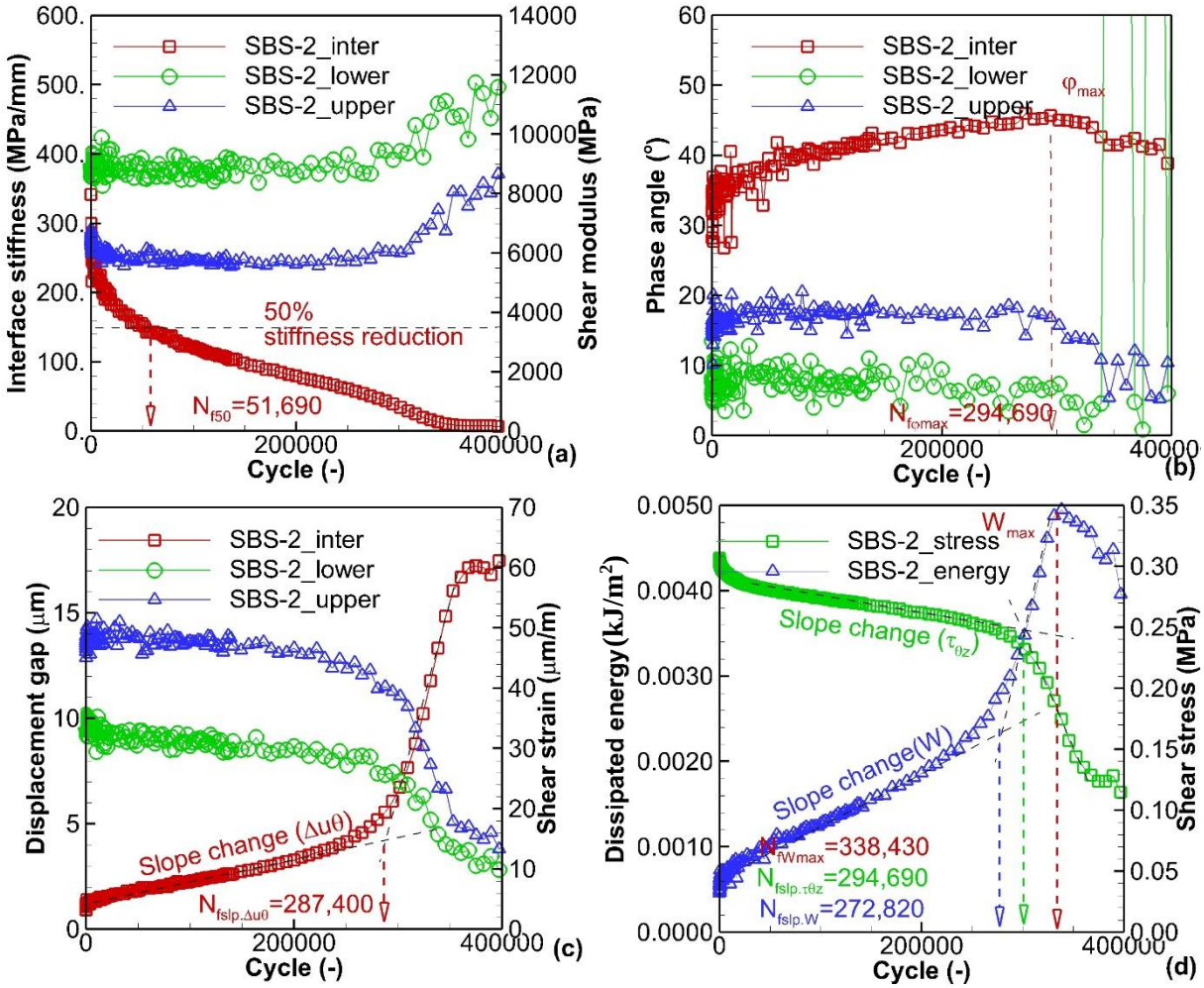

Figure B.14: Fatigue evolution for sample SBS-2 tested with $\varepsilon_{\theta zg\_0}$= 50 μm/m, , σ_{zz} = -0.026 MPa: (a) norm of interface shear stiffness ($|K^*_{\theta z}|$), and of complex shear moduli of upper and lower layers ($|G^*_{\theta z.up}|$, and$|G^*_{\theta z.low}|$(b) phase angle of interface complex shear stiffness ($\varphi_{K\theta z}$), and of complex shear moduli of layers ($\varphi_{G.up}$, $\varphi_{G.low}$); (c) amplitude of displacement gap at the interface (Δu_{θ_0}) and shear strains in layers ($\varepsilon_{\theta z.up\_0}$, $\varepsilon_{\theta z.low\_0}$), (d) dissipated energy at the interface (W) and shear stress amplitude ($\tau_{\theta z\_0}$)

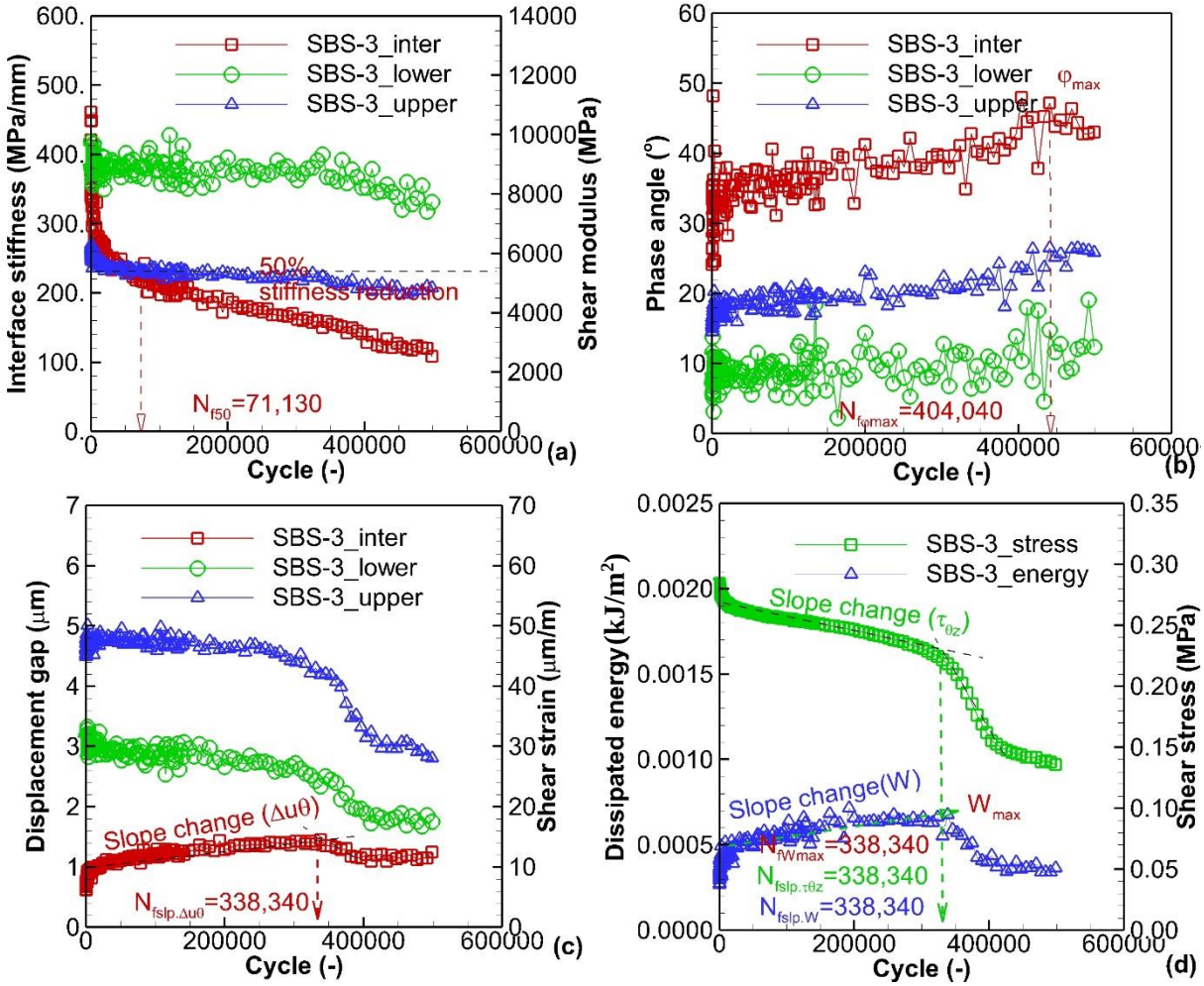

Figure B.15: Fatigue evolution for sample SBS-3 tested with $\varepsilon_{\theta zg\_0}$= 50 µm/m, , σ_{zz} = -0.026 MPa: (a) norm of interface shear stiffness ($|K^*_{\theta z}|$), and of complex shear moduli of upper and lower layers ($|G^*_{\theta z.up}|$, and$|G^*_{\theta z.low}|$(b) phase angle of interface complex shear stiffness ($\varphi_{K\theta z}$), and of complex shear moduli of layers ($\varphi_{G.up}$, $\varphi_{G.low}$); (c) amplitude of displacement gap at the interface (Δu_{θ_0}) and shear strains in layers ($\varepsilon_{\theta z.up\_0}$, $\varepsilon_{\theta z.low\_0}$), (d) dissipated energy at the interface (W) and shear stress amplitude ($\tau_{\theta z\_0}$)

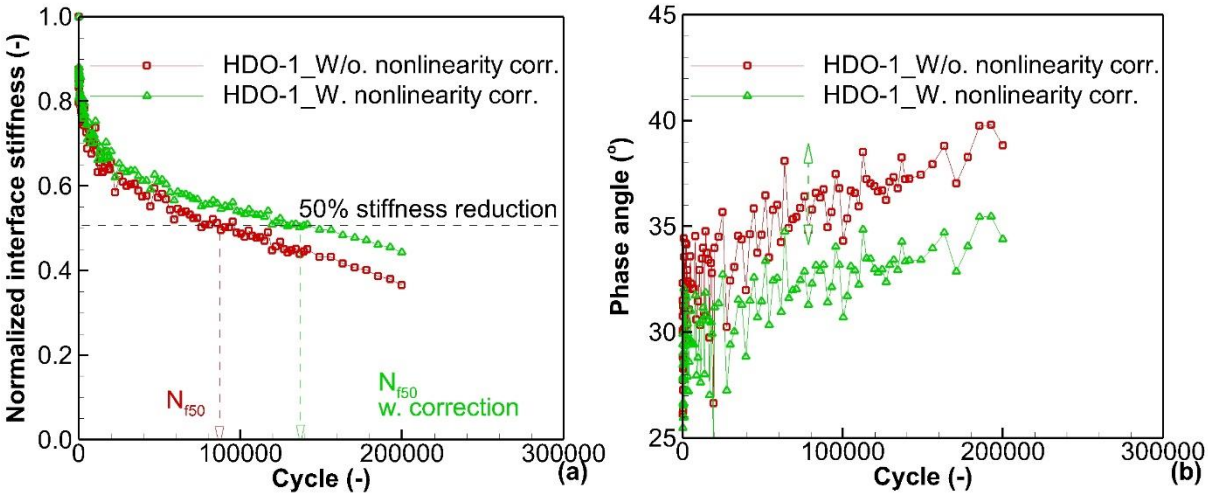

Figure B.16: The influence of nonlinearity to (a) norm and (b) phase angle of complex interface stiffness during a fatigue test of the sample HDO-1

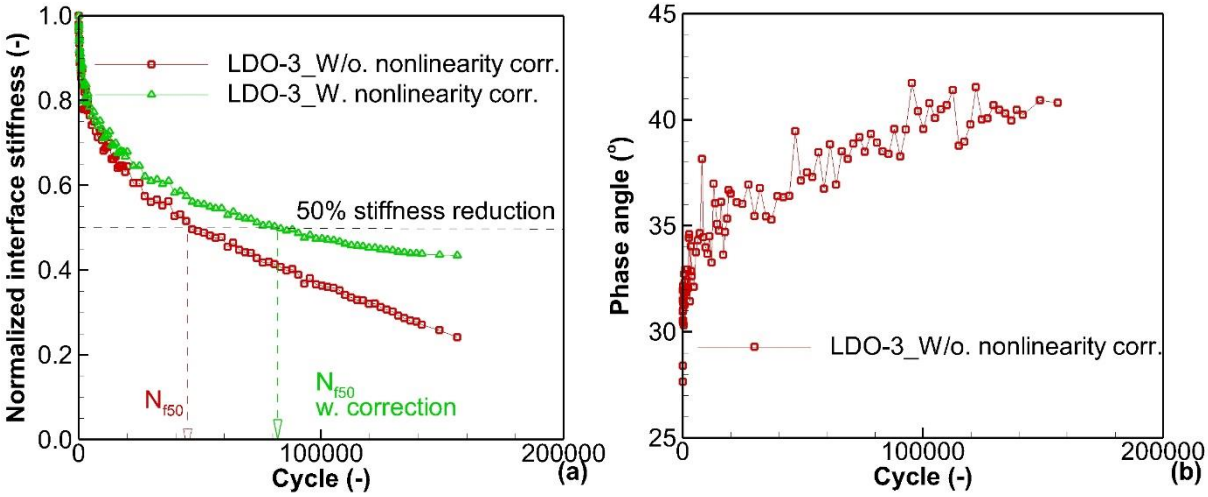

Figure B.17: The influence of nonlinearity to (a) norm and (b) phase angle of complex interface stiffness during a fatigue test of the sample LDO-3

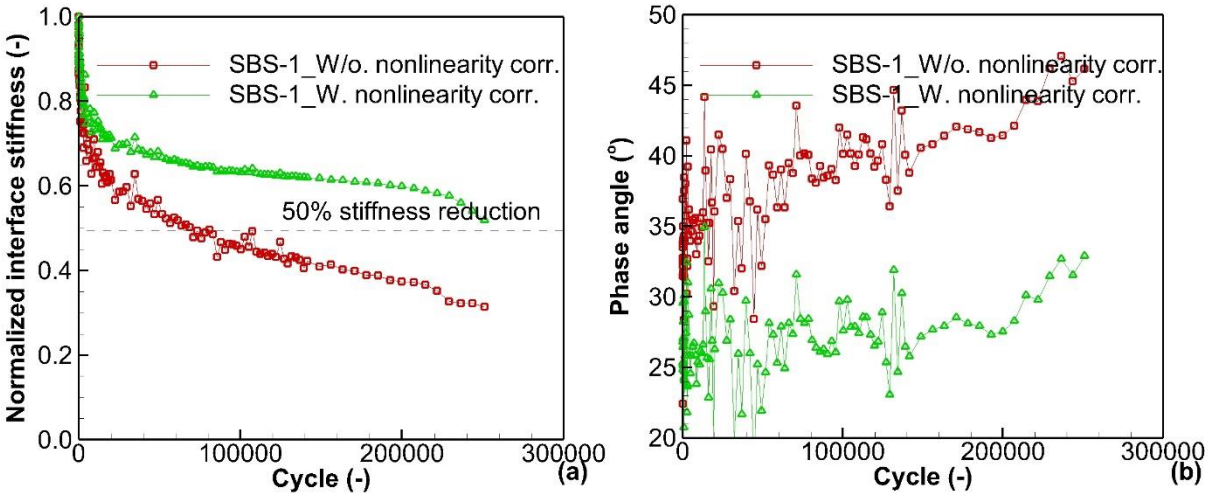

Figure B.18: The influence of nonlinearity to (a) norm and (b) phase angle of complex interface stiffness during a fatigue test of the sample SBS-1

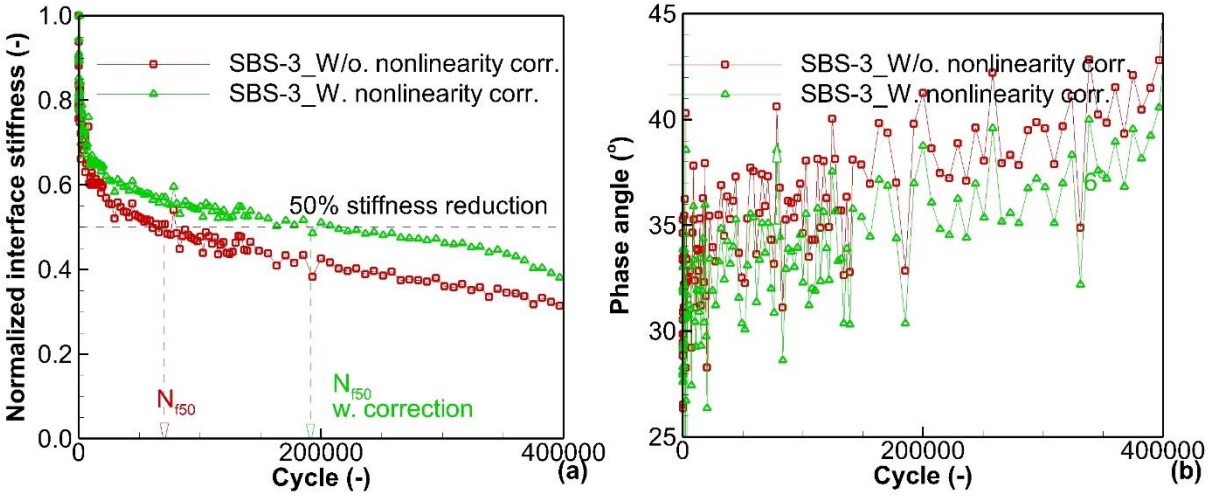

Figure B.19: The influence of nonlinearity to (a) norm and (b) phase angle of complex interface stiffness during a fatigue test of the sample SBS-3